



Ferguson, Ciaran (2016) Imaging spin textures in advanced magnetic nanostructures using Lorentz microscopy. PhD thesis

<http://theses.gla.ac.uk/7238/>

Copyright and moral rights for this thesis are retained by the author

A copy can be downloaded for personal non-commercial research or study, without prior permission or charge

This thesis cannot be reproduced or quoted extensively from without first obtaining permission in writing from the Author

The content must not be changed in any way or sold commercially in any format or medium without the formal permission of the Author

When referring to this work, full bibliographic details including the author, title, awarding institution and date of the thesis must be given.

# Imaging spin textures in advanced magnetic nanostructures using Lorentz microscopy

Ciaran Ferguson

A Thesis presented for the degree of  
Doctor of Philosophy



Materials and Condensed Matter Physics Group  
School of Physics and Astronomy  
University of Glasgow  
United Kingdom

August 2015



# Abstract

This thesis focuses on the imaging of nanomagnetic systems using Lorentz transmission electron microscopy (LTEM), through which their complex structure, magnetisation processes and interactions may be understood.

Magnetic domain walls (DWs) in cylindrical and square nanowires, that possess a complex three dimensional structure, were studied initially. Micromagnetic simulations were used to characterise the structure and stability of cylindrical nanowires and nanotubes across a range of dimensions thus calculating a phase diagram. The phase diagram showed that the less well known asymmetric transverse DW is a metastable state. Square nanowires were fabricated using electron beam lithography and imaged using LTEM. Three different DW types were identified, which were shown to be metastable states.

The effect of anti-symmetric exchange induced at the interface of a magnetic thin film, the Dzyaloshinskii-Moriya interaction (DMI), was simulated for magnetic vortices in permalloy (Py) discs. The results were used to assess methods by which its effect could be measured. The DMI was found to cause the magnetisation around the vortex core to become divergent, depending on its strength. In addition, the DMI modified the magnetisation processes of the disc, causing the vortex to be more easily expelled with increasing DMI strength. By depositing Py thin films capped with Pt and a control sample with Cu, the vortex expulsion field was determined for both samples using LTEM in-situ magnetising experiments. This allowed the strength of DMI to be estimated.

Finally, the magnetostatic interactions of an array of nanomagnets, a variation of artificial spin ice, was investigated. By using LTEM to image the entire array, a reversal sequence was obtained. This showed that the array behaved in a similar manner to a ferromagnetic thin film with strong anisotropy, since the net moment of the array preferred to be directed along the same direction. Micromagnetic simulations revealed that, contrary to artificial spin ice systems, the system did not display frustration. Further simulations suggested that the behaviour of the array could be changed from ferromagnetic to anti-ferromagnetic by reducing the space between elements.

# Declaration

This thesis is a record of research carried out by myself at the Materials and Condensed Matter Physics group, School of Physics and Astronomy at the University of Glasgow from 2011-2015. The work described herein is my own, with the exception of micromagnetic simulations and calculations in Chapter 4 (Fig 4.5c) and 4.8), which were performed by Kayla Fallon. Some of the work in this thesis can be found in the following paper:

- C.A. Ferguson, D.A. MacLaren and S. McVitie “Metastable magnetic domain walls in cylindrical nanowires” J. Magn. Magn. Mater. **381**, 457-462 (2015)

This thesis has not been submitted elsewhere for any other degree or qualification.

**Copyright © 2015 by Ciaran Ferguson.**

“The copyright of this thesis rests with the author. No quotations from it should be published without the author’s prior written consent and information derived from it should be acknowledged”.

*“If you are reading this, I hope something nice happens to you  
today.”*

Graffiti seen in Partick - Anonymous

**Dedicated to my family, le grá mór**

# Acknowledgements

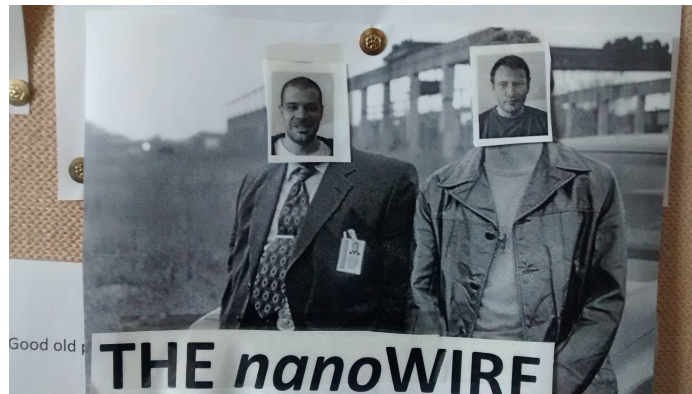
I must first express my gratitude to JEOL Ltd; for both the financial contribution to my studentship and for the opportunity this has given me to work on an exciting project with the new, state-of-the-art JEOL ARM microscope in Glasgow. There are also many individuals to whom I owe a debt of gratitude for their help, advice and friendship over the last four years. First, I would like to thank my supervisors Dr Donald MacLaren and Dr Stephen McVitie for giving me the opportunity to work under their supervision and their guidance and support throughout my time here (including our meetings!). I would also like to thank the other academics, postdocs, technicians, PhD students, visiting students and project students who have made the MCMP group a great place to work. Regarding the work in this thesis, I must acknowledge Prof Bob Stamps for useful discussions and constructive criticism. Thanks to Dr Sam McFadzean for keeping the microscopes working, thanks also to Billy Smith and Colin How for keeping all of the equipment/IT running. In addition, thanks to the staff of the JWNC for their help on numerous occasions with nanofabrication problems. Much appreciated is the help and advice provided by the postdocs: Dr Kerry O'Shea, Dr Maria José Benitez-Romero and Dr Gary Paterson.

Cheers to all my office mates Aaron, Pedro, Shabir, Pablo, Francisco and Marco, it's been great to work in the same place as you all. I won't forget our conversations over coffee about football, politics (not physics!) etc., which I miss already! Thanks to all the people I've played football with, especially the Saturday games and Internazionale, and all the people I've met in Glasgow who have made it a great

place to be! Special thanks to Pedro, Aaron and Francisco for dinners, parties and barbecues!

Thanks to my family in Belfast: my parents, whose support over the years has put me in this position; and my sisters, Fiona (Vote Fiona Ferguson on 5/5/2016!) and Jenny (start writing as soon as possible, trust me!). Finally, special thanks to my girlfriend, Stefanie Lewis, whose love and encouragement have kept me going, and who has had to live with me during this last year! Thank you.

(Below: An interesting representation of the early days of the PhD by Shabir.)



# Contents

<b>Abstract</b>	<b>ii</b>
<b>Declaration</b>	<b>iii</b>
<b>Acknowledgements</b>	<b>v</b>
<b>1 Micromagnetism of thin films and nanostructures</b>	<b>1</b>
1.1 Introduction . . . . .	1
1.2 Ferromagnetic materials . . . . .	2
1.3 Magnetic energy terms . . . . .	5
1.3.1 Exchange energy . . . . .	6
1.3.2 Magnetostatic energy . . . . .	10
1.3.3 Zeeman energy . . . . .	13
1.3.4 Magnetocrystalline anisotropy . . . . .	13
1.4 Micromagnetic simulations . . . . .	14
1.5 Domain walls in thin films and nanowires . . . . .	15
1.6 Spin structures in magnetic systems . . . . .	18
<b>2 Experimental techniques</b>	<b>21</b>
2.1 Introduction . . . . .	21
2.2 Transmission electron microscopy . . . . .	22
2.2.1 Introduction . . . . .	22
2.2.2 Imaging in TEM . . . . .	23

2.2.3	Structural characterisation . . . . .	31
2.2.4	Lorentz microscopy . . . . .	34
2.3	Electron beam lithography . . . . .	50
2.3.1	Overview . . . . .	50
2.3.2	Resist configuration . . . . .	52
2.3.3	TEM substrates . . . . .	57
2.3.4	Metallisation methods . . . . .	58
2.4	Focused ion beam/ scanning electron microscope . . . . .	61
2.5	Atomic force microscopy . . . . .	62
2.6	Pulsed laser deposition . . . . .	64
<b>3</b>	<b>Domain walls in three dimensional nanowires</b>	<b>68</b>
3.1	Introduction . . . . .	68
3.2	Simulation of cylindrical nanostructures . . . . .	71
3.2.1	Methods . . . . .	71
3.2.2	Simulation results . . . . .	73
3.2.3	Experimental image calculation . . . . .	83
3.3	Experimental . . . . .	91
3.3.1	Fresnel imaging . . . . .	93
3.3.2	DPC imaging . . . . .	96
3.4	Conclusions . . . . .	105
<b>4</b>	<b>Interface induced Dzyaloshinskii-Moriya interaction in Py/Pt bi-</b> <b>layers</b>	<b>106</b>
4.1	Introduction . . . . .	106
4.2	Simulations . . . . .	109
4.2.1	Methods . . . . .	109
4.2.2	Results . . . . .	110
4.3	Experimental . . . . .	118
4.4	Conclusions . . . . .	124

---

<b>5</b>	<b>Tunable frustration in nanomagnet arrays</b>	<b>125</b>
5.1	Introduction . . . . .	125
5.2	Methods . . . . .	131
5.3	Results . . . . .	136
5.4	Conclusions . . . . .	147
<b>6</b>	<b>Conclusions and future work</b>	<b>149</b>
	<b>Appendix</b>	<b>172</b>
<b>A</b>	<b>Nmag interpolation</b>	<b>172</b>
<b>B</b>	<b>Artificial spin ice processing from Fresnel image</b>	<b>175</b>



# List of Figures

1.1	Hysteresis loop that is characteristic of a ferromagnetic sample. Important points are marked on the loop. . . . .	2
1.2	Schematic representation of the density of states in a metallic ferromagnet, notably, the occupancy of one spin sub-band is larger than the other. . . . .	4
1.3	Spontaneous magnetisation as a function of temperature for a ferromagnetic material. Loss of ferromagnetic ordering occurs above the Curie temperature, $T_c$ . At this temperature the material becomes paramagnetic and the spins are disordered in the absence of applied fields. . . . .	5
1.4	Arrows representing the orientation of neighbouring spins in a ferromagnet. As defined by Eq 1.4, a) corresponds to a minimum of exchange energy, whereas non-parallel alignment of spins in b) results in increased energy, depending on the angle, $\phi$ , between spins. c) illustrates the situation where the spins are canted to lower DMI energy where the orientation of spins depends on depends on the relative strength of $\mathbf{D}_{ij}$ in Eq 1.8 and $J$ in Eq 1.4. . . . .	7
1.5	Schematic illustrating the three site mechanism of IDMI, which results in a $\mathbf{D}$ vector parallel to the plane of the film, directed along the positive $y$ direction. . . . .	8

1.6	Possible effect of IDMI on two otherwise parallel spins $\mathbf{S}_1$ and $\mathbf{S}_2$ . Two cases are considered, a) for $\mathbf{D}$ perpendicular to the directions of the spins and b) $\mathbf{D}$ parallel to the spins' direction. . . . .	9
1.7	Depiction of the origin of magnetic charges. a) shows a cross-section through a thin film where divergent magnetisation generates charge and b) is a plan view of a uniformly magnetised element that results in magnetisation normal to the surface. c) shows how multi-domain states form to reduce charge in a rectangular element. . . . .	12
1.8	Illustration of shape anisotropy in an ellipsoidal particle. $H_d$ is larger in b) compared to a), which results in larger magnetostatic energy. . .	12
1.9	Vectorial representation of the LLG equation. A magnetic moment precesses about the effective field with damping so that they eventu- ally align. . . . .	14
1.10	Domain walls found in magnetic thin films. a) Bloch walls are found in the thickest films, b) Néel walls are stable for thinner films, while c) cross-tie walls stabilise at intermediate thicknesses. . . . .	16
1.11	Film plane views of a) Transverse, b) asymmetric transverse and c) vortex DWs found in thin planar nanowires, depending on the wire width and thickness. . . . .	18
1.12	Spin structures studied in this thesis. a) shows a 3-D domain wall in a magnetic nanowire; b) is an Lorentz TEM image of a magnetic vortex; and c) shows an artificial spin ice vertex with a monopolar configuration. . . . .	19
2.1	Ray diagrams for a) imaging and b) diffraction mode on the JEOL ARM. The rays are defined and focused by apertures and lenses to illuminate the sample. Depending on the object plane of the diffraction lens (IL1), a real-space image or diffraction pattern is projected onto the viewing screen. . . . .	24

2.2	STEM ray diagram in the JEOL ARM. A probe is formed at the sample which is scanned across the sample. The projector system simply images the BFP and detectors pick up signals associated with a range of scattering angles, bright field (BF) and annular dark field (ADF) detectors are shown as examples. . . . .	26
2.3	Overview of a thermionic emission gun a) and a cold field emission gun b). . . . .	28
2.4	Cross-section view of a split pole piece lens. a) increasing current through its copper coils increases the magnetic field strength which focuses electrons more strongly, b) illustrates the magnetic field distribution produced by the lens. . . . .	30
2.5	Illustration of $C_s$ aberrations in an electron lens. Rays that are further off-axis have cross-over points closer to the lens. . . . .	30
2.6	Schematic diagram of the Ewald sphere construction in a reciprocal lattice. . . . .	32
2.7	Diffraction patterns from a) a single crystal, b) polycrystalline and c) amorphous samples. . . . .	32
2.8	Ray diagrams for a) bright field and b) dark field imaging. The direct beam in a) is tilted in b) so that rays that were previously scattered off-axis are scattered back on-axis. . . . .	33
2.9	TEM images from a polycrystalline thin film with diffraction patterns corresponding to the images inset; a) shows a bright field image which the image is formed from unscattered electrons and b) is a dark field image where the outer rings of the diffraction pattern are selected. . .	34
2.10	Representation of the classical Lorentz force where the electron beam is travelling in the z-direction, path shown by arrows, is deflected by magnetic induction in the x-y plane by an angle $\beta$ . . . . .	35
2.11	A representation of the thought experiment of the Aharonov-Bohm effect. Electron beams interfere after taking opposite paths either side of a uniformly magnetised magnet. . . . .	36

- 2.12 Diagram showing the principle behind Fresnel imaging. Defocusing the image allows the observation of contrast which corresponds in this case to two  $180^\circ$  domain walls. Bright and dark walls are labelled as convergent and divergent, respectively. Dashed lines show how using a negative value of defocus selects a virtual object above the object plane where the contrast is reversed. . . . . 38
- 2.13 A series of Fresnel images taken at increasing (a-d) defocus values. No magnetic contrast is visible in a); b) - d) have increasing contrast at the expense of blurring of the image. Defocus values are indicated in  $\mu\text{m}$  on the images. . . . . 39
- 2.14 Fresnel images calculated using Eq 2.21. Two vortices of opposite chirality, in  $1 \mu\text{m}$  discs, are calculated. Each results in reversed contrast at the core. . . . . 40
- 2.15 Low angle diffraction image showing the scattering of the beam from a cross-grating sample. The scale here is  $\sim 3$  orders of magnitude smaller than the images in Fig 2.7. . . . . 41
- 2.16 Simple split detector to show how the deflection of the beam is quantified. For the imaging to be linear, the convergence semi-angle,  $\alpha$ , needs to be much larger than the Lorentz deflection,  $\beta$ , so that the area  $2\alpha\beta$  is rectangular. . . . . 42
- 2.17 Schematic displaying the operating principle of DPC. A focused probe is scanned across the sample and is deflected by the sample's in-plane magnetisation due to the Lorentz force. Deflection results in a displacement from the centre of a segmented detector, this results in a net difference when subtracting signal from opposite quadrants. . . 43
- 2.18 DPC images of a magnetic vortex core confined to a  $2 \mu\text{m}$  permalloy disc. a) and b) show orthogonal components of magnetic induction, c) shows a colour map corresponding to rotational magnetisation, as indicated by the inset arrows, and d) is a bright field "sum" image; images a)-c) correlate with simulated images, shown in Fig 2.19. . . . 44

2.19	Simulated DPC images from the result of a micromagnetic simulation of a 2 $\mu\text{m}$ permalloy disc that contains a magnetic vortex state. a) and b) show orthogonal components of the magnetic induction, integrated through the sample. . . . .	44
2.20	Eight quadrant detector used in modified DPC. Opposite external (Ext) sectors are subtracted from each other to quantify the beam deflection. . . . .	45
2.21	a) Graph showing the variation of lens strength with camera length for standard camera lengths in the JEOL ARM microscope for each lens of the projector system. b) shows a truncated version, relevant to this work. . . . .	46
2.22	GUI written to tune the camera length of Lorentz STEM beyond standard camera lengths. . . . .	47
2.23	Two sets of images showing the effect of varying $\kappa$ in MDPC. Difference, colour images and line profiles of a 180° domain wall are shown for a), b), c) $\kappa = 0.86$ and d), e), f) $\kappa = 0.95$ . The larger $\kappa$ value clearly improves the magnetic contrast. . . . .	47
2.24	GUI written to control the tilt angle of the stage on the JEOL ARM microscope and thus automate a tilt series. The GUI allows the user to input start, end and increment angles, or equivalent in-plane fields. The option also exists to acquire and save images taken on the CCD camera. . . . .	49
2.25	Schematic showing the difference between positive (left) positive and (right) negative resist tones. The electron beam weakens the positive resist which results in the removal of exposed areas during development; the opposite occurs for negative resists, only the exposed regions remain after development. . . . .	51
2.26	Schematic illustrating the process stages following development. The sample is metallised then the remaining resist is dissolved (lift-off), leaving the pattern. . . . .	51

2.27	Single layer (left) and bilayer (right) configurations of the lift-off technique. The single layer ultimately leads to flagging on the nanostructures after lift-off, this is avoided by using the bilayer technique. . . .	53
2.28	Examples of situations where lift-off has resulted in a) flagging and b) the metal not lifting off at all. . . . .	53
2.29	Measured nanowire widths versus designed size. Lines represents linear fits to the data. . . . .	55
2.30	Measured width of spin ice elements for increasing dose. Two designs are investigated; for a minimum separation of a) 50 nm and b) 100 nm . Lines represent linear fits to the data. . . . .	56
2.31	TEM image of an overexposed spin ice array. Elements are misshapen at close proximity or joined as within the box in the bottom left-hand corner. . . . .	56
2.32	Silicon nitride membrane array with $2 \times 2$ membranes, each with an electron transparent window in the centre. . . . .	57
2.33	Representations of the a) inter- and b) intra- proximity effect. The dotted line represents the written area, the red shading is the actual developed area. . . . .	58
2.34	SEM images of extreme flagging associated with structures fabricated using PLD as metallisation technique with lift-off. Height of the flags depends on the thickness of the bottom layer of resist. . . . .	59
2.35	Schematic of the thermal evaporator vacuum system showing the relative positions of substrate, QCM and evaporation source (crucible). .	59
2.36	a) a bright field, b) dark field and c) diffraction pattern images from TEM, showing the polycrystallinity of thermally evaporated Py films. d) shows a characteristic hysteresis loop. . . . .	60
2.37	a) imaging in SEM and b) milling using FIB lithography. . . . .	61
2.38	The operation of tapping mode AFM. . . . .	62
2.39	Examples of AFM images. a) shows a surface scan, while b) and c) shows, respectively, a step height scan and a line profile across the step.	63

2.40	Overview of the PLD vacuum system. A focused laser is directed through the window onto the target carousel. . . . .	64
2.41	The ablation process in PLD. a) As the laser strikes the target, some material is vaporised; b) if dense enough, it expands; c) the expansion sputters material from the target. . . . .	65
2.42	SEM image of the PLD Py target. a) shows the general morphology of the target and b) is a higher magnification image of globule-like structures. . . . .	66
2.43	Reduction of droplets for a situation a) without and b) with an aperture. . . . .	67
3.1	Starting states used for preliminary simulation results, each forcing the magnetisation to lie head-to-head: a) a wire with a central 100 nm section of magnetisation transverse to the wire axis; b) an abrupt 180° transition; c) a central 100 nm section where the magnetisation curls around the wire. . . . .	72
3.2	Illustration showing the process of interpolating a result onto a mesh of different size. This shows (top) the original mesh with the simulation result for a cylindrical nanowire of radius 25 nm and (bottom) the new mesh with the original result interpolated onto the smaller mesh, to be used as a starting state for a nanowire of radius 10 nm. . . . .	73
3.3	A 3-D view of the micromagnetic structure of a) a transverse domain wall (TDW), b) an asymmetric transverse wall (ATDW) and c) a Bloch point wall (BPW). The TDW radius is 17.5 nm, ATDW and BPW radii are both 25 nm. Colours indicate the axial component, $M_z$ , and the arrows show the direction of surface magnetisation. The transition from red to blue gives an illustration of the wall width, although d) shows profiles of axial magnetisation taken where the DW is widest (calculated widths indicated in the legend). Cross-sections through the $r, \theta$ plane, taken at the positions of the wireframes, are inset. . . . .	75

- 3.4 Micromagnetic phase diagram for domain walls in cylindrical nanowires, showing the variation of magnetic energy density wire with nanowire radius for transverse (TDW), asymmetric transverse (ATDW) and Bloch point (BPW) domain walls. The total energy density is plotted with a full line; its two components, magnetostatic and exchange energy, are plotted with dashed lines. . . . . 76
- 3.5 Schematic illustrating the process, from bottom to top, of unrolling surface magnetisation to produce a schematic with  $z$  and  $\theta$  aligned horizontally and vertically, respectively. . . . . 77
- 3.6 “Unrolled” surface magnetisation of a typical a) TDW, b) ATDW and c) BPW. Colours represent the radial component,  $M_r$ , while the arrows represent contributions of the axial and tangential components,  $M_z$  and  $M_\theta$ , respectively. The horizontal scale is in nm. . . . . 78
- 3.7 Cross-sections through the centre of each domain wall showing the divergence of magnetisation,  $\nabla \cdot \mathbf{M}$  (arbitrary units): a) a TDW, radius 17.5 nm; b) an ATDW, radius 25 nm; c) a BPW, radius 25 nm. The wire edges contribute notably more charge than the volume of the wire. . . . . 80
- 3.8 Variation of surface charge with cylindrical nanowire radius for the three domain wall types. Charge is calculated by summing over each node on the surface and normalising to the total charge associated with head-to-head magnetisation,  $\rho_0 = 2M_s A$ , where  $A$  is the cross-sectional area. Positive and negative contributions to the charge are plotted. . . . . 81
- 3.9 Phase diagram for domain walls in cylindrical nanotubes. Magnetic energy density is plotted as a function of radius for nanotubes of inner radius (filled markers, full line) 5 nm and (empty markers, dashed line) 10 nm. Single points are plotted for ATDW of inner radius 5 nm and TDW of inner radius 10 nm. . . . . 82
- 3.10 Unrolled view of the inner and outer surfaces of a nanotube. This shows directly the extra surface charge introduced by the inner surface. 83



- 3.11 Illustration of the two extremes in Fresnel imaging of a TDW. In a), the transverse component is parallel to the electron beam and thus does not deflect the beam; the nanowire has been rotated  $90^\circ$  in b) and the transverse component is perpendicular to the beam, resulting in deflection. . . . . 84
- 3.12 Calculated Fresnel images for cylindrical nanowires with a) a TDW, b) an ATDW and c) a BPW. Domain wall orientation, with respect to the electron beam, is shown on the left-hand side, resulting Fresnel images on the right-hand side. Two orientations are shown for the ATDW and TDW, as outlined by Fig 3.11. The contribution of electrostatic phase contrast has not been included in these images. . . 85
- 3.13 Calculated DPC images for the TDW. Images on the left show the axial component of integrated induction, images on the right show the component perpendicular to the axis, for a) the transverse component perpendicular and b) parallel to the beam direction, as indicated by double ended arrows. Units are in nTm and the wire diameter is 35 nm. . . . . 87
- 3.14 Calculated DPC images for the ATDW. Images on the left show the axial component of integrated induction, images on the right show the component perpendicular to the axis, for a) the transverse component perpendicular and b) parallel to the beam direction, as indicated by double ended arrows. Units are in nTm and the wire diameter is 50 nm. . . . . 88
- 3.15 Calculated DPC images for the BPW. The image on the left shows the axial component of integrated induction, the image on the right shows the component perpendicular to the axis, as indicated by double ended arrows. Units are in nTm and the wire diameter is 50 nm. . . . . 89
- 3.16 Sine of calculated electron phase for each DW (of diameter): a) TDW (35 nm), b) ATDW (50 nm) and c) BPW (50 nm). Different orientations are displayed for the TDW and ATDW. . . . . 90

3.17	Result of an OOMMF simulation showing a 3-D view of an ATDW stabilised in a square cross-section nanowire ( $80 \times 80 \text{ nm}^2$ ). . . . .	91
3.18	Schematic diagrams and SEM images, respectively, of curved nanowires, a) and c), and domain wall trap structures, b) and d). Ideally, an applied magnetic field perpendicular to the wire axis forces the magnetisation head-to-head, forming a domain wall. . . . .	92
3.19	a) In-focus and b) defocused Fresnel images of a nanowire measuring 95 nm in width. Arrows indicate the change of bright edge contrast from one side of the wire to the other; this flip to opposite sides is indicative of a DW, as in b), which shows an enlarged view of a chain-link structure. . . . .	93
3.20	(left) Proposed magnetisation and (right) resulting Fresnel image for two different 2-D DWs. In both cases, the Fresnel contrast does not match that of the chain-link DW. . . . .	94
3.21	Proposed 3-D structure for the chain-link DW. Red and blue arrows represent axial magnetisation of opposite sign and a black line traces the magnetisation in the domain wall. . . . .	95
3.22	In-focus a) and defocused b) images of a nanowire of width 180 nm. The edge contrast travels diagonally across the wire with a dot that is slightly off-centre, as circled in the inset of b). . . . .	96
3.23	DPC images of 95 nm wide wire showing a either a BPW or TDW (with transverse component parallel to the beam direction). The change in colours in b) from magenta to yellow shows a change in the axial magnetisation, which is reflected in the difference image in c) and the inset profile. . . . .	97
3.24	DPC images of a displaced vortex DW (DVDW) in a wire of width 160 nm. The colour image shows the circulation of the magnetisation, the difference image in d) shows asymmetry in the component perpendicular to the wire. . . . .	99
3.25	Outline of the structure of the DVDW alongside the colour image from Fig 3.24b). . . . .	99

3.26	3-D view of the result of a simulation whose starting state was based on the outline in Fig 3.25. The top and bottom surfaces are shown to indicate that the structure is 3-D, varying through the thickness. Calculated DPC images are shown at the bottom for (left) the axial component and (right) the transverse component of integrated induction. . . . .	101
3.27	Calculated Fresnel image of the simulated DVDW. The bright contrast travelling diagonally across the wire is consistent to the experimental Fresnel images. . . . .	101
3.28	Chart showing the range of widths for which each DW was experimentally observed (wire thickness is 75 nm). The regions where the bars overlaps indicate metastability. . . . .	102
3.29	Three sets of images showing a nanowire containing a DW at increasing applied field. Applied field strength is (top) 0 Oe, (middle) 10 Oe and (bottom) 26 Oe. A field of 320 Oe was required to uniformly magnetise the wire (image not shown). a), c) and e) are colour maps showing direction of induction; b), d) and f) are the respective sum images. The wire is 115 nm wide. . . . .	103
3.30	Schematic of the charge configuration associated with the pinned DW. The final colour image from Fig 3.29e) is shown in a), while b) shows an outline of the wire with arrows to indicate magnetisation direction and plus and minus symbols to represent magnetic charge. . . . .	104
4.1	Series of images showing the effect of IDMI on the region near the core of magnetic vortices confined to discs for $D =$ a) 0, b) 1 and c) $2.5 \text{ mJm}^{-2}$ . Left to right shows the in-plane direction of magnetisation, divergence of in-plane magnetisation, the out-of-plane component, $M_z$ , and line profiles of $M_z$ normalised to $M_s$ (blue) and $\nabla \cdot \mathbf{M}$ normalised to the maximum value of divergence (red). All images are 200 nm wide. . . . .	111

- 4.2 Representation of the magnetisation direction when taking a cross-sectional view through the core region of the disc for  $D = 0$  and  $D \neq 0$ . . . . . 112
- 4.3 Illustration of how the combination of vortex rotation  $c$  and polarity  $p$  leads to a definition of chirality. Here  $cp = 1$  corresponds to a right-handed system and  $cp = -1$  to a left-handed system. . . . . 113
- 4.4 Colour map showing  $M_z$  at the edge of the disc. Some out-of-plane tilting of the magnetisation occurs for  $D \neq 0$ . Images are  $400 \times 400$  nm<sup>2</sup>. Units are  $M_z$  normalised to  $M_s$ . . . . . 113
- 4.5 a) One component of a calculated DPC image from micromagnetic simulations that relaxed to a vortex state and b) the profile across the core, shown by the blue dashed line in a), and its gradient, from which the FWHM is obtained. c) plots the effect of  $D$  strength on the FWHM, using the method in a) and b). . . . . 114
- 4.6 Simulated images based on the magnitude of out-of-plane component of stray field, calculated at a height of 20 nm above the sample for a) 0, b) 1 and c) 2.5 mJm<sup>-2</sup>. Left and right images correspond to left and right-handed systems of magnetisation rotation sense  $c$  and polarity  $p$ . . . . . 115
- 4.7 Schematic diagram providing an interpretation for the  $H_z$  maps in Fig 4.6. There is chiral symmetry for  $D = 0$ ; however, depending on the divergence of the magnetisation, an imbalance of charge is created around the core, modifying the stray field. . . . . 116
- 4.8 Simulation results showing the variation of the field required to expel the core of a vortex confined to a disc for increasing  $D$  strength. Field values are normalised to the field required to expel the core for  $D = 0$ ,  $H_0$ . . . . . 117
- 4.9 CTEM bright (with diffraction patterns inset) and dark field images of PLD deposited a) Py/Cu and b) Py/Pt bilayers on Si<sub>3</sub>N<sub>4</sub> membranes showing polycrystalline structure. . . . . 119

- 4.10 Hysteresis loops from the BH-Looper for Py/Pt (dashed-blue) and Py/Cu(solid-red) showing behaviour consistent with identical Py films. 120
- 4.11 Series of images of focused ion beam (FIB) milled discs: a) an example of a  $5 \times 5$  array of discs; b) and c) CTEM bright and dark field images of disc edges after milling for Py/Cu and Py/Pt, respectively. Arrows indicate grains that have become enlarged following FIB milling. . . . 121
- 4.12 Fresnel imaging of vortices in discs with vortex cores revealed as dark or bright spots. The array in a) contains vortices at approximately zero applied field; b) shows a selection of Py/Cu discs at an applied field strong enough to push the cores to the edge (circled); c) shows the same discs as b), the field is increased so that all cores have been expelled. . . . . 122
- 4.13 Vortex expulsion fields for Py/Pt (blue) and Py/Cu (red) disc arrays, represented by histograms. There is a clear separation between the two distributions, indicating that it is easier to expel the core from Py/Pt disc, as predicted in Fig 4.8. . . . . 122
- 5.1 By projecting through different crystallographic orientations of the bulk spin ice crystal (top) the a) square and b) kagome vertices that comprise the most commonly studied artificial spin ice systems can be created (bottom). The spins on the crystal lattice (blue circles and red arrows) are replaced by single-domain elongated nanomagnets. 126
- 5.2 All possible vertex configurations for square ASI ranked in terms of energy. Green arrows, placed at the vertex centre, show size and direction of net moment, where applicable. . . . . 127
- 5.3 Anti-ferromagnetic ground state for square artificial spin ice, which is composed of degenerate Type 1 vertices. Green circles show the circulation of magnetic flux. . . . . 128
- 5.4 Diagram showing a) the transformation between square and rotated square ASI and b),c) the difference in number of degenerate states considering adjacent elements, only. . . . . 129

- 5.5 All possible configurations of magnetisation in single-domain RS elements. Vertices are categorised in terms of charge and net moment. Moment is represented by green arrows. . . . . 130
- 5.6 Geometry of the RS array and b) the direction in which it is repeated. 132
- 5.7 Fresnel imaging of an ASI array. a) shows a typical Fresnel image of the array and b) shows a simple schematic representation of the contrast expected from Fresnel imaging; depending on the orientation of magnetisation along the axis of an element, the order of bright/dark contrast changes. c) shows an enlarged image of the area bounded by the red box on the image in a); the line profile across the element shows that one side is “brighter” than the other allowing the direction of magnetisation to be determined. Scale in the line profile is  $\sim 5$  nm per pixel. . . . . 132
- 5.8 First step in processing of Fresnel images - finding a lattice for each magnetisation orientation. a) Thresholded Fresnel image and individual thresholded element are cross-correlated. By thresholding the b) cross-correlation gives the c) lattice of points. . . . . 134
- 5.9 Convolution of an arrow with the lattice defined in Fig 5.8b). The binary images are shown in a) and the result of the convolution and the binary version are displayed in b). The final image is in c). . . . . 135
- 5.10 DPC colour image of an ASI array (left) alongside a bright field “sum” images. Different orientations of magnetisation within elements are directly mapped. . . . . 135
- 5.11 All vertex configurations ranked by energy. As energy increases, net moment associated with vertex configurations decreases.  $Q$  denotes the net charge at the centre of the vertex. . . . . 137

5.12	Characteristic example of reversal of the array. Each stage is shown: a) uniform magnetisation; b) nucleation (circled) of a domain of opposite magnetisation; c) growth of domains aligned with the field; d) islands opposed to the field; and e) uniform magnetisation in the field direction. f) shows a sketched hysteresis loop with each image placed at an estimated position. . . . .	138
5.13	Outline of reversal sequence shown in Fig 5.12 highlighting each stage: a) uniform magnetisation; b) nucleation of a domain of opposite magnetisation; c) growth of domains aligned with the field; d) islands opposed to the field; and e) uniform magnetisation in the field direction.	140
5.14	Images showing the nucleation process. a) shows a uniformly magnetised domain, which terminates at the vertical line, at zero field. b) and c) contrast the situations for a single spin flip, when a field is applied, at the edge and in the bulk. Outlines of boxes show higher energy vertices present after the spin flip. . . . .	141
5.15	Identification of vertices at a DW from Fig 5.12c). . . . .	142
5.16	Illustration of most common DW configuration that occurs during the reversal of the array. The vertices at the DW position are from the $E_1$ level. By drawing the moment in between vertices (magenta arrows), the DW can be seen to resemble a Néel wall in thin films. . .	144
5.17	Representation of a head-to-head domain wall in which two domains with oppositely oriented magnetisation meet. In between the vertices (magenta annotations), configurations associated with $E_2$ vertices are found <i>i.e.</i> high energy configurations. . . . .	144
5.18	Geometry for which only two elements are simulated. Two different energy levels will be present, for parallel and anti-parallel alignment of spins. . . . .	145
5.19	Energy difference of parallel alignment and anti-parallel alignment of vertical elements only in an RS array plotted as a function of corresponding element separation in a full vertex. . . . .	146

---

5.20	Calculated energy levels for vertices where the minimum spacing between elements is 20 nm, corresponding to $a = 340$ nm. . . . .	147
------	---	-----



# List of Tables

5.1	Table listing the calculated energies for RS vertices of the same dimensions as the fabricated array. Energies are normalised to the lowest energy, $E_0$ . . . . .	139
5.2	Table listing the calculated energies for square ASI vertices where the element dimensions are the same as the fabricated array with a minimum spacing of opposite elements of 180 nm. Energies are normalised to the lowest energy, which is the Type 1 vertex. . . . .	139

# 1

## Micromagnetism of thin films and nanostructures

### 1.1 Introduction

The characterisation of magnetic materials on the nanoscale has been driven by technological applications that have resulted from the functionality offered by magnetic thin films and nanostructures. As the dimensions of a sample begin to approach fundamental length scales, such as the exchange length, the extrinsic properties of the material play a more important role in determining the behaviour of magnetic samples. Using modern lithography techniques, nanostructures can be fabricated whose magnetisation processes differ dramatically from bulk magnets. In addition, more recently, the Dzyaloshinskii-Moriya interaction has provided a method to modify the intrinsic properties of magnetic materials [1], resulting in exotic spin structures.

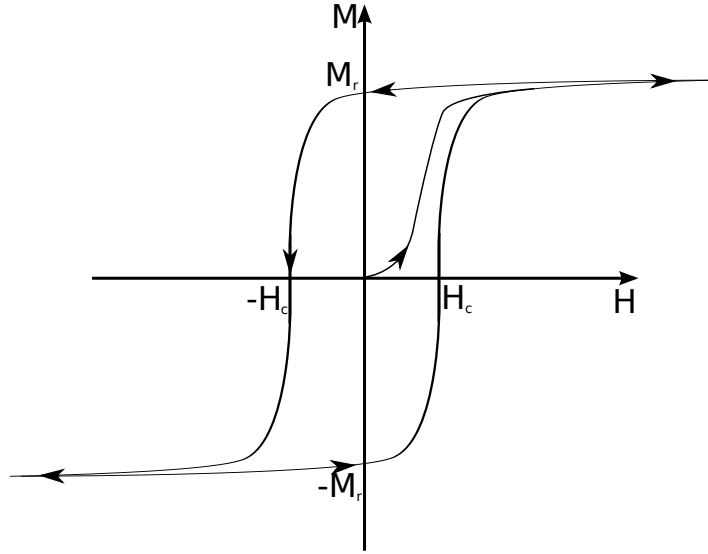


**Figure 1.1:** Hysteresis loop that is characteristic of a ferromagnetic sample. Important points are marked on the loop.

This introduction describes the magnetic energy terms relevant to the systems studied here, within the framework of micromagnetics. Ultimately, the behaviour of the systems studied in this thesis can each be understood through the characteristic configurations of the magnetisation. Therefore, the final two sections of this chapter introduce spin textures in well-known magnetic systems and then to the systems studied in this thesis.

## 1.2 Ferromagnetic materials

Magnetism in materials arises from the magnetic moments of their constituent atoms or molecules. Electrons orbiting a nucleus resemble a current loop with an associated magnetic moment due to their orbital and spin angular momentum. In the absence of spontaneous ordering a material's atoms/ions, which gives ferromagnetic (or anti-ferromagnetic) ordering, materials are classified paramagnetic or diamagnetic, depending on the response of a material to an applied field. The moments in a paramagnet align with the field whereas they oppose the field in a diamagnet. The magnetisation of the materials, defined as the magnetic moment per unit volume, scales linearly with applied field, depending on the susceptibility. Typical values for paramagnets and diamagnets are  $10^{-5}$ - $10^{-3}$  and  $-10^{-5}$ , respectively.

In contrast to paramagnetic and diamagnetic materials, ferromagnetic materials exhibit a spontaneous magnetisation due to the fact that the magnetic moments (or spins) of each atom align with each other. This results in magnetisation and susceptibility around five orders of magnitude larger than paramagnetic materials, which Weiss originally attributed to an internal molecular field [2]. In fact, the large “internal field” found in ferromagnets was a result of the moment associated with the spin angular momentum of the electron and the spontaneous magnetisation was due to the Heisenberg exchange interaction [3, 4]. The exchange interaction arises as a result of Coulomb repulsion between electrons on neighbouring atoms and the Pauli exclusion principle, caused by overlap of the electron wavefunctions. Since Pauli’s exclusion principle [5] requires that the total wavefunction (the combination of spin and spatial parts) of fermions must be anti-symmetric, electrons that have the same spin state *i.e.* symmetric must have anti-symmetric (anti-bonding) orbitals. This is energetically favourable due to Coulomb repulsion between the electrons. The Hamiltonian for Heisenberg exchange for neighbouring spins  $\mathbf{S}_i$  and  $\mathbf{S}_j$  is given by,

$$H_{ex} = -2 \sum_{i < j} J_{ij} \mathbf{S}_i \cdot \mathbf{S}_j, \quad (1.1)$$

where  $J_{ij}$  is the material dependent exchange constant. As Eq 1.1 shows, the energy is minimised when the spins are parallel. For ferromagnets,  $J$  is positive, meaning that parallel alignment of spins is preferred; for anti-ferromagnets the sign is reversed and anti-parallel alignment is energetically favourable. This picture is useful when thinking of localised spins on atoms; however, this model is not valid for the ferromagnetic metals studied in this thesis in which electrons are delocalised within the solid. For example, the fact that the magnetic moment per atom in Fe, Co and Ni is a non-integral value of  $\mu_B$  is a simple demonstration of the failure of a model based on localised moments to accurately describe the ferromagnetism of metals [6].

Models that consider itinerant electrons in unfilled bands, such as that developed by Stoner [7, 8], are used to describe ferromagnetism associated with delocalised electrons. Stoner made three assumptions: that the structure of the 3d band near the Fermi level is parabolic, the exchange interaction could be represented by a molecular field and that the electrons (or holes) obey Fermi-Dirac statistics [9]. Therefore, the

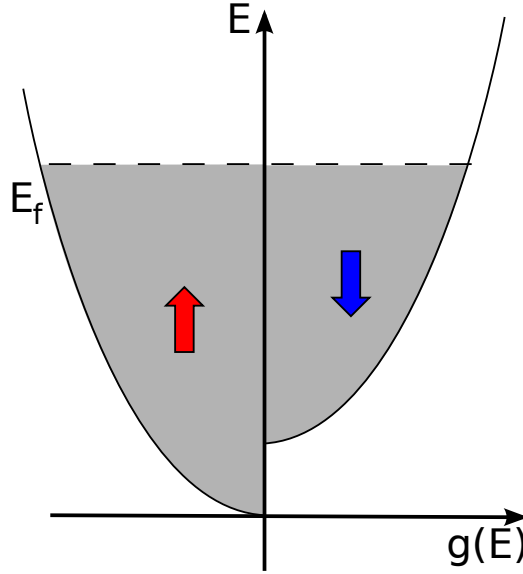


**Figure 1.2:** Schematic representation of the density of states in a metallic ferromagnet, notably, the occupancy of one spin sub-band is larger than the other.

number of electrons with spins parallel or anti-parallel to the magnetisation can be calculated by integrating the Fermi-Dirac distribution where the energy of the electrons,  $E$ , is a sum of the kinetic energy and the energy associated with alignment with the molecular field,

$$E = \frac{\hbar^2 k^2}{2m^*} \pm N_W M \mu_B \quad (1.2)$$

where  $k$  is the wavevector,  $m^*$  is the effective mass of the electron and  $N_W$  is the molecular field constant. Thus, in the presence of an exchange interaction, bands are spin-split into up and down sub-bands, as shown in Fig 1.2, which shows a sketch of the density of states as a function of energy; the spin-up sub-band has a higher occupancy than spin down, resulting in net magnetisation. The relative change in occupancy of sub-bands in Fig 1.2 reflects the saturation magnetisation of a ferromagnet and the spontaneous splitting of sub-bands is dependent on whether the material fulfils the Stoner criterion, given as [10],

$$IN(\epsilon_F) > 1, \quad (1.3)$$

where  $I$  is the Stoner exchange parameter, which is usually  $\sim 1$  eV for 3d transition metals, and  $N(\epsilon_F)$  is the density of states per atom for each spin state. For 3d transition metals, only Fe, Co and Ni meet this criterion [10].

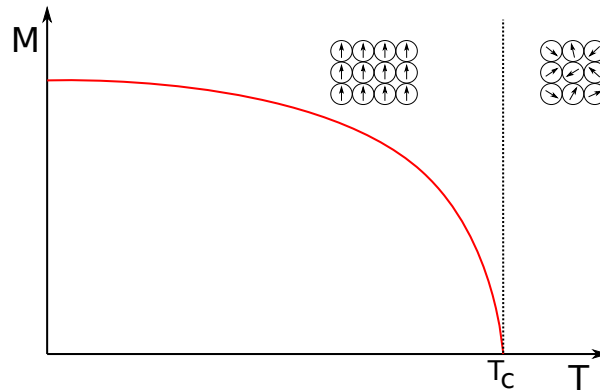


**Figure 1.3:** Spontaneous magnetisation as a function of temperature for a ferromagnetic material. Loss of ferromagnetic ordering occurs above the Curie temperature,  $T_c$ . At this temperature the material becomes paramagnetic and the spins are disordered in the absence of applied fields.

In ferromagnets, the exchange interaction results in regions of spontaneous magnetisation called domains that align to minimise the total energy of the system. All terms contributing to the total energy will be described in the following section. A consequence of the domain structure of ferromagnets is their hysteretic behaviour under an applied field. Fig 1.1 shows a hysteresis loop, which illustrates the irreversible character of a ferromagnet. The sample begins in a demagnetised, zero moment state until a saturating field is applied. Characteristic points on the curve are noted as the field is reduced and then reversed: remanence,  $M_r$ , is the state at zero field; and the coercive field,  $H_c$ , the point during the reversal at which the sample has zero net moment.

The spontaneous magnetisation of a ferromagnet is temperature dependent, as shown in Fig 1.3. When heated above the Curie temperature  $T_c$ , thermal energy,  $k_B T$  is large enough to cause the moments to become misaligned in the absence of an applied field, where  $k_B$  is the Boltzmann constant. Therefore, above  $T_c$ , the material becomes paramagnetic. This behaviour is reversible, when cooled below  $T_c$ , the material becomes ferromagnetic again.

### 1.3 Magnetic energy terms

The magnetic energy of a sample can be given as the sum of several terms, which will be described individually in this section. The competition between these terms

defines the magnetisation processes of the sample. Until now, the only term that has been described is the exchange energy, which alone would allow the energy to be minimised simply through parallel alignment of the spins, resulting in a single domain sample. In fact, the magnetostatic energy causes domains of different orientation to form, reducing the overall moment of the sample and resulting in non-zero exchange energy at the regions where the magnetisation rotates from one direction to the other *i.e.* the domain wall. These terms, in addition to the Zeeman energy, associated with an applied external field, are the most important for the metallic alloy studied in this thesis, permalloy ( $\text{Ni}_{80}\text{Fe}_{20}$ ). Permalloy (Py) is a soft magnetic material meaning that there is no strong anisotropy resulting from the crystal structure of the material. This magneto-crystalline anisotropy, which causes the material to have one or more so-called easy axes for the magnetisation will only be mentioned briefly. In addition, the Dzyaloshinskii-Moriya interaction (DMI), an anti-symmetric exchange energy, is considered where energy is minimised when neighbouring spins are canted. While this interaction was previously thought to be limited to bulk crystals and was overlooked in thin films; however, it has recently been shown to be crucial in ultrathin films in contact with a heavy metal. In this thesis, the magnetic energy terms can be understood within the framework of micromagnetics. This is the principle that the magnetisation in a ferromagnet can be represented as a continuous vector field where the value of the magnetisation is equal to the saturation magnetisation,  $M_s$ . In this continuum theory, atomic-scale variations in the magnetic structure are ignored [11, 12].

### 1.3.1 Exchange energy

Eq 1.1 defines the microscopic form of exchange energy summed over all spins in a lattice, which can be written as,

$$H_{ex} = -2JS^2 \sum_{ij} \cos\phi_{ij}, \quad (1.4)$$

for neighbouring spins  $i$  and  $j$ , so that when the angle between the spins,  $\phi$ , is zero, the energy is minimised for  $J > 0$ . Assuming that the variation of  $\phi$  between spins is small, the exchange can be considered analogous to an elastic medium [6] where

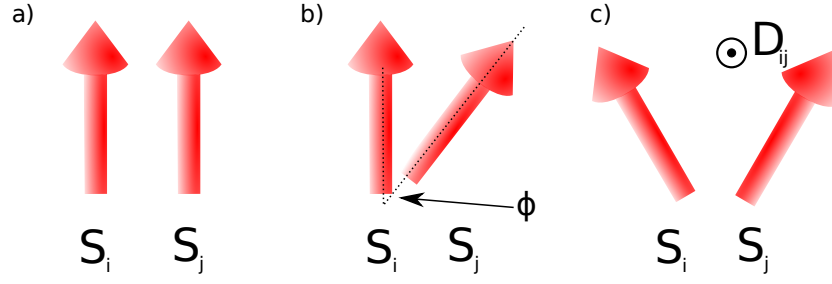


**Figure 1.4:** Arrows representing the orientation of neighbouring spins in a ferromagnet. As defined by Eq 1.4, a) corresponds to a minimum of exchange energy, whereas non-parallel alignment of spins in b) results in increased energy, depending on the angle,  $\phi$ , between spins. c) illustrates the situation where the spins are canted to lower DMI energy where the orientation of spins depends on depends on the relative strength of  $\mathbf{D}_{ij}$  in Eq 1.8 and  $J$  in Eq 1.4.

a restoring force acts when the medium is deformed, with a material dependent exchange stiffness,  $A$ , given by;

$$A = \frac{n}{a} 2JS^2, \quad (1.5)$$

where  $n$  is the number of atoms per unit cell and  $a$  is the lattice constant. For permalloy,  $A = 1.3 \times 10^{-11} \text{ Jm}^{-1}$ . From this, the exchange length,  $l_{ex}$ , can be defined as [13],

$$l_{ex} = \sqrt{\frac{2A}{\mu_0 M_s^2}}. \quad (1.6)$$

The exchange length is the distance over which the magnetisation is expected to be uniform. Using  $M_s = 860 \text{ kAm}^{-1}$ , the value for Py is 5.3 nm. In the continuum theory of micromagnetics, ignoring the atomic lattice, the exchange energy is written as

$$E_{ex} = A \int_V (\nabla \mathbf{M})^2 dV \quad (1.7)$$

which indicates that any deviation from parallel alignment of magnetisation results in non-zero energy.

### Dzyaloshinskii-Moriya interaction

The Dzyaloshinskii-Moriya interaction [14, 15] (DMI) is an anti-symmetric exchange interaction that favours perpendicular rather than the parallel alignment of spins preferred by Heisenberg exchange. The presence of the DMI was first found in bulk



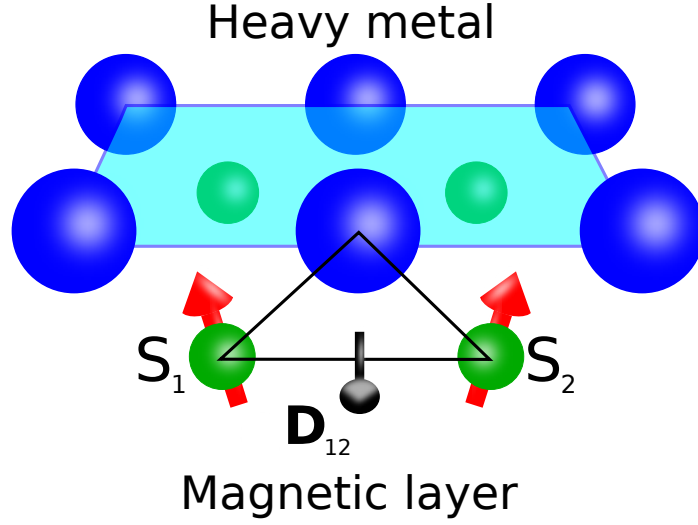


**Figure 1.5:** Schematic illustrating the three site mechanism of IDMI, which results in a  $\mathbf{D}$  vector parallel to the plane of the film, directed along the positive  $y$  direction.

crystals whose low symmetry gives rise to an additional exchange energy between spins  $\mathbf{S}_i$  and  $\mathbf{S}_j$ , which was expressed phenomenologically by Dzyaloshinskii [14] as,

$$H_{DMI} = -\mathbf{D}_{ij} \cdot (\mathbf{S}_i \times \mathbf{S}_j), \quad (1.8)$$

where  $\mathbf{D}_{ij}$  is a vector whose direction depends on the local symmetry of the crystal [15]. Moriya derived the microscopic origin of the DMI by taking into account spin-orbit coupling (SOC) in Anderson's superexchange theory [16]. A simple example of the possible effect of the DMI on two neighbouring spins is shown in Fig 1.4c). If  $\mathbf{D}_{ij}$  happens to lie perpendicular to a line connecting the spins, then  $H_{DMI}$  would be minimised for a mutual angle between spins of  $90^\circ$ , as indicated by Eq 1.8; however, due to the competition between the DMI and the stronger Heisenberg exchange interaction, the spins are only slightly canted. Typical values of the strength of the DMI relative to Heisenberg exchange range from 10-20% [17, 18].

In addition to naturally occurring bulk crystals, it was shown that the DMI could be induced in CuMn spin glasses [17] using high SOC impurities (Pt and Au), causing an increase in effective anisotropy field. Since inversion symmetry is broken at the surface of a thin film, the presence of large SOC was predicted to induce a DMI at the surface [19]. This interface-induced DMI (IDMI) is mediated through the three site mechanism [20], shown in Fig 1.5. Symmetry is broken at the interface of the magnetic film (green atoms) and nonmagnetic, large SOC film (blue) atoms,

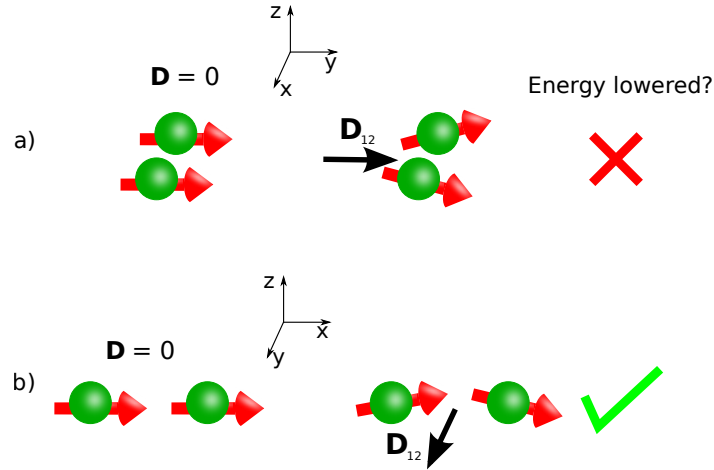


**Figure 1.6:** Possible effect of IDMI on two otherwise parallel spins  $\mathbf{S}_1$  and  $\mathbf{S}_2$ . Two cases are considered, a) for  $\mathbf{D}$  perpendicular to the directions of the spins and b)  $\mathbf{D}$  parallel to the spins' direction.

which results in  $\mathbf{D}_{12}$  between two neighbouring spins, shown with a black arrow, lying parallel to the plane of the film, along the positive  $y$  direction. Evidence of IDMI was first gained from the measurement of a spin-cycloid spin structure, rather than simple anti-ferromagnetic ordering, in a Mn monolayer on a W(110) substrate [21]. Following this observation, the effects of the IDMI were observed in ultrathin perpendicularly magnetised Pt/Co/Pt multilayers, where the Néel walls were energetically favourable to Bloch walls due to IDMI [22, 23, 24]. Chapter 4 researches the effect of the IDMI on soft magnetic materials where the magnetisation prefers to lie in the plane of the film. Fig 1.6 shows the possible effect of the IDMI on neighbouring spins in a soft magnetic film, depending on the orientation of  $\mathbf{D}_{ij}$ ; parallel aligned spins on the left, in the absence of IDMI, are contrasted with the situation where IDMI is introduced.  $\mathbf{D}_{ij}$  is always directed along the positive  $y$  direction, as in Fig 1.5. Two situations are shown: a), where  $\mathbf{D}_{ij}$  is parallel to the direction of neighbouring spins and b), where  $\mathbf{D}_{ij}$  is perpendicular. In a), the IDMI energy cannot be lowered by the spins gaining some out-of-plane component, as shown. The dot product in Eq 1.8 would be zero, meaning no energy decrease. In b), if there is some canting of the spins with respect to each other, resulting in an out-of-plane ( $z$  component) of magnetic moment, the energy can be reduced, as in Eq 1.8. The degree to which this occurs depends on the relative strength of

Heisenberg and IDMI exchange. In addition, the exchange length given in Eq 1.6, can be expected to be different in the presence of DMI whose energy is lowered for non-uniform magnetisation; since DMI favours non-uniform magnetisation, the distance over which it is expected to be uniform would be lower.

### Other exchange interactions

In addition to Heisenberg exchange and the DMI, it is possible to have other exchange interactions present in a magnetic sample. The Ruderman-Kittel-Kasuya-Yosida (RKKY) interaction [25, 26, 27] is an example of indirect exchange where the spin-polarisation of conduction electrons by localised moments results in coupling of this polarisation to a neighbouring localised moment [6]. The RKKY exchange integral has an oscillatory dependence on distance between localised moments, which means that coupling flips between ferromagnetic and anti-ferromagnetic. This oscillatory behaviour is seen in the context of thin films where the (anti-)ferromagnetic coupling of two magnetic layers, separated by a non-magnetic spacer layer, depends on the thickness of the non-magnetic layer [28].

Exchange bias [29] is an interface-induced exchange interaction that occurs between a ferromagnet and anti-ferromagnet in which the Curie temperature of the ferromagnet is larger than the Néel temperature of the anti-ferromagnet. By depositing one onto the other in the presence of an applied field and cooling through the Néel temperature, the ferromagnet is observed to have a preferred direction of magnetisation, which is the same as the direction of the field applied during deposition [6].

### 1.3.2 Magnetostatic energy

The magnetostatic energy is the result of the interaction of dipole-dipole interactions in the sample, related to the stray magnetic field generated by the sample,  $\mathbf{H}_d$ . Magnetostatic energy arises from interaction of  $\mathbf{H}_d$  with  $\mathbf{M}$  and can be written as

$$E_{mag} = -\frac{\mu_0}{2} \int \mathbf{H}_d \cdot \mathbf{M} dV \quad (1.9)$$

where the integration is over the entire sample.  $\mathbf{H}_d$  is given by

$$\mathbf{H}_d(\mathbf{r}) = \frac{1}{4\pi} \left( \int_V \frac{-\nabla \cdot \mathbf{M}}{|\mathbf{r} - \mathbf{r}'|^2} dV + \int_S \frac{\mathbf{M} \cdot \hat{\mathbf{n}}}{|\mathbf{r} - \mathbf{r}'|^2} dS \right) \quad (1.10)$$

Unlike the exchange energy, the magnetostatic energy is non-local as it depends on the contribution from all points in the sample.

The origin of  $\mathbf{H}_d$ , and thus magnetostatic energy, is magnetic volume,  $\rho$ , and surface,  $\sigma_s$ , “charges”, where  $\rho = -\nabla \cdot \mathbf{M}$  and  $\sigma_s = \mathbf{M} \cdot \hat{\mathbf{n}}$ , as in Eq 1.10. These charges act as sources and sinks of stray field, in an analogous manner to electric charges. Unlike electric charges, the net sum of all charges in all cases must be zero *i.e.* magnetic monopoles are forbidden. Fig 1.7a) and b) show simplified situations where surface and volume charges act as sources of stray field; a) shows a cross-section through a  $180^\circ$  domain wall (identified later as a Néel wall) in a thin film where volume charge arises simply from the divergent magnetisation; b) shows a plan view of a rectangular thin film element with uniform magnetisation *i.e.* a bar magnet configuration, resulting in surface charge. Fig 1.7c) shows that, through the formation of domains in the rectangular shaped element in b), the magnetostatic energy may be lowered as there is reduced stray field; although the magnetostatic energy is not eliminated as there is some charge associated with the domain walls. However, this comes at a cost of exchange energy, which becomes non-zero at the domain walls of this flux-closure state.

Due to the magnetostatic energy, the geometry of a sample strongly influences its magnetic behaviour as it seeks to minimise magnetostatic energy. This is particularly important for nanostructures and thin films where dimensions approach the exchange length of the material [30] because flux-closure states, such as that in Fig 1.7d), are more difficult to form as the cost in exchange energy becomes larger than the reduction in magnetostatic energy. Samples may display an anisotropic spin alignment due to their physical shapes, which is known as shape anisotropy. This is often illustrated using the example of a small single-domain ellipsoidal particle, compared to symmetric spherical particle. Here, the magnetisation of which prefers to lie parallel to the long, rather than the short axis due to an effective shape anisotropy, as shown in Fig 1.8a) and b). The energy,  $E_s$ , is minimised for

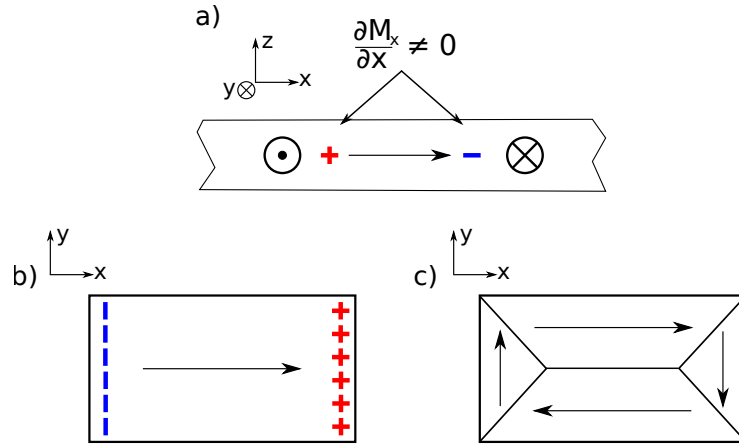


**Figure 1.7:** Depiction of the origin of magnetic charges. a) shows a cross-section through a thin film where divergent magnetisation generates charge and b) is a plan view of a uniformly magnetised element that results in magnetisation normal to the surface. c) shows how multi-domain states form to reduce charge in a rectangular element.

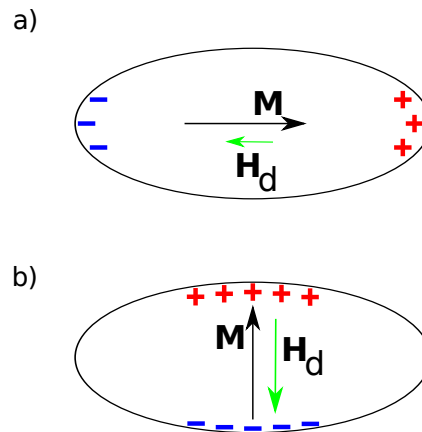


**Figure 1.8:** Illustration of shape anisotropy in an ellipsoidal particle.  $H_d$  is larger in b) compared to a), which results in larger magnetostatic energy.

magnetisation pointing along the long axis as

$$E_s = - \int_V K \sin^2 \theta dV, \quad (1.11)$$

where  $\theta$  is the angle that the magnetisation makes with the long axis and  $K$  is the effective anisotropy, given by

$$K = \frac{1}{2} \mu_0 (N_b - N_a) M_s^2 \quad (1.12)$$

where  $N_a$  and  $N_b$  are demagnetising factors that depend on the dimensions of the ellipsoid [12]. The ellipsoidal particle is a special case that can be solved analytically; however, the principle of shape anisotropy extends to other nanostructures such as long, thin planar and cylindrical nanowires, as discussed later.

### 1.3.3 Zeeman energy

The Zeeman energy is the energy associated with the interaction between the magnetisation and an external applied field,  $\mathbf{H}$ . It is given by

$$E_Z = -\mu_0 \int_V \mathbf{M} \cdot \mathbf{H} \quad (1.13)$$

so that the energy is minimised when the magnetisation is aligned with the external field.

### 1.3.4 Magnetocrystalline anisotropy

Crystalline samples exhibit one or more preferred “easy” axes, the direction of which depends on the crystal structure of the sample. This magnetocrystalline anisotropy,  $E_{anis}$ , is minimised when the magnetisation is aligned with the easy axes. Using the example of a cubic system

$$E_{anis} = \frac{K_1}{M_s^4} (M_x^2 M_y^2 + M_y^2 M_z^2 + M_z^2 M_x^2) \quad (1.14)$$

where  $K_1$  is a material dependent constant. The permalloy samples studied in this thesis are polycrystalline and thus have no net preferred easy direction; however, each grain has its own preferred direction, which results in ripple contrast when imaged using Fresnel mode of Lorentz TEM [31].

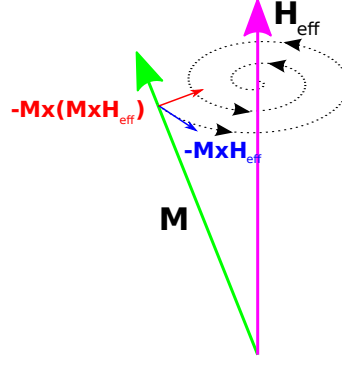


**Figure 1.9:** Vectorial representation of the LLG equation. A magnetic moment precesses about the effective field with damping so that they eventually align.

## 1.4 Micromagnetic simulations

Micromagnetic simulations are invaluable to the investigation of the behaviour of magnetic nanostructures studied in this thesis; by solving micromagnetic equations, they allow the prediction of the behaviour of magnetic nanostructures or aid the understanding of experimental results. Micromagnetic simulation packages used in this thesis, all freely available, are: Object Oriented MicroMagnetic Framework (OOMMF) [32] (Chapters 3 and 5), Nmag [33] (Chapter 3) and mumax<sup>3</sup> [34] (Chapter 4). All micromagnetic codes work in a similar way: they discretise the sample to be simulated into volume elements  $dV$ , which contain a moment  $\mathbf{M}dV$ ; an initial state is specified from which the system is allowed to relax; and the Landau-Lifshitz-Gilbert (LLG) equation is integrated forward in time until a convergence criterion is reached. The LLG is

$$\frac{\partial \mathbf{M}}{\partial t} = -\gamma \mathbf{M} \times \mathbf{H}_{eff} - \frac{\gamma \alpha}{|\mathbf{M}|} \mathbf{M} \times (\mathbf{M} \times \mathbf{H}_{eff}), \quad (1.15)$$

where  $\alpha$  is the damping parameter and  $\gamma$  is the gyromagnetic ratio and  $\mathbf{H}_{eff}$  is the effective field. The LLG is a phenomenological equation describing the gyroscopic precession by a magnetic moment due to the torque it experiences in an (effective) field and its damping, as given by the first and second terms, respectively. This process is sketched in Fig 1.9, which shows illustrates the damped precession of the  $\mathbf{M}$  vector about  $\mathbf{H}_{eff}$ .  $\mathbf{H}_{eff}$  contains contributions from all magnetic energy terms; for the work in this thesis, the relevant terms are from the magnetostatic (Eq 1.9), Heisenberg exchange (Eq 1.7) and Zeeman (Eq 1.13) energy terms.  $\mathbf{H}_{eff}$  is related

to the total energy,  $E$ , by

$$\mathbf{H}_{eff} = -\frac{1}{\mu_0} \frac{\partial E}{\partial \mathbf{M}}. \quad (1.16)$$

The simulations in Chapter 4 include an additional energy term for interface induced DMI,  $E_{DMI}$ , which is given by,

$$E_{DMI} = t \iint D \left[ \left( M_x \frac{\partial M_z}{\partial x} - M_z \frac{\partial M_x}{\partial x} \right) + \left( M_y \frac{\partial M_z}{\partial y} - M_z \frac{\partial M_y}{\partial y} \right) \right] d^2 \mathbf{r}, \quad (1.17)$$

where  $t$  is the thickness of the sample. By adjusting the configuration of magnetisation, the total energy, and hence the effective field, is reduced, until the torque reaches a critical value. This value, the convergence criterion, was set to be 0.01 degrees/ns for all of the simulations in this thesis.

The discretisation method depends on whether the package uses finite difference or finite element methods to solve the LLG equation. For finite difference methods (OOMMF and mumax<sup>3</sup>), the geometry is split into regular cubic cells; on the other hand, finite element methods (Nmag) require a finite element mesh, composed of irregular tetrahedra. The use of a mesh means that curved geometries are better represented and for this reason Nmag was used to simulate cylindrical nanowires and nanotubes in Chapter 3; however, calculations take longer compared to finite difference methods. For both methods, for the results to be valid, the discretisation length needs to be smaller than the exchange length of the material studied.

Finally, it should be noted that the micromagnetic simulations in this thesis are performed at zero temperature. It is not expected that this will have a significant impact on the outcome of simulations that relax into a static state. Simulations that involve dynamics, as in Chapter 4 where the behaviour of a magnetic vortex under an applied field is investigated, may be affected; in this case, the actual switching fields may be different than those in experiment.

## 1.5 Domain walls in thin films and nanowires

The formation of domain walls (DWs) in two dimensional (2-D) soft magnetic thin films and nanostructures provides a useful illustration of the competition between the exchange and magnetostatic energy terms and the formation of spin textures in



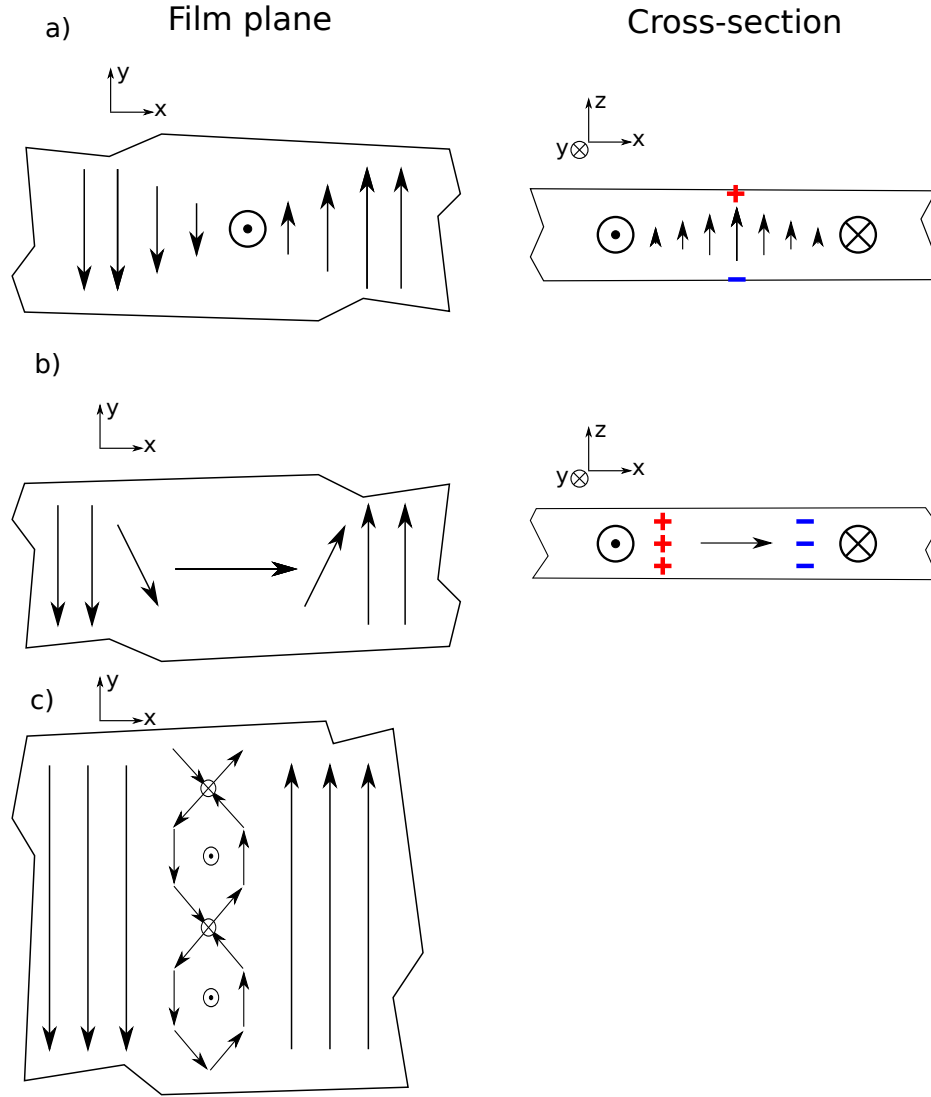


**Figure 1.10:** Domain walls found in magnetic thin films. a) Bloch walls are found in the thickest films, b) Néel walls are stable for thinner films, while c) cross-tie walls stabilise at intermediate thicknesses.

magnetic nanostructures. 2-D in this case means that the configuration of magnetisation does not change through the thickness of the structure. The shape anisotropy of these systems is such that the magnetisation prefers to lie in-plane and different DWs form to minimise magnetostatic energy, depending on the film thickness. Bloch walls, first proposed by Landau and Lifshitz [35], are energetically favourable in thicker films. Fig 1.10a) shows the structure of a Bloch wall with a views of the film plane and cross-section. The magnetisation rotates  $180^\circ$  with the rotation of spins in the plane of the DW. This configuration is divergence-free and there is no

magnetostatic energy associated with the internal wall structure, making it energetically favourable. There are some charges at the upper and lower film surfaces but, for thick films, the magnetostatic energy is low because the charge is sufficiently separated. Below a critical thickness ( $\sim 30$  nm for permalloy [11]), the lowest energy DW is a Néel wall, the structure of which is shown in Fig 1.10b). Unlike the Bloch wall, the Néel wall has divergent magnetisation as it rotates in the plane of the film, which avoids the surface charges found in the Bloch wall structure but produces volume charge. Néel predicted this transition by modelling DW structures as single domain ellipsoids and calculating a demagnetising factor for the DW structures that depended on the film thickness. The simple rotation of spins found in the Bloch and Néel walls can be contrasted with the complex structure of the cross-tie wall, shown in Fig 1.10c). Unlike the Bloch and Néel walls, the cross-tie wall varies through its cross-section and consists of alternating vortex and anti-vortex spin states. These are topologically protected spin structures with an associated winding number [36]. Cross-tie walls are found at intermediate thicknesses, typically 30 to 70 nm for Py [37]; the reason for this is that it becomes favourable to have  $45^\circ$  and  $90^\circ$  rather than  $180^\circ$  Néel walls [12]. This makes the cross-tie wall favourable as its vortex/anti-vortex pairs comprise a combination of  $45^\circ$  and  $90^\circ$  Néel walls and Bloch walls.

DWs in thin films may be contrasted with those found in planar magnetic nanowires, where the width is much larger than the thickness. The magnetisation is restricted to point along the axis of the wire, due to strong shape anisotropy, which means that, unlike in continuous thin films, a head-to-head DW is formed when the magnetisation rotates  $180^\circ$ . Three basic DW types have been shown to exist in 2-D nanowires, as shown in Fig 1.11: a) the transverse DW; b) the asymmetric transverse DW; and c) the vortex DW. The transverse DW consists of two Néel walls that are separated by a section of transverse magnetisation; the asymmetric transverse wall has a curling nature, which lowers the symmetry compared to the transverse wall; and the vortex wall has a rotational vortex spin state similar to that found in magnetic discs [38] and resembles two asymmetric transverse walls combined. Depending on the wire thickness and width, different DWs are stable, as shown by calculated phase diagrams [39]. The vortex spin state stabilises

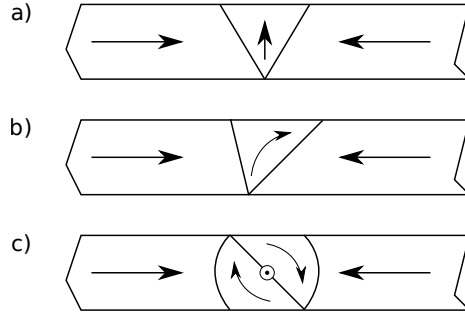


**Figure 1.11:** Film plane views of a) Transverse, b) asymmetric transverse and c) vortex DWs found in thin planar nanowires, depending on the wire width and thickness.

in thicker wires, to reduce the magnetostatic energy associated with the transverse wall; however, a minimum wire width exists, below which the benefits of reducing magnetostatic energy is outweighed by the cost of exchange energy. At this point, the transverse DW is the lower energy state despite the surface charge arising from its large transverse component. The asymmetric transverse DW is stable at intermediate thickness and width and can mediate the transition between transverse and vortex walls. As shown in Fig 1.10b), it has some of the curling character of the vortex DW while maintaining a significant component of transverse magnetisation.

## 1.6 Spin structures in magnetic systems

As illustrated by the example of DWs in 2-D thin films and nanowires in the previous section, different spin structures can form in magnetic systems to minimise the total energy. The nature of the spin configuration depends on the dimensions to which it is confined. In this thesis, Lorentz transmission electron microscopy is used to directly image the structure of the magnetisation in advanced magnetic nanostructures, thus providing an understanding of their behaviour. The principles of Lorentz microscopy, in addition to the JEOL ARM 200-F microscope used for magnetic imaging, are described in **Chapter 2**. Each of the following chapters explores spin configurations in distinct systems.

**Chapter 3** investigates the structure of three dimensional (3-D) DWs in cylindrical and square cross-section nanowires. Like the 2-D DWs discussed in the previous section, shape anisotropy forces the magnetisation to meet head-to-head; however,

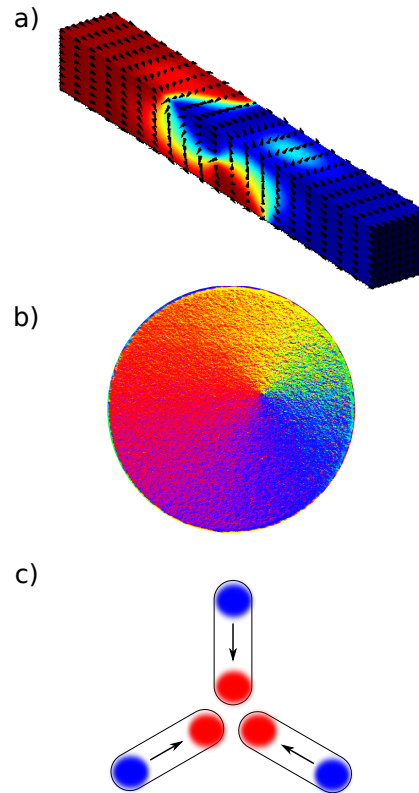


**Figure 1.12:** Spin structures studied in this thesis. a) shows a 3-D domain wall in a magnetic nanowire; b) is an Lorentz TEM image of a magnetic vortex; and c) shows an artificial spin ice vertex with a monopolar configuration.

3-D nature of these DWs means that they are structurally more complex. Fig 1.12a) shows the result of a micromagnetic simulation of one such DW, with magnetisation represented by black cones; adjacent sides can be seen to support spin structures similar to transverse and vortex DW structures. It is expected that the stability of these DWs will depend on the nanowire dimensions.

**Chapter 4** focuses on the behaviour of the well-known vortex spin state confined to a micron-sized disc, shown in Fig 1.12b). Unlike previous studies, the influence of an interface-induced Dzyaloshinskii-Moriya interaction (IDMI) on the vortex structure is investigated. As described earlier in this chapter, the IDMI favours canting of the magnetisation and can thus be expected to modify the structure of the vortex, the extent of which will depend on its strength relative to Heisenberg exchange.

Finally, **Chapter 5** studies the behaviour of an artificial spin ice array, shown in Fig 1.12c). This consists of an array of nanomagnets in which shape anisotropy forces the magnetisation to lie along their long axis but are designed to be sufficiently

small so as to be single domain. The schematic in Fig 1.12c) shows a high energy, monopolar vertex that arises in kagome artificial spin ice [40]. Therefore, unlike the other studies in this thesis, the manner in which nanostructures interact with each other that defines their spin configurations.

# 2

## Experimental techniques

### 2.1 Introduction

A number of techniques were used for the fabrication and characterisation of magnetic thin films and nanostructures in this thesis, the operating principle of which are outlined in this chapter. The description starts with transmission electron microscopy in Section 2.2, which describes the instrument as well as contrast mechanisms associated with imaging modes used for structural and magnetic characterisation. In addition, work showing development of electron microscopy are detailed in Sections 2.2.4.3 and 2.2.4.4. Section 2.3 describes the entire electron beam lithography process used to fabricate magnetic nanostructures including a description of: resist configuration, substrates and metallisation. As with Section 2.2, the electron beam lithography description also includes development results. Section 2.4 describes the focused ion beam/scanning electron microscope system used for ion

beam milling and characterisation. Section 2.5 outlines the operation of atomic force microscopy. Section 2.6 describes the pulsed laser deposition system used for the deposition of permalloy thin films; optimisation of deposition conditions are described.

## 2.2 Transmission electron microscopy

Transmission electron microscopy (TEM) is the principal technique used to characterise samples in this thesis. Magnetic imaging modes were used to determine the structure of magnetic domain walls confined to nanowires in Chapter 3, magnetic vortices in Chapter 4 and map the switching of artificial spin ice arrays in Chapter 5. In addition, TEM provided essential information on the size and structure of patterned elements and the crystal structure of deposited thin films using standard structural imaging modes. In this section, the basics of image formation in TEM and how the microscope components influence imaging conditions are described. This is followed by details of the structural and magnetic imaging modes elsewhere in the thesis. The main microscope used in this work, the JEOL ARM 200-F (JEOL ARM), will be described. The optimisation of its operation using JEM Toolbox, a programming package based in MATLAB, will also be discussed, where appropriate.

### 2.2.1 Introduction

The development of the transmission electron microscope instrument started during the 1930's [41], shortly after Louis de Broglie postulated wave-particle duality, and subsequent experimental verification of the wave nature of electrons [42]. The obvious advantage of TEM over optical microscopy is that the wavelength of accelerated electrons is much smaller than that of visible light, thus allowing smaller features to be resolved. Common accelerating voltages used in TEM are tens to hundreds of kV. The relativistically corrected wavelength is given by

$$\lambda = \frac{h}{p} = \frac{h}{\left[2m_0eV \left(1 + \frac{eV}{2m_0c^2}\right)\right]^{0.5}}, \quad (2.1)$$

where  $h$  is the Planck constant,  $m_0$  is the rest mass of the electron,  $e$  is the electron charge,  $V$  is the accelerating voltage,  $c$  is the speed of light in a vacuum and  $p$  is the relativistically corrected momentum of the electron. For an accelerating voltage of 200 kV, the sole accelerating voltage used in this work,  $\lambda = 2.51$  pm. The corresponding diffraction limit is approximately half of  $\lambda$ ; however, due to lens aberrations, it is not practically possible to reach this limit. The present limit, achieved in a fifth-order aberration-corrected microscope operating at 300 kV, has sufficient resolution to image 47 pm spacing of an oriented Ge crystal [43]. In addition to the superior spatial resolution compared to optical microscopy, TEM is able to extract further information as a result of electron-solid interactions. For example, spectroscopy of inelastically scattered electron and generated X-rays provides information on the sample chemistry. In addition, and crucially for this work, the modification of the electron wave phase by magnetic samples allows the imaging of magnetic structure in TEM.

While the manufacture and operation of microscopes have been vastly improved since the first instruments, the basic components required to form an image are the same. An electron gun is used to produce a beam that travels through an evacuated column and electromagnetic lenses and deflectors allow the beam to be focused, tilted and shifted. The interaction of the beam with an electron transparent specimen contributes to contrast in the final image, which is recorded using an appropriate device, typically a CCD camera or photo-multiplier tube detector.

### 2.2.2 Imaging in TEM

The configuration of lenses, deflectors and apertures in a microscope defines its alignment which, in turn, defines the imaging mode. Imaging modes can be split into two main categories, conventional TEM (CTEM) and scanning TEM (STEM), the main difference being that the beam is fixed in CTEM, whereas it is scanned across the sample in STEM. CTEM mode will be described first, before moving to STEM.

Fig 2.1 shows ray diagrams for CTEM imaging for the primary microscope used in this work, the JEOL ARM, a) shows imaging and b) shows diffraction modes.



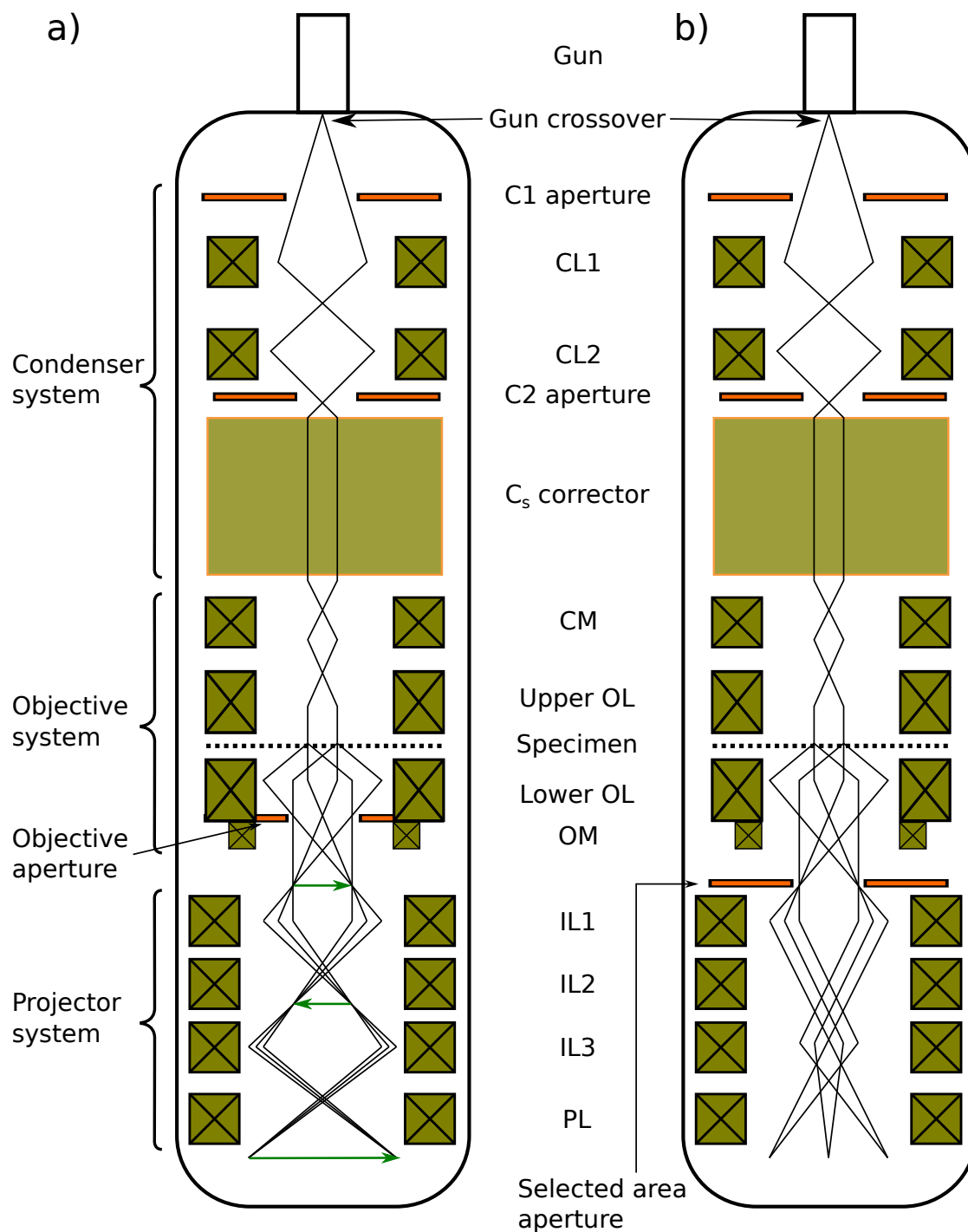


**Figure 2.1:** Ray diagrams for a) imaging and b) diffraction mode on the JEOL ARM. The rays are defined and focused by apertures and lenses to illuminate the sample. Depending on the object plane of the diffraction lens (IL1), a real-space image or diffraction pattern is projected onto the viewing screen.

While the specific lenses are different for the Tecnai T20, the imaging concepts are the same. Black lines are used to show rays that are focused using lenses, represented by olive coloured boxes. As indicated on Fig 2.1, the microscope can be split into three sections: the condenser, objective and projection systems. The condenser system is responsible for defining the illumination of the sample, the intensity and spot size of the beam. In CTEM imaging, as Fig 2.1 shows, the sample illumination is brought to be (approximately) parallel by the condenser system and the upper part of the objective lens. The objective lens is split into two pieces, with the upper part acts as a final condenser lens, while the lower part acts as the main imaging lens of the microscope. In this situation, the specimen is immersed in the magnetic field of the upper objective lens “pre-field”. The rays are transmitted through the sample before which the lower objective lens brings all of the rays, including diffracted and straight through beam, to a focus at the back focal plane (BFP) of the lens, where an aperture is positioned. In Lorentz TEM, this focusing is done using the objective mini lens (OM) as the objective lens is switched off to avoid applying a large magnetic field to the sample.

Figs 2.1a) and b) are identical until after the beam passes through the sample. The difference between imaging and diffraction mode is defined by the projector system. The first lens of the projector system (IL1) is called the diffraction lens; depending on its strength, the BFP or the first image plane can be selected as its object plane. This results in either a diffraction pattern or real space image projected onto the viewing screen, respectively *i.e.* the microscope is in diffraction or imaging mode. The rest of the projector lenses are used only for magnification of the image or, equivalently for diffraction patterns, increasing/decreasing the camera length. For imaging mode, as in Fig 2.1a), the objective aperture can be inserted at the BFP to select a part of the diffraction pattern to contribute to the final image; in diffraction mode, Fig 2.1b) an area of the specimen is selected by placing a selected area aperture at a plane conjugate with the specimen so that, equivalently, the diffraction pattern arises from scattering in a selected area of the sample.

In contrast to CTEM, the condenser system of the microscope is strongly excited in STEM so that the beam forms a focused probe at the sample. Use a set of scan

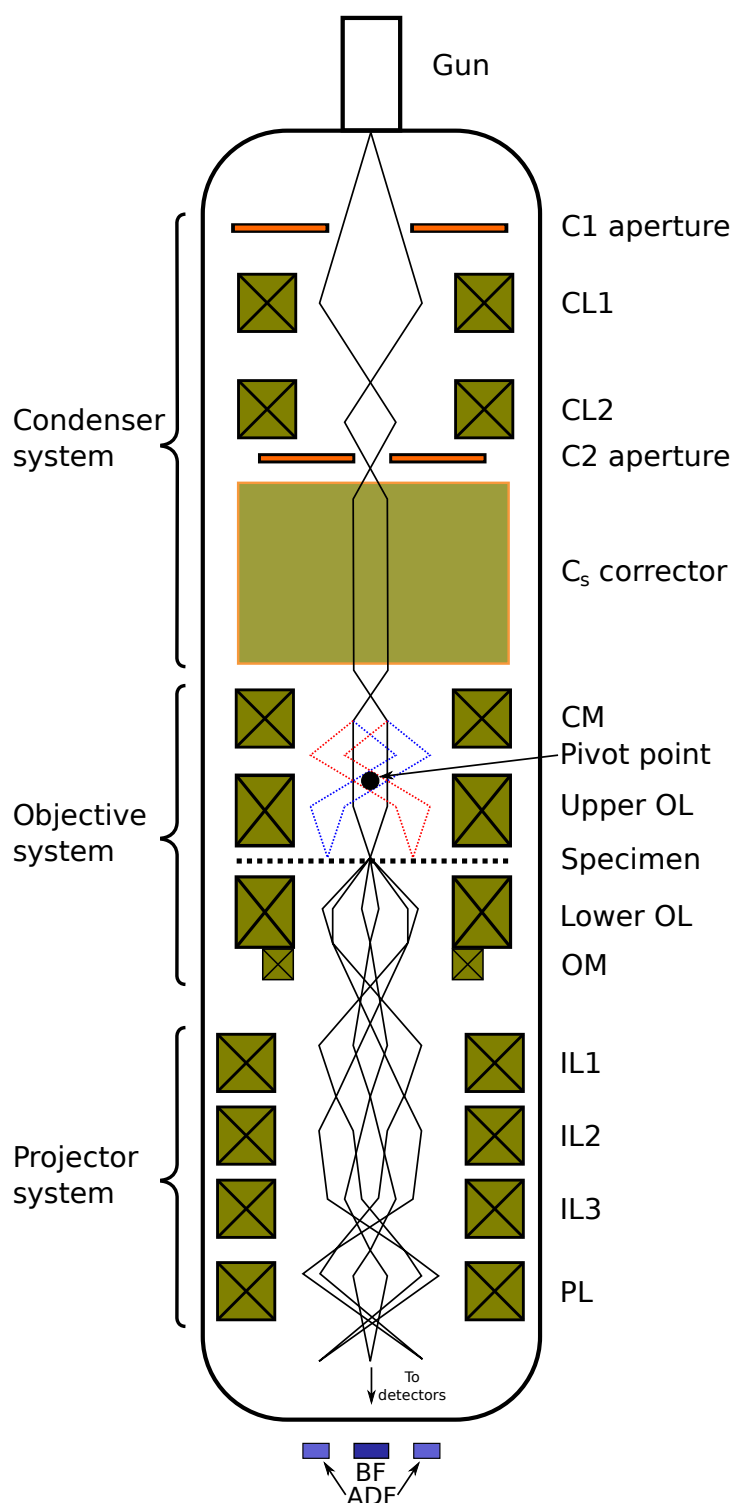


**Figure 2.2:** STEM ray diagram in the JEOL ARM. A probe is formed at the sample which is scanned across the sample. The projector system simply images the BFP and detectors pick up signals associated with a range of scattering angles, bright field (BF) and annular dark field (ADF) detectors are shown as examples.

coils (not shown) the probe is scanned across the sample surface through a series of tilts and shifts, as shown by the dotted blue and red lines in Fig 2.2. The angle the probe makes with the sample needs to be constant, otherwise the resultant diffraction pattern will change; therefore, the beam is tilted about a single pivot point on the optic axis at the front focal plane (FFP) of the upper objective lens, marked by a black dot on Fig 2.2, which ensures that the probe is parallel to the optic axis. In STEM, the microscope is always in diffraction mode, so the projector system is responsible for varying the camera length of the diffraction pattern. Unlike CTEM, where a camera is used to record the entire image at once, solid and annular detectors, placed at the bottom of the column, are used to build up images pixel-by-pixel. As indicated by Fig 2.2, different detectors collect signals associated with the range of scattering angles found in the diffraction pattern.

Contrast in TEM images can arise from changes in the amplitude and phase of the electron wave. Usually, images contain contrast from both sources, with one source particularly dominant. In this thesis, diffraction contrast falls into the category of amplitude contrast whereas Lorentz TEM is a form of phase contrast imaging. Mathematically, image formation in TEM can be described as

$$g(\mathbf{r}) = f(\mathbf{r}) \otimes h(\mathbf{r} - \mathbf{r}'); \quad (2.2)$$

essentially, the image represents a convolution of the specimen  $f(\mathbf{r})$  with  $h(\mathbf{r} - \mathbf{r}')$ , a point-spread function which depends on the microscope imaging conditions. In reciprocal space, Eq 2.2 can be expressed in terms of spatial frequencies

$$G(\mathbf{k}) = H(\mathbf{k})F(\mathbf{k}). \quad (2.3)$$

$H(\mathbf{k})$  is the contrast transfer function, which describes how well spatial frequencies are transferred to the image and depends on imaging conditions such as defocus, lens aberrations and apertures.

### 2.2.2.1 Electron guns

Electron guns are the source of illumination in TEM and the different types of gun influence the imaging conditions. The two microscopes used in this work have

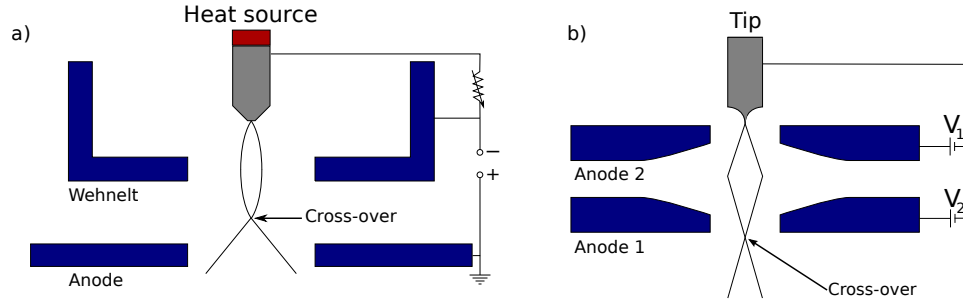


**Figure 2.3:** Overview of a thermionic emission gun a) and a cold field emission gun b).

different gun types: the Tecnai T20 has a thermionic emission gun, whereas the JEOL ARM uses a cold field emission gun (CFEG).

Thermionic emitters function by heating a tungsten or lanthanum hexaboride ( $\text{LaB}_6$ ) tip to a high enough temperature so that their electrons have enough energy to overcome the work function  $\Phi$  of the material. The current density (in  $\text{Am}^{-2}$ ) is given by

$$J = AT^2 \exp\left(\frac{\Phi}{kT}\right), \quad (2.4)$$

where  $A$  is a material dependent parameter, Richardson's constant, which is  $\sim 10^9 \text{ Am}^{-2}\text{K}^{-2}$ ,  $T$  is the temperature and  $k$  is Boltzmann's constant. As Eq 2.4 shows, suitable materials need to have low  $\Phi$ , as with  $\text{LaB}_6$ , or a high melting temperature, such as tungsten. The apparatus required to extract and accelerate the electrons, shown in Fig 2.3a), in thermionic guns is a triode system. The tip acts as the cathode, held at a negative voltage and an anode is placed below and is electrically grounded. In between these is a circular electrode, called the Wehnelt. The Wehnelt is at a bias of a few hundred volts less negative than the cathode and effectively acts as an electrostatic lens, focusing the electrons to a cross-over. This cross-over then acts as a source for the rest of the microscope. The bias of the Wehnelt is optimised to minimise the source size while maintaining emission current.

CFEGs work by applying a voltage to a sharp tungsten tip to generate a large electric field. The energy barrier is then lowered sufficiently to allow the electrons to tunnel through. The current density,  $J$  is given by the Fowler-Nordheim equation,

$$J = \frac{k_1 |\mathbf{E}|}{\Phi} \exp\left(\frac{k_2 \Phi^{\frac{3}{2}}}{|\mathbf{E}|}\right), \quad (2.5)$$

where  $k_1$  and  $k_2$  are empirically determined constants and  $\mathbf{E}$  is the electric field

strength at the tip. As shown by Fig 2.3b), the tip is a cathode with two anodes. The first cathode extracts the electrons with a voltage of  $>1$  kV, the second partially accelerates them to the operating voltage. Both extraction/acceleration methods focus the beam into a cross-over, the size of which determines the spatial coherence of the beam. This is important for the Lorentz TEM work in this thesis as spatially coherent sources produce superior phase contrast images. Typical source sizes [44] of thermionic and CFEG sources are  $10\text{ }\mu\text{m}$  and  $3\text{ nm}$ , respectively. For this reason, the JEOL ARM is better suited to Lorentz TEM experiments since coherent beams provide better phase contrast [45]. In addition, the gun brightness, defined as the current density per unit solid angle, is around two orders of magnitude larger for CFEG sources [44].

### 2.2.2.2 Electron lenses

Electron lenses used in TEM are electromagnets. Unlike lenses used in optical microscopy, whose strength is fixed and position is varied to adjust focus, the strength of electron lens can be varied by changing the current passing through its coils. The most common lens type, shown in Fig 2.4, is a “split pole-piece” configuration which produces an axially symmetric magnetic field parallel to the beam direction. As shown in the ray diagrams Fig 2.1 and 2.2, this acts like a convex lens in visible light optics. Rays can be focused to a cross-over point on the optic axis, the position of which depends on the lens strength, as sketched in Fig 2.4, where the rays represented by the dotted-blue line are focused more strongly than the solid-green line. As shown in Fig 2.4b), the magnetic field produced by the electron lens is axially symmetric but its strength varies because the field is stronger further away from the optic axis. As a result, the further electrons are off-axis, the stronger they are focused, as shown in Fig 2.5 *i.e.* the lenses suffer from spherical ( $C_s$ ) aberration. A consequence of  $C_s$  aberrations is that rays from a point in an object can only be focused to a disc of finite size, known as the disc of least confusion. For paraxial conditions, it can be shown [44] that the radius  $\delta$  of this disc is

$$\delta = C_s \beta^3, \quad (2.6)$$

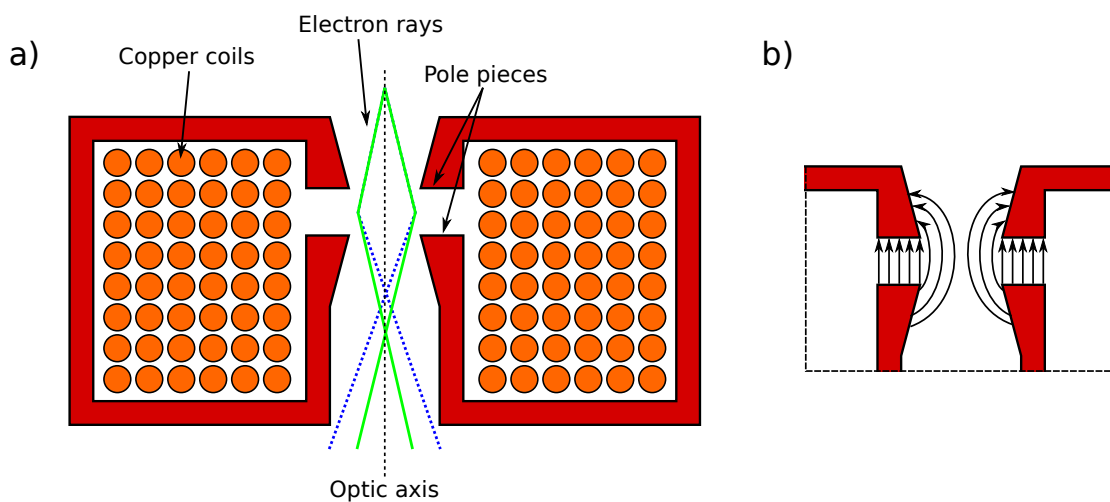


**Figure 2.4:** Cross-section view of a split pole piece lens. a) increasing current through its copper coils increases the magnetic field strength which focuses electrons more strongly, b) illustrates the magnetic field distribution produced by the lens.

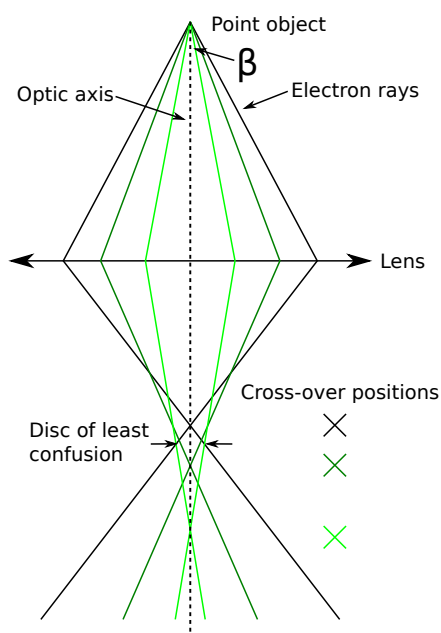


**Figure 2.5:** Illustration of  $C_s$  aberrations in an electron lens. Rays that are further off-axis have cross-over points closer to the lens.

where  $\beta$  is the angle that the ray makes with the optic axis. This effect smears the information from the specimen, it is partly responsible for the point spread function in Eq 2.2 and ultimately limits the resolution of the microscope. Given the  $\beta^3$  dependence, the convergence angles of rays are usually limited by apertures as in Fig 2.1.

As shown in Fig 2.1 and Fig 2.2, the JEOL ARM has a CEOS [46] probe  $C_s$  corrector whose effect in STEM mode is to act as a divergent, concave lens and “reverse” the over-focusing of off-axis electrons, which means that higher probe angles can be used. In CTEM mode, the  $C_s$  corrector is optically neutral.

## 2.2.3 Structural characterisation

### 2.2.3.1 Diffraction

Electron diffraction is useful for providing information on the crystal structure of a sample. In this work, the structure of deposited thin films was routinely checked. Diffraction patterns in TEM are formed by the interference of electron waves that have been scattered from atomic planes. Waves are reflected from successive parallel atomic planes in a crystal lattice and produce constructive interference if they satisfy Bragg’s equation

$$n\lambda = d\sin\theta, \quad (2.7)$$

where  $n$  is an integer,  $d$  is the spacing of the planes and  $\theta$  is the scattering angle. For  $\lambda = 2.51$  pm,  $\theta$  is of the order of 10 mrad. Another method of expressing the condition for constructive interference is using reciprocal lattice vectors. If  $\mathbf{k}$  and  $\mathbf{k}'$  are, respectively, the incident and scattered wavevectors then the change in wavevector on scattering,  $\Delta\mathbf{k}$ , is given by

$$\Delta\mathbf{k} = \mathbf{k}' - \mathbf{k}. \quad (2.8)$$

The diffraction condition is met when  $\Delta\mathbf{k}$  is equal to a reciprocal lattice vector  $\mathbf{G}$  [47]. This can be illustrated with the Ewald sphere construction, as shown in Fig 2.6. A sphere of radius  $\lambda^{-1}$  ( $= |\mathbf{k}|$ ) is shown in a reciprocal lattice with incident wavevector  $\mathbf{k}$  reflecting from an atomic plane. The reciprocal lattice points that



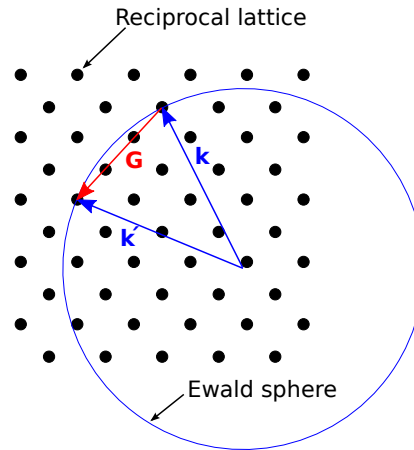


**Figure 2.6:** Schematic diagram of the Ewald sphere construction in a reciprocal lattice.

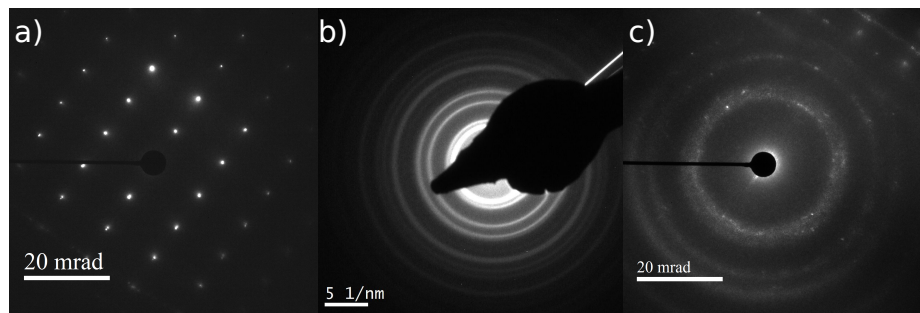


**Figure 2.7:** Diffraction patterns from a) a single crystal, b) polycrystalline and c) amorphous samples.

intersect the circumference of the circle therefore meet the diffraction condition *i.e.* Eq 2.8 is fulfilled.

The resulting diffraction pattern for a single crystal is a series of spots, such as that shown in Fig 2.7a). For a polycrystalline material, the grains have the same crystal structure but are randomly oriented so that the diffraction pattern is made up of a central spot surrounded by concentric rings, as shown in Fig 2.7b). An amorphous sample will produce a diffraction pattern consisting of a series of diffuse rings, as in Fig 2.7c). Amorphous samples do not have ordered lattice planes as (poly-) crystalline samples but still have some short range order, which causes some scattering angles to be more likely than others.

Diffraction patterns are formed in the back focal plane of the objective lens, as shown by Fig 2.1b). The diffraction lens (IL1 in the JEOL ARM) selects this plane as its object plane. A selected-area aperture is placed at a plane conjugate with the

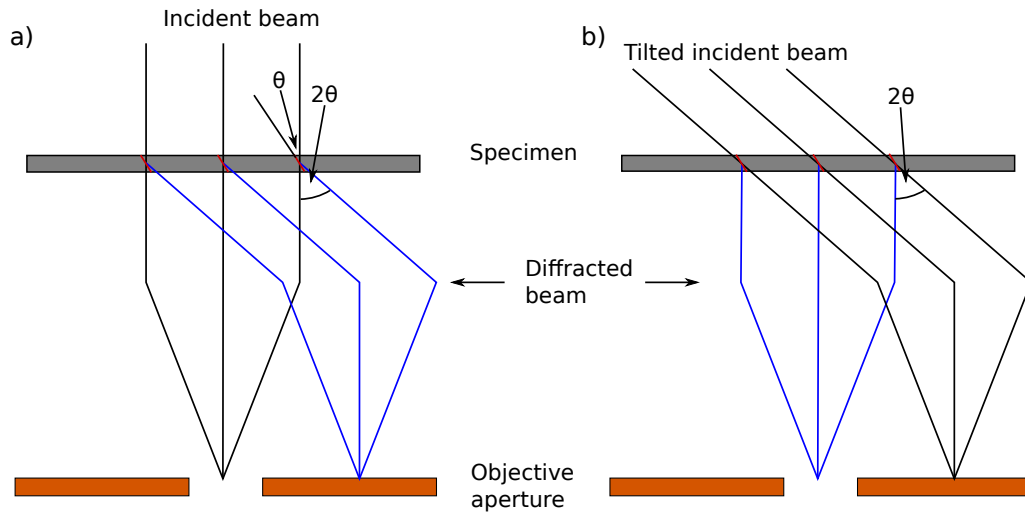


**Figure 2.8:** Ray diagrams for a) bright field and b) dark field imaging. The direct beam in a) is tilted in b) so that rays that were previously scattered off-axis are scattered back on-axis.

specimen to, as the name suggests, select the area of the sample that contributes to the diffraction pattern.

### 2.2.3.2 Bright and dark field imaging

Using the objective aperture, various parts of the diffraction pattern can be selected to contribute to the final image *i.e.* the unscattered beam or some of the diffracted rays. This is the principle behind bright field (BF) and dark field (DF) imaging. Fig 2.8 shows a ray diagram for both situations; for BF imaging, diffracted rays do not contribute to the final image due to the position of the objective aperture. In DF, by tilting the beam, electrons that would have been scattered off-axis are now diffracted back on axis and the direct beam is now blocked by the objective aperture.

These techniques were used to image deposited thin films and allowed characterisation of their grain sizes. Fig 2.9a) shows a BF image with inset a diffraction pattern showing that the objective aperture is centred on the central diffraction spot, thus only allowing the unscattered beam and the first diffraction ring is allowed to contribute to the final image. For a polycrystalline sample, this results in an image where grains whose orientation is such that the electron beam is scattered off-axis appear darker than those who cause no scattering *i.e.* we see diffraction contrast.

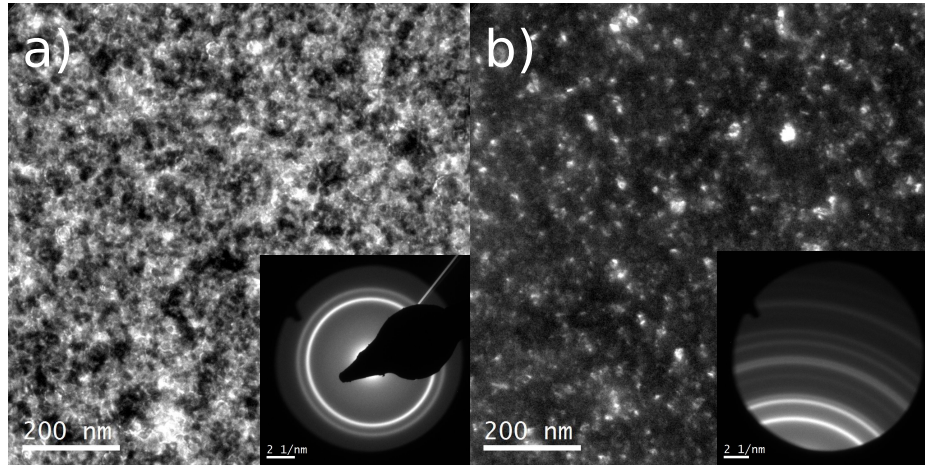


**Figure 2.9:** TEM images from a polycrystalline thin film with diffraction patterns corresponding to the images inset; a) shows a bright field image which the image is formed from unscattered electrons and b) is a dark field image where the outer rings of the diffraction pattern are selected.

On the other hand, DF images use some of the electrons that have been scattered off-axis. This means that the objective aperture selects a part of the diffraction pattern which does not include the central spot, as in the inset of Fig 2.9b) where the objective aperture now selects some of the outer rings of a diffraction pattern from a polycrystalline thin film.

### 2.2.4 Lorentz microscopy

Lorentz microscopy (LTEM), the imaging of magnetic structure using TEM, is the principal method of characterising the magnetic behaviour of samples in this thesis. LTEM offers superior spatial resolution compared to other magnetic imaging techniques, as well as, in some modes, quantitative information on the magnetic induction in a sample. Three different modes are used: Fresnel imaging, low angle diffraction and differential phase contrast (DPC) imaging.

LTEM is unlike other TEM modes in that the main lens of the microscope, the objective lens, is switched off. The reason for this is that the sample is positioned in the objective lens and the strong magnetic fields generated, 1-2 T, are strong enough to saturate typical ferromagnetic samples, destroying any internal domain structure. To compensate for the lack of an objective lens, a pair of Lorentz lenses, placed above and below the sample, are normally used [48] to perform the focusing

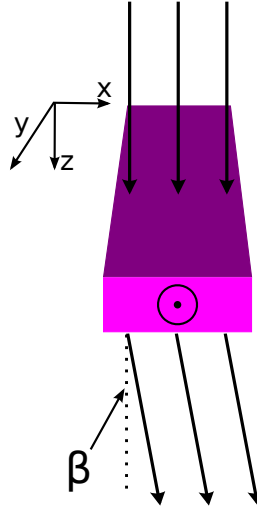


**Figure 2.10:** Representation of the classical Lorentz force where the electron beam is travelling in the  $z$ -direction, path shown by arrows, is deflected by magnetic induction in the  $x$ - $y$  plane by an angle  $\beta$ .

action of the objective lens; however, on the JEOL ARM, the objective mini (OM) lens, which is placed below the sample, performs this function.

The classical origin of contrast in LTEM is through the deflection of the electrons by the Lorentz force,  $\mathbf{F}$ , given by

$$\mathbf{F} = -e(\mathbf{v} \times \mathbf{B}), \quad (2.9)$$

where  $e$  is the electron charge,  $v$  is the velocity and  $\mathbf{B}$  is the magnetic induction. Eq 2.9 shows that the electrons only experience a force when the direction of  $\mathbf{B}$  is perpendicular to their direction of propagation. That is, for samples with in-plane magnetisation since the magnetic induction is related to the magnetisation,  $\mathbf{M}$ , and demagnetising field,  $\mathbf{H}$ ,

$$\mathbf{B} = \mu_0(\mathbf{H} + \mathbf{M}). \quad (2.10)$$

This is illustrated schematically by Fig 2.10, in which magnetisation in the plane of the sample causes a deflection of the electron beam, which is travelling perpendicular to the direction of magnetisation. The deflection angle,  $\beta$ , can be calculated by integrating along the electron beam path, assuming that the electron beam direction remains approximately parallel to the initial direction

$$\beta = \frac{e\lambda}{h} \int_{-\infty}^{\infty} (\mathbf{B} \times \hat{\mathbf{n}}) \cdot d\mathbf{l}, \quad (2.11)$$

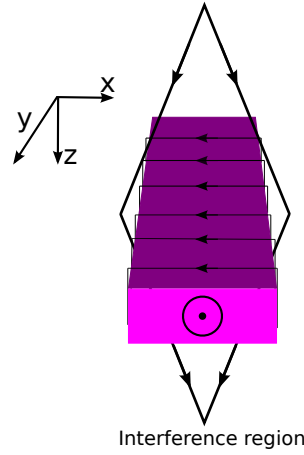


**Figure 2.11:** A representation of the thought experiment of the Aharanov-Bohm effect. Electron beams interfere after taking opposite paths either side of a uniformly magnetised magnet.

where  $h$  is Planck's constant, the direction of the electron beam is defined by the unit vector  $\hat{\mathbf{n}}$  and  $d\mathbf{l}$  is the path of the electron beam. In fact, for the situation illustrated in Fig 2.10 *i.e.* a film of uniform thickness  $t$ , with uniform in-plane magnetisation and electrons travelling normal to the plane of the sample, Eq 2.11 can be simplified [49] to

$$\beta = \frac{e\lambda B_s t}{h}, \quad (2.12)$$

where  $B_s$  is the saturation induction of the material. For a permalloy thin film ( $B_s = 1$  T) of thickness 10 nm, an accelerating voltage of 200 kV *i.e.*  $\lambda = 2.51$  pm gives  $\beta \sim 6.4 \mu\text{rad}$ . This demonstrates that the assumption for Eq 2.11 is valid,  $\beta$  is small, especially compared to the typical angles associated with Bragg scattering.

In order to describe LTEM in a quantitative manner, a quantum mechanical approach must be used. This makes use of the Aharonov-Bohm effect [50], which describes the quantum effect of electromagnetic potentials on charged particles. This effect is a calculation of the phase of the electron wave

$$\phi_m = -\frac{e}{\hbar} \int_{-\infty}^{\infty} (\mathbf{A} \cdot \hat{\mathbf{n}}) dl \quad (2.13)$$

where  $\mathbf{A}$  is the magnetic vector potential, given by,

$$\mathbf{A}(\mathbf{r}) = \frac{1}{4\pi} \iiint \frac{\nabla \times \mathbf{B}(\mathbf{r}')}{|\mathbf{r} - \mathbf{r}'|} d^3\mathbf{r}' \quad (2.14)$$

The original work uses a thought experiment where an electron beam is split then interferes either side of a solenoid. Fig 2.11 shows a similar setup where two waves take separate paths either side of an infinitely long uniformly magnetised section of material and interfere afterwards. Considering that there are no  $\mathbf{B}$  fields outside the sample in this situation, it is counter-intuitive to think that there could be a phase shift as in Eq 2.13. However, as shown in Fig 2.11, each beam experiences a different magnetic vector potential. The phase shift can be directly related to the in-plane magnetic induction [51] by

$$\nabla_{\perp} \phi_m = \frac{e}{\hbar} \int_{-\infty}^{\infty} (\mathbf{B} \times \hat{\mathbf{n}}) dl \quad (2.15)$$

where  $\nabla_{\perp}$  is the two-dimensional (in the plane of the sample) grad operator. However, this relies on a knowledge of the entire electron path for image calculation. From Eq 2.10,  $\nabla \times \mathbf{B}$  can be written as a sum of conduction and Ampèrian current densities *i.e.*  $J_c = \nabla \times \mathbf{H}$  and  $J_m = \nabla \times \mathbf{B}$ , respectively. Using this and substituting Eq 2.14 into Eq 2.13, the phase can be calculated. Following this, in the absence of conduction currents, it can be shown [52] that, for a sample in the  $x - y$  plane with a beam at normal incidence, as in Fig 2.11,

$$\phi_m = -\frac{e}{\hbar} \frac{\mu_0}{4\pi r} \otimes \int_0^t (\nabla \times \mathbf{M}) \cdot \hat{\mathbf{z}} dz. \quad (2.16)$$

Therefore, the phase depends only on the component of the Ampèrian current that is parallel to the beam. The gradient of  $\phi$  can be related to the deflection angle through Eqs 2.11 and 2.15. This result is significant as it means that Lorentz images may be calculated simply by knowing the configuration of  $\mathbf{M}$  through the sample thickness,  $t$ . This also implies that LTEM is a form of phase contrast imaging. This will be useful later for calculating Fresnel and DPC images.

In fact, the phase is affected by electrostatic and magnetic potentials so that

$$\phi = \phi_m + \phi_e \quad (2.17)$$

where  $\phi_e$  is the contribution from the electrostatic potential, which is present whether the material is magnetic or not and depends on the inner potential of the material,  $V$

$$\phi_e = \frac{\pi V t}{\lambda E} \quad (2.18)$$

## 2.2.4.1 Fresnel imaging

The Fresnel image mode of LTEM is a useful method for imaging magnetic structure in thin films and nanostructures [53, 54, 55]. It is used in Chapter 3 and Chapter 4 to image domain walls in low aspect-ratio nanowires and vortex cores in permalloy discs, respectively. As shown in Fig 2.12, Fresnel imaging is a CTEM mode where a parallel beam illuminates a sample and magnetic contrast is generated when the image is defocused by a distance  $\Delta$ . The figure shows two domains which have the same direction of in-plane magnetisation, separated by a domain in which the magnetisation is oriented  $180^\circ$ . Depending on the orientation of magnetisation,

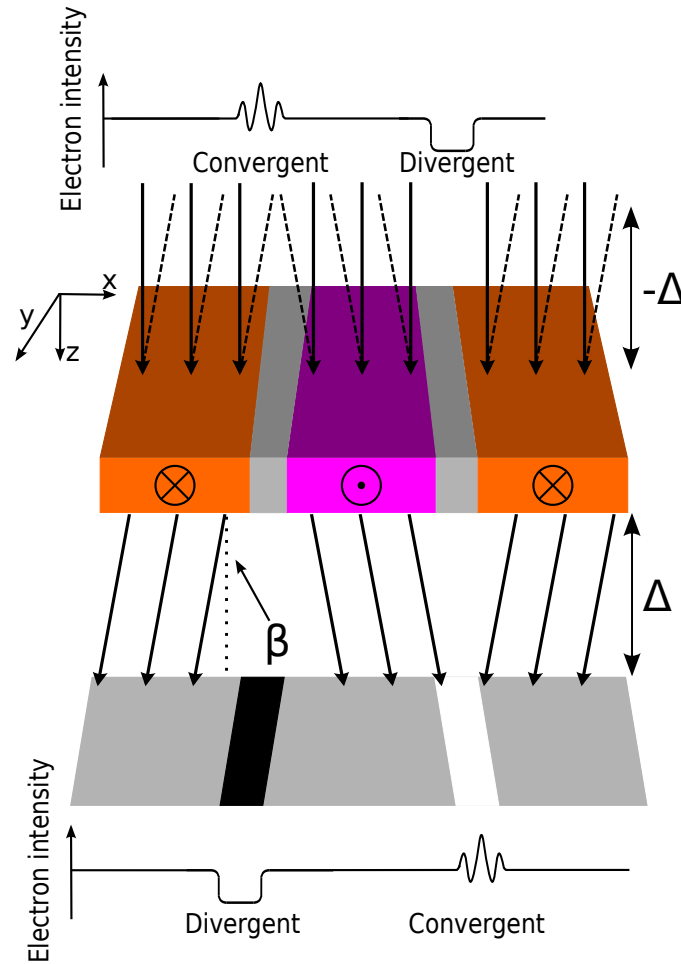


**Figure 2.12:** Diagram showing the principle behind Fresnel imaging. Defocusing the image allows the observation of contrast which corresponds in this case to two  $180^\circ$  domain walls. Bright and dark walls are labelled as convergent and divergent, respectively. Dashed lines show how using a negative value of defocus selects a virtual object above the object plane where the contrast is reversed.

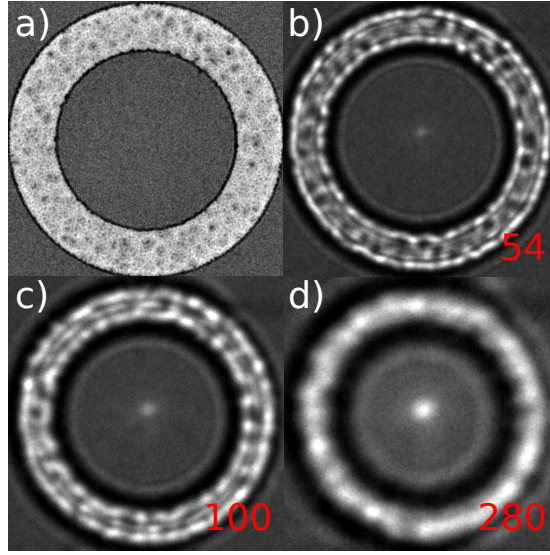


**Figure 2.13:** A series of Fresnel images taken at increasing (a-d) defocus values. No magnetic contrast is visible in a); b) - d) have increasing contrast at the expense of blurring of the image. Defocus values are indicated in  $\mu\text{m}$  on the images.

the electrons are deflected in directions defined by Eq 2.9, by an angle  $\beta$ , given by Eq 2.12. Defocusing means that an object plane below the specimen is imaged which shows the result of the deflection as bright and dark lines, defining the DW position in Fig 2.12. Bright and dark contrast arises from convergent and divergent electron beams, respectively. The contrast is reversed if the value of defocus is negative; the object plane is a virtual object above the specimen, as shown by following the dotted lines in Fig 2.12. The value of  $\Delta$  used needs to be chosen carefully; larger defocus produces higher magnetic contrast, at a cost of resolution. This is illustrated by Fig 2.13, which shows a series of Fresnel images, with increasing values of defocus, of a permalloy disc with a vortex state. Fig 2.13a) does not show magnetic contrast that is clearly present in b), the first non-zero value of defocus, c) uses a larger value of defocus and shows magnetic contrast more clearly and, finally, d) is an example of an image where the defocus is too high and the magnetic contrast is indistinct.

For image calculation, the intensity in a Fresnel image is given by [52]

$$I(\mathbf{r}, \Delta) = 1 - \frac{\Delta\lambda}{2\pi} \nabla_{\perp}^2 \phi_m(\mathbf{r}) \quad (2.19)$$

where  $\phi_m$  is obtained from Eq 2.16 so that

$$I(\mathbf{r}, \Delta) = 1 - \frac{\Delta e \mu_0 \lambda}{h} \int_0^t (\nabla \times \mathbf{M}(\mathbf{r})) \cdot \hat{\mathbf{z}} dz. \quad (2.20)$$



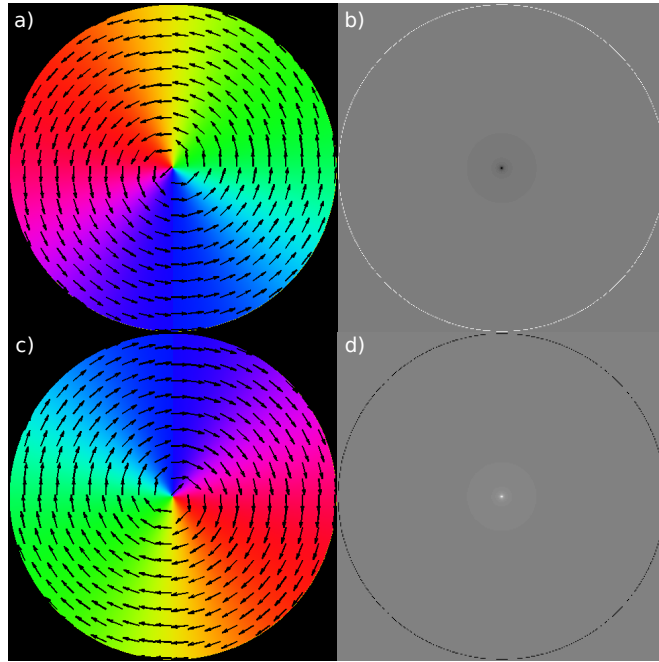


**Figure 2.14:** Fresnel images calculated using Eq 2.21. Two vortices of opposite chirality, in  $1\ \mu\text{m}$  discs, are calculated. Each results in reversed contrast at the core.

This allows Fresnel images to be interpreted quantitatively for small  $\Delta$ ; however, in this work, a qualitative picture is used, as obtained from

$$I(\mathbf{r}) \sim \int_0^t (\nabla \times \mathbf{M}(\mathbf{r})) \cdot \hat{\mathbf{z}} dz. \quad (2.21)$$

An example of this is shown in Fig 2.14, where two different vortex states in magnetic discs of opposite rotation sense are shown. Fig 2.14a) shows a counter-clockwise vortex with b) as the resulting calculated Fresnel image with dark core. This is reversed for c) and d) where, for a clockwise vortex, the core contrast is bright. This reversal of contrast is intuitive when Eq 2.21 is considered.

#### 2.2.4.2 Low angle diffraction

Low angle diffraction (LAD) is a CTEM technique that provides information of the magnetic scattering that occurs in a sample. As the name suggests, this is a diffraction mode; however, unlike the technique used to characterise the structural properties of materials, this mode works at much longer camera lengths thus magnifying the central diffraction spot because  $\beta$  is small compared to typical Bragg scattering angles. Fig 2.15 illustrates the range of angles considered in LAD, this

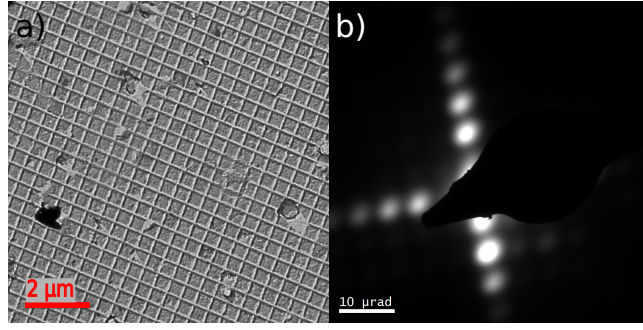


**Figure 2.15:** Low angle diffraction image showing the scattering of the beam from a cross-grating sample. The scale here is  $\sim 3$  orders of magnitude smaller than the images in Fig 2.7.

shows the diffraction pattern from a cross-grating sample of 2160 lines per millimetre. The periodic array of lines results in an array of spots, separated by an angle of  $5.5 \mu\text{rad}$ . For opposite in-plane magnetisation directions, the central diffraction is split by  $2\beta$ . By measuring the splitting of the central diffraction spot, it is possible to quantify the saturation magnetisation of a sample using Eq 2.12.

#### 2.2.4.3 Differential phase contrast

The differential phase contrast (DPC) imaging mode of Lorentz microscopy, being an in-focus technique, offers higher spatial resolution than Fresnel imaging [53, 55]. Unlike Fresnel, quantitative information can be readily obtained from its images. DPC imaging in this thesis was performed using the JEOL ARM. DPC is a STEM mode, the operating principle of which is outlined in Fig 2.17. The beam is focused to a fine probe, scanned across the sample, deflected by an angle,  $\beta$ , and the central diffraction spot falls onto a segmented detector. Fig 2.16 shows the position of the disc on the detector in the presence of a net magnetic deflection for a simple detector with only two segments. The difference in intensity between two segments (difference signal),  $\Delta I$ , depends on the Lorentz deflection,  $\beta$ , the convergence semi-angle at the sample surface,  $\alpha$ , and total electron intensity  $I$ . From the difference signal  $\beta$  can be calculated, which assumes that  $\beta$  is small compared to  $\alpha$  so that the increase in “area” can be considered to be rectangular, as shown in Fig 2.16. For this condition to be met,  $\beta$  needs to be less than 10% of  $\alpha$ . Considering typical values of  $\beta = 6.4 \mu\text{rad}$  (10 nm of permalloy) and  $\alpha = 500 \mu\text{rad}$ , this condition is

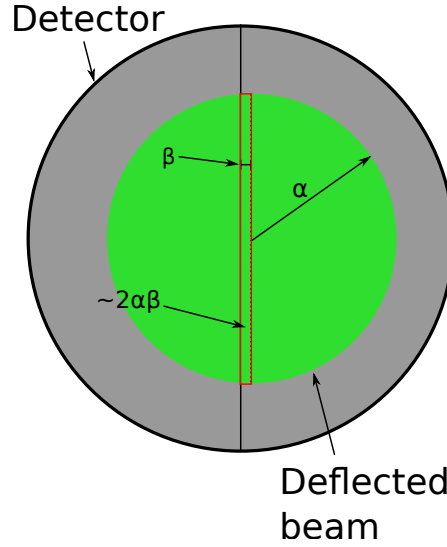


**Figure 2.16:** Simple split detector to show how the deflection of the beam is quantified. For the imaging to be linear, the convergence semi-angle,  $\alpha$ , needs to be much larger than the Lorentz deflection,  $\beta$ , so that the area  $2\alpha\beta$  is rectangular.

usually satisfied. The difference signal is given by the fractional change of the area,  $A$ , of the disc times  $I$

$$\Delta I = I \frac{\Delta A}{A} = \frac{I}{\pi\alpha^2} \left[ \left( \frac{\pi\alpha^2}{2} + 2\alpha\beta \right) - \left( \frac{\pi\alpha^2}{2} - 2\alpha\beta \right) \right] = \frac{4I\beta}{\pi\alpha} \quad (2.22)$$

Thus, as the beam is scanned across the sample, a map of  $\beta$  is generated pixel-by-pixel. Increasing  $\alpha$  results in better resolution, as the probe size is smaller; however, this comes at a cost of sensitivity, since  $\beta$  is detected against a larger background.

To map the beam displacement in two directions, a more complex segmented detector is required than in Fig 2.16. In DPC, a detector with four segments is used to allow vertical, as well as horizontal, components of  $\beta$  to be measured by subtracting signal from opposite quadrants. By summing the signal over all quadrants, a bright field image is formed. Thus, it is possible to map the magnetic configuration of the sample while simultaneously imaging its microstructure.

An example of DPC imaging is shown in Fig 2.18, which shows a vortex state in a permalloy disc. Four images are shown: two difference signal images, each indicating the component of the magnetic induction that they are sensitive to, a colour image generated from the difference images which shows the direction of integrated magnetic induction and a bright field “sum” image which shows the granular character of the permalloy thin film. The change in contrast in Fig 2.18a)

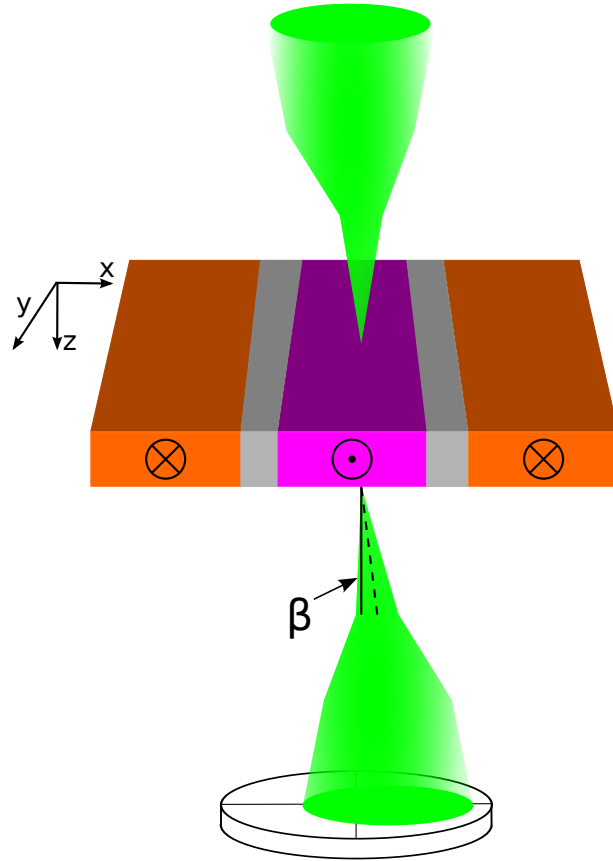


**Figure 2.17:** Schematic displaying the operating principle of DPC. A focused probe is scanned across the sample and is deflected by the sample’s in-plane magnetisation due to the Lorentz force. Deflection results in a displacement from the centre of a segmented detector, this results in a net difference when subtracting signal from opposite quadrants.

and b), top to bottom and left to right, respectively, indicates a change in the sign of the magnetic induction that they are sensitive to; this demonstrates the existence of a vortex state, as shown by the colour image and the schematic inset. The calculated DPC difference images, shown in Fig 2.19, demonstrate that the contrast seen in Fig 2.18 is consistent with a vortex state. This shows a result of a micromagnetic simulation on  $2\ \mu\text{m}$  disc and calculated images of orthogonal components of magnetic induction, calculated using Eq 2.15 and 2.16, as detailed elsewhere [56]. It was demonstrated [57] that the use of a detector with eight segments in DPC, such as that shown in Fig 2.20, gives improved magnetic contrast. The detector is now split into internal and external parts, denoted on Fig 2.20 as “Ext 0” and “Int 3” etc. In this version of DPC, called modified DPC (MDPC), the central diffraction disc partially covers the outer segments and difference images are

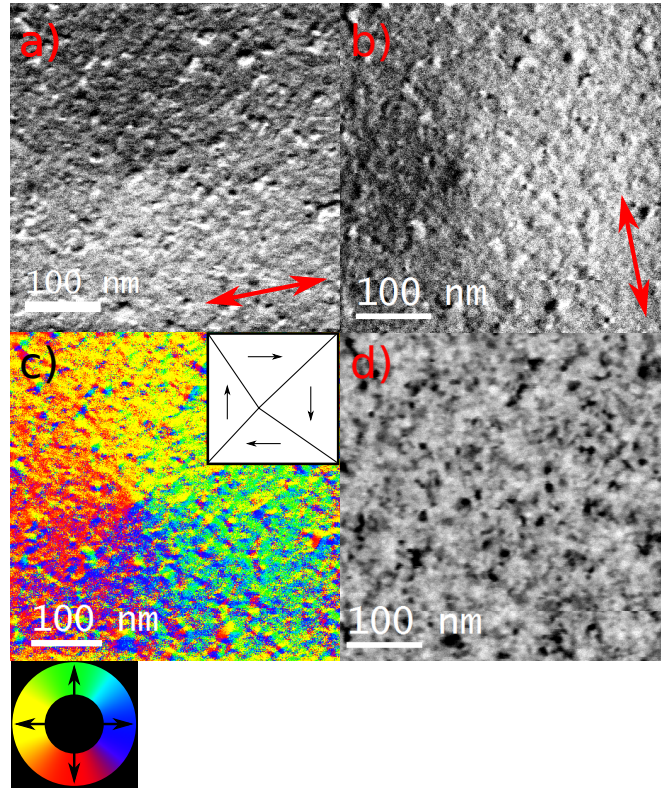


**Figure 2.18:** DPC images of a magnetic vortex core confined to a  $2\ \mu\text{m}$  permalloy disc. a) and b) show orthogonal components of magnetic induction, c) shows a colour map corresponding to rotational magnetisation, as indicated by the inset arrows, and d) is a bright field “sum” image; images a)-c) correlate with simulated images, shown in Fig 2.19.

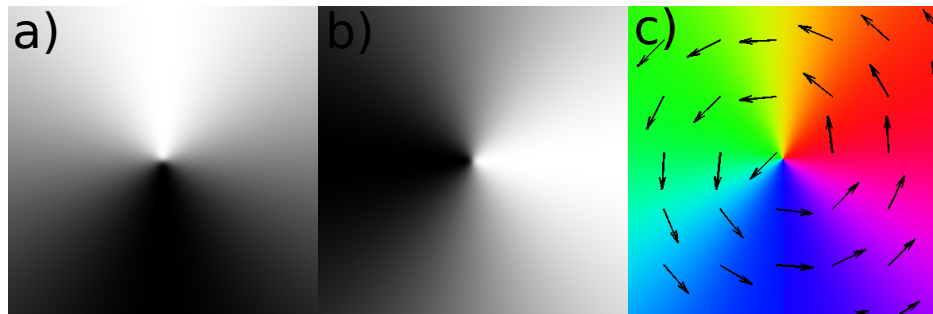


**Figure 2.19:** Simulated DPC images from the result of a micromagnetic simulation of a  $2\ \mu\text{m}$  permalloy disc that contains a magnetic vortex state. a) and b) show orthogonal components of the magnetic induction, integrated through the sample.

generated by subtracting signals from opposite external segments of the detector. Since DPC relies only on the *shift* of the disc about the centre of the detector, the information contained in the centre of the disc is not relevant to magnetic images. By subtracting outer segments *i.e.* Ext0 minus Ext2 and Ext1 minus Ext3, the shift

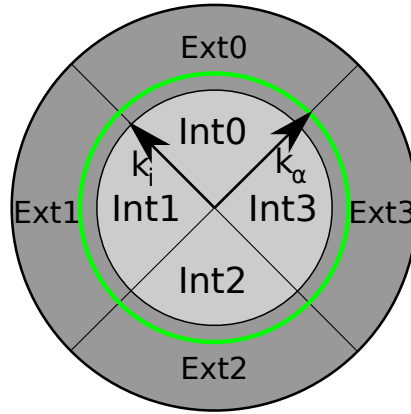


**Figure 2.20:** Eight quadrant detector used in modified DPC. Opposite external (Ext) sectors are subtracted from each other to quantify the beam deflection.

of the disc is calculated and better sensitivity is achieved since a large change is now detected in a small signal, compared to a small change in a large signal, as in the split detector in Fig 2.16. All DPC images in this thesis are, in fact, taken using the MDPC technique. It was also shown [57] for MDPC that the ratio of the inner detector size,  $k_i$ , to the disc size,  $k_\alpha$ ,

$$\kappa = \frac{k_i}{k_\alpha} \quad (2.23)$$

influences the quality of the magnetic image by modifying the phase contrast transfer function so that the spatial frequencies associated with diffraction contrast are suppressed. This is useful for polycrystalline magnetic samples since diffraction contrast obscures magnetic contrast. Comparing DPC images in Fig 2.18a) and b) to simulated images in Fig 2.19a) and b) illustrates the role that diffract contrast from random orientation of grains plays in DPC images. Images contain less contribution from diffraction contrast for larger  $\kappa$ . This means that the size of the disc, relative to the detector, needs to be varied to optimise the imaging conditions. The magnification of the diffraction disc, or camera length, is controlled by the projector system of the microscope, shown in Fig 2.1. In order to achieve camera lengths outside the “standard” values provided by the manufacturer, the strengths of each individual lens of the projector system must be adjusted. Fig 2.21a) plots the percentage excitation of each lens for the entire range of standard camera lengths (40 - 6000 cm) and Fig 2.21b) plots a smaller range of camera lengths, more relevant to this work. The camera length is effectively controlled by IL1, IL2 and IL3 as the other

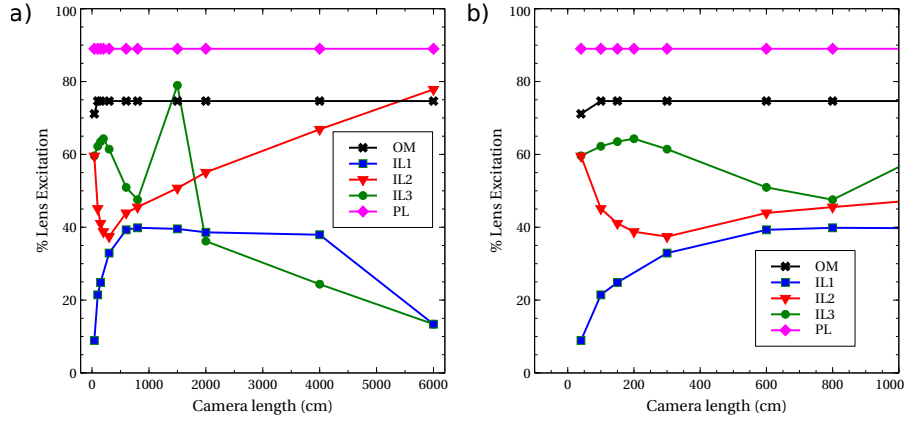


**Figure 2.21:** a) Graph showing the variation of lens strength with camera length for standard camera lengths in the JEOL ARM microscope for each lens of the projector system. b) shows a truncated version, relevant to this work.

lenses are held constant. The camera length can easily be varied by changing only one lens; however, this results in image rotation due to the curved trajectories of electrons take through lenses. A similar situation occurs for increasing/decreasing two or more lenses together. Therefore, it is common in TEM to have lenses working together to avoid this; for example, a first lens increasing its strength to increase the camera length and the second becoming weaker to compensate for image rotation, as in Fig 2.21b) where the strength of IL2 is reduced to compensate for the increase in strength of IL1, between 40 and 300 cm.

JEM Toolbox is a package developed within MATLAB to customise the control aspects of the operation of the JEOL ARM such as the electron optic system and sample stage. Using this, various procedures in the operation of the microscope can be customised or automated. JEM Toolbox was used to create a graphical user interface (GUI) to enable the camera length to be changed to non-standard values, a screenshot of this is shown in Fig 2.22. The main function of the MDPC GUI is that a user may select any camera length in the range 40-6000 cm, rather than the discrete values plotted in Fig 2.21. This works by linearly interpolating between the points on Fig 2.21 given by the standard camera lengths then setting each lens to whichever value is required to produce the desired camera length. There may be problems with the linear interpolation for camera lengths where the mode changes, as at 1500 cm in Fig 2.21a); however, this range was not used in this work. Fig 2.23



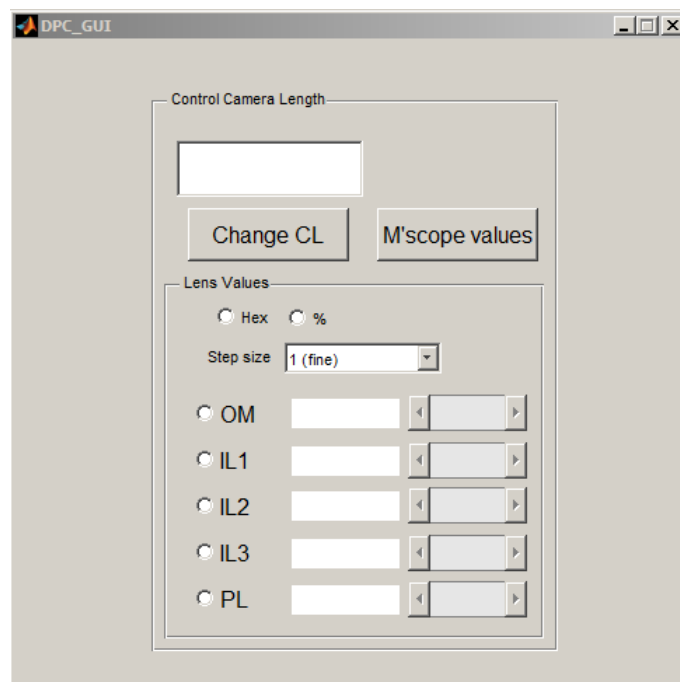


**Figure 2.22:** GUI written to tune the camera length of Lorentz STEM beyond standard camera lengths.

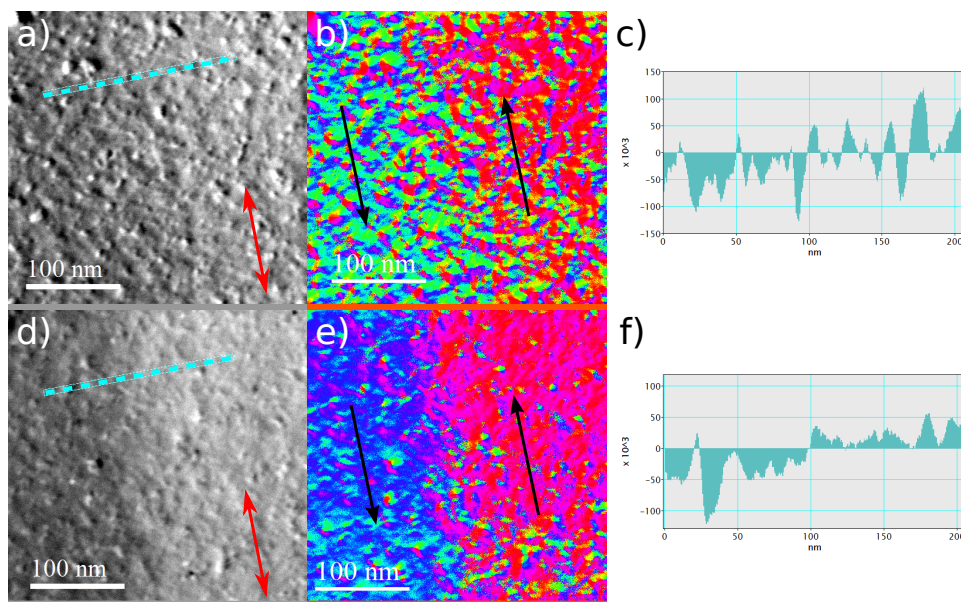


**Figure 2.23:** Two sets of images showing the effect of varying  $\kappa$  in MDPC. Difference, colour images and line profiles of a  $180^\circ$  domain wall are shown for a), b), c)  $\kappa = 0.86$  and d), e), f)  $\kappa = 0.95$ . The larger  $\kappa$  value clearly improves the magnetic contrast.



shows two sets of images, taken with two different camera lengths, corresponding to two  $\kappa$  values (the ratio of disc diameter to inner detector diameter):  $\kappa = 0.86$  for a), b) and c);  $\kappa = 0.95$  for d), e) and f). The images show the same  $180^\circ$  domain wall. The difference images in a) and d) are sensitive to changes in magnetic induction corresponding to the opposite directions in the domains; corresponding profiles in c) and f) show a change from positive to negative counts. It is immediately obvious that the images for  $\kappa = 0.86$  contains more contrast from crystallites compared to  $\kappa = 0.95$ . A comparison of line profiles across the domain wall, confirms this; f) has a much smoother profile than c).

While the MDPC GUI is currently usable for objective off STEM mode, its functionality could easily be extended to include other modes, which opens the possibility of non-standard microscope alignment for other imaging modes. This includes the potential for optimisation of existing TEM modes or the development of new modes.

#### 2.2.4.4 Mapping magnetisation reversal

By weakly exciting the objective lens or using its remanent field, in-situ magnetising experiments may be performed in LTEM. The objective lens produces a field vertical to the sample and an in-plane component of the field may be applied to the sample by tilting the stage. The ability to perform in-situ magnetising experiments means that the reversal of magnetic thin films and nanostructures can be directly imaged. The strength of in-plane applied field depends only on the tilt angle of the stage and the excitation of the objective lens field; however, collecting a long series of images at a range of tilt angles is both time consuming and tedious. Therefore, a tilt series GUI was written using JEM Toolbox to automate this process. The primary function of the GUI is to accept an input range of tilt angles and increment angle and automatically proceed to each, pausing at each increment for a user-specified amount of time. Additional functionality is shown in a screenshot in Fig 2.24, the most important of these is the ability to capture and save images using the CCD camera on the JEOL ARM, which was used to record the data presented in Chapter 4 and 5. Images can also be put together and viewed as a movie in MATLAB or

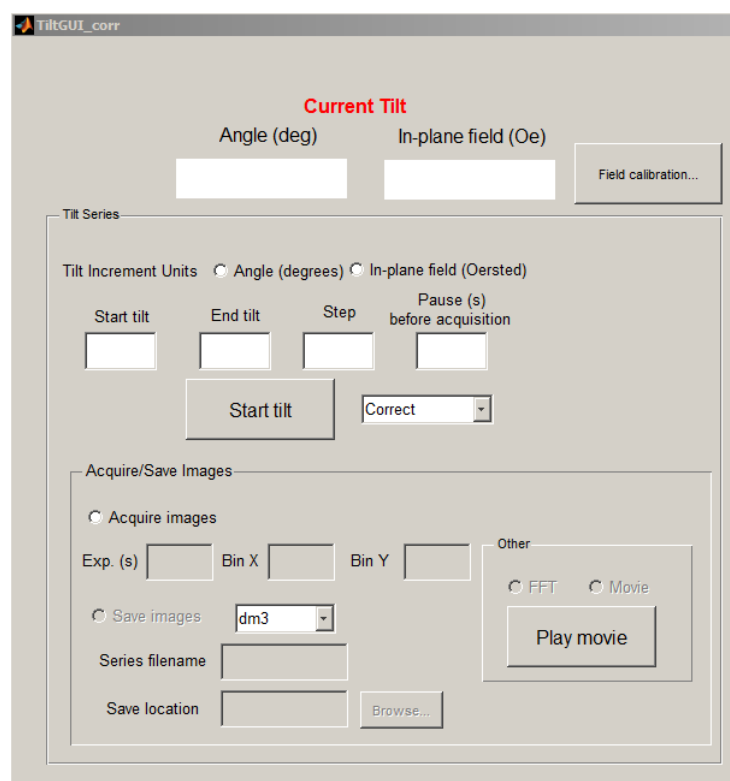


**Figure 2.24:** GUI written to control the tilt angle of the stage on the JEOL ARM microscope and thus automate a tilt series. The GUI allows the user to input start, end and increment angles, or equivalent in-plane fields. The option also exists to acquire and save images taken on the CCD camera.

processed to give a fast Fourier transform.

The tilt series GUI is also designed with in-situ magnetising experiments in mind, rather than simply tomography. If the lens field strength is calibrated as a function of excitation, then the stage can be driven to an angle that is equivalent to an in-plane applied field, which is useful if the switching fields of the sample are already known. In addition, the GUI allows the user to choose whether the program corrects any overshooting or undershooting of tilt increment steps that may arise due to backlash in the stage motor. In standard tomography software, this correction happens automatically; however, for magnetising experiments, this is not necessarily desirable. For example, if the stage overshoots, moving to a large tilt angle, the consequence of reducing the angle means reducing the field, which is not desirable until the sample has been saturated.

## 2.3 Electron beam lithography

### 2.3.1 Overview

Electron beam lithography (EBL) was used to fabricate the square cross-section nanowires in Chapter 3 and the array of nanomagnetic elements that comprise artificial spin ice in Chapter 5. The facilities at the James Watt Nanofabrication Centre (JWNC), within the School of Engineering, were used to fabricate EBL samples presented in this thesis.

An overview of the process will be given here and, where appropriate, expanded upon in the following subsections. The first step is the application of a thin film of an electron sensitive polymer, known as a resist, to a flat substrate. The resist is kept in solution and dropped onto the substrate and spun at a few thousand rpm, during which time most of the solvent evaporates. This is followed by a baking process to make sure that the remainder of the solvent has evaporated. The pattern is then written by the beam writer, which scans a focused beam of electrons across the sample, in a manner similar to the upper column of a STEM or scanning electron microscope. Depending on whether the resist is positive or negative tone, the regions exposed to the electron beam are removed or remain when placed in a developer solution. This is shown by Fig 2.25, which shows a sequence of steps for positive (left) and negative (right) resists. During exposure, the molecules in the exposed region of the positive resist undergo chain scission, making them soluble to the developer; molecules in negative resist experience cross-linking meaning that exposed areas remain following development. In this thesis, only positive resists were used.

Once the pattern has been defined, it needs to be transferred to the substrate, the technique used in this thesis is the lift-off technique, using positive resist, as shown in Fig 2.26. Following development, the sample is metallised *i.e.* a thin metal film was deposited. After metallisation, the remaining resist was dissolved, leaving the metal pattern.

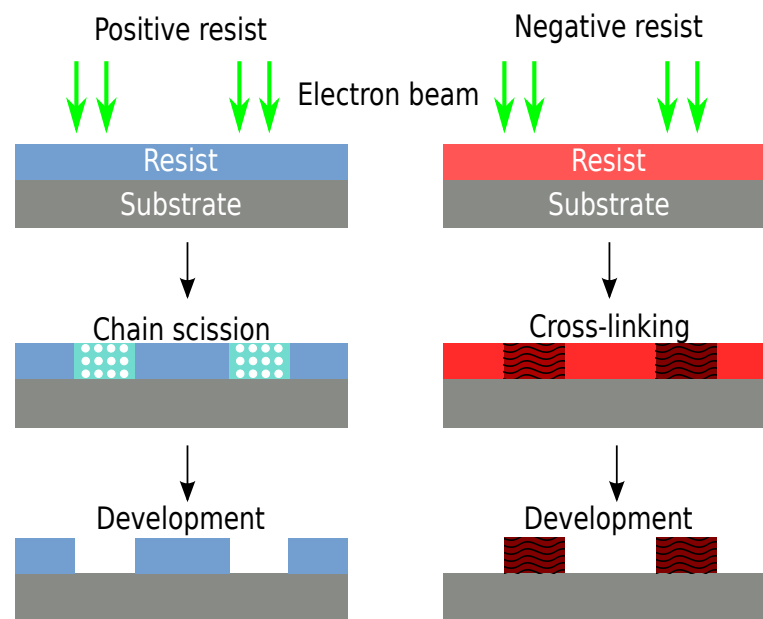


**Figure 2.25:** Schematic showing the difference between positive (left) positive and (right) negative resist tones. The electron beam weakens the positive resist which results in the removal of exposed areas during development; the opposite occurs for negative resists, only the exposed regions remain after development.

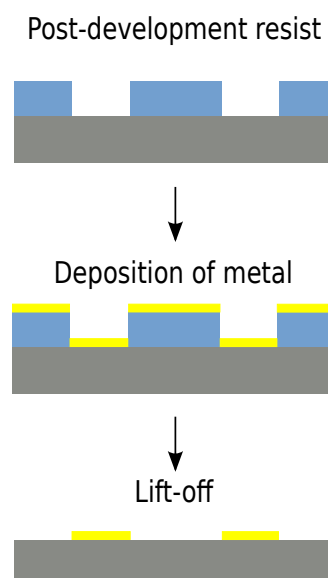


**Figure 2.26:** Schematic illustrating the process stages following development. The sample is metallised then the remaining resist is dissolved (lift-off), leaving the pattern.

### 2.3.2 Resist configuration

All EBL samples presented in this thesis were fabricated using polymethyl methacrylate (PMMA), a widely available, high resolution, positive tone resist, using the lift-off technique. With lift-off either a single layer or a bilayer of resist can be used, as depicted on the left and right of Fig 2.27, which shows the difference between the two after development. The single layer setup in Fig 2.27 shows a more realistic sequence of images compared to Fig 2.26, when the sample is metallised, some of the deposited material sticks to the resist sidewalls, which means that “flags” are left at the edges of the structure after the resist has been dissolved. Flags are small pieces of metal that stick out from the edges of nanostructures. Flagging is a problem for magnetic nanostructures; the flags can act as pinning sites for the magnetisation and can obscure useful edge contrast in Lorentz TEM images. This is a particular problem for the high aspect-ratio nanowires of Chapter 3, where, as in Fig 2.28a), the flags can be approximately half of the nanowire width. The bilayer, shown in Fig 2.27, includes a top layer of resist that is of higher molecular weight than the bottom, meaning that it develops at a slower rate, resulting in an undercut profile post-development. In principle, flagging can be avoided by the use of the resist undercut profile; therefore, all magnetic nanostructures were fabricated using the bilayer technique.

Factors that influence the undercut profile obtained with the bilayer technique are exposure dose, development conditions and resist layer thickness. The wrong combination of parameters can result in flagging or no lift-off at all. This is shown in Fig 2.28: a) shows a nanowire with large flags present along its edges; b) shows an array of patterned nanoelements where lift-off of resist did not happen, metal is covering the entire surface so that elements are not isolated. In addition, particular problems exist for the structures fabricated in Chapters 3 and 5, which push the limits of the lift-off technique.

For the square cross-section nanowires in Chapter 3, the width of the wires ideally need to be  $\leq 100$  nm. Magnetic nanowires have been fabricated successfully using lift-off [58]; unlike the nanowires here, they were wide, thin planar structures, typically around 300 nm wide and 20 nm thick. The nanowires here, with square

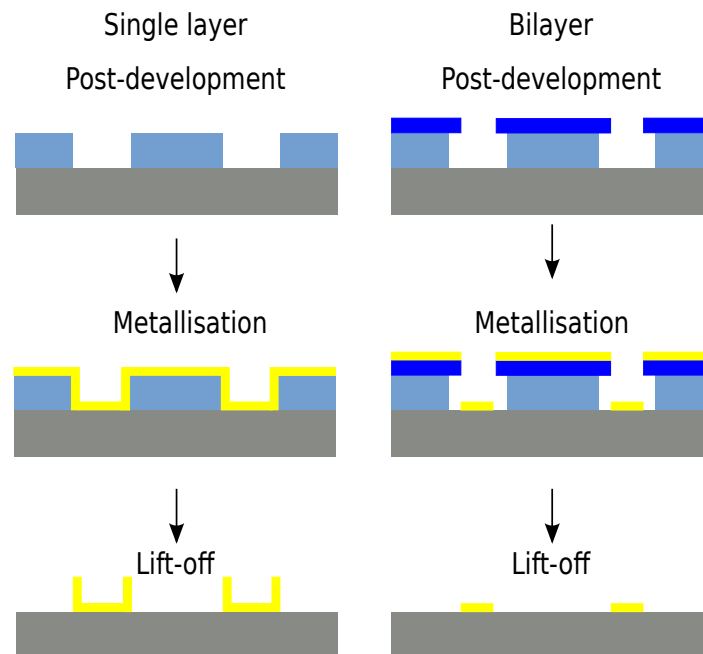


**Figure 2.27:** Single layer (left) and bilayer (right) configurations of the lift-off technique. The single layer ultimately leads to flagging on the nanostructures after lift-off, this is avoided by using the bilayer technique.

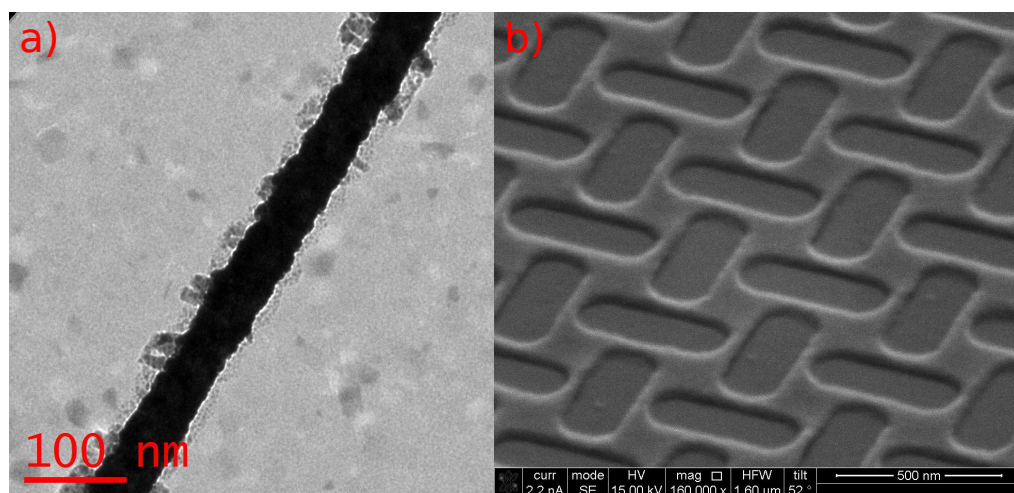


**Figure 2.28:** Examples of situations where lift-off has resulted in a) flagging and b) the metal not lifting off at all.

cross-sections around 60-100 nm, are more challenging to fabricate, being narrower *and* thicker. Increasing the thickness of resist comes at a cost, the electron beam broadens as it passes through the resist

$$\Delta d(nm) = 0.9 \left( \frac{t_{res}}{V} \right)^{1.5} \quad (2.24)$$

where  $\Delta d$  is the increase in beam diameter,  $t_{res}$  is the total thickness of the resist in nm and  $V$  is the electron beam accelerating voltage in kV. Given that the resist thickness should be 2-3 times the thickness of the structure,  $t_{res} = 300$  nm and  $V = 100$  kV corresponds to an increase of beam diameter of  $\sim 5$  nm. This means an additional 10 nm width for a nanowire whose desired width is 50-100 nm. A broader beam will result in wider structures, therefore, the resist thickness needs to be minimised. The exposure dose also needs to be high enough so that the bonds in the resist are broken, if the dose is too low then structures may have flagging or be missing from the pattern after lift-off. However, if the dose is too high, the resist will be over-exposed and, thus, the structures' actual size will be greater than the designed pattern. Dose tests were run to optimise nanowire fabrication; for given resist thicknesses, a series of doses and design widths were used. Doses used in this work are larger than usually required for PMMA [59], this is due to the non-bulk substrates used, as described in the following section.

The square cross-section nanowires were fabricated using the following resist configuration: a bottom layer of PMMA 8% 2010, a top layer of PMMA 2.5% 2041. Each layer was spun for 1 minute at 5000 and 3000 rpm for bottom and top layers, respectively and baked for 30-60 minutes each at 180°C. This resulted in a bottom layer 200 nm thick and a top layer 70 nm thick. Fig 2.29 shows a graph plotting measured width of nanowires versus their designed width, for the resist thickness used. This graph shows that the measured width is always larger than the designed width, regardless of the dose used; this effect is largest for the highest dose, 4000  $\mu C/cm^2$ . The trend for all doses appears to be linear and, as such, linear fits have been added to the plots. Error bars indicate uncertainty in the measurement of width, which was performed using bright field TEM imaging. The increase in width can partly be attributed to the broadening of the beam within the resist, using

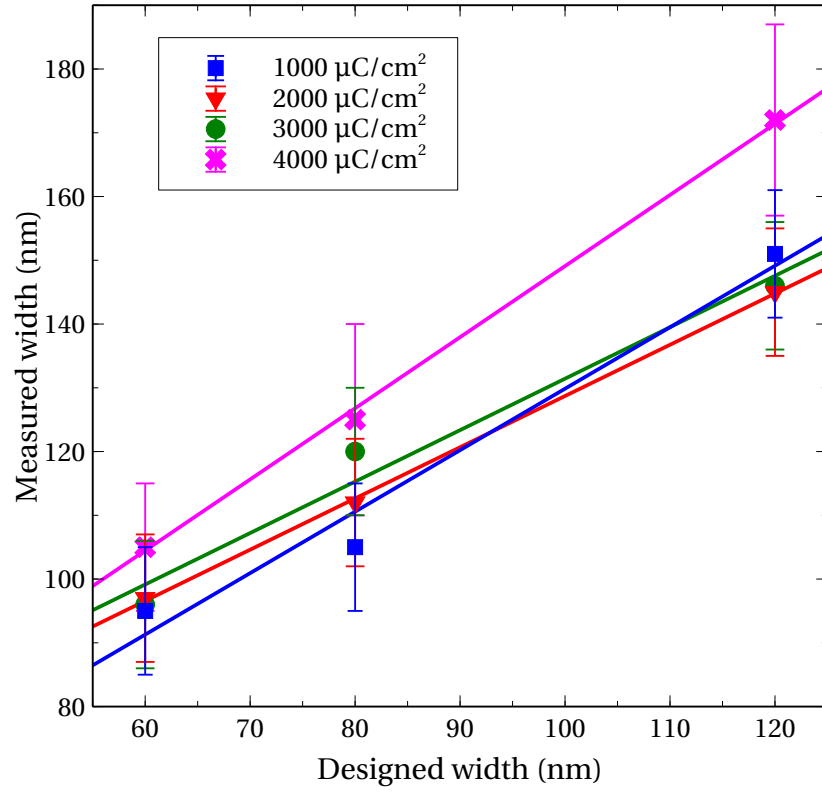


**Figure 2.29:** Measured nanowire widths versus designed size. Lines represents linear fits to the data.

Eq 2.24 this corresponds to 4 nm; however, even when doubled for each side of the wire, this cannot account for the widening of the wires. For this work, this widening is not a major problem - the design width need only be scaled to get the desired width; however, it is clear that this may not continue indefinitely and there must be a lower limit on the width.

The challenge in fabricating nanoelements arrays in Chapter 5 is similar to that of the nanowires. In this case, the total resist thickness needs to be minimised as resist aspect ratios (height:width) exceeding 3:1 are not mechanically stable [60]. The key parameter is the minimum separation of elements, in some cases designed to be 50 nm, which places as upper limit of 150 nm on the total resist thickness. In fact, when beam broadening (see Eq 2.24) and possible over-exposure are taken into account, the actual separation of the elements will be less than this. Elements were designed to be 470 nm long and 170 nm wide with two different unit cell sizes,  $a$ , 370 and 420 nm, which results in a minimum separation between elements of



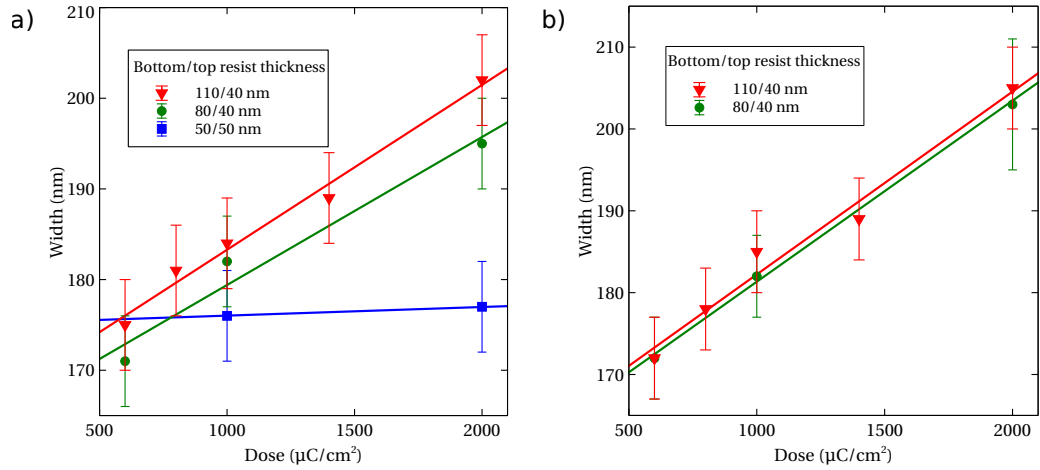


**Figure 2.30:** Measured width of spin ice elements for increasing dose. Two designs are investigated; for a minimum separation of a) 50 nm and b) 100 nm. Lines represent linear fits to the data.

50 and 100 nm, respectively. Fig 2.30, shows the variation of the elements' width, ideally 170 nm, with dose for both unit cell sizes. The graphs show that the width of the elements increases with larger exposure doses; the trend does not appear to change for different resist thicknesses. Linear fits have been added to the data as in Fig 2.29. Considering that the lowest dose ( $600 \mu\text{C}/\text{cm}^2$ ) is not sufficient to avoid flagging, it is clear that the elements need to be designed slightly smaller to achieve the desired width, just as the case with the square cross-section nanowires. Fig 2.30

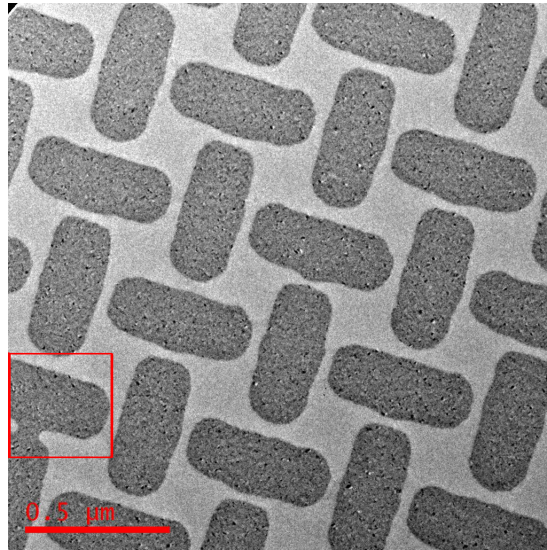


**Figure 2.31:** TEM image of an overexposed spin ice array. Elements are misshapen at close proximity or joined as within the box in the bottom left-hand corner.

shows the same trend for both unit cell sizes, which would indicate that there is no influence of the proximity of the elements. However, for doses of  $2000 \mu\text{C}/\text{cm}^2$  in Fig 2.30, the highest dose elements are misshapen at the point of closest contact, as circled in Fig 2.31, an SEM image of this array. Indeed, as shown by the red box, in some cases the elements become conjoined.

### 2.3.3 TEM substrates

As the primary technique for characterising nanostructures in this thesis was TEM, the substrates had to be electron transparent. For accelerating voltages of 200 kV, an overall thickness of less than 100 nm is desirable. To achieve this, silicon nitride ( $\text{Si}_3\text{N}_4$ ) membranes were used; they are commercially available from Kelvin Nanotechnology (KNT) Ltd. These substrates, shown schematically in Fig 2.32, are  $500 \mu\text{m}$  thick Si chips with approximately 35 nm of  $\text{Si}_3\text{N}_4$  deposited on top that have been back etched to leave a  $100 \times 100 \mu\text{m}^2$  window onto which nanostructures are fabricated.  $2 \times 2$  sets of membranes, measuring  $9 \times 9 \text{ mm}^2$ , are used for spinning resist. As shown in Fig 2.32, membrane arrays have an etched cross and each individual membrane has etched squares for pattern registration. Cleave lines on these chips allow individual membranes to be broken apart easily.

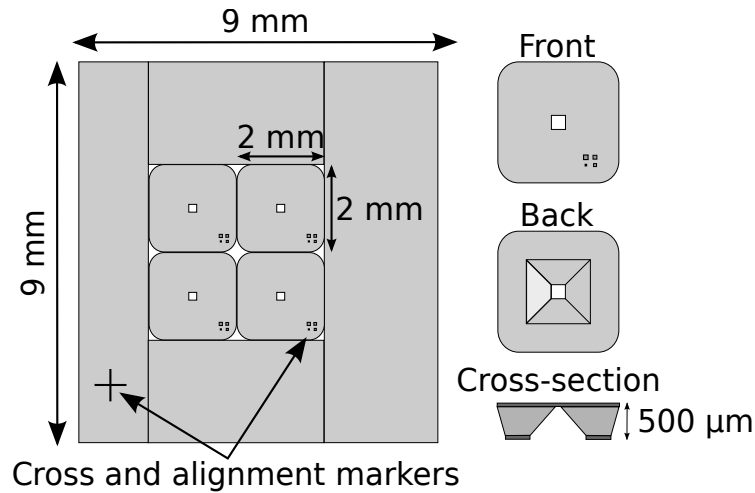


**Figure 2.32:** Silicon nitride membrane array with  $2 \times 2$  membranes, each with an electron transparent window in the centre.

Crucially,  $\text{Si}_3\text{N}_4$  membranes are unlike the bulk substrates typically used for EBL

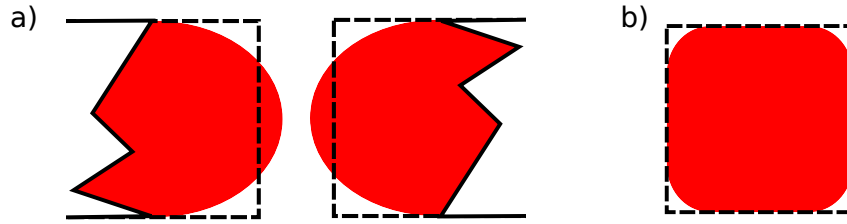


**Figure 2.33:** Representations of the a) inter- and b) intra- proximity effect. The dotted line represents the written area, the red shading is the actual developed area.

patterning in that far fewer backscattered electrons (BSEs) are generated when exposed to an electron beam. BSEs are incident electrons that have been elastically scattered from the substrate. For a bulk silicon substrate, it has been shown [61] that the energy they deposit is equal to 80% of the energy deposited by the incident electrons; however, this is spread out over a larger area, BSEs can deposit energy at a distance of  $40\text{ }\mu\text{m}$  from a  $20\text{ nm}$  irradiated line [61]. This introduces a proximity effect, which manifests in two forms, inter- and intra-shape proximity effects, illustrated in Fig 2.33. In both cases, the dashed outline shows the written area while the red shading shows the developed area. In Fig 2.33a), the dose from neighbouring elements extends to outside the written area; in b), the corners, which receive less dose than the centre of the square, have not received a high enough dose to clear the resist. This does not limit resolution but the proximity effect must be corrected for. The consequences for work on  $\text{Si}_3\text{N}_4$  membranes, as shown previously [58, 62], is that dose corrections due to the inter- and intra-shape proximity effect are unnecessary but a larger dose is required to clear out the resist.

### 2.3.4 Metallisation methods

Metal thin film deposition, metallisation, of EBL samples was ultimately performed using thermal evaporation, a common technique for the deposition of thin films. While the deposition of Py thin films using PLD was suitable for the work in Chapter 4, it was found to be unsuitable for metallisation of substrates with EBL patterned resist.

This is due to the fact that, after lift-off, extremely large flags, shown in Fig 2.34,

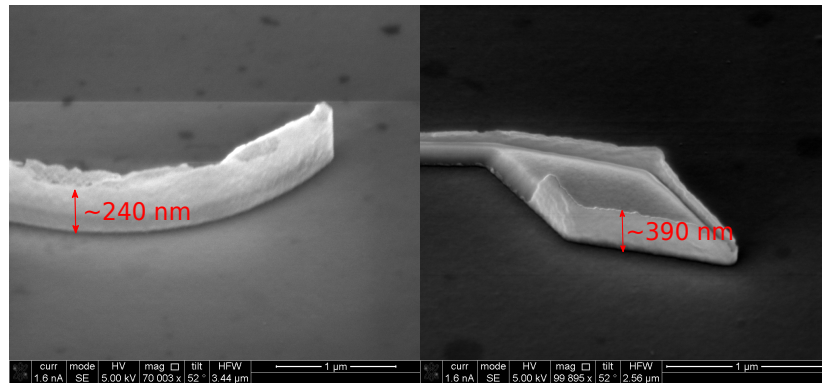


**Figure 2.34:** SEM images of extreme flagging associated with structures fabricated using PLD as metallisation technique with lift-off. Height of the flags depends on the thickness of the bottom layer of resist.

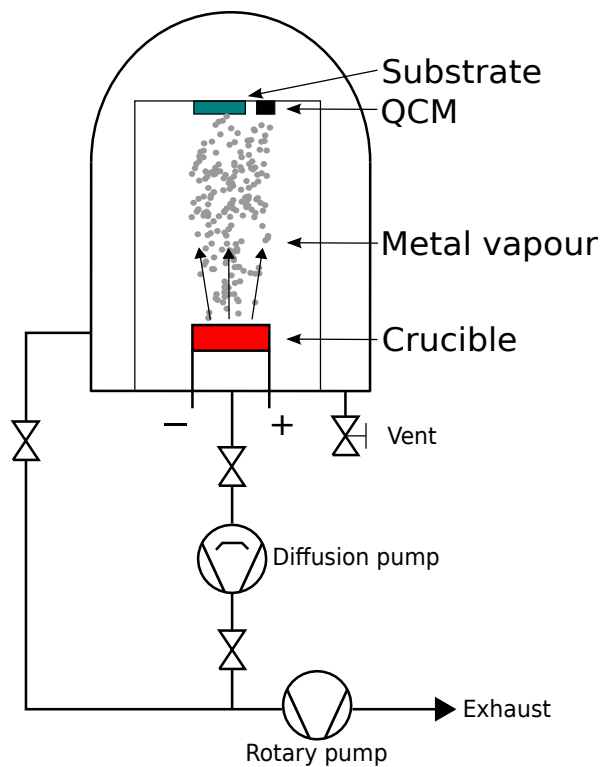


**Figure 2.35:** Schematic of the thermal evaporator vacuum system showing the relative positions of substrate, QCM and evaporation source (crucible).

remain at the edges of the structure. Unlike the flagging shown in Fig 2.28a), this structure almost completely surrounds the pattern. Interestingly, this remained a problem regardless of changes to resist layer thickness and dose. As indicated on Fig 2.34a) and b), the height of the flags increases with increasing bottom layer resist thickness which suggests that the deposited material is coating the resist sidewalls.

This may be because of a large angular spread of the ablated PLD species or because the fact that it consists of a large proportion of charged particles which are attracted to the sidewalls.

Thermal evaporation was used as an alternative to PLD deposition. An overview of the vacuum system of a thermal evaporator is shown in Fig 2.35, which illustrates the principle behind thermal evaporation. A crucible, that contains the material to be evaporated is placed inside a high vacuum chamber. During deposition, the crucible is heated resistively by direct current, using typically  $\sim 5$  A; this heats the material to the point of evaporation, forming a metal vapour. As shown in Fig 2.35, the vapour travels in a directional manner to the substrate, placed above, and condenses to form a thin film. A quartz crystal microbalance (QCM) is used to monitor the film thickness during deposition. This is a quartz crystal resonator whose resonant frequency decreases as more material is deposited onto it; typical deposition rates are 0.1 to 0.5 nm per second. The base pressure in the thermal evaporator's vacuum chamber was  $\sim 8 \times 10^{-7}$  mbar, while the pressure during deposition was typically  $\sim 5 \times 10^{-6}$  mbar, due to out-gassing. The properties of the

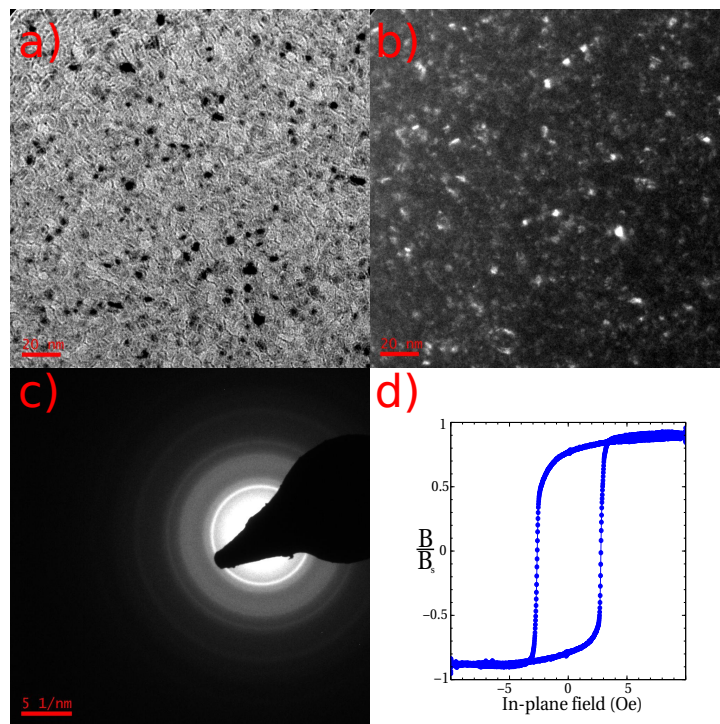


**Figure 2.36:** a) a bright field, b) dark field and c) diffraction pattern images from TEM, showing the polycrystallinity of thermally evaporated Py films. d) shows a characteristic hysteresis loop.

Py films produced by thermal evaporation are summarised by Fig 2.36: a), b) and c) show, respectively, bright field, dark field and diffraction images from TEM, indicating that the deposited films are polycrystalline; and d) shows a hysteresis loop obtained from the BH Looper which shows that the saturation induction of the thermally evaporated films is  $\sim 0.8$  T. While this is not the ideal value of 1 T, the thin films are not expected to behave much differently magnetically to those with ideal saturation induction, though the contrast in Lorentz TEM would be reduced. The reduction in moment may either be attributed to the increase in chamber pressure during deposition causing some unwanted oxidation of the films or to a variation in stoichiometry from  $\text{Ni}_{80}\text{Fe}_{20}$ .

## 2.4 Focused ion beam/ scanning electron microscope

Focused ion beam (FIB) lithography was used to fabricate discs in Chapter 4 and scanning electron microscopy (SEM) was used to characterise the structure of all fabricated nanostructures. The instrument used for both these techniques is the FEI Nova Dual-Beam, which combines an ion and electron column.

The electron column in SEM is constructed similarly to the top half of a scanning transmission electron microscope (STEM), a ray diagram of which is shown in Fig 2.2. In contrast to TEM, typical accelerating voltages are 5-15 kV. As shown by Fig 2.37a), the electron beam is focused to a probe and scanned across the sam-

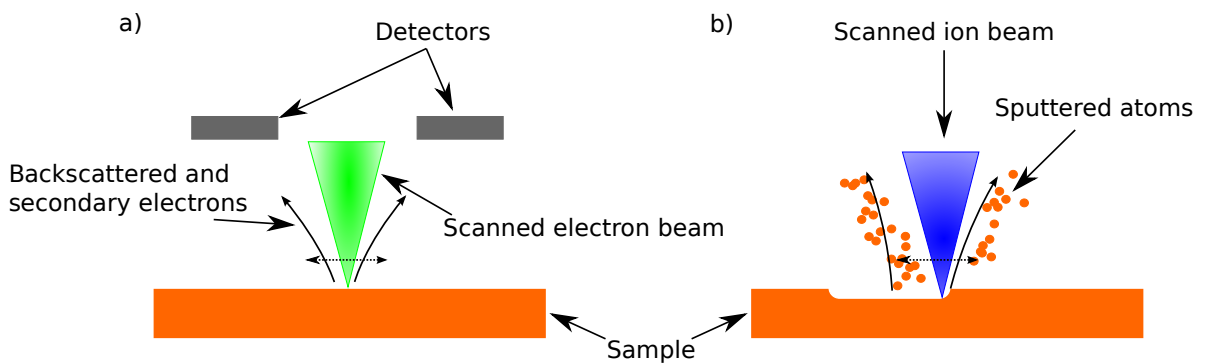


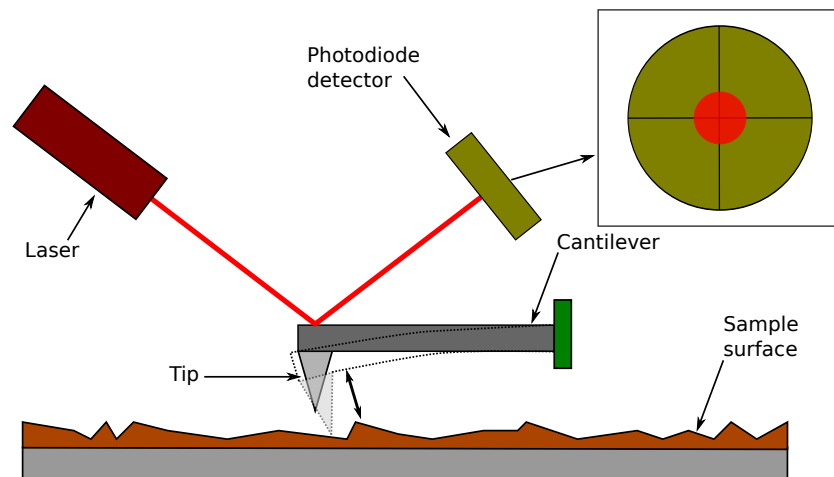
**Figure 2.37:** a) imaging in SEM and b) milling using FIB lithography.

ple surface. Thus, through the detection of generated backscattered and secondary electrons, an image of the sample surface is generated pixel-by-pixel.

The FIB uses a  $\text{Ga}^+$  source, chosen due to its low melting point ( $\sim 30^\circ\text{C}$ ), which is then ionised and accelerated towards the sample. Typical accelerating voltages of 30 kV mean that the  $\text{Ga}^+$  ions have enough energy to cause sputtering from the sample, thus milling material from the surface, as illustrated schematically in Fig 2.37b). In addition, imaging may be performed using the ion beam [63], due to secondary electron generation. The discs studied in Chapter 4 were fabricated by milling rings onto continuous thin films by using ring shapes that are standard patterns in the Dual-Beam software. As the films were deposited onto 50 nm thick  $\text{Si}_3\text{N}_4$  membranes, low ion currents (93 nA) were used, to avoid milling through the substrate.

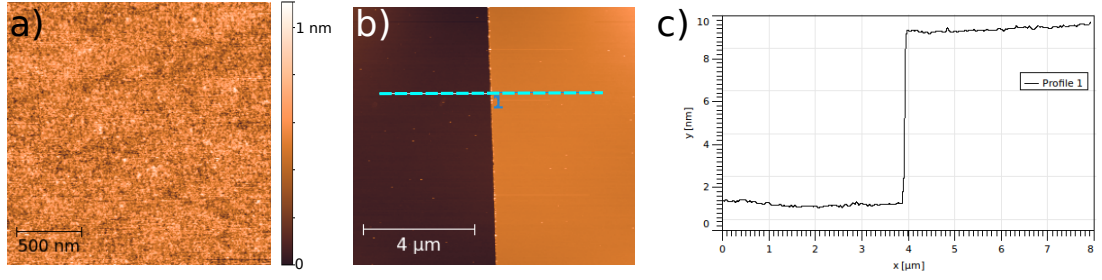
## 2.5 Atomic force microscopy

Atomic force microscopy (AFM) was used to measure the thickness of deposited films throughout this thesis. In addition, magnetic force microscopy (MFM), a subset of AFM, is discussed as a possible imaging technique in Chapter 4. AFM, which was invented in 1986 [64], falls within the wider category of scanning probe microscopy, a technique in which a sharp tip, also called a probe, is scanned across a sample surface and information is gained through the tip-surface interactions.



**Figure 2.38:** The operation of tapping mode AFM.





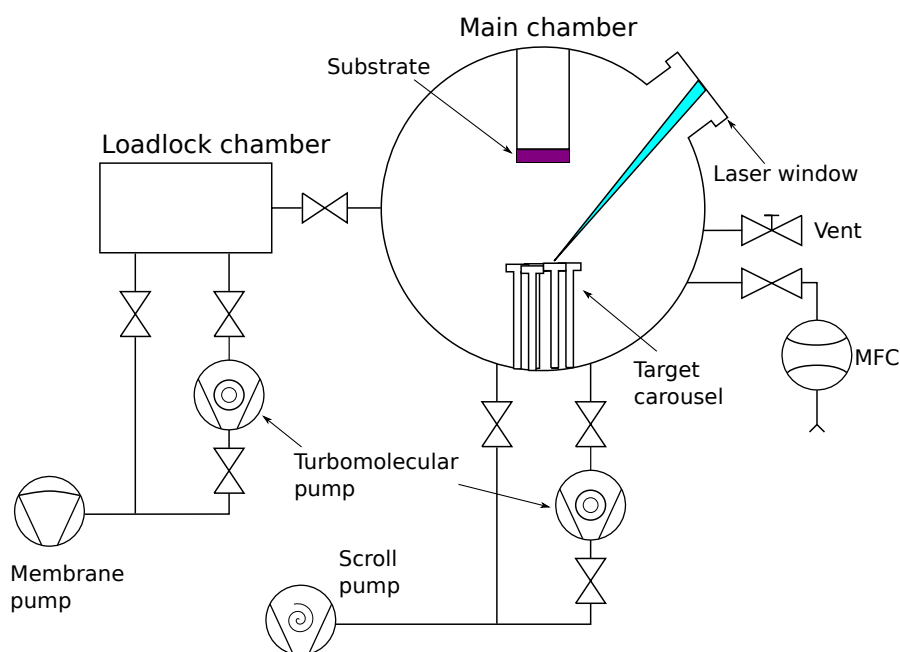
**Figure 2.39:** Examples of AFM images. a) shows a surface scan, while b) and c) shows, respectively, a step height scan and a line profile across the step.

Fig 2.38 shows a schematic diagram of the operation of AFM. A tip is positioned at the end of a cantilever that can be rastered across the sample, the tip-sample interactions are detected by monitoring the deflection of a laser that reflects from the top surface of the cantilever onto a photodiode detector, similar to the detection method of the TEM DPC imaging mode. A Dimension 3100 microscope was operated in semi-contact tapping mode throughout this thesis. This works by oscillating the cantilever using piezo-actuators at or close to its resonant frequency. As the name suggests, the tip makes contact with the surface at the bottom of its oscillation. Using the signal on the photodiode detector, a feedback loop with the controller electronics maintains a constant oscillation amplitude and, for each pixel in the plane of the sample, the height change required to maintain the oscillation amplitude is recorded. Thus, an image of the surface topography is generated. In the case of MFM, the tip is coated in a magnetic alloy and exhibits a magnetostatic coupling with the sample [65]. Contrast is generated by magnetic charge, which allows magnetic domain walls to be imaged [56]. An example of AFM images is shown in Fig 2.39: a) shows a surface scan of a typical permalloy film deposited by pulsed laser deposition, described in the following section, showing peak-to-peak roughness of less than 1 nm; and b) and c) show, respectively, a scan across the a step between a deposited permalloy thin film and substrate and a line profile from which the film thickness may be measured.



## 2.6 Pulsed laser deposition

Pulsed laser deposition (PLD) was used to deposit the metal magnetic/non-magnetic bilayers characterised in Chapter 4. The materials deposited were  $\text{Ni}_{80}\text{Fe}_{20}$  (permalloy, Py), Cu and Pt. PLD became widely used following the deposition of superconducting cuprates in the 1980's [66]. This highlighted the key strength of the technique, the ability to successfully transfer target stoichiometry to the substrate. In contrast, thermal evaporation is not suited to the deposition of co-elemental materials whose constituents have significantly different vapour pressures. While sputter deposition can be used to deposit elementally complex films, PLD offers greater control over the deposition pressure since a background of Ar is required to strike a plasma in sputtering. PLD is a technique well known for the deposition of complex oxide films [67], it may also be used to successfully grow metal thin films [68]. Indeed, due to the high energy of deposited species in PLD, novel phases of metal thin films have been grown [69]. The formation of macroscopic particulates, called droplets, is a major disadvantage to using PLD. A method to suppress droplets will be shown here.



**Figure 2.40:** Overview of the PLD vacuum system. A focused laser is directed through the window onto the target carousel.

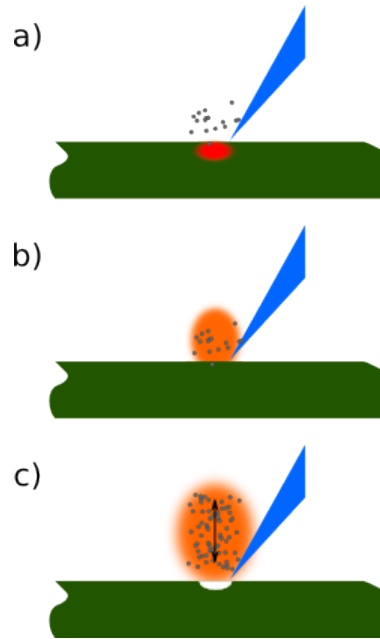


**Figure 2.41:** The ablation process in PLD. a) As the laser strikes the target, some material is vaporised; b) if dense enough, it expands; c) the expansion sputters material from the target.

The equipment used was a Neocera PLD system with an ultra-violet KrF excimer laser: pulse duration  $\tau = 20$  ns,  $\lambda = 248$  nm and repetition rate 1 - 20 Hz. The laser fluence is typically  $1\text{--}5 \text{ Jcm}^{-2}$  and base pressure is  $\sim 5 \times 10^{-9}$ . An overview of the PLD vacuum system is shown in Fig 2.40. During deposition, the laser is directed through a window and focused to a spot on a material target in the main (deposition) vacuum chamber. Six targets, held on a carousel, can be rotated and rastered so that a different area is ablated each time and preferential etching prevented. The PLD system has a mass flow controller (MFC) to control the inlet of gas into the deposition chamber; in this work Ar used during metal deposition. The laser is intense enough to ablate some material from the surface which travels to a substrate held above the targets. Key stages of the ablation process are illustrated in Fig 2.41. As shown in a), the laser first strikes the target, heating the surface of the target and vaporising some material. In metals, the conduction electrons absorb the energy from the laser pulse and transfer it to the lattice by electron-phonon interaction., this happens within a few picoseconds. If the initial vaporised material is dense enough, it absorbs the remainder of the laser pulse, forming a plasma, as in Fig 2.41b). This plasma “plume” expands, sputtering more material from the

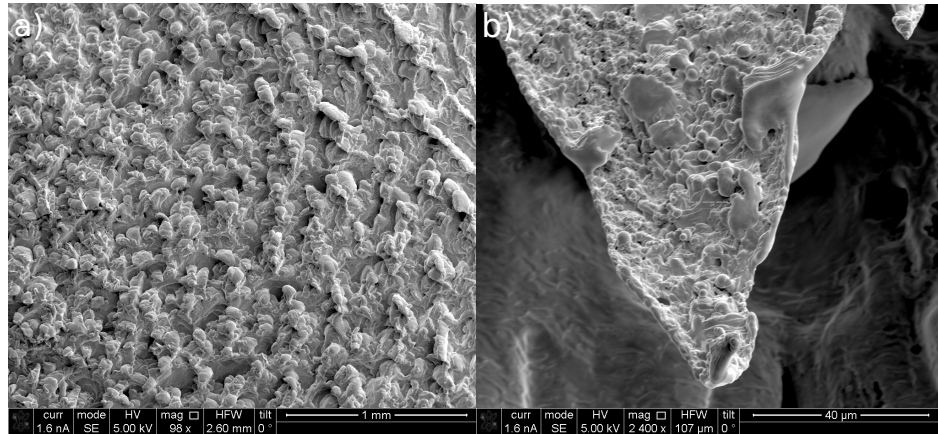


**Figure 2.42:** SEM image of the PLD Py target. a) shows the general morphology of the target and b) is a higher magnification image of globule-like structures.

target surface.

The formation of droplets in PLD occurs via two processes, the first of which is hydrodynamical sputtering. The process in Fig 2.41a), as well as causing a surface layer to be evaporated, heats the target, causing subsurface melting. The subsequent plasma plume expansion is then responsible for recoil forces that eject the molten material from the target, which has been called “splashing”. The second mechanism occurs due to multiple melt/freeze cycles that occur through repeated ablation of the target. This shapes the morphology of the target, resulting in a characteristic roughening of the target, shown in Fig 2.42a), an SEM image of the target. The higher magnification image, Fig 2.42b), reveals the presence of globule-like particles, similar to droplets. In order to reduce the droplet density, a beam limiting aperture was introduced into the laser optic system, which was placed before the focusing lens. The consequence of this is that the laser profile before focusing was modified: the least intense parts of the pulse, the “tails”, are removed and the most intense parts remain. The effect of the aperture is shown in Fig 2.43a) and b) which shows SEM images of a Py film deposited with and without the aperture, respectively, with the same deposition conditions. The introduction of an aperture drastically reduces the number of droplets, the areal density falls by just over a factor of two; in addition, the number of droplets of diameter  $> 1 \mu\text{m}$  is also massively reduced. It is thought that the reason is that the volume of molten material of the target is reduced, thus reducing the amount of material ejected as droplets. A consequence

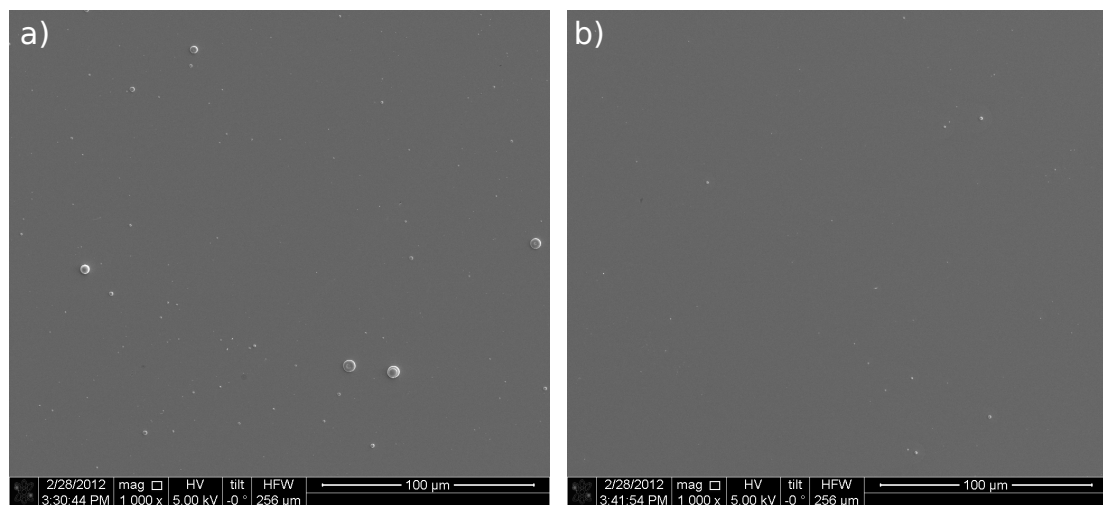


**Figure 2.43:** Reduction of droplets for a situation a) without and b) with an aperture.

of the aperture is that growth rates are reduced, the films in Fig 2.43a) and b) are both 10 nm in thickness but the number of shots required to achieve this for the film grown with an aperture is three times higher than without. As measured using low angle diffraction, the value of  $B_s$  for PLD deposited Py films was found to be  $\sim 0.8$  T; however, with the use of a capping layer, as in Chapter 4 this value is  $\sim 1$  T. This is presumably because oxidation of the Py film is prevented.

# 3

## Domain walls in three dimensional nanowires

### 3.1 Introduction

The majority of research into domain walls (DWs) in nanostructures has been focused on flat, planar, two dimensional (2-D) nanowires due their potential applications as next generation devices such as racetrack memory[70], shift registers [71] and logic devices [72] based on DW motion. For materials without strong magnetocrystalline anisotropy *i.e.* soft magnetic materials, the shape anisotropy of these nanostructures forces the magnetisation to lie along the wire axis, forming head-to-head or tail-to-tail DWs as it rotates from one axial direction to another. These DWs, like the nanostructures that support them, are 2-D in character as their structure does not change through the thickness of the wire. DWs can propagate along

the wires under an applied magnetic field or spin-polarised current. While the potential exists for devices based on these 2-D DWs, their motion suffers from Walker breakdown [73] in planar nanowires. During this process, an anti-vortex structure is periodically nucleated and annihilated at the wire edges, above a threshold field [74]. This causes non-uniform, oscillatory DW motion, making this system potentially unsuitable for applications.

Three dimensional (3-D) nanostructures, such as cylindrical nanowires (CNWs) and cylindrical nanotubes (CNTs), contain DWs whose structure varies through the thickness. In contrast to 2-D nanowires, it has been shown that Walker breakdown is suppressed under certain circumstances [75, 76]. Since CNWs and CNTs lack lateral edges, the process by which Walker breakdown occurs is different. Nucleation of an individual anti-vortex, as in the case of 2-D nanowires, is prevented; it has thus been predicted that Walker breakdown mediated by single anti-vortex nucleation is topologically forbidden [77], which makes 3-D systems attractive for device applications. In other regards, despite the 3-D nature of these nanostructures and the DWs they support, many phenomena associated with them are also found in 2-D nanowires. This is perhaps unsurprising given that the ground states of 2-D and 3-D wires are similar, with 3-D structures supporting states analogous to the C or S states found in 2-D elements [78, 79]. Phenomena common to both include the dependence of wire dimensions on stable DWs, the presence of metastable states and the influence of chirality. In the 2-D case, for thicker wires, a vortex DW forms to minimise magnetostatic energy; however, due to the exchange energy, there is a minimum vortex width, at which point the most stable DW becomes a transverse DW [39]. This lacks the chirality of the vortex DW, forming a triangular region perpendicular to the wire axis. The transition between these two types may be mediated by the formation of another, the asymmetric transverse DW. This also contains a section of magnetisation which points perpendicular to the wire axis; however, its shape is asymmetric, retaining some of the curling nature of the vortex DW. The asymmetric transverse DW is an example of DW metastability, also seen when DWs change type when propagating along the wire. An understanding of this is essential for applications due to the different dynamic behaviour of each DW.

Indeed, chiral symmetry breaking occurs for some of the same DW types, having been shown to influence the DW pinning potential [55].

The phenomena seen in 2-D nanostructures are reflected in the 3-D case. Studies into the reversal of CNWs have revealed that there are two stable DW types: a Bloch point wall (BPW), stable in thicker wires, and a transverse wall (TDW), found in thinner wires [80, 81]. This size dependence is similar for CNTs except that the hollow core removes the necessity for the Bloch point singularity, replacing the BPW with a similar structure known as a vortex wall (VDW). Like in 2-D nanowires, a minimum vortex size means that the BPW/VDW is stable for thicker wires until above a critical radius, with the TDW becoming stable in thinner wires. Simulations have shown that Walker breakdown is suppressed for a particular chirality of field direction/VDW rotation [77, 82], breaking chiral symmetry.

CNTs and CNWs have been fabricated using free-standing nanowires using the vapour-liquid-solid method [83, 84], ion beam techniques [85] and electrodeposition into anodic alumina pores, which in particular has provided a route through which densely packed arrays of CNWs and CNTs may be fabricated with a high degree of control over the geometry [86, 87, 88, 89, 90, 91]. Consistent with simulations, the reversal mode, identified through characteristic hysteresis loops, is seen to depend on the nanostructure dimensions [88, 92]. The behaviour of individual CNWs has also been characterised using magnetic force microscopy and electron holography revealing different micromagnetic structure such as uniform/flower [93, 94] and vortex ground states [95]. Studies on individual nanostructures have also confirmed reversal by BPW [96, 97]; however, depending on the angle of the applied field with respect to the wire axis, reversal by coherent rotation is possible [98]. The possibility of metastable states in 3-D DWs had not been explored until an asymmetric transverse wall (ATDW) was experimentally observed in nickel nanowires using electron holography [99]. However, the range of stability/metastability of the ATDW is unknown and its spin structure is still poorly understood as well as the prospect of other metastable DWs in 3-D nanostructures.

Therefore, this work investigates the presence of metastable DWs in 3-D nanostructures. Micromagnetic simulations are used to model DWs in CNWs and CNTs

across a range of dimensions: this allows their complex structure to be characterised and the range of their stability determined. In addition, since instances of experimental observation of 3-D DWs are relatively scarce, Lorentz transmission electron microscopy (LTEM) is used to image the magnetic structure of square cross-section nanowires (SNWs), fabricated using electron beam lithography (EBL). SNWs are used as they support the same 3-D DWs as CNWs [100] and, as discussed later, to simplify their characterisation with LTEM. EBL allows SNWs of different dimensions to be fabricated and thus the issue of size dependence of DW type can be investigated, as well as DW metastability.

## 3.2 Simulation of cylindrical nanostructures

### 3.2.1 Methods

Simulations of CNWs and CNTs were performed using Nmag [33], a finite element simulation package, which is suited to curved geometries due to the fact that its discretisation method is a mesh of tetrahedra. A range of radii, from 5-50 nm, were investigated and the wire length was fixed at  $L = 2 \mu\text{m}$ , which is sufficient to ensure that the DW structure is not influenced by the formation of end states [79]. Material parameters typical of permalloy were used throughout: magnetisation,  $M_s = 8.6 \times 10^5 \text{ Am}^{-1}$ , exchange constant,  $A = 1.3 \times 10^{-11} \text{ Jm}^{-1}$  and magnetocrystalline anisotropy constants,  $K_1 = K_2 = 0$ . The damping parameter was set as  $\alpha = 0.5$ , which is artificially high and thus allows the simulation to relax quickly without otherwise compromising results, a method used elsewhere [101]; it should be stated that this value of  $\alpha$  would not be appropriate for simulations of magnetisation dynamics. The maximum node spacing was set to be below 5 nm *i.e.* less than the exchange length of permalloy, which is 5.3 nm. Preliminary simulations were set up with several initial states, each of which forces the magnetisation to meet head-to-head, as shown in Fig 3.1. The initial states differ only in the middle of the wire, where the magnetisation meets. They are: a) a state with a section of transverse magnetisation, b) an abrupt  $180^\circ$  transition and c) a state with a section of magnetisation that curls around the wire c). The direction of magnetisation at the end of each



wire was fixed to point along the wire axis in the Nmag script, thus preventing the formation of flux closure states [79] and the magnetisation was allowed to relax into a stable state.

Preliminary results showed that three DW types could be stabilised: the TDW, BPW and ATDW. Using the initial starting states in Fig 3.1 was insufficient for determining the metastability of the DWs across the range of dimensions because all of the starting states in Fig 3.1 may result in the same DW type; however, this does not necessarily rule out the DWs as unstable in that geometry. In order to assess the stability/metastability of the DWs, each individual structure (TDW, BPW and ATDW) would have to be used as the starting state of the simulations for each geometry. If the DW failed to stabilise, it would be deemed unstable at those particular dimensions. To accomplish this, the final 3-D magnetisation vector field of each DW from the preliminary results were taken and expanded or compressed

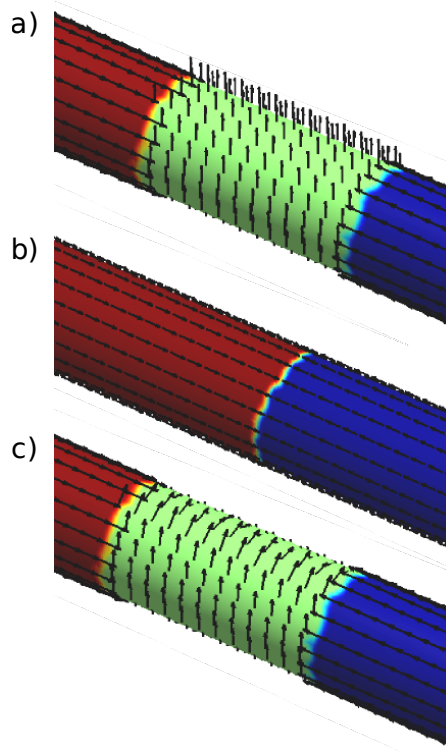


**Figure 3.1:** Starting states used for preliminary simulation results, each forcing the magnetisation to lie head-to-head: a) a wire with a central 100 nm section of magnetisation transverse to the wire axis; b) an abrupt  $180^\circ$  transition; c) a central 100 nm section where the magnetisation curls around the wire.

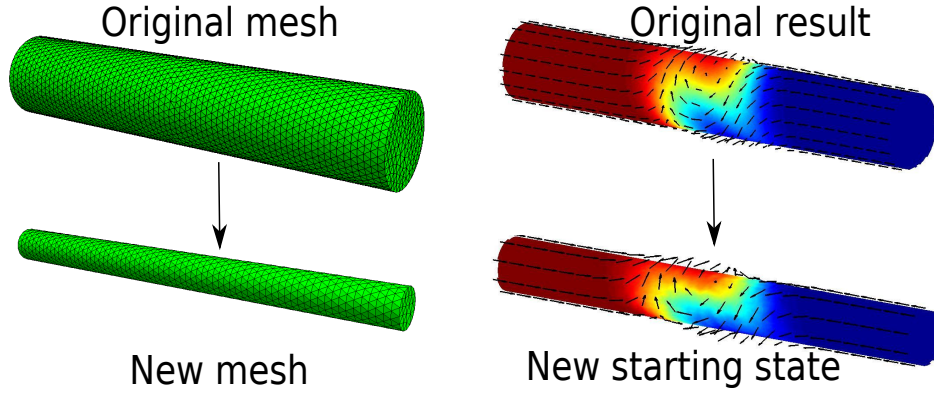


**Figure 3.2:** Illustration showing the process of interpolating a result onto a mesh of different size. This shows (top) the original mesh with the simulation result for a cylindrical nanowire of radius 25 nm and (bottom) the new mesh with the original result interpolated onto the smaller mesh, to be used as a starting state for a nanowire of radius 10 nm.

and interpolated onto a larger or smaller mesh to be used as a starting state. The process is illustrated by Fig 3.2, where an ATDW state that is stable for a wire of radius 25 nm is interpolated onto a smaller mesh of radius 10 nm. The relaxed ATDW spin structure was then allowed to relax, as before. If the final state is not an ATDW, then this DW type was found to be unstable for this geometry. Thus, for any given dimension, the starting state could be TDW, ATDW or BPW and the stability of each DW type could be determined. The interpolation was performed using a MATLAB code which has been included in Appendix A.

It should be noted that the simulations did not include an applied field oriented perpendicular to the wire axis. This would be included to mimic the effect of the vertical field of the objective lens in a transmission electron microscope.

### 3.2.2 Simulation results

#### 3.2.2.1 Cylindrical nanowires

A 3-D view of each of the three stable DW types, with cross-sections through each, is shown in Fig 3.3 with a), b) and c) representing the TDW, ATDW and BPW, respectively. Fig 3.3a) and c) will be described first, before contrasting with b).

The colours represent the axial component of magnetisation,  $M_z$ , while the arrows show the direction of the surface magnetisation. The TDW, which is stable for the thinnest wires, has magnetisation meeting head-to-head before rotating to point perpendicular to the wire axis, breaking the cylindrical symmetry. Unlike the 2-D TDW, which has two degenerate states, the transverse component here can point at any azimuthal angle. In contrast to the TDW, the BPW curls around the wire axis, forming a vortex-like spin state, as shown by the cross-section in Fig 3.3c), a Bloch point lies at the centre of this structure. Bloch points are micromagnetic singularities, near which the direction of magnetisation is undefined. The ATDW, shown in Fig 3.3b), is named in Ref [99] (a convention that will be followed here) by analogy with the asymmetric transverse DW in 2-D nanowires; however, from the 3-D view, it bears little resemblance to either the TDW or BPW. The magnetisation rotation is mediated through a vortex-like spin structure on the surface of the wire and it will be shown later that this is coupled to an anti-vortex on the opposite side of the wire. Cross-sections show a transverse section with vortices on either side; unlike the BPW, these axial vortices are of opposite chirality. From Fig 3.3 it can be seen that the ATDW lacks the cylindrical symmetry of the BPW and the mirror plane symmetry of the TDW. It is clear from Fig 3.3 that the TDW is narrower than the other two DWs; the colours that show the change in  $M_z$  indicate that the change in direction of magnetisation is much more extended for the ATDW and BPW. In regards to width, the TDW is similar to 2-D DWs, with a width approximately equal to the width/diameter of the wire; the ATDW and BPW are closer to twice the diameter of the CNW. The width of the DWs in Fig 3.3 can be calculated from the profile of axial magnetisation, shown for each DW in d). The wall width is calculated in this instance by taking the start/end of the wall to be where  $|M_z| < 0.95$ . Wall widths calculated in this way are shown in the legend of Fig 3.3d): TDW is 46 nm; ATDW is 112 nm; and BPW is 102 nm.

A phase diagram, derived from micromagnetic simulations, is presented in Fig 3.4 which plots the magnetic energy density as a function of cylinder radius for each of the stable DWs. This identifies each DW as stable or metastable, depending on the wire radius. The total energy density is plotted as well as its two contributions,

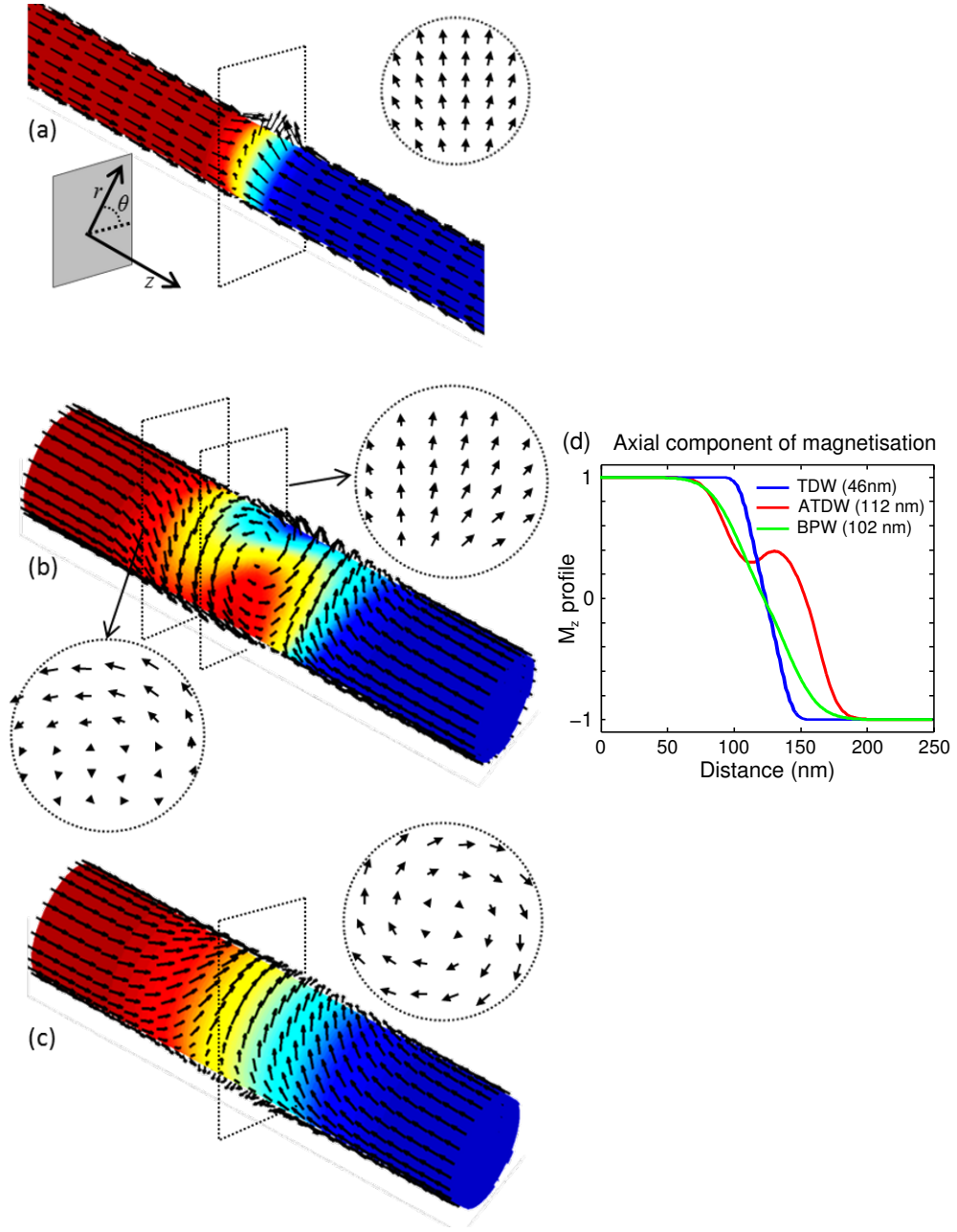


**Figure 3.3:** A 3-D view of the micromagnetic structure of a) a transverse domain wall (TDW), b) an asymmetric transverse wall (ATDW) and c) a Bloch point wall (BPW). The TDW radius is 17.5 nm, ATDW and BPW radii are both 25 nm. Colours indicate the axial component,  $M_z$ , and the arrows show the direction of surface magnetisation. The transition from red to blue gives an illustration of the wall width, although d) shows profiles of axial magnetisation taken where the DW is widest (calculated widths indicated in the legend). Cross-sections through the  $r, \theta$  plane, taken at the positions of the wireframes, are inset.

magnetostatic and exchange energy density. Energy *density* is plotted to allow comparison of wires of different thickness and to better display relative changes across the phase diagram, which is valid for wires of the same length. It is expected that this phase diagram will scale with the exchange length for other soft magnetic materials, as with studies on other magnetic nanostructures [102, 103]. Fig 3.4 shows that the TDW is the ground state for thin wires, the BPW for thicker wires, with a phase change at a radius of 20 nm, in agreement with previous studies [104]. In Ref [104] a phase diagram is calculated using analytical expressions of the magnetic energy associated by a BPW and TDW; this assumes only the TDW and BPW can stabilise, then dimensions for which either are the ground state can be determined by comparing energy values. The phase diagram identifies the ATDW as a metastable state that stabilises at radii of 20 nm and above. By using the interpolation method detailed in Section 3.2.1, the stability of all DWs has been tested for each radius; for example, a TDW cannot be forced to stabilise at the largest radius of 50 nm.

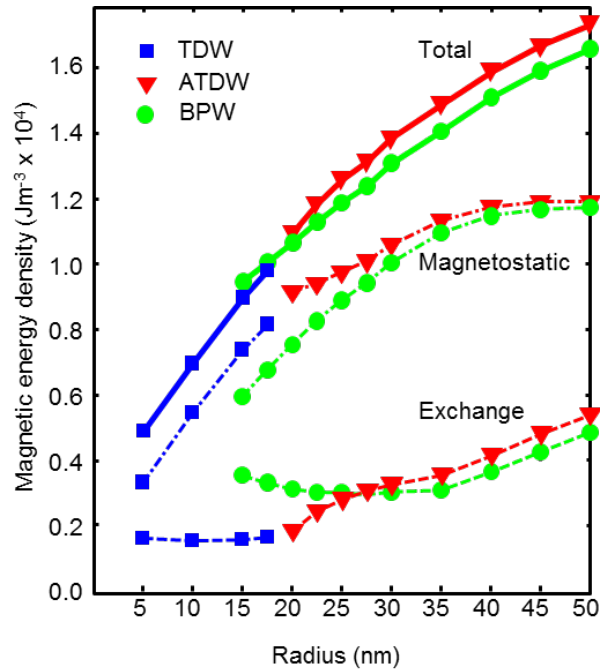


**Figure 3.4:** Micromagnetic phase diagram for domain walls in cylindrical nanowires, showing the variation of magnetic energy density wire with nanowire radius for transverse (TDW), asymmetric transverse (ATDW) and Bloch point (BPW) domain walls. The total energy density is plotted with a full line; its two components, magnetostatic and exchange energy, are plotted with dashed lines.

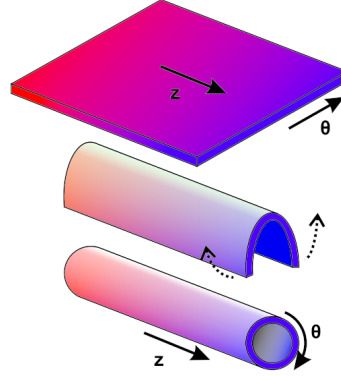


**Figure 3.5:** Schematic illustrating the process, from bottom to top, of unrolling surface magnetisation to produce a schematic with  $z$  and  $\theta$  aligned horizontally and vertically, respectively.

The phase change from the BPW to the TDW, comparable to the 2-D case, can readily be understood when the individual energy components, shown in Fig 3.4, are considered. The formation of the BPW, with its curl state cross-section, minimises magnetostatic energy at a cost of exchange energy; below the critical radius this is no longer beneficial as the exchange energy associated with the magnetisation curling around the wire becomes large, which makes the low exchange energy TDW favourable, in spite of its larger magnetostatic energy. The ATDW is not able to stabilise below 20 nm and its total energy is always larger than the BPW, which makes it a metastable state across the range of radii simulated. Significantly, and especially from the perspective of device applications, the plots for total energy density for the BPW and ATDW in Fig 3.4 are in close proximity. This shows that the difference in energies between the TDW and BPW ground states and the metastable ATDW is small, suggesting that any imperfections in real systems could act as a pinning site and aid transitions between the two DW types.

Another interesting feature of Fig 3.4 is that there seems to be a continuity between the plots of TDW and ATDW, suggesting that there is a similarity between the two walls that is not captured well by Fig 3.3. A more useful way of visualising the walls' spin structure is by “unrolling” the outer surface layer of magnetisation, as illustrated schematically in Fig 3.5. The axial,  $M_z$ , and tangential,  $M_\theta$  magnetisation components of the 3-D vector field are projected onto a 2-D plane. The results of this for each DW type is shown in Fig 3.6. This visualisation of the unrolled magnetisation uses a colour map to represent the radial component,  $M_r$ , and arrows

indicate the direction of in-plane magnetisation,  $M_z$  and  $M_\theta$ .

Fig 3.6a) shows that, when unrolled, the TDW offers the most remarkable topology,

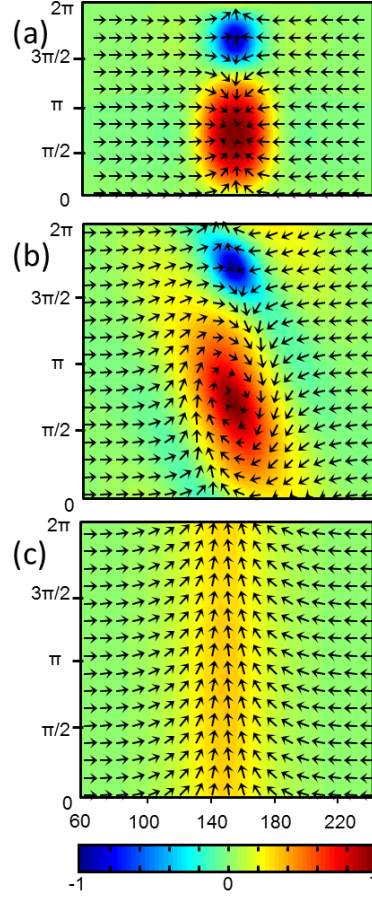


**Figure 3.6:** “Unrolled” surface magnetisation of a typical a) TDW, b) ATDW and c) BPW. Colours represent the radial component,  $M_r$ , while the arrows represent contributions of the axial and tangential components,  $M_z$  and  $M_\theta$ , respectively. The horizontal scale is in nm.

consisting of two surface spin structures. The smaller of these, at the top of Fig 3.6, is recognisable as an anti-vortex structure, similar to that found in various magnetic thin film systems [105, 106]. Below the anti-vortex is a highly divergent spin state, which is reminiscent of a meron state where spins point radially inward/outward to/from a core. Meron states are topologically equivalent to vortex states [36] and have the same exchange energy but, compared to the curl state of the vortex, have substantially higher magnetostatic energy. This monopolar, divergent structure is thus highly unlikely to stabilise in magnetic thin films, although effective meron states have been observed in antiferromagnetically coupled discs [107, 108]. In this

situation, the overall magnetostatic energy is reduced compared to a single disc due to the equal and opposite charges in the two coupled layers. In the case of an ATDW, the meron-like state and the anti-vortex are not coupled in this way, instead connected by the wire volume.

The similarities between the TDW and ATDW implied by Fig 3.4 are made clear by Fig 3.6. It can now be seen that the ATDW is composed of two surface spin states that form a vortex/anti-vortex pair, a configuration commonly seen in magnetic thin films in the form of cross-tie walls [105]. Interestingly, the vortex/anti-vortex configuration is similar to a transient structure seen in CNTs [77]. Ref [77] investigates the situation where symmetry is broken between the two field direction/vortex rotation handednesses in CNTs; for one handedness, Walker breakdown is mediated through the nucleation of a vortex/anti-vortex pair (the transient structure), which exists briefly before annihilating. From Fig 3.6 it can be seen that the transition from TDW to ATDW occurs by a simple rotation of spins about a core to change between meron-like and vortex states. This results in symmetry breaking and a switch from an achiral to a chiral spin state. The simple rotation of spins, along with the ATDW and TDW plots in Fig 3.4, shows that the ATDW is merely a continuation of the TDW for thicker wires.

The simplest surface spin configuration in Fig 3.6 is the BPW, which resembles a transverse DW in 2-D nanowires. However, unlike the 2-D transverse DW, the colour map in Fig 3.6c), which displays  $M_r$ , shows that the wall has a non-zero out-of-plane component. This radial component is not observable from the 3-D view in Fig 3.3. The transition from TDW or ATDW to BPW, as well as reducing the magnetostatic energy, removes all topological spin structures from the surface of the wire, which may mean that it is difficult to change between the transverse walls and the BPW, as the spin structures are topologically protected and thus difficult to remove.

A useful way of comparing the magnetostatic energy associated with each DW is to consider the source of this energy *i.e.* the magnetic charge. The total charge associated with the magnetisation meeting head-to-head for a wire of cross-sectional area  $A$  is  $\rho_0 = 2M_s A$ . In this case it is more useful to consider the surface charge,  $\sigma_s = \mathbf{M} \cdot \hat{\mathbf{n}}$ , because the volume charge  $\rho = -\nabla \cdot \mathbf{M}$  is small in comparison. The



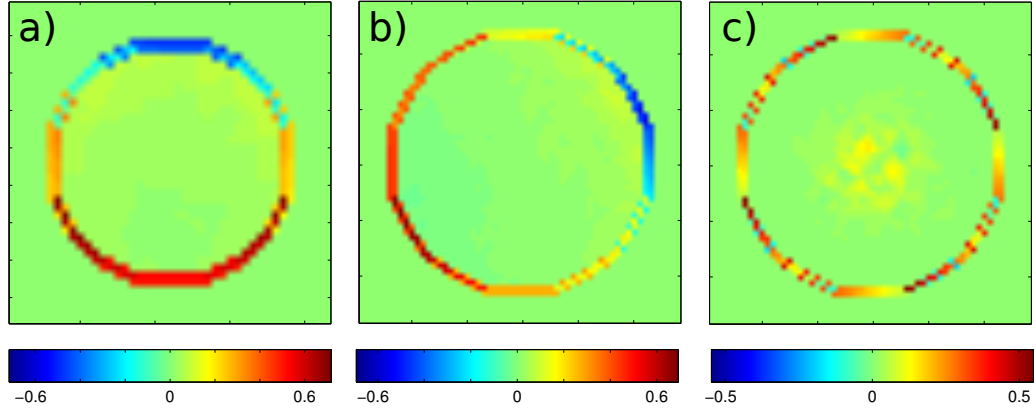


**Figure 3.7:** Cross-sections through the centre of each domain wall showing the divergence of magnetisation,  $\nabla \cdot \mathbf{M}$  (arbitrary units): a) a TDW, radius 17.5 nm; b) an ATDW, radius 25 nm; c) a BPW, radius 25 nm. The wire edges contribute notably more charge than the volume of the wire.

dominance of the surface over volume charge is shown in Fig 3.7 where three cross-sections of the divergence of magnetisation for each DW show that the majority of the charge is concentrated at the wire surface.

The individual positive and negative contributions to the magnetic surface charge, calculated by summing over each node, have been plotted as function of CNW radius in Fig 3.8. The plots are normalised to the total charge  $\rho_0$ . Therefore, a net charge of (positive) unity means that all of the charge arising from the magnetisation meeting head to head is transported to the surface. It is necessary to plot the positive and negative contributions to  $\sigma_s$  instead of the net value because the latter can give a false impression of the magnetostatic energy. For example, the BPW has the highest net surface charge and yet, as shown by Fig 3.4, the lowest magnetostatic energy. Given the relatively small volume charge, Fig 3.8 gives a representation of the magnetostatic energy arising from the DW surface spin states.

The BPW plot in Fig 3.8 confirms that there is very little bulk divergence; the normalised  $\sigma_s$  is exclusively positive and close to unity. This is consistent with the internal spin structure which is a non-divergent curl state. The plots of the TDW and ATDW have both positive and negative contributions due to the opposite directions of the anti-vortices and vortex/meron-like states. Interestingly, they show

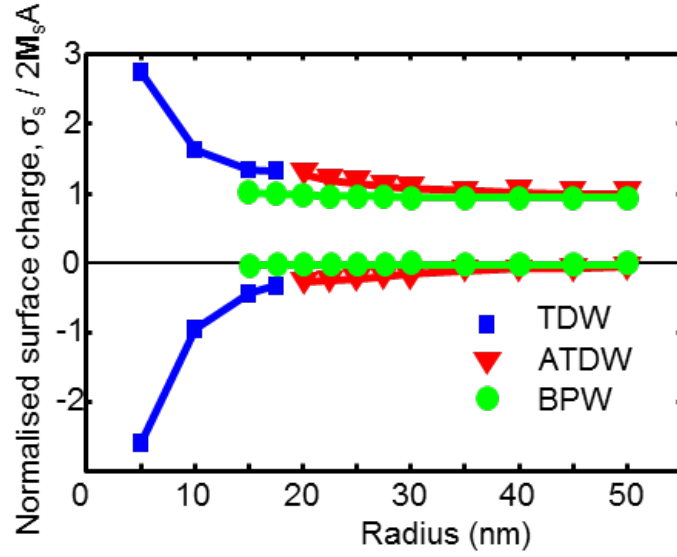


**Figure 3.8:** Variation of surface charge with cylindrical nanowire radius for the three domain wall types. Charge is calculated by summing over each node on the surface and normalising to the total charge associated with head-to-head magnetisation,  $\rho_0 = 2M_s A$ , where  $A$  is the cross-sectional area. Positive and negative contributions to the charge are plotted.

a continuous trend as a function of radius, which is intuitive when considering the simple rotation of spins to change from the divergent to curl state. This transition is analogous to the change from a flower to C or S states in patterned rectangular 2-D elements or CNW/CNT ground states [78, 79]. In fact, when viewing the TDW and ATDW in cross-section, as in the insets to Fig 3.3, they resemble the flower and C/S state, respectively. As with these examples, the transition is accompanied by breaking of mirror symmetry and induced chirality, reflected in the change from meron-like to vortex surface states. In both cases, wider structures have magnetisation pointing primarily along the axis with partial flux closure states at the ends to lower magnetostatic energy at the cost of exchange energy; thinner structures also have mainly axial magnetisation but the spins at the end are only able to fan out slightly due to the high cost in exchange energy. The chirality of the ATDW is likely to cause its dynamic behaviour to be different from the TDW, especially given predictions of chiral symmetry breaking in DW motion [77, 82]; the symmetry of a DW under applied field is broken depending on the field direction and rotational sense.

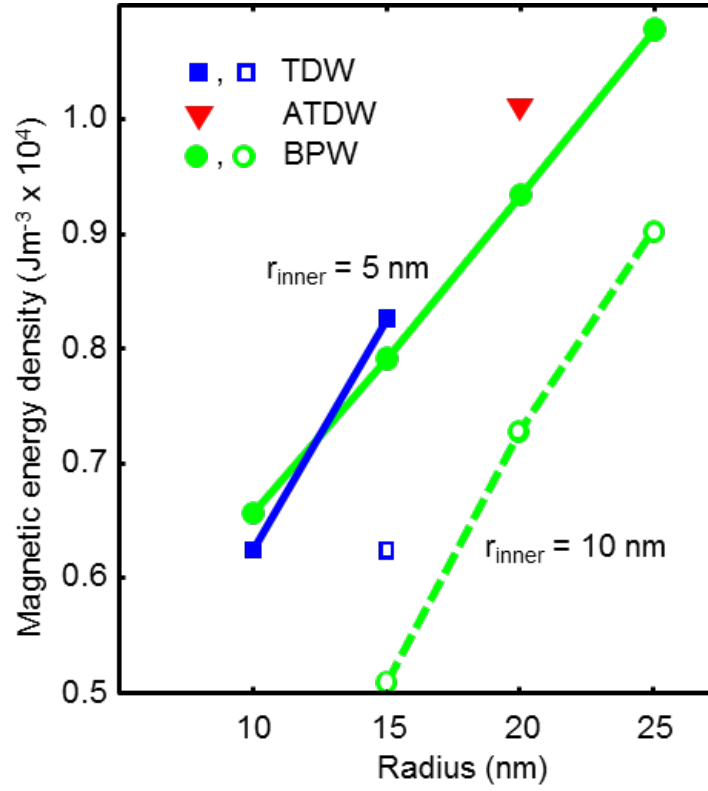


**Figure 3.9:** Phase diagram for domain walls in cylindrical nanotubes. Magnetic energy density is plotted as a function of radius for nanotubes of inner radius (filled markers, full line) 5 nm and (empty markers, dashed line) 10 nm. Single points are plotted for ATDW of inner radius 5 nm and TDW of inner radius 10 nm.

### 3.2.2.2 Cylindrical nanotubes

While CNTs are topologically different structures to CNWs, the DWs that are stabilised in the two are similar. The main difference is that the BPW in CNWs becomes the VDW due to the loss of the core material along the wire axis; the external spin structure of the TDW and VDW is very similar to that of the corresponding DWs in CNWs. Despite the existence of transient vortex/anti-vortex states [77], the prospect of ATDWs as stable DWs in CNTs has, until now, not been examined. Fig 3.9 shows a phase diagram for CNTs which includes plots of magnetic energy density as a function of radius for two values of inner radius, 5 nm and 10 nm. This plot shows that the VDW is stable across the entire range simulated, unlike the other two DWs.

The ATDW is found to be stable for only one particular inner/outer radius

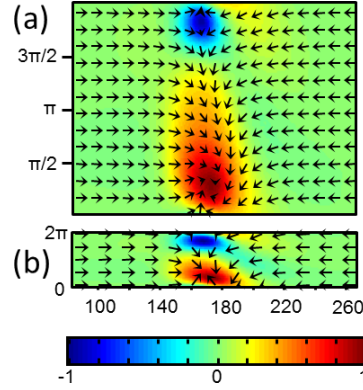


**Figure 3.10:** Unrolled view of the inner and outer surfaces of a nanotube. This shows directly the extra surface charge introduced by the inner surface.

combination, a CNT with an inner radius of 20 nm and outer radius of 5 nm. The unrolled view of this solitary ATDW is shown in Fig 3.10. In fact, Fig 3.10 shows that the ATDW here has an anti-vortex and a spin state that does not fully have the divergent, symmetric character of the meron-like state nor the curling, chiral nature of the vortex state; it is similar to the effective meron state seen in antiferromagnetically coupled discs [108]. The ATDW in CNTs can therefore be seen as an intermediate state. This state could not be stabilised at any other dimension, regardless of how the initial state was constructed. The reason for this is that when moving from CNWs to CNTs, the wire core is removed and the low divergence volume is replaced by an internal surface which has extra surface charge, as directly visualised in Fig 3.10. Fig 3.10 also shows that the magnetisation does not curl around the wire in a way which resembles “onion” states [109], perhaps this is because the cost in exchange energy would be too high. As the radius is reduced below 20 nm, the exchange energy starts to become large, as shown by Fig 3.4.

### 3.2.3 Experimental image calculation

Micromagnetic simulations are useful as an aid in interpreting experimental images. The simulations presented in the previous section will be used to calculate Lorentz microscopy images, an experimental technique described in Chapter 2. Ultimately, it was decided that SNWs should be fabricated in order to characterise 3-D DWs. SNWs are more attractive from an experimental point of view, in that their uniform

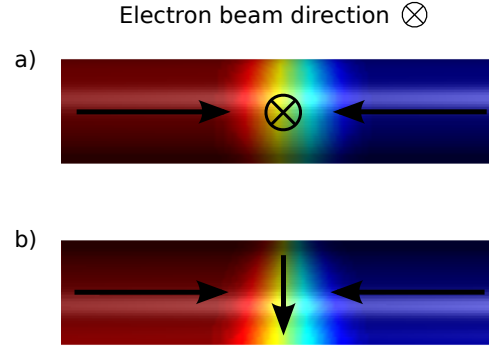


**Figure 3.11:** Illustration of the two extremes in Fresnel imaging of a TDW. In a), the transverse component is parallel to the electron beam and thus does not deflect the beam; the nanowire has been rotated  $90^\circ$  in b) and the transverse component is perpendicular to the beam, resulting in deflection.

thickness produces uniform electrostatic phase contrast; unlike CNWs where the opposite is true. Since the bulk of simulations were performed on CNWs, these are used for Lorentz TEM image calculation; however, the contribution of electrostatic phase contrast is not included so that they may be compared with SNW results presented later.

It should be noted, however, that the unrolled views of CNWs and CNTs, used to characterise surface spin structures, are also useful from an experimental perspective. Fig 3.6 and 3.10 show  $M_r$ , a direct visualisation of the surface charge,  $\sigma_s$ , which is the source of contrast in magnetic force microscopy (MFM). The TDW and ATDW can be distinguished from the BPW by the magnitude and the polarity of the charge. The charge associated with the BPW is evenly distributed around its surface, whereas the ATDW and TDW have concentrated regions of charge of opposite polarity due to the spin states on their surfaces. The ATDW is also wider than the TDW, which may be used to distinguish between the two transverse walls. Simply from Fig 3.3, it can be seen that the TDW width is approximately equal to the diameter of the wire, while the ATDW is twice the diameter.

### 3.2.3.1 Lorentz image calculation

Details on calculating Lorentz TEM (LTEM) images from micromagnetic simulation data are given in Chapter 2. As described in Ch 2.2.4, the orientation of the DWs

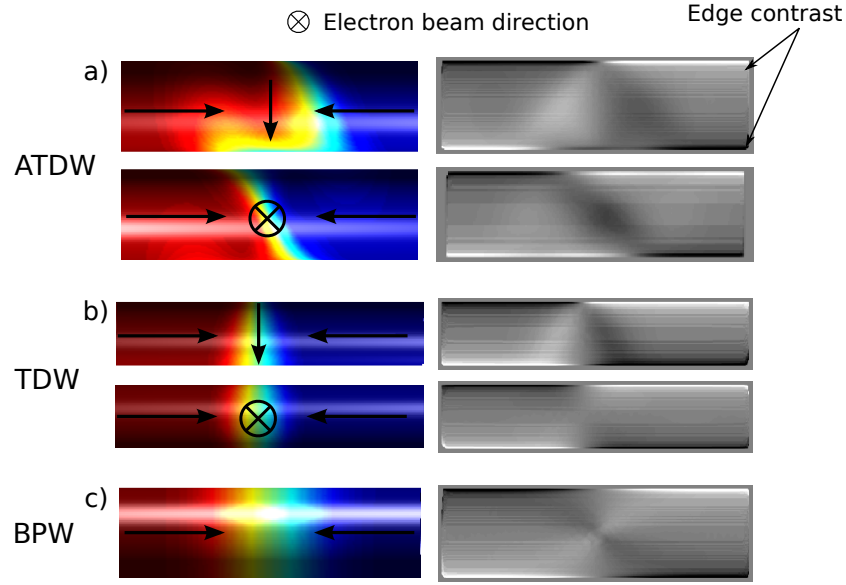


**Figure 3.12:** Calculated Fresnel images for cylindrical nanowires with a) a TDW, b) an ATDW and c) a BPW. Domain wall orientation, with respect to the electron beam, is shown on the left-hand side, resulting Fresnel images on the right-hand side. Two orientations are shown for the ATDW and TDW, as outlined by Fig 3.11. The contribution of electrostatic phase contrast has not been included in these images.

with respect to the direction of the electron beam is important for determining the contrast produced in the final image because the final 2-D projection of the magnitude of magnetisation changes with the orientation of the DW in the wire, as shown by Fig 3.11. The example used is that of a TDW where the transverse component is aligned a) parallel and b) perpendicular to the electron beam, the colours here show the axial component of magnetisation and schematic arrows are used to indicate direction of magnetisation. Each scenario will produce different magnetic contrast. From Eq 2.9, there will be no electron deflection when the transverse component is aligned with the beam compared to the situation where the transverse component is perpendicular to the direction of propagation. The same situation will occur for the ATDW, while the BPW's symmetry means that it will always appear the same at any orientation. Throughout the remainder of this section, calculated Fresnel and DPC images are shown that display two images for the TDW and ATDW, one each for the transverse component lying parallel and perpendicular to the electron beam direction. Fig 3.12 shows calculated Fresnel images for the three different CNW types. The left-hand side shows a visualisation

of the axial component of each DW to indicate its orientation with respect to the electron beam direction; the right-hand side shows the calculated Fresnel image produced by a 2-D projection of the magnetisation. Calculations are shown for two orientations of the TDW and ATDW, at  $90^\circ$  to each other *i.e.* corresponding to the two extremes highlighted in Fig 3.11; however, the contrast could be at any intermediate level between these two in an experiment. While there is detail in the centre of the wires, it may be difficult to image this experimentally. This is because the calculation only considers the change in magnetic phase contrast but not the non-uniform electrostatic phase contrast arising from the non-uniform thickness, which is much stronger than the magnetic contrast. Therefore, the best way to distinguish between the DWs may be by using the contrast at the wire edges, indicated by the arrows on the top Fresnel image of Fig 3.12. This contrast is dark and bright on opposite sides of the wire and switches order on either side of a DW. Considering the transition from dark to bright edge contrast, each DW may be distinguished from the other. The edge contrast of the BPW is symmetric on either side of the wire while the ATDW, shown in Fig 3.12a), has asymmetric contrast, no matter what its orientation. This may allow the ground state BPW to be distinguished from the metastable ATDW. The TDW has symmetric or asymmetric contrast depending on its orientation, but this problem may be overcome by tilting the sample to change the orientation, thus producing a different projection of the magnetisation. Thus, if an image as that in Fig 3.12c) is obtained, by tilting the sample and observing no change or asymmetric edge contrast then the wire contains a BPW or TDW, respectively.

Images have also been calculated for the DPC mode of LTEM. One advantage of this technique over Fresnel imaging is that it is capable of imaging external magnetic fields as well as the magnetic configuration inside a sample. This may be a more suitable way of distinguishing between the DWs given the problem posed by the non-uniform thickness of the sample *i.e.* strong electrostatic phase contrast which obscures magnetic phase contrast. The calculated DPC images presented here do not include the contribution of electrostatic phase contrast. Figs 3.13 - 3.15 show DPC images calculated for each DW. For Figs 3.13 - 3.14, corresponding to the TDW

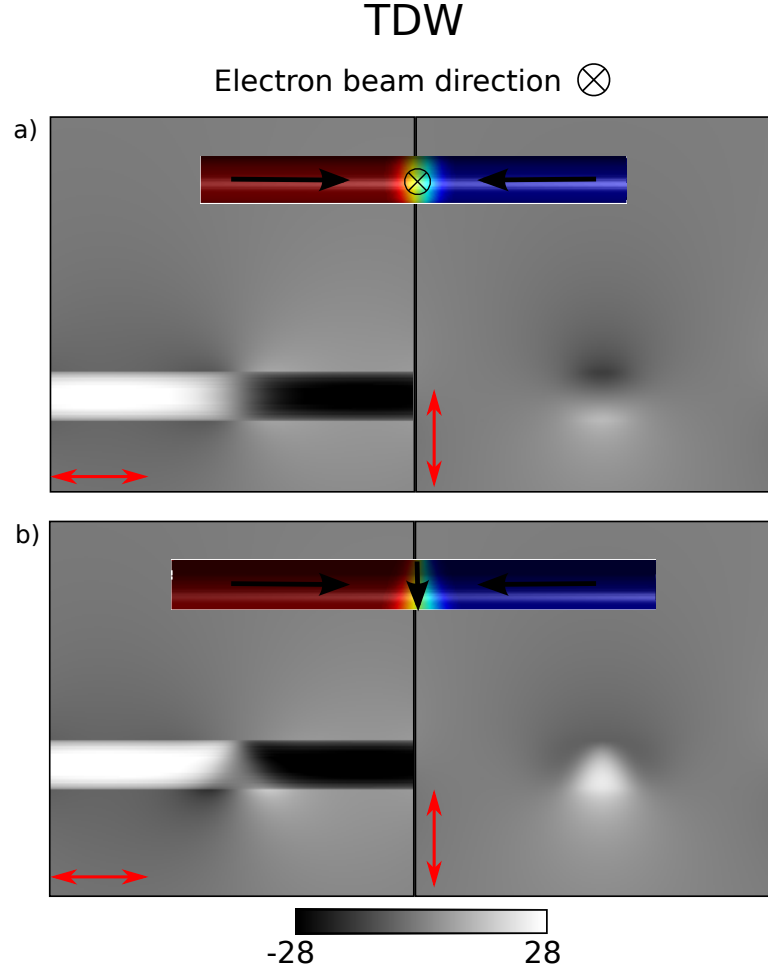


**Figure 3.13:** Calculated DPC images for the TDW. Images on the left show the axial component of integrated induction, images on the right show the component perpendicular to the axis, for a) the transverse component perpendicular and b) parallel to the beam direction, as indicated by double ended arrows. Units are in nTm and the wire diameter is 35 nm.

and ATDW, two orientations of the DW with respect to the electron beam direction are shown, as with Figs 3.11 and 3.12. The left-hand side of each image shows the axial component of the integrated magnetic induction, while the right-hand side shows the component perpendicular to the axis. A view of the axial component of the magnetisation is included to show the orientation of the wire.

Comparing Figs 3.13 and 3.14, the simulations suggest that the TDW can clearly be distinguished from the ATDW. For the case where the transverse component is parallel to the beam direction, the external field distribution of the TDW resembles that of the BPW in Fig 3.15 *i.e.* the axial component is symmetric on both sides of the wire and the field from the perpendicular component is equal and opposite in



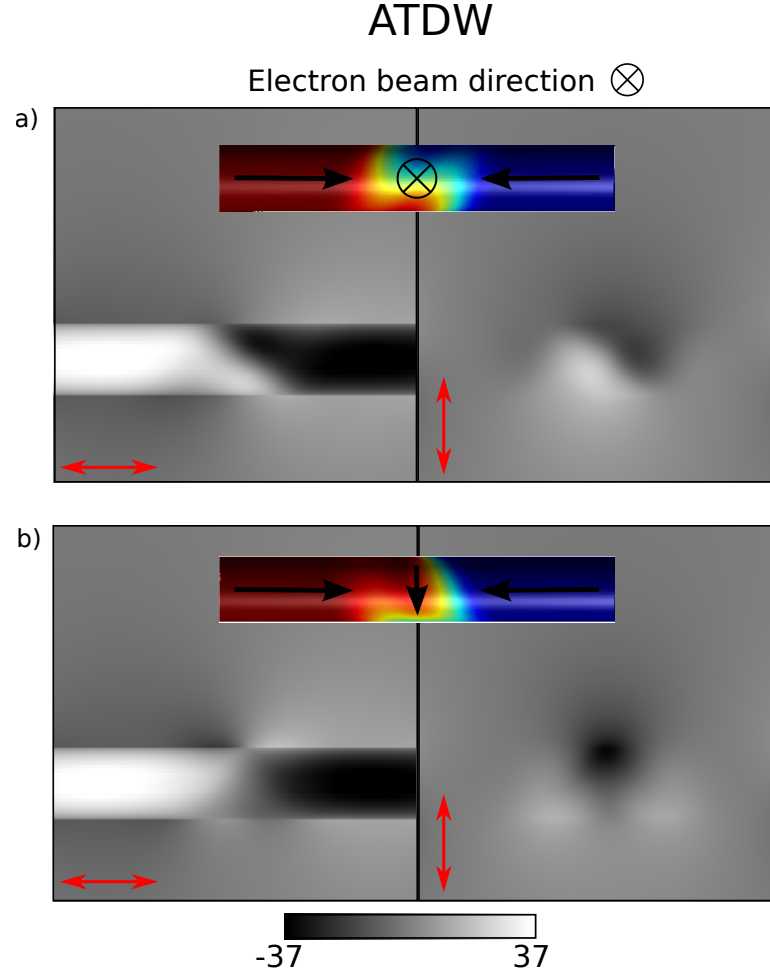


**Figure 3.14:** Calculated DPC images for the ATDW. Images on the left show the axial component of integrated induction, images on the right show the component perpendicular to the axis, for a) the transverse component perpendicular and b) parallel to the beam direction, as indicated by double ended arrows. Units are in nTm and the wire diameter is 50 nm.

magnitude, either side of the wire. In contrast, the external field from the ATDW in Fig 3.14a) is asymmetric in both images. For the opposite case, when the transverse component is perpendicular to the beam direction, in Fig 3.13b) and 3.14b), the external fields from the axial component alone differ. Again, the external fields are asymmetric for the ATDW, unlike the TDW, which is symmetric about the DW. It is simplest to distinguish the ground state BPW from the metastable ATDW by comparing Fig 3.14 and Fig 3.15. The external fields from the BPW are symmetric, compared to the ATDW where the external fields are asymmetric, no matter what the orientation of the wire. The TDW and BPW resemble each other only when the transverse component is parallel to the beam direction. However, by tilting

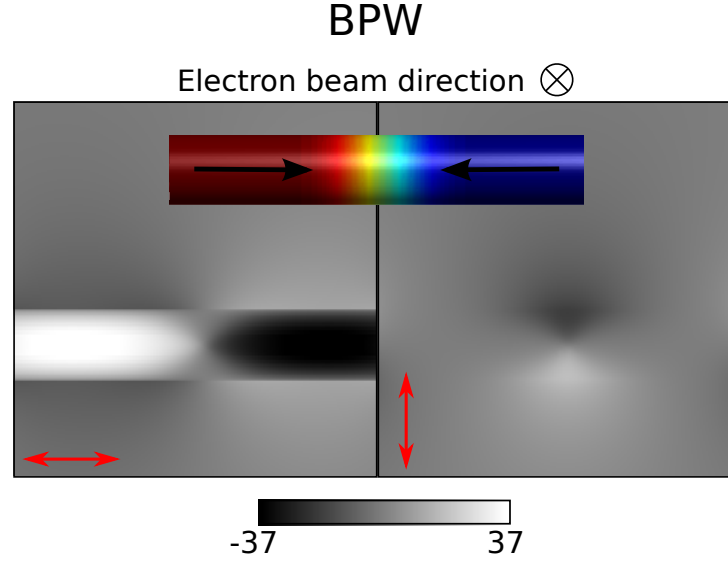


**Figure 3.15:** Calculated DPC images for the BPW. The image on the left shows the axial component of integrated induction, the image on the right shows the component perpendicular to the axis, as indicated by double ended arrows. Units are in nTm and the wire diameter is 50 nm.

the wire, the projected field distribution will be different for the TDW, while the BPW will always have a symmetric distribution. It should be noted that the field distribution will change depending on the wire length; however, independent of this, by analysing the symmetry of the external fields, the DWs may be distinguished.

The differences between each DW is enlarged in Fig 3.16, which shows a visualisation of the sine of the electron phase after traversing the wire. This shows the contours of the phase, which resembles magnetic flux in and around the nanowire and images obtained using electron holography [99]. The contrast between the ground state BPW and metastable ATDW is clear, reflected in the respective “flux” distributions either side of the wire. The density of flux lines either side of the wire is symmetric for the BPW in Fig 3.16c) and asymmetric for the ATDW in Fig 3.16b). As with the calculated DPC images, the “flux” distributions depend on the length of the wire but the changes in symmetry can be used to identify DW types.

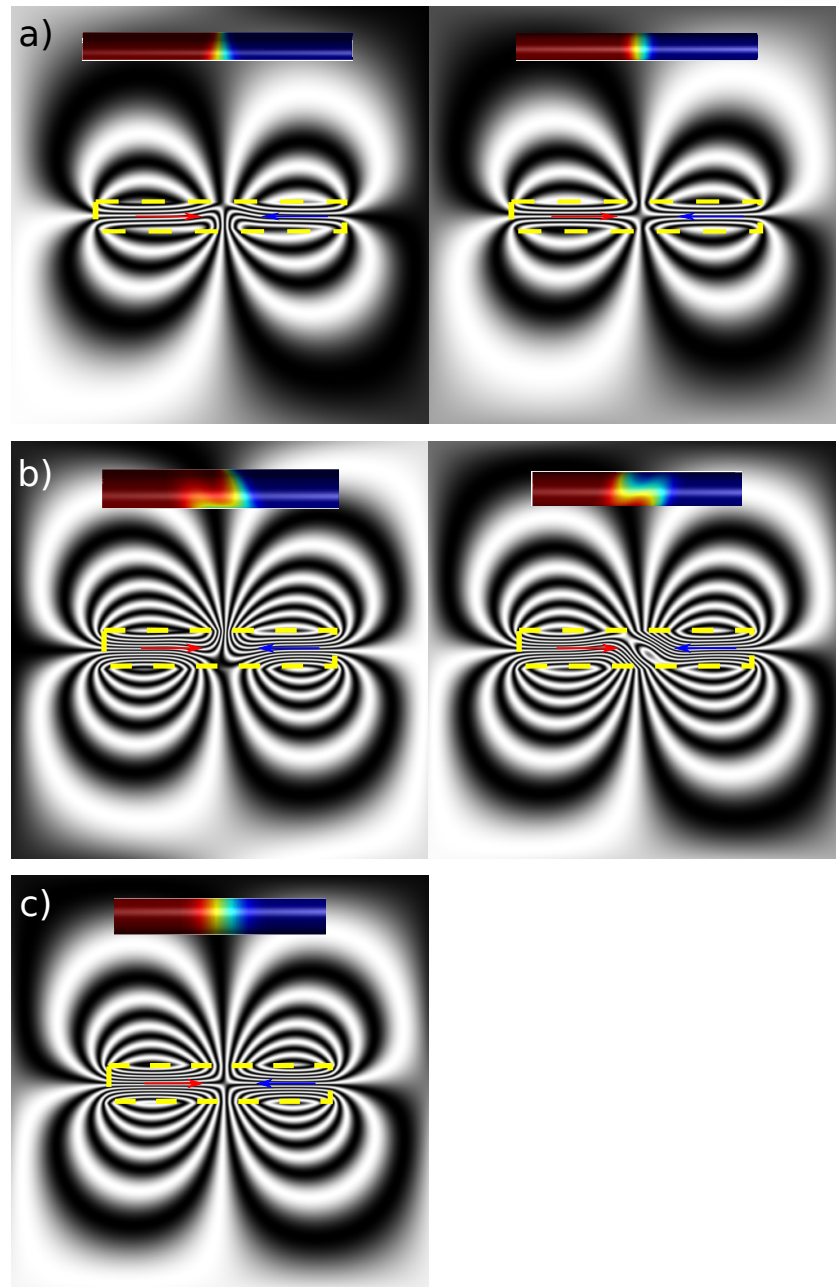


**Figure 3.16:** Sine of calculated electron phase for each DW (of diameter): a) TDW (35 nm), b) ATDW (50 nm) and c) BPW (50 nm). Different orientations are displayed for the TDW and ATDW.

### 3.3 Experimental

In order to characterise 3-D DWs, square cross-section nanowires (SNWs) were fabricated using electron beam lithography (EBL) and subsequently characterised using LTEM. Details on both of these techniques are given in Chapter 2. The justification for using square NWs, rather than cylindrical NWs, is that they support the same DWs as CNWs [100] and offer advantages in experimental characterisation. Additional OOMMF simulations were performed and indicate that the ATDW also stabilises in SNWs. A 3-D view of an ATDW in a SNW of cross-section  $80 \times 80 \text{ nm}^2$  is shown in Fig 3.17, this shows a DW that contains the same vortex spin structure as that in Fig 3.3b).

Experimentally, working with SNWs rather than cylindrical structures is simpler for a number of reasons. The first is that the uniform thickness across the wire eliminates non-uniform electrostatic phase contrast that would be present due to the non-uniform thickness of the CNW, although electrostatic edge contrast would still be present. The difference in electrostatic phase contrast associated with the non-uniform thickness of the wire is expected to be around an order of magnitude larger than the magnetic phase contrast. Given that the calculated images in the previous section do not include the contribution of electrostatic phase contrast, they can be used as a guide for the contrast expected for the SNWs. The second reason is that SNWs fabricated by EBL offer the advantage of more uniform nanowire structure compared to other fabrication methods, with lower edge roughness. In

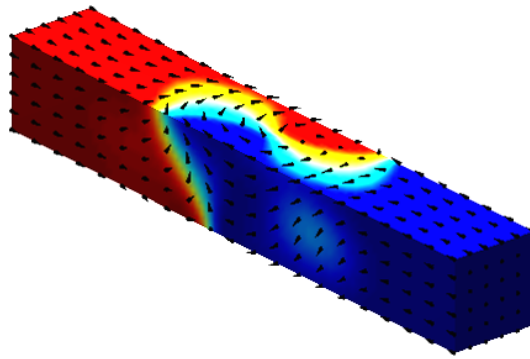


**Figure 3.17:** Result of an OOMMF simulation showing a 3-D view of an ATDW stabilised in a square cross-section nanowire ( $80 \times 80 \text{ nm}^2$ ).

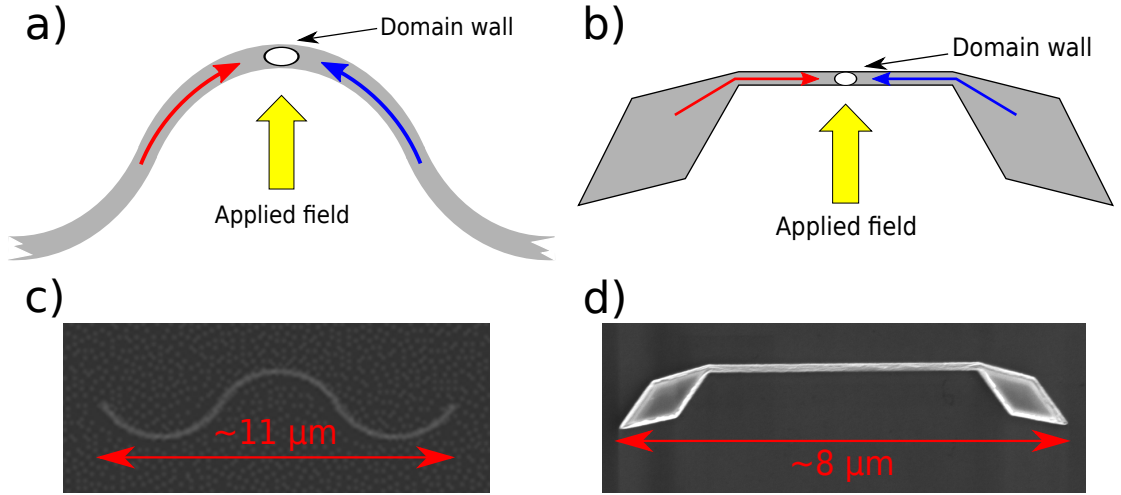


**Figure 3.18:** Schematic diagrams and SEM images, respectively, of curved nanowires, a) and c), and domain wall trap structures, b) and d). Ideally, an applied magnetic field perpendicular to the wire axis forces the magnetisation head-to-head, forming a domain wall.

addition, by fabricating SNWs on flat  $\text{Si}_3\text{N}_4$  membranes, SNWs are easier to image as all of the wire is at the same height, which is not necessarily the case with other fabrication methods. Another experimental advantage of SNWs is that, due to the square cross-section, the transverse components of the TDW or ATDW must lie along a defined axis, unlike the CNWs, where any azimuthal angle is possible; this restriction on the transverse component may make the DWs easier to identify. Challenges arise in fabrication, as detailed in Chapter 2, and in TEM imaging where the combined thickness of the sample and substrate is  $\sim 100 \text{ nm}$ .

Based on previous work, two different designs were chosen to facilitate the nucleation of DWs: curved nanowires and domain wall traps (DWTs) [101, 58]. These designs are sketched in Fig 3.18 alongside SEM images of fabricated structures. As Fig 3.18a) and b) shows, the structures are designed such that applying a magnetic field perpendicular to the wire axis forces the magnetisation to meet head-to head, causing DW formation. The structures characterised here are permalloy wires of thickness  $75 \text{ nm}$  and widths ranging from  $95\text{-}180 \text{ nm}$ . While these do not have perfectly square cross-sections, with aspect ratios (width/thickness) of  $\sim 1.3$  at best, simulations show that aspect ratios of  $1.5$  support ATDWs, which was demonstrated for a wire of width  $160 \text{ nm}$  and thickness  $80 \text{ nm}$ . While it is a misnomer in this case, SNWs will be used when referring to these low aspect ratio (height/width)

nanowires.

The remainder of this section is dedicated to experiments characterising 3-D DWs using a combination of Fresnel and DPC modes of LTEM. By imaging a range of nanowire dimensions, it is possible to identify the presence of metastable DWs.

### 3.3.1 Fresnel imaging

Initially, Fresnel imaging was used in the Tecnai T20 microscope to identify DWs in the SNWs. Optimal imaging conditions were obtained by using a condenser (C2) aperture of 50  $\mu\text{m}$  and an intermediate spot size, which increases beam coherence while maintaining good signal-to-noise ratio. To form DWs in the wires, a field of 350 Oe was applied perpendicular to the wire axis by tilting the sample, then reduced to zero.

DWs readily formed in curved nanowires after applying a field. Two different DW types were identified using Fresnel imaging, the first of which is shown in Fig 3.19. An in-focus image of a nanowire of width 95 nm is shown alongside Fresnel images. The position of the DW can be identified in Fig 3.19b) by observing the change in edge contrast; moving left to right, the bright edge contrast switches from the top edge to the bottom edge of the wire, as indicated by the arrows. In SNWs, the electrostatic phase contrast is uniform across the wire, which means

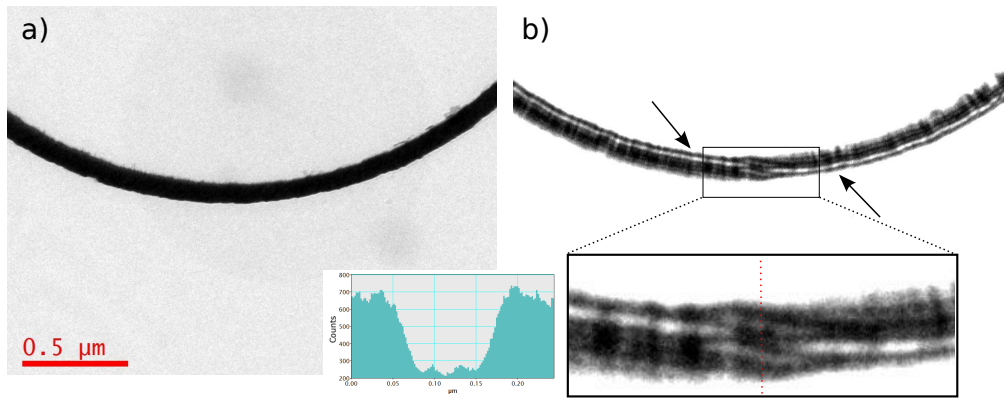


**Figure 3.19:** a) In-focus and b) defocused Fresnel images of a nanowire measuring 95 nm in width. Arrows indicate the change of bright edge contrast from one side of the wire to the other; this flip to opposite sides is indicative of a DW, as in b), which shows an enlarged view of a chain-link structure.

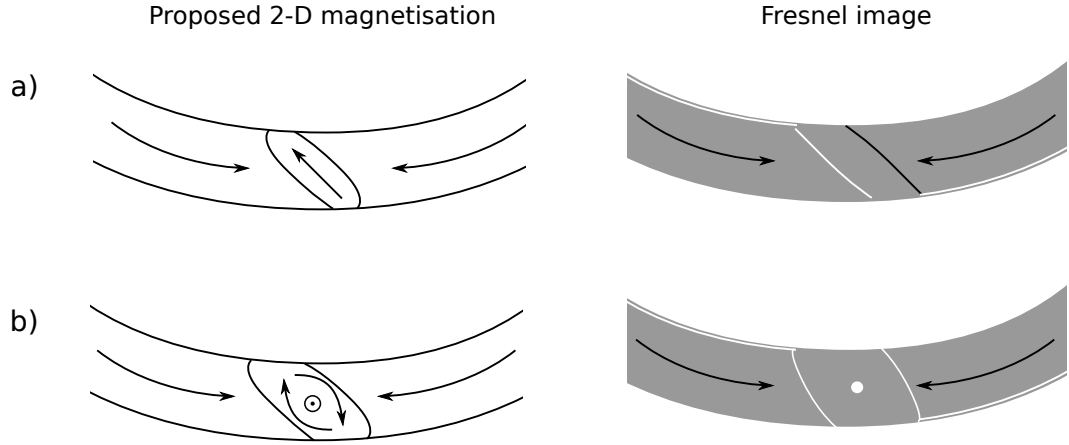


**Figure 3.20:** (left) Proposed magnetisation and (right) resulting Fresnel image for two different 2-D DWs. In both cases, the Fresnel contrast does not match that of the chain-link DW.

that the structure in the centre of the wire is observable. The enlarged view of this Fresnel image, from the centre of the wire, shows that the DW produces contrast resembling a link in a chain. The same “chain-link” DW is also found in wires of width 115 nm. An estimate of the DW width can be obtained using the point at which the edge contrast switches sides, which gives a width of  $\sim 200$  nm. This is approximately equal for both DWs found in 95 and 115 nm wide wires. The DW width estimate correlates with simulations of 3-D DWs in previous sections, in that the DW width seems to be approximately twice the width of the wire, which is unlike the case of 2-D, planar nanowires.

The Fresnel contrast associated with the chain-link DW in Fig 3.19 is not seen in any of the calculated Fresnel images of Fig 3.12. The calculated image at the bottom of Fig 3.12a), most resembles the experimental image; however, the chain-link DW has two lines of bright (or equivalently dark) contrast running diagonally across the wire. It is likely from the experimental Fresnel image in Fig 3.19 that this DW has a 3-D structure. This is illustrated schematically by Fig 3.20, which shows the expected Fresnel contrast for two proposed 2-D structures, both of which would fail to give the chain-link contrast. Fig 3.20a) shows the first case, where a simple head-to-head DW that consists of a section of magnetisation that lies  $45^\circ$  to the wire axis. The resulting Fresnel image for this structure would not produce the chain-link contrast as both sides of the “link” are not the same *i.e.* both bright or both dark. The second structure, in Fig 3.20b), shows a DW that resembles a

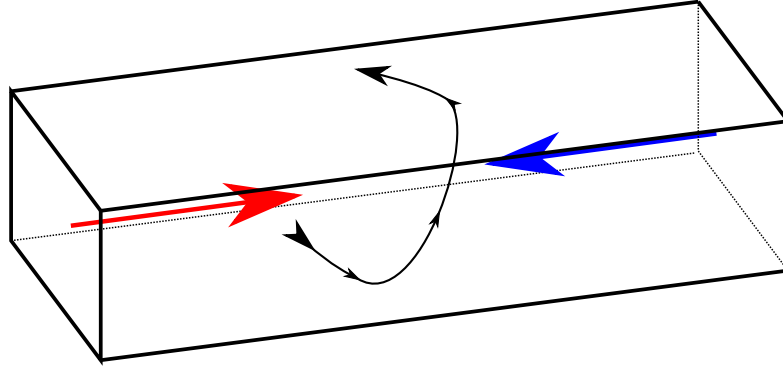


**Figure 3.21:** Proposed 3-D structure for the chain-link DW. Red and blue arrows represent axial magnetisation of opposite sign and a black line traces the magnetisation in the domain wall.

vortex DW. The Fresnel image in this case would not match the chain-link contrast because of the bright (or dark) contrast that would arise in the centre from the rotational magnetisation. In addition, this rotation would have to happen in  $\sim 50$  nm (from Fig 3.19b)), which is unlikely given that this would result in a large amount of exchange energy. Ultimately, the Fresnel contrast in Fig 3.19b) must be attributed to a more complicated, 3-D structure than the simple structures proposed in Fig 3.20. Noting that the contrast in the centre of the wire is weaker than at the edges of the wire, it is likely that the structure of the chain-link DW has a large component of magnetisation parallel to the direction of the electron beam. Such a proposed structure is illustrated schematically in Fig 3.21, axial magnetisation is separated by a DW in which the direction of magnetisation varies between top and bottom surfaces. While this structure could feasibly match the structure of the chain-link DW, DPC imaging is required to confirm this.

Fig 3.22 shows an example of another DW type revealed by this experiment, for a 180 nm wide wire. Using the same methods of estimating the DW width as the chain-link DW, this DW is found to be more extended, measuring approximately 300 nm. The edge contrast follows a single diagonal path as it switches to the opposite side of the wire, seemingly having a simpler structure than the chain-link DW. Along this diagonal line is a spot of slightly brighter contrast, which is highlighted in the enlarged image in Fig 3.22b) by a red circle. This diagonal DW somewhat resembles the calculated Fresnel image the bottom of Fig 3.12a) *i.e.* contrast produced by the ATDW; however, it will be shown with DPC imaging in the next section that the



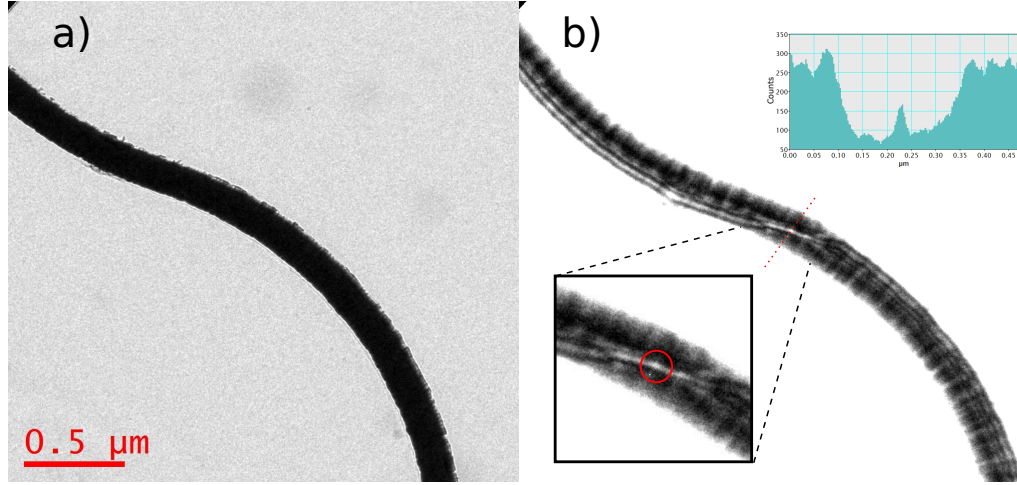


**Figure 3.22:** In-focus a) and defocused b) images of a nanowire of width 180 nm. The edge contrast travels diagonally across the wire with a dot that is slightly off-centre, as circled in the inset of b).

structure is not the same as the ATDW. The DPC imaging in the next section allows a discussion of its possible micromagnetic structure. At this point, the data seems to suggest a size dependence; the chain-link DW is seen in wires of width 95-150 nm while the diagonal DW was found for the widest wires, 180 nm. However, DPC results are presented in the following section that show that the diagonal DW seems to be found in all but the thinnest (95 nm) wires, which immediately indicates the presence of metastable DWs in these SNWs.

### 3.3.2 DPC imaging

DPC imaging was performed on the JEOL ARM and revealed two DW types present in the SNWs; the first that will be described was not imaged in the previous subsection, the other can be identified as the diagonal DW imaged with Fresnel mode in Fig 3.22. A preliminary search for DWs in Fresnel mode after applying a field perpendicular to the wires did not identify the chain-link DW, it was therefore not imaged in DPC mode. The first DW, not imaged in Fresnel mode, is shown in Fig 3.23, which contains a series of images acquired in DPC mode of a DW in a nanowire 95 nm wide. These images are: a) the “sum” image, essentially a bright field image; b) the colour image, showing different directions of magnetic induction; c) and d) difference images, which are sensitive to changes of magnetic induction

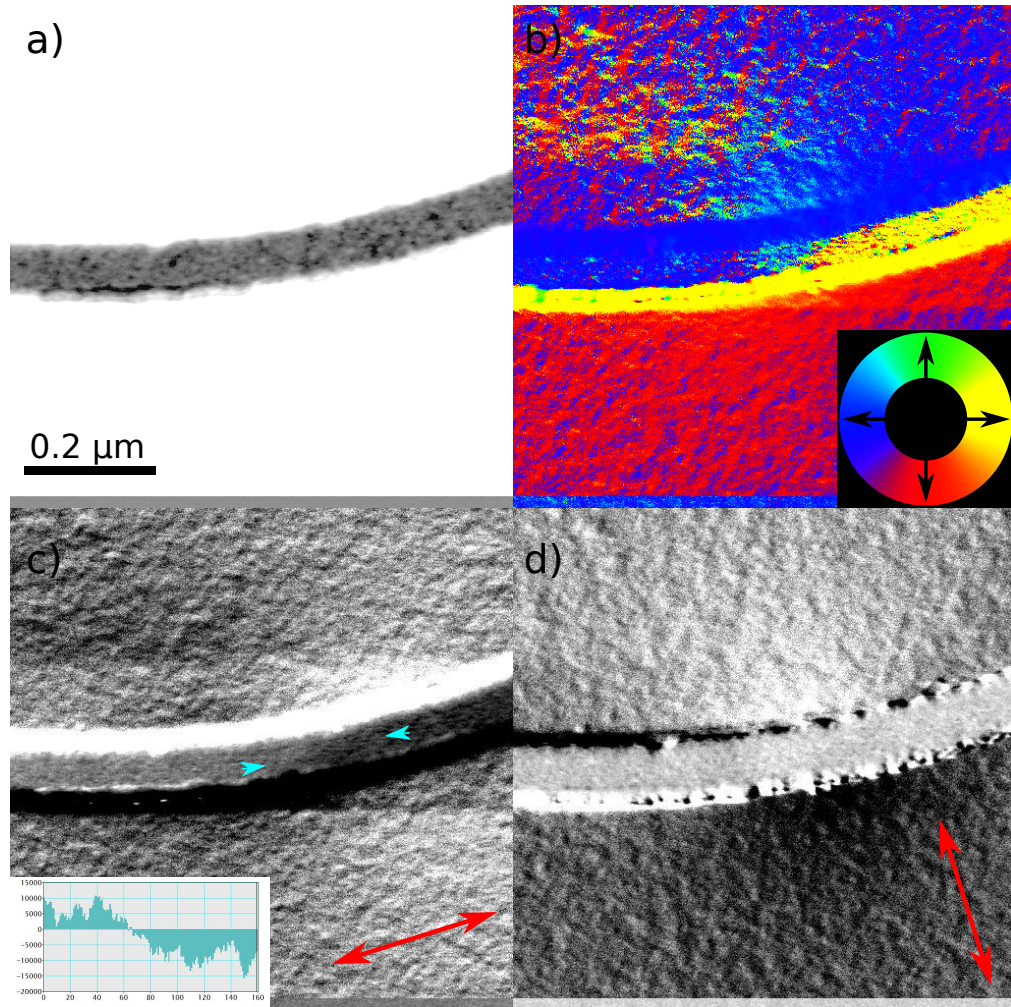


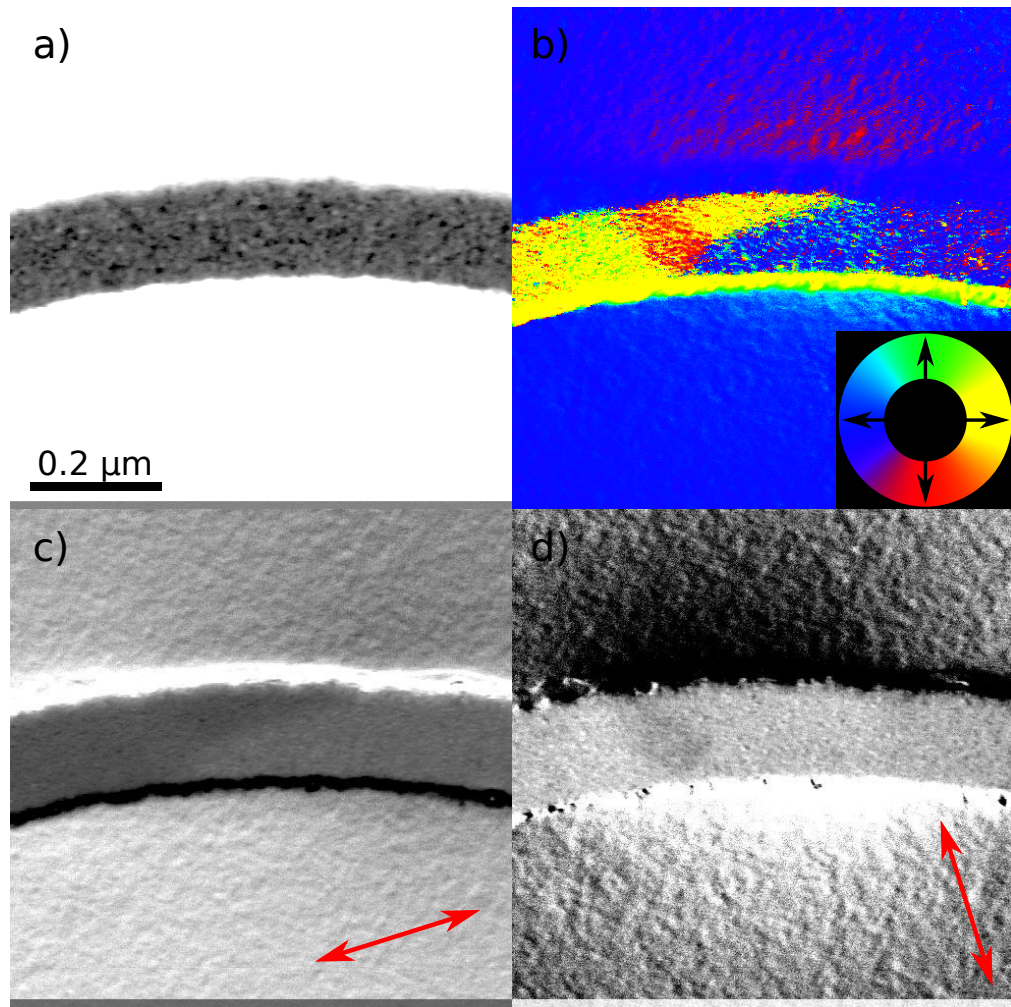
**Figure 3.23:** DPC images of 95 nm wide wire showing a either a BPW or TDW (with transverse component parallel to the beam direction). The change in colours in b) from magenta to yellow shows a change in the axial magnetisation, which is reflected in the difference image in c) and the inset profile.

for two orthogonal directions, indicated by the double-ended arrows. It should be noted that the contrast in DPC images here appear to have unusual contrast outside the wire, which may be due to charging and therefore the structure inside the wire will be focused on. In addition, it is useful to calculate a “magnitude” image from the two difference images by taking the square root of the sum of their squares, this can be used to indicate out-of-plane induction; however, these images are very noisy, possibly due to the large thickness of the wires and are therefore not used. The colour change in b) from blue/magenta to yellow indicates a  $180^\circ$  change in the direction of magnetisation. This  $180^\circ$  rotation is also shown by the contrast within

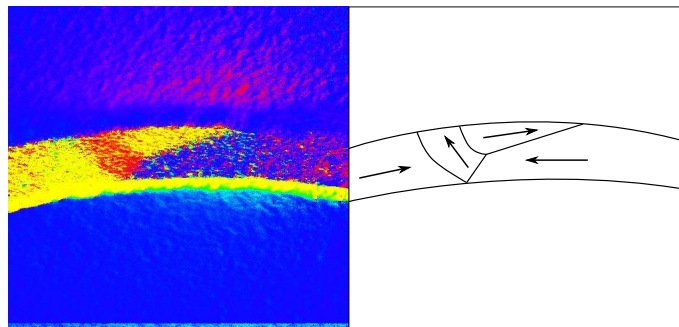
the wire in Fig 3.23c), which changes from bright to dark, indicating a change in the direction of magnetisation, a DW. A line profile is inset in Fig 3.23b) taken between the two arrow heads on the wire. The contrast shows that the change of magnetisation along the axis is quite abrupt, which is consistent with the contrast change expected for a BPW or a TDW, comparing to calculated images in Figs 3.13a) and 3.15. This is supported by looking at the external fields in Fig 3.23d). The field distribution here is equal and opposite and symmetric about an axis perpendicular to the wire axis. Comparing calculated images with the DPC image in Fig 3.23d), the DW is more likely to be a TDW as the contrast is weaker and less extended in Fig 3.13a) than that in Fig 3.15. This is somewhat surprising, as it would be expected that the transverse component of the TDW would be perpendicular to the plane of the image, which is an energetically unfavourable situation given that the wire is wider than it is thick. However, to confirm this, an image taken at a high tilt angle ( $\sim 30^\circ$ ) would have to be taken to get a different view. From now on, this DW will be referred to as BPW/TDW.

Fig 3.24 shows the second DW type imaged by DPC. The colour image in Fig 3.24b) shows that, unlike the BPW/TDW, this DW appears more extended with clear internal structure; from this image alone the DW resembles a vortex spin state, without the rotational symmetry. The difference images confirm this; while Fig 3.24c) shows a symmetry in the axial component, Fig 3.24d) is asymmetric, with dark contrast corresponding to a component transverse to the wire axis, identifiable as the red section in the colour image. This “vortex” has a core that is displaced relative to the centre of the wall and will be referred to as a displaced vortex domain wall (DVDW). It appears that the DVDW is a vortex state with net transverse moment. None of the calculated DPC images in Fig 3.13 - 3.15 exactly match the contrast of the DVDW. The set of images that have the closest resemblance is in Fig 3.14b); the axial component Fig 3.24c) is similar to that of Fig 3.14b) but the perpendicular component is not. The component perpendicular to the axis is less symmetric in the experimental image than the simulated image; there are two equal and opposite regions of perpendicular induction in the simulated image whereas there is only one region in the experimental image.





**Figure 3.24:** DPC images of a displaced vortex DW (DVDW) in a wire of width 160 nm. The colour image shows the circulation of the magnetisation, the difference image in d) shows asymmetry in the component perpendicular to the wire.



**Figure 3.25:** Outline of the structure of the DVDW alongside the colour image from Fig 3.24b).

In order to correlate the contrast in Fig 3.24 with a micromagnetic structure, OOMMF simulations were performed that used a 2-D starting state similar to the outline shown in Fig 3.25. The result of the DVDW simulation is shown in Fig 3.26, which shows a 3-D view of a DW with a spin structure on its top surface similar to that of the DVDW. However, as indicated by the two slice of top and bottom layers the structure varies through the thickness *i.e.* the DW is 3-D in character. This DW had not been identified in simulations prior to experiments, possibly due to the fact that none of the starting states were completely asymmetric as the outline in Fig 3.25. Calculated DPC images are shown at the bottom of Fig 3.26 for this DW structure for the situation where the beam direction is perpendicular to the plane of these spin structures; the left image shows the axial component and the right shows the perpendicular component. The axial component is very similar to the axial component measured by DPC in Fig 3.24c); however, the component perpendicular to the axis does not resemble the experimental equivalent in Fig 3.24d). The experimental image shows only one region that points transverse to the wire axis, whereas the calculated DPC images contain two regions that point in opposite directions, as indicated by the bright and dark regions. Therefore, this is similar, though not identical, to the experimentally imaged DVDW.

A Fresnel image, shown in Fig 3.27, was also calculated. Interestingly, the bright contrast that runs diagonally across the wire resembles the contrast seen for the DW imaged in the previous subsection, shown in Fig 3.22b); a bright core is circled, indicating the similarity with the Fresnel imaging. Therefore, the simulation result in Fig 3.26 is a very similar DW as that imaged in Fig 3.24; the two have a similar character, though it is likely that the experimentally imaged DVDW has a more 2-D structure.

Including Fresnel imaging, a total of three DWs have been identified: the BPW/TDW, the chain-link DW (observed by Fresnel imaging only) and the DVDW. The fact that these DWs are found at the same dimensions indicates the presence of metastable states. The range of widths at which each DW was observed is shown in Fig 3.28, the width is indicated along a horizontal scale and coloured bars indicate the width range. The imaging method by which the DW was identified is also indicated. The

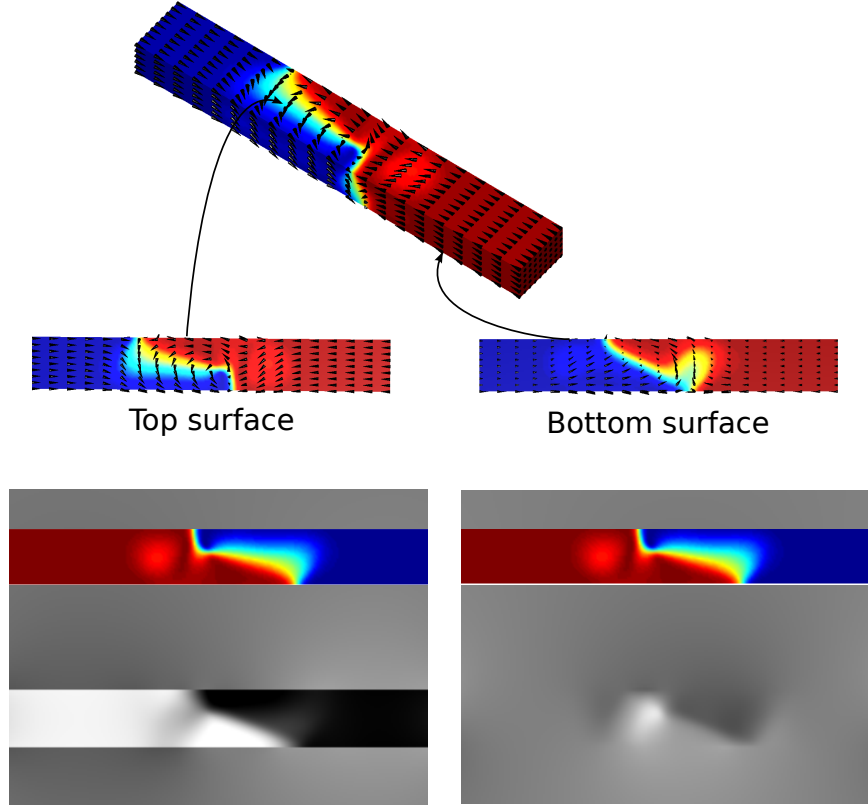


**Figure 3.26:** 3-D view of the result of a simulation whose starting state was based on the outline in Fig 3.25. The top and bottom surfaces are shown to indicate that the structure is 3-D, varying through the thickness. Calculated DPC images are shown at the bottom for (left) the axial component and (right) the transverse component of integrated induction.

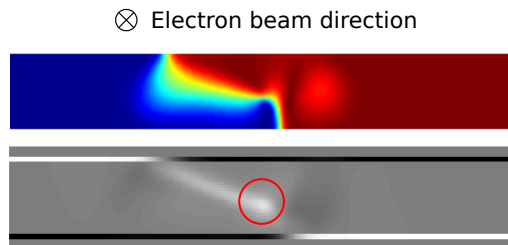


**Figure 3.27:** Calculated Fresnel image of the simulated DVDW. The bright contrast travelling diagonally across the wire is consistent to the experimental Fresnel images.

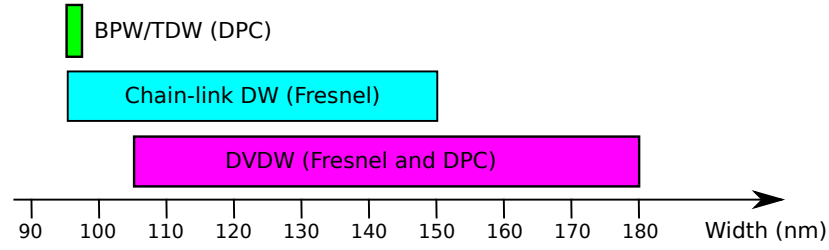


**Figure 3.28:** Chart showing the range of widths for which each DW was experimentally observed (wire thickness is 75 nm). The regions where the bars overlaps indicate metastability.

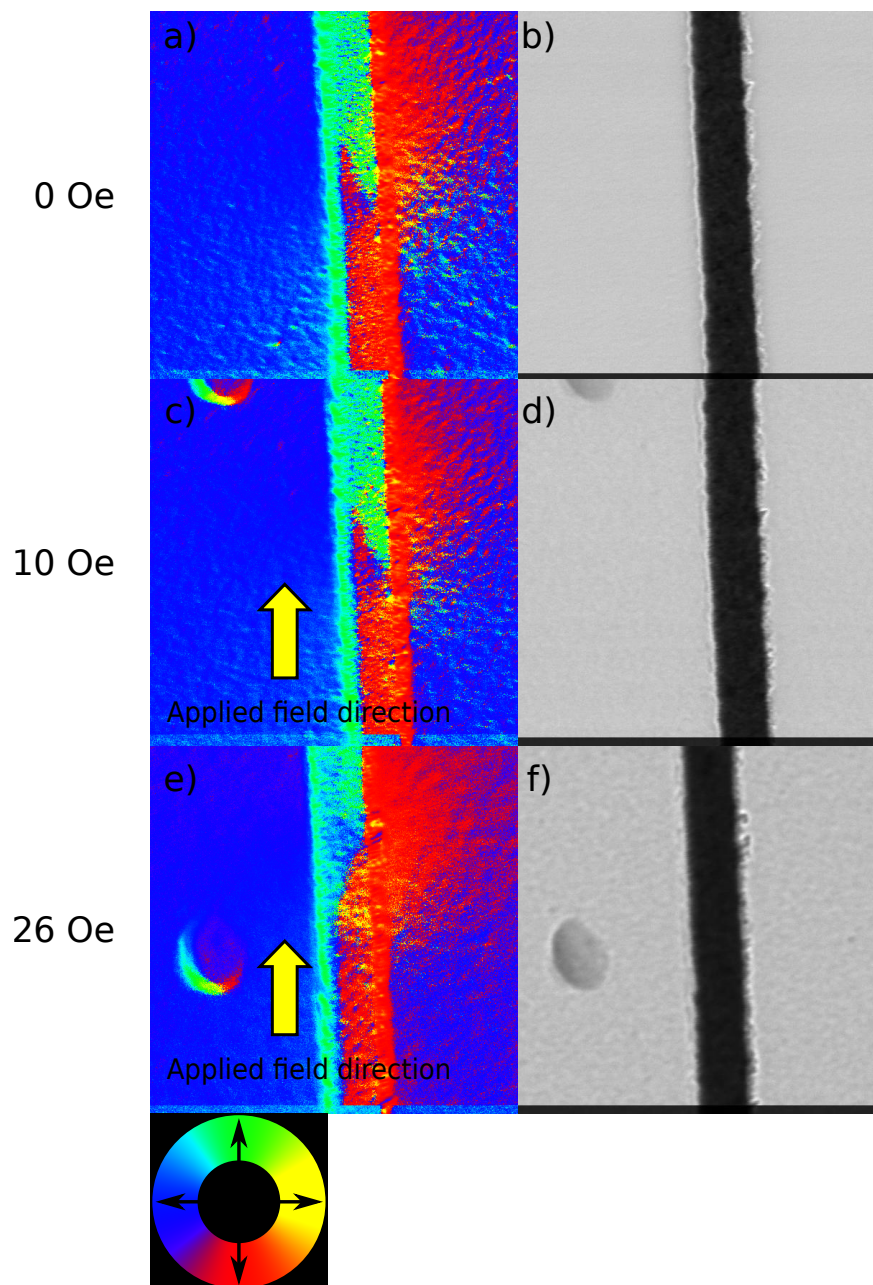
DVDW covers the largest range, from 105 to 180 nm; next is the chain-link wall, stable from 95 to 150 nm; and the BPW/TDW was observed in the thinnest wires only, of width 95 nm. The range of widths where the bars overlap indicates where there are metastable DWs *i.e.* the chain-link DW and the BPW/TDW at 95 nm and the chain-link and DVDW from 105 to 115 nm. It should be noted that this represents the range for which the DWs were experimentally observed and does not rule their stability at other dimensions. In addition, while the BPW/TDW are known to be 3-D DWs, the other two DWs are not necessarily so. The chain-link DW is very likely to be 3-D, whereas the DVDW is more likely to be 2-D. Referring to Fig 3.28, this suggests that lower aspect-ratio wires are more likely to support 3-D DWs.

It should be noted that none of the simulations performed included a magnetic field applied perpendicular to the wire axis to mimic the effect of the objective lens in this experiment. This factor could explain the discrepancy between experiment and simulation; the effect of a vertical field will be much larger compared to 2-D nanowires, given the 3-D nature of these DWs.

### 3.3.2.1 Tilt series

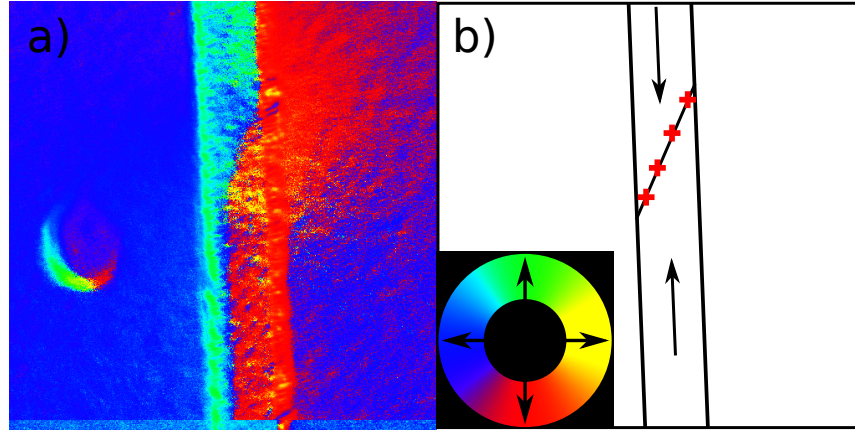
The behaviour of the new DVDW under an applied field was characterised by applying a field along the axis of a DWT. A DW was nucleated by applying a field perpendicular to the wire axis; the sample was then rotated 90° so that the field was aligned along the wire axis. The DWTs were all approximately 115 nm wide, meaning that a chain-link or DVDW was possible.

Fig 3.29 shows a series of images taken at increasing tilt angle and, thus, increasing applied field. The images on the left-hand side show the colour maps, on the



**Figure 3.29:** Three sets of images showing a nanowire containing a DW at increasing applied field. Applied field strength is (top) 0 Oe, (middle) 10 Oe and (bottom) 26 Oe. A field of 320 Oe was required to uniformly magnetise the wire (image not shown). a), c) and e) are colour maps showing direction of induction; b), d) and f) are the respective sum images. The wire is 115 nm wide.





**Figure 3.30:** Schematic of the charge configuration associated with the pinned DW. The final colour image from Fig 3.29e) is shown in a), while b) shows an outline of the wire with arrows to indicate magnetisation direction and plus and minus symbols to represent magnetic charge.

right-hand side corresponding sum images are shown. Fig 3.29a) shows the DVDW which, initially, has no applied field. An in-plane field of  $\sim 10$  Oe, whose direction is indicated by the yellow arrow, was applied and depinned the DW which propagated along the wire until it was pinned again, as shown in Fig 3.29c). The field is then increased to a value of 26 Oe, which is enough to depin the DW which then jumps to a new pinning site Fig 3.29e), with a different structure; the displaced vortex now no longer exists, with the core expelled from the wire. Using the piece of material beside the wire as a fiducial marker, the distance moved from c) to e) is  $\sim 0.6 \mu\text{m}$ . The structure of the DW in Fig 3.29e) is in a more concentrated charge configuration than the DVDW, with the magnetisation changing direction quite abruptly, as indicated by Fig 3.30, which shows the colour image from Fig 3.29e) and a schematic of the pinned wall structure with charges indicated where the magnetisation meets. Despite this high charge configuration, the DW remains pinned at this location until the field is increased to 320 Oe. This field is quite large compared to depinning fields measured in typical 2-D DWs. For example, the depinning field for a vortex DW in planar nanowires [55] with patterned notches *half* the wire width was approximately half of the depinning field here. Considering that, at most, the edge roughness here is  $\sim 20\%$ , the DW is easily and strongly pinned in comparison. At an applied field of 320 Oe, the rest of the wire section of the DWT reverses, causing it to be uniformly magnetised. In terms of applications, this means that

the edge roughness would have to be carefully controlled to avoid unwanted pinning.

### 3.4 Conclusions

3-D DWs were characterised using micromagnetic simulations and experimentally using Lorentz microscopy. Micromagnetic simulations were used to construct a phase diagram showing the stability/metastability of 3-D DWs in CNWs and CNTs. The TDW and BPW are ground states for thinner and thicker wires, respectively, with a critical radius of 20 nm for permalloy. The ATDW can now be identified as a metastable state in CNWs which is stable at and above the critical radius. The plot on the phase diagram suggests that the ATDW is simply a continuation of the TDW for larger radii. By unrolling the surface magnetisation of the ATDW and TDW, the ATDW is shown to consist of a chiral, asymmetric vortex/anti-vortex pair while the TDW comprises two symmetric states, an anti-vortex and a divergent meron-like state. This confirms that the ATDW is simply an asymmetric version of the TDW at radii of 20 nm and above. The transition from ATDW to TDW is shown to come with a reduction in surface charge. For CNTs, the additional surface charge, compared to CNWs, arising from the inner surface means that the ATDW is not stable for CNTs, except as an intermediate state.

Lorentz TEM was used to identify 3-D DWs in EBL fabricated SNWs. From simulations, the BPW and ATDW would be expected to stabilise at the dimensions studied. In contrast to simulations, three DWs were identified, two of which did not appear in simulation results. The new DWs were termed a chain-link and a displaced vortex DW, due to their respective appearance in Fresnel and DPC images. The chain-link DW is likely to have a 3-D structure, whereas the DVDW is thought to be 2-D. The fact that different DWs were observed at the same dimensions shows the presence of metastability in these DWs. The DVDW is shown to be strongly pinned by nanowire roughness, a factor that would need to be closely controlled if this system were to be used in device applications.

# 4

## Interface induced Dzyaloshinskii-Moriya interaction in Py/Pt bilayers

### 4.1 Introduction

The Dzyaloshinskii-Moriya interaction (DMI) is an anti-symmetric exchange interaction that was originally identified as being responsible for weak ferromagnetism in anti-ferromagnets with low crystal symmetry [14, 15]. This weak ferromagnetism arose due to canting of spins, which allowed the DMI energy to be lowered; the Hamiltonian for DMI for neighbouring spins  $\mathbf{S}_i$  and  $\mathbf{S}_j$ , was expressed phenomenologically by Dzyaloshinskii as,

$$H_{DMI} = -\mathbf{D}_{ij} \cdot (\mathbf{S}_i \times \mathbf{S}_j) \quad (4.1)$$

where the direction of  $\mathbf{D}_{ij}$  depends on the local symmetry of the crystal. More recently, it has been found to stabilise non-collinear magnetic ordering in non-

centrosymmetric crystals, which results in exotic spin textures such as skyrmions [110]. In addition to the DMI in bulk crystals, it has been predicted to be induced at the surface of thin films in the presence of strong spin-orbit coupling (SOC) [17, 19]. Therefore, the possibility exists for magnetic thin films that share an interface with a metal with strong SOC to have induced anti-symmetric exchange interaction. Early evidence of this interface-induced DMI (IDMI) was obtained from the observation of non-collinear magnetic ordering and chiral symmetry breaking in the spin structure of ultrathin films and multilayers [21, 111, 112, 113]. Mn atoms on a W(110) substrate is a system where IDMI leads to a realignment of otherwise anti-ferromagnetically ordered Mn moments to have a cycloidal spin spiral order [21, 111]; in this case, the period of the spin spiral is set by a competition between IDMI and Heisenberg exchange. In another study, a ferromagnetically ordered material such as Fe, Néel domain walls (DWs) offer a way to lower the DMI energy, and are thus favoured over Bloch walls, despite costing more in magnetostatic energy [113]. IDMI was also shown to break the symmetry in a helical ordering of Dy/Y, stabilised by the Ruderman-Kittel-Kasuya-Yosida exchange, so that left-handed configurations (defined as a combination of helix and applied field) are energetically preferable.

The influence of the IDMI has been predicted and observed to affect the static and dynamic behaviour of micromagnetic objects such as DWs in thin films and planar nanowires. This is attractive from the perspective of spintronic devices as it offers more control over DW properties; however, measurement of the strength of IDMI,  $D$ , can be difficult and/or limited to a particular materials system. For materials with perpendicular magnetic anisotropy (PMA) that causes the magnetic easy-axis to be out-of-plane, models show that the IDMI causes the preferred static DW type in planar nanowires to be homochiral Néel DWs rather than Bloch DWs [22]. A consequence of this is that the value of the Walker field increases with increasing  $D$ . The reason for this is that the IDMI prefers the magnetisation to be aligned in the Néel wall orientation, thus suppressing the spins' precession. However, measuring the strength of  $D$  using this method is difficult as Walker breakdown may not be reached. The observation of asymmetric Néel DW expansion in Pt/Co/Pt PMA thin films [23, 24] using magneto-optical Kerr effect (MOKE) microscopy

revealed the influence of IDMI and provides a method for the measurement of  $D$ . In this case, an in-plane field,  $H_x$ , is applied in addition to the out-of-plane field,  $H_z$ , which breaks the symmetry of the system. The energy density of the DW is modified depending on the magnitude of  $H_x$ . Crucially, MOKE enables the DW velocity to be measured, from which  $D$  may be determined by fitting to the experimentally measured velocity as a function of  $H_x$ . Another route through which the strength of  $D$  could be measured in the same material system is to observe the annihilation of  $360^\circ$  DWs in perpendicularly magnetised Co films [114, 115]; the IDMI stabilises antiparallel Néel walls that form a  $360^\circ$  wall when in close proximity to each other, the annihilation field increases with increasing  $D$ . In this case, the annihilation field depends on  $D$  and can be directly imaged using Lorentz TEM. In addition, the strength of the IDMI depends on the strength of the SOC. Therefore, by changing the non-magnetic layer in the Pt/Co/Pt system,  $D$  can be tuned. The strength was shown to depend on the thickness of Pt layers [23], while the insertion of another strong SOC metal, Ir, was shown to reverse the sign of the effective IDMI [24].

Studies of the effect of the DMI on soft magnetic thin films, in which the magnetisation prefers to lie in-plane, have been limited to models where the formulation associated with DMI in bulk crystals has been used [116, 117]. In contrast, the work presented in this chapter investigates the effect of the interface-induced DMI on such films. It also differs from other studies in that the magnetic films investigated here are not ultrathin; the thickness here is of the order of the exchange length of the material investigated, which for permalloy (Py) is  $l_{ex} = 5.3$  nm. Therefore, the magnetisation is not expected to vary through the thickness. As outlined in Chapter 1, the IDMI is expected to be able to lower the energy when spins are canted with respect to each other. Given that the direction of  $D$  is restricted to the plane of the interface [22], the only way in which the IDMI energy may be lowered is through tilting of the spins out-of-plane. Since soft magnetic materials prefer to have in-plane magnetisation, unlike PMA (Pt/Co/Pt) systems, the effect of the IDMI may be expected to be relatively weak, as there is competition between exchange energy and strong shape anisotropy of the thin film. Micromagnetic simulations are used to investigate the effect of the IDMI in soft magnetic discs, a situation where vortices

are expected to form and have an out-of-plane core, where the effect of the IDMI is expected to be most evident. In order to test the predictions of the simulations, pulsed laser deposition (PLD) is used to deposit two different Py/X bilayers, where X is a non-magnetic metal. Pt is chosen as the material with strong SOC and Cu is deposited for the control sample. Focused ion beam is used to define discs in the continuous film and Lorentz TEM (LTEM) is used to characterise their magnetic behaviour. Ultimately, the aim of the investigation is to provide a method to directly measure the strength of  $D$  in soft magnetic films.

## 4.2 Simulations

### 4.2.1 Methods

Simulations were performed using mumax<sup>3</sup> [34], a micromagnetic simulation package which uses graphical processing units to accelerate calculations, as described in Chapter 1. The simulated geometry was a disc of diameter 2048 nm and thickness 8 nm, a vortex ground state in Py. Discs of this diameter are also trivial to fabricate by FIB. The material parameters used for simulations were: saturation magnetisation,  $M_s = 860 \text{ kAm}^{-1}$ ; exchange constant,  $A = 1.3 \times 10^{-11} \text{ Jm}^{-1}$ ; magnetocrystalline anisotropy constants,  $K_1 = K_2 = 0$ ; damping parameter,  $\alpha = 0.02$ . A cell size of  $1 \times 1 \times 8 \text{ nm}^3$  was used, which gives higher resolution than simulations used elsewhere in this thesis.

Two sets of simulations were performed: one where the simulations were simply allowed to relax in zero field and another where a magnetic field was applied. These two sets were performed to assess, respectively, whether the IDMI affected the structure of the vortex and whether this caused the vortex to behave differently under applied field; the focus was to assess the possibility that any effects could be used to detect the influence of the IDMI and measure its strength. For the first set, a vortex state was used as the starting state, the IDMI was “switched on” and the simulation was allowed to relax. This was performed for a number of simulations with increasing effective IDMI strength,  $D$ , from 0 to  $2.5 \text{ mJm}^{-2}$ . The results of the initial simulations were used as the starting state for the second set where, for each

relaxed state, a uniform applied field was increased in strength, in increments of 0.2 mT, until the disc was uniformly magnetised. Therefore, the relaxed magnetic state of the disc and the strength of applied field required to expel the vortex core was determined for a range of  $D$  values.

While problems can arise from modelling of vortices and their reversal, this is not expected to be an issue here. For example, reversal of the vortex *core* using field or current involves the annihilation of a vortex and anti-vortex [118, 119] and nucleation of a Bloch point [120] singularity, an object which is known to violate the underlying assumption of micromagnetics that the direction of spins varies slowly compared to the lattice parameter of the material. A consequence of Bloch point nucleation is that the energy barrier for vortex core reversal is always underestimated by micromagnetic simulations [121]; in fact, a multiscale simulations (micromagnetics/atomistic simulations) are required to accurately simulate Bloch point dynamics [122]. While expulsion of the vortex core by applying an in-plane field involves a discontinuous change in magnetisation, the process does not involve the nucleation of a Bloch point. Indeed, a direct comparison of simulation and experiment yields similar values for vortex expulsion fields [123]. In addition, the reduction of the cell size well below the exchange length is not considered problematic [121].

As with all other simulations in this thesis, the effect of an applied magnetic field perpendicular to the sample, to replicate the effect of the objective lens in LTEM, is not included. It is not expected that this will significantly effect results given that the magnetisation is mostly in-plane.

### 4.2.2 Results

The effect of the IDMI on the ground states of the discs is illustrated in Fig 4.1 where three visualisations of the final, relaxed states of the initial simulations are shown for increasing values of  $D$ : Fig 4.1 a), b) and c) correspond to  $D = 0, 1$  and  $2.5 \text{ mJm}^{-2}$ , respectively, as labelled to the left of the figure. The upper value of  $D$  is chosen based on the largest measured values in the literature [124]. From left to right, Fig 4.1 shows: a colour map with arrows overlaid to indicate the direction of in-plane magnetisation; the magnitude of the divergence of the in-plane components of

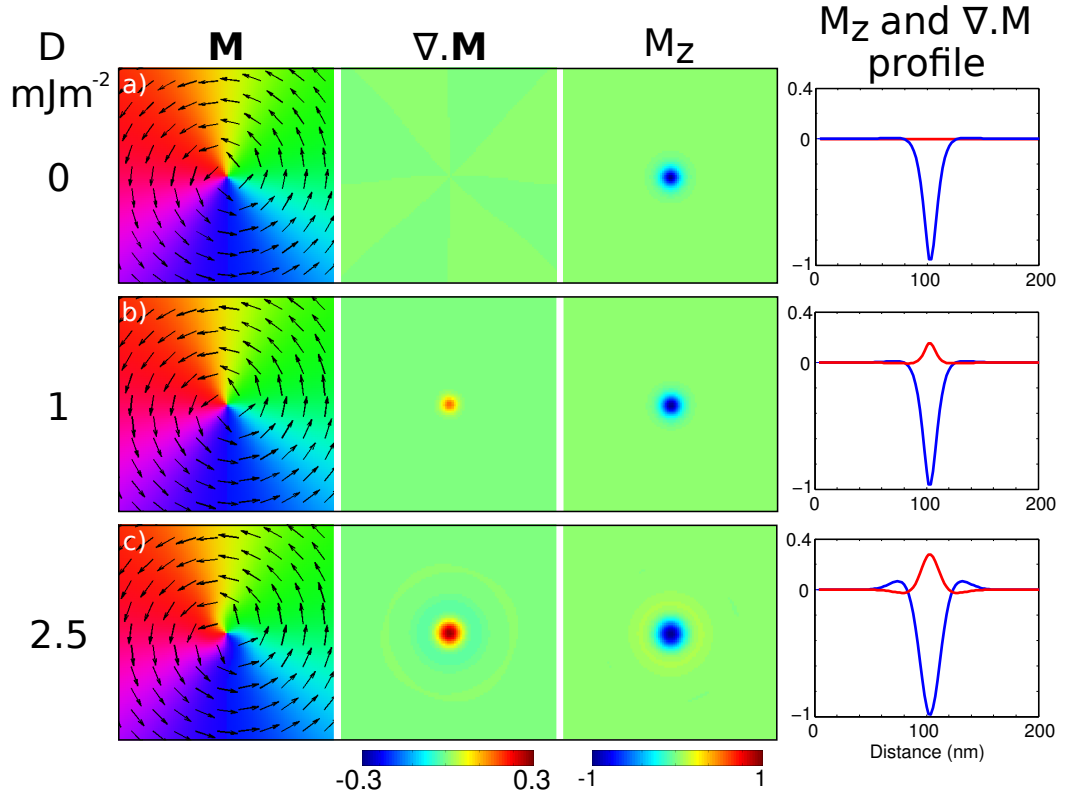


**Figure 4.1:** Series of images showing the effect of IDMI on the region near the core of magnetic vortices confined to discs for  $D =$  a) 0, b) 1 and c) 2.5  $\text{mJm}^{-2}$ . Left to right shows the in-plane direction of magnetisation, divergence of in-plane magnetisation, the out-of-plane component,  $M_z$ , and line profiles of  $M_z$  normalised to  $M_s$  (blue) and  $\nabla \cdot \mathbf{M}$  normalised to the maximum value of divergence (red). All images are 200 nm wide.

magnetisation,  $M_x$  and  $M_y$ ; the out-of-plane component of magnetisation,  $M_z$ ; and a line profile taken horizontally across the centre of the  $M_z$  image. The divergence and  $M_z$  images are visualisations of the volume charge,  $-\nabla \cdot \mathbf{M}$ , and surface charge,  $\mathbf{M} \cdot \hat{\mathbf{n}}$ , respectively. From the magnetisation maps it can be seen that the discs all relax into a vortex state; however, with increasing  $D$ , the magnetisation around the core of the vortex twists inward, an effect that is particularly evident for the colour map of  $D = 2.5 \text{ mJm}^{-2}$ . The images of the divergence of in-plane magnetisation clearly show the effect of the twisting of the magnetisation around the vortex core: a divergenceless, curl state is, of course, seen for  $D = 0$ ; for non-zero  $D$ , the strength and extent of the divergence around the core increases with increasing  $D$ , causing increased magnetostatic energy.

The effect on the core can also be seen in the images of  $M_z$ , which directly shows



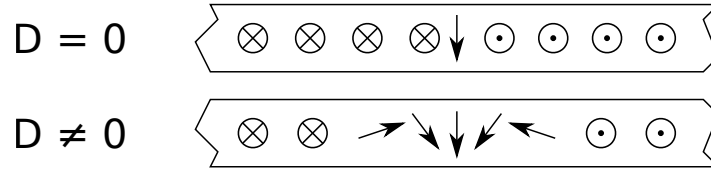


**Figure 4.2:** Representation of the magnetisation direction when taking a cross-sectional view through the core region of the disc for  $D = 0$  and  $D \neq 0$ .

that increasing  $D$  strength results in more surface charge. Once again, the most dramatic effect is seen for  $D = 2.5 \text{ mJm}^{-2}$ . As well as producing a wider core, the IDMI also causes  $M_z$  to point opposite to the core direction, seen as a yellow “halo” around the blue core but more clearly seen by comparing the  $M_z$  line profile across the vortex cores. The modification to the magnetisation around the core is illustrated schematically in Fig 4.2 for the cases where  $D = 0$  and  $D \neq 0$ . Fig 4.2 shows cross-sections through the magnetisation at the core, showing that it becomes more extended for  $D \neq 0$  and begins to resemble a Néel wall that, coincidentally, stabilises in PMA systems with IDMI.

The effect on  $M_z$  is similar to another previous study [116] on the effect of bulk DMI on vortex states where, depending on the sign of  $D$ , the DMI favoured one chirality over another. It is useful to define chirality at this point as the combination of the rotation sense of the vortex, defining  $c = \pm 1$ , for (+) clockwise and counter-clockwise (-), respectively, and the polarity of the core,  $p = \pm 1$ . This is shown in Fig 4.3 where the product  $cp$  defines the chirality of the state as  $cp = -1$  for a right-handed system and  $cp = 1$  for a left-handed system. In the work of Ref [116], right-handed vortices have a wider core than left-handed vortices for  $D > 0$ , and vice-versa for  $D < 0$ . This effect was tested in this work and it was found that the IDMI had the same effect on the magnetisation for both left- and right-handed vortices. However, it will be shown that the chiral symmetry is broken as the external field distributions are different for  $D \neq 0$  compared to  $D = 0$ .

At this point it is important to address an important issue: if there is net positive charge around the core of the vortex, then there must be corresponding negative charges. This requirement is answered by Fig 4.4, which shows an image of  $M_z$  at the disc edge, for the same values of  $D$  as Fig 4.1. For  $D = 0$ , the image is

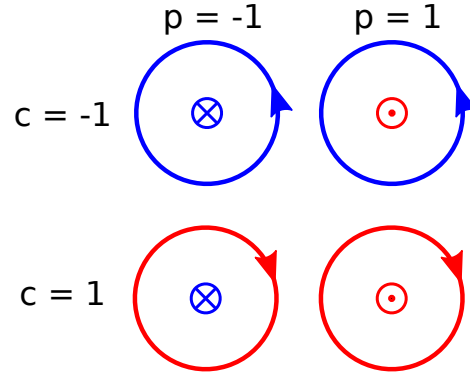


**Figure 4.3:** Illustration of how the combination of vortex rotation  $c$  and polarity  $p$  leads to a definition of chirality. Here  $cp = 1$  corresponds to a right-handed system and  $cp = -1$  to a left-handed system.

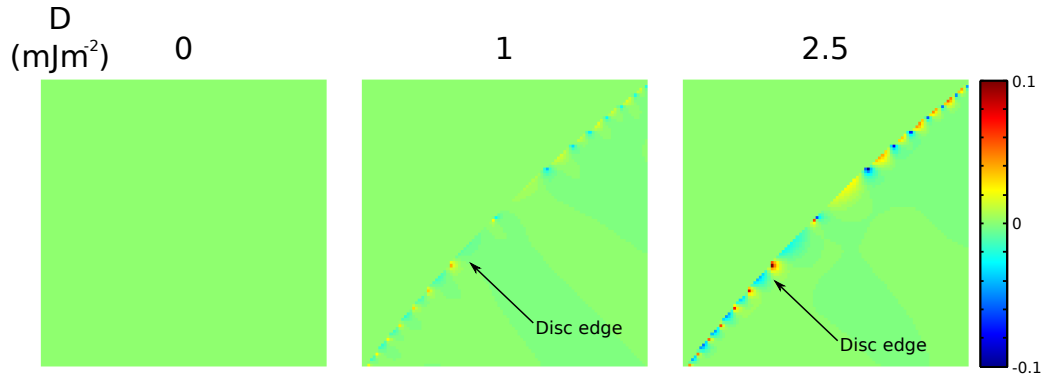


**Figure 4.4:** Colour map showing  $M_z$  at the edge of the disc. Some out-of-plane tilting of the magnetisation occurs for  $D \neq 0$ . Images are  $400 \times 400 \text{ nm}^2$ . Units are  $M_z$  normalised to  $M_s$ .

uniform; however, for  $D > 0$ , there is some variation in  $M_z$  *i.e.* there is some tilting out-of-plane. This tilting at the edge is seen in PMA systems with IDMI [125] and accounts for the additional charge at the centre of the disc; calculations indicate that the net sum of the charge from divergent magnetisation, considering the centre only, is of equal magnitude and opposite sign to the net sum of the surface edge charge.

The effect that the IDMI has on the core of the vortex is evident from Fig 4.1; however, experimentally measuring these effects is challenging. One possible method is using the differential phase contrast (DPC) mode of Lorentz TEM (see Ch 2.2.4.3), which is sensitive to changes in in-plane magnetisation with spatial resolution down to  $\sim 1 \text{ nm}$  on the ARM instrument [126], described in Chapter 2. DPC ultimately produces a map of two components of the magnetic induction integrated through the

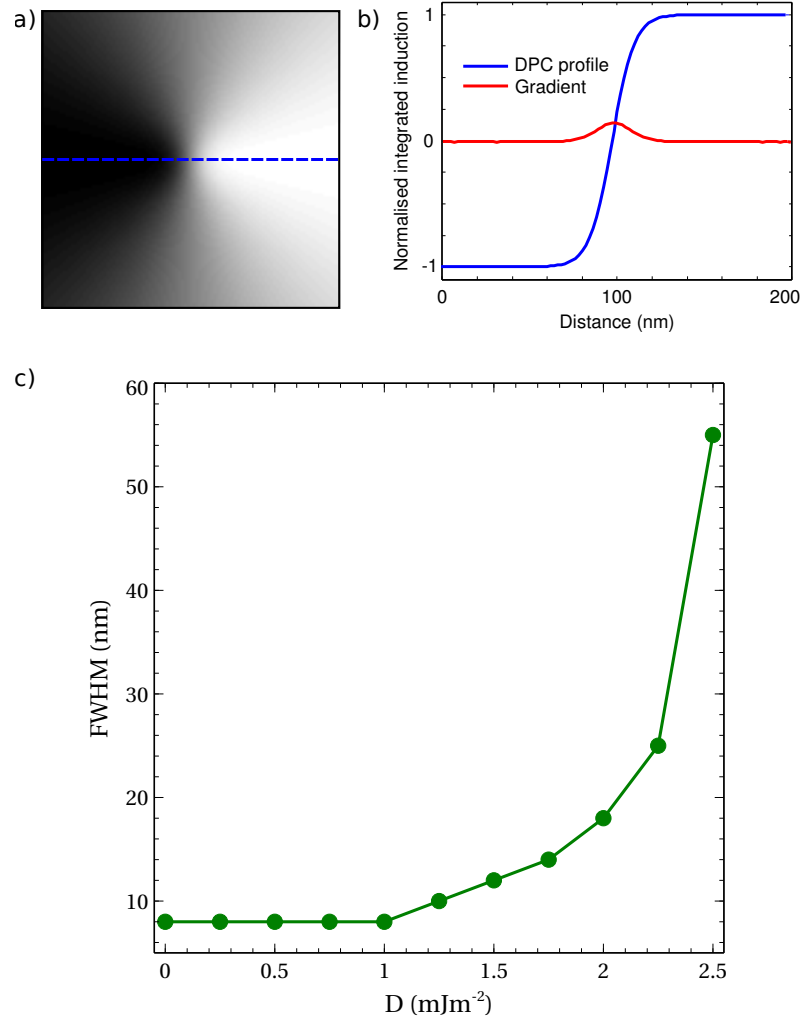


**Figure 4.5:** a) One component of a calculated DPC image from micromagnetic simulations that relaxed to a vortex state and b) the profile across the core, shown by the blue dashed line in a), and its gradient, from which the FWHM is obtained. c) plots the effect of  $D$  strength on the FWHM, using the method in a) and b).

thickness of the sample, which can be calculated from the simulation data displayed in Fig 4.1. Fig 4.5a) shows an example of one component of a calculated DPC image, showing the configuration at the core of a vortex, contained within a disc. The width of the vortex can be measured in the same way as a DW; a hyperbolic tangent function can be fitted to the profile, as shown by the dashed line in the image, and the full width at half maximum (FWHM) of the gradient of the fitted function can be taken as the effective width of the core, as shown in Fig 4.5b). The calculated FWHM for different  $D$  values using this method are plotted as a function of  $D$  in Fig 4.5c). This shows that, for the more modest values of measured

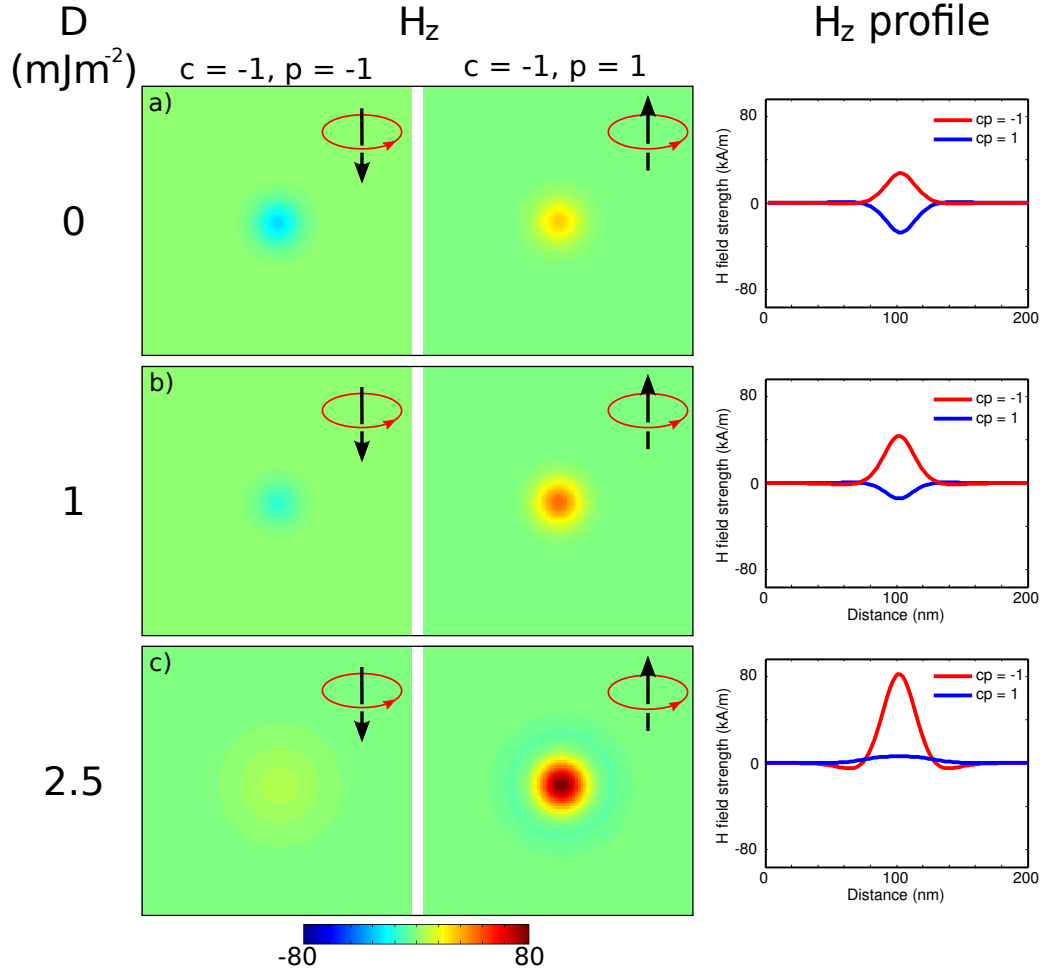


**Figure 4.6:** Simulated images based on the magnitude of out-of-plane component of stray field, calculated at a height of 20 nm above the sample for a) 0, b) 1 and c) 2.5  $\text{mJm}^{-2}$ . Left and right images correspond to left and right-handed systems of magnetisation rotation sense  $c$  and polarity  $p$ .

$D$  reported [24, 115] of  $\leq 1.2$   $\text{mJm}^{-2}$ , the core width varies by a few nm, if at all. However, it should be noted that the resolution of the simulations was 1 nm per pixel. Considering that noise is present in DPC images due to the polycrystalline character of the thin films imaged, as described in Ch 2.2.4, this is a difficult measurement to make.

Another experimental technique that could be used to directly measure IDMI effects is magnetic force microscopy (MFM). A MFM tip uniformly magnetised perpendicular to the plane of the sample is highly sensitive to stray fields from the sample that are aligned parallel or anti-parallel with the moment of the tip. Fig 4.6 shows calculated images of the magnitude of the out-of-plane component of the stray

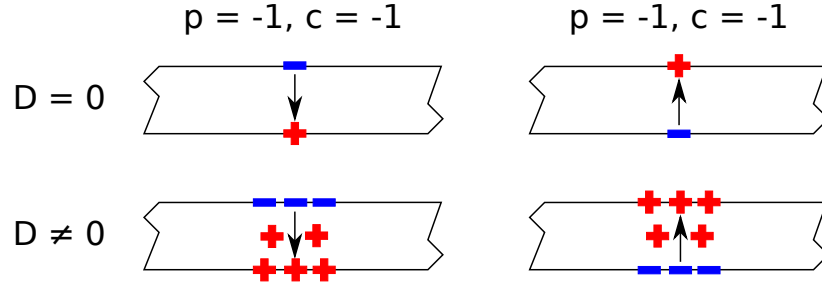


**Figure 4.7:** Schematic diagram providing an interpretation for the  $H_z$  maps in Fig 4.6. There is chiral symmetry for  $D = 0$ ; however, depending on the divergence of the magnetisation, an imbalance of charge is created around the core, modifying the stray field.

field,  $H_z$ , at a height of 20 nm above the sample; these images correspond to the same  $D$  values as Fig 4.1. A comparison is made between  $H_z$  for left- and right handed states, as defined in Fig 4.3. The colour maps on the left of Fig 4.6 show left-handed ( $cp = 1$ ) vortices and the right side shows the right-handed state ( $cp = -1$ ) *i.e.* corresponding to the top-left and top-right configurations in Fig 4.3. Profiles across the centre of the colour maps are shown along the right side of Fig 4.6 with left-handed and right-handed profiles represented by blue and red lines, respectively.

Fig 4.6 shows that, for  $D = 0$ , as expected, the strength of  $H_z$  from the cores is equal and of opposite sign; in contrast, for  $D \neq 0$ , the left-handed systems have increasingly weaker  $H_z$ , to the point where  $D = 2.5 \text{ mJm}^{-2}$  results in positive  $H_z$ , despite having  $p = -1$ , as shown by the line profiles. The right-handed systems, in contrast, possess a much stronger core. In both cases, this effect can be attributed to the additional magnetic charge around the core that is induced by the IDMI, as illustrated in Fig 4.7. This figure shows that, consistent with  $D = 0$ , equivalent surface charges are present for  $p = -1$  and  $p = 1$ , which would produce  $H_z$  of equal and opposite magnitude. For  $D \neq 0$ , in addition to the surface charge that would ordinarily arise from the core, extra charge from the divergence of in-plane magnetisation caused by the IDMI produces stronger or weaker  $H_z$  above the sample. The core is wider for non-zero  $D$ , which results in more surface charge, as in Fig 4.1. The images in Fig 4.7 be reversed for both handedness for calculations at a height “below” the sample. Thus, it could be concluded that MFM could potentially be used to detect the evidence of IDMI by measuring the difference between IDMI and

non-IDMI samples, but the feasibility of this experiment depends on the strength of  $D$ . For  $D = 2.5 \text{ mJm}^{-2}$ , the difference would be obvious, as for one chirality the field from the core almost disappears; for  $D = 1 \text{ mJm}^{-2}$  the effect is more subtle but, nonetheless, should be detectable with MFM.

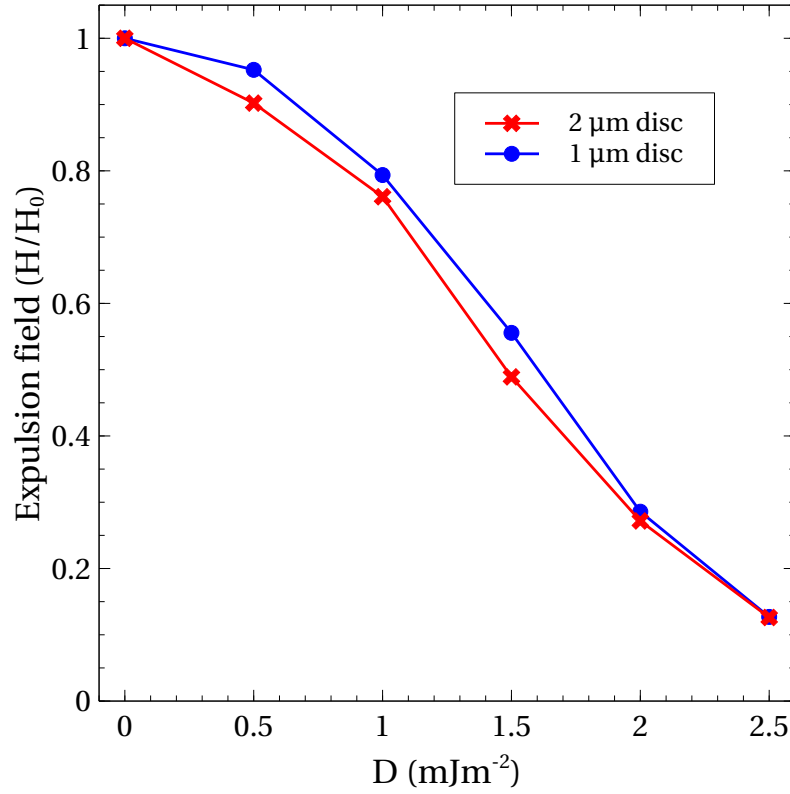


**Figure 4.8:** Simulation results showing the variation of the field required to expel the core of a vortex confined to a disc for increasing  $D$  strength. Field values are normalised to the field required to expel the core for  $D = 0$ ,  $H_0$ .

Given the increase of surface and volume charge with increasing  $D$  and, thus, magnetostatic energy, the presence of a divergent core can be expected to affect the magnetisation processes of the disc, such as the vortex expulsion field. This is shown in Fig 4.8, a graph which plots the vortex expulsion field as a function of the strength of  $D$ . As  $D$  increases, the strength of the applied field required to push the vortex from the disc decreases, which is presumably due to the increasingly divergent magnetisation around the core. This effect is useful from two perspectives: first, the vortex expulsion field is dependent on  $D$ , which can therefore be determined by direct comparison of experiment and modelling; second, the dramatic reduction

of the vortex expulsion field for the highest  $D$  value, which is useful from the perspective of devices based on magnetic nanostructures [71]. Given recent work [24] that shows that the IDMI may be tuned, if it is possible to induce IDMI with values close to  $2.5 \text{ mJm}^{-2}$  the behaviour of magnetic nanostructures could be significantly manipulated.

### 4.3 Experimental

In order to test the predictions of the simulations, Py thin films were grown and capped with two different layers, Pt and Cu. Pt, a material with high SOC, would be expected to induce some IDMI in one sample, while the Cu capped sample would act as a control sample that provides a similar granularity and interfacial roughness and which provides a cap against oxidation without inducing DMI effects. A value of  $D$  could be measured by comparing the expulsion field of a vortex core from a disc for both samples then referring to the graph in Fig 4.8. Given that the experiment is a comparison between the two samples, they would have to be as similar as possible. PLD was used to co-deposit the bilayers onto 35 nm thick, electron transparent  $\text{Si}_3\text{N}_4$  membranes (see Ch 2.3.3) so that they could be characterised using TEM. Py was deposited onto both substrates before the PLD system shutter was used to mask each sample in turn for the deposition of the non-magnetic Pt and Cu layers. This deposition method ensured that, capping layer aside, the films were identical and that there would be no vacuum break after Py deposition, preventing undesired oxidation. The thickness of each layer was measured using AFM: Py = 9 nm, Pt = 4 nm and Cu = 4.5 nm. Fig 4.9 shows CTEM bright and dark field images of the deposited films, which show that the PLD grown bilayers show polycrystalline structure with no texturing apparent from tilted diffraction patterns (not shown). Notably, the grain size of Cu appears to be smaller than Pt; from this point of view, it may be that the interfacial structure of each bilayer is different, a cross-section would be useful to assess this. The saturation induction and coercivity of the films is also found to be the same, as shown by Fig 4.10, which shows a hysteresis loop measured by the BH-Looper. This result is corroborated by low angle diffraction

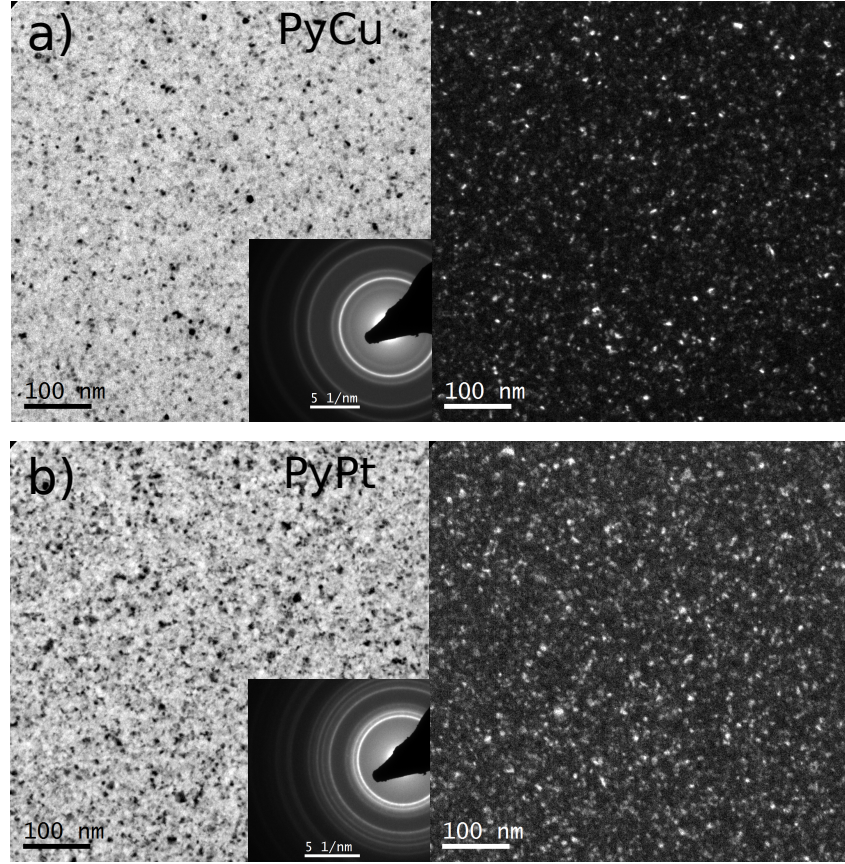


**Figure 4.9:** CTEM bright (with diffraction patterns inset) and dark field images of PLD deposited a) Py/Cu and b) Py/Pt bilayers on  $\text{Si}_3\text{N}_4$  membranes showing polycrystalline structure.

measurements on both films which gives a value of  $B_s = 1.0 \pm 0.1$  T.

FIB milling was used to define rings in the continuous film of inner radius  $2 \mu\text{m}$  and outer radius  $3 \mu\text{m}$ , to leave a disc  $2 \mu\text{m}$  in diameter isolated from the rest of the continuous film.  $5 \times 5$  arrays of discs were milled on each sample, an example of which is shown in the SEM image of Fig 4.11a). Fig 4.11b) and c) show CTEM bright and dark field images of a disc edge on the Py/Cu and Py/Pt samples, respectively. For both samples, the grains at the edge of the disc are enlarged compared to those closer to the centre, an effect which has been observed in the fabrication of planar nanowires using FIB [127] as a result of heating caused by the tails of the ion beam, which causes recrystallisation. The region for which the enlargement occurs is approximately equal for both samples, approximately 100 nm.

Following FIB milling, the Fresnel mode of Lorentz TEM was used to determine



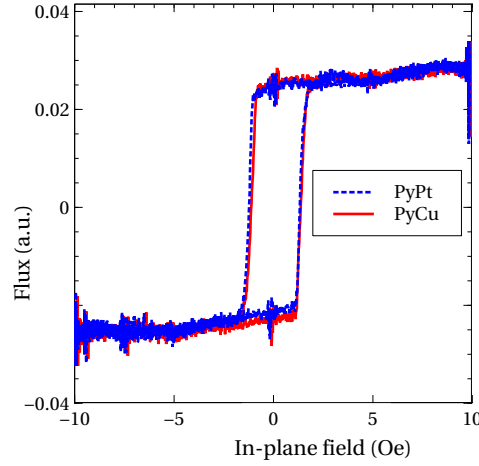


**Figure 4.10:** Hysteresis loops from the BH-Looper for Py/Pt (dashed-blue) and Py/Cu (solid-red) showing behaviour consistent with identical Py films.

the vortex expulsion field for the discs in the arrays. In-situ magnetising experiments were performed by weakly exciting the objective lens of the TEM and tilting the sample, thus applying an in-plane field. The Fresnel mode is ideal for this experiment, especially given the fact that magnetising experiments can be automated by the scripting described in Ch 2.2.4.4. Fig 4.12a) shows a Fresnel image of a disc array, at approximately zero in-plane applied field, which shows the core of the vortices appearing as bright or dark spots, depending on the rotation sense of the magnetisation, as described in Chapter 2. Fig 4.12b) and Fig 4.12c) show consecutive Fresnel images taken in the tilt series, with increasing in-plane applied field. Circles are used in Fig 4.12b) to show the position of the core at the edge of the disc; Fig 4.12c) shows that the cores have been expelled. To determine the vortex expulsion field, the sample was tilted to both positive and negative tilt angles and an average of the two was taken to avoid any systematic error arising from the sample not being perfectly flat in the TEM sample holder. After all vortices in the array were expelled, a much larger field was applied to make sure that all discs were saturated before applying the field in the opposite direction. The samples were tilted to positive and negative tilt angles three times each, so that an average was taken from three expulsion fields for each disc in every sample. The experimentally determined vortex expulsion fields for both samples are plotted in Fig 4.13. There is a clear separation between the Py/Pt and Py/Cu distributions, represented by blue and red

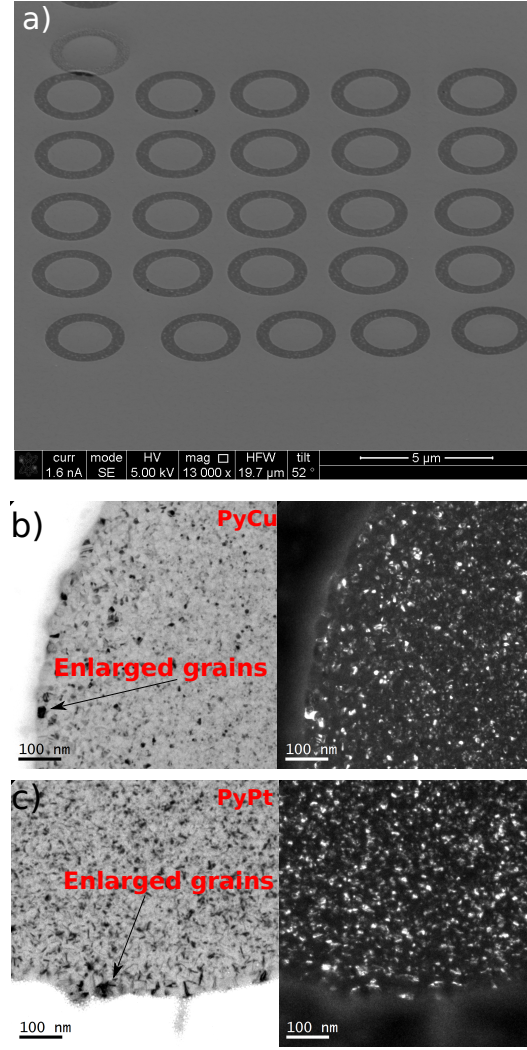


**Figure 4.11:** Series of images of focused ion beam (FIB) milled discs: a) an example of a  $5 \times 5$  array of discs; b) and c) CTEM bright and dark field images of disc edges after milling for Py/Cu and Py/Pt, respectively. Arrows indicate grains that have become enlarged following FIB milling.

histograms, respectively. The error bars represent the applied field that corresponds to the tilt angle step, which is  $\sim 1$  Oe. Assuming that the effect on the expulsion field is solely down to the IDMI, by comparing the graph in Fig 4.8 with the experimentally obtained expulsion fields in Fig 4.13, a value of  $D$  can be obtained. However, some material difference between the films, suggested by Fig 4.9, cannot be ruled out. By taking an average of all the points in Fig 4.13 for both samples and taking  $H_{Cu}$  to be  $H_0$ , the expulsion field for  $D = 0$ ,  $H_{Pt}/H_{Cu}$  gives a value of  $D \simeq 0.5 \text{ mJm}^{-2}$ . This figure does not change significantly when possible outliers in Fig 4.13 are removed; it is likely that the outliers arise when the magnetisation is

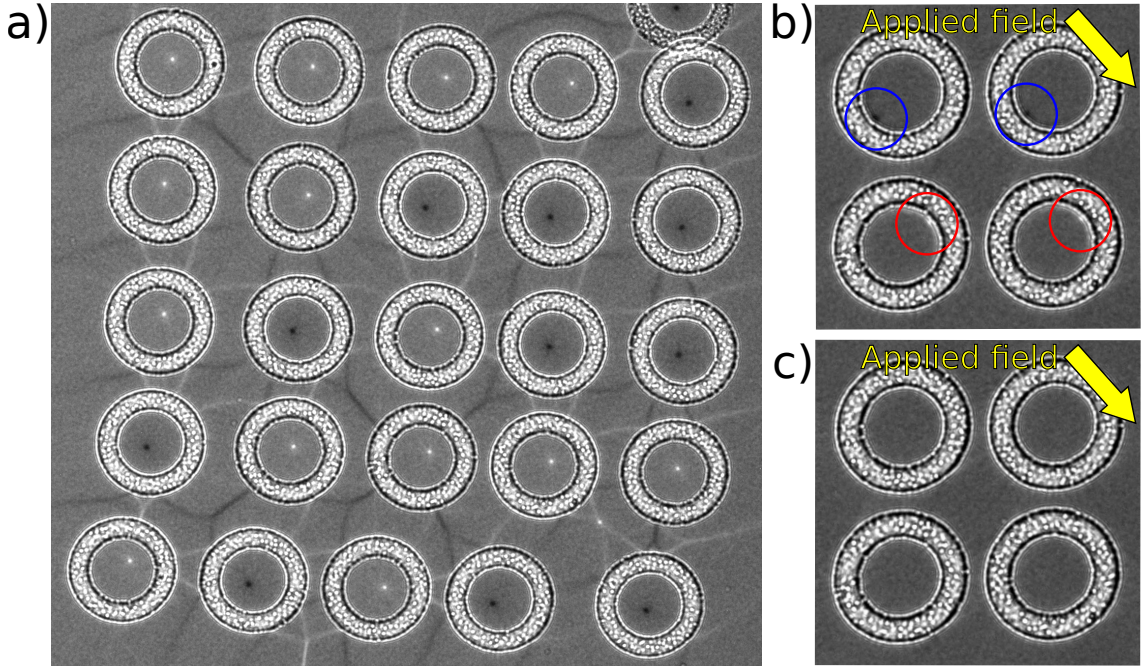


**Figure 4.12:** Fresnel imaging of vortices in discs with vortex cores revealed as dark or bright spots. The array in a) contains vortices at approximately zero applied field; b) shows a selection of Py/Cu discs at an applied field strong enough to push the cores to the edge (circled); c) shows the same discs as b), the field is increased so that all cores have been expelled.

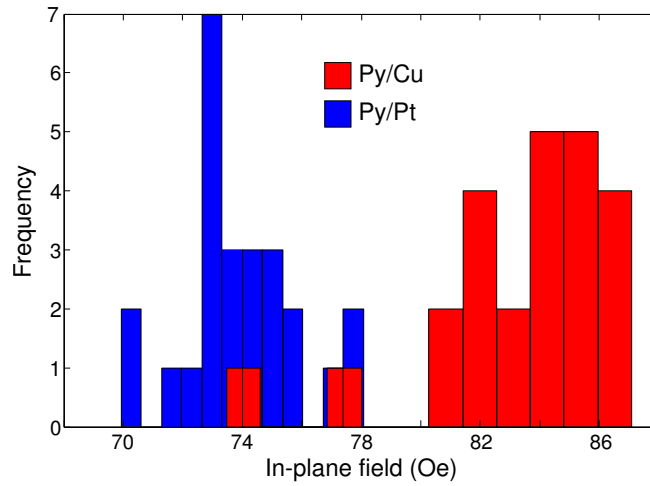


**Figure 4.13:** Vortex expulsion fields for Py/Pt (blue) and Py/Cu (red) disc arrays, represented by histograms. There is a clear separation between the two distributions, indicating that it is easier to expel the core from Py/Pt disc, as predicted in Fig 4.8.

pinned at an unusually rough edge of the disc.

The measurement of vortex expulsion fields in Fig 4.13 therefore provides a method by which the strength of  $D$  may be measured for soft magnetic materials.

To the author's knowledge,  $D$  has not yet been measured for IDMI in magnetic materials with in-plane anisotropy; however,  $D = 0.5 \text{ mJm}^{-2}$  falls within the range of values measured for out-of-plane materials,  $0.33$  [115] -  $2.2 \text{ mJm}^{-2}$  [124]. While this measurement method is not applicable for out-of-plane materials, it can be applied to all in-plane materials. In addition, while the automated Fresnel imaging used here is a highly efficient way of determining the expulsion field, the method is not restricted to Lorentz microscopy, for example, MFM offers an alternative. As the extent of the divergent magnetisation around the core is set by a competition between Heisenberg exchange and IDMI, the strength of  $D$  can be expected to scale with the exchange length of the material.

The prospect of other possible measurements can now be assessed using the value of  $D = 0.5 \text{ mJm}^{-2}$ . Referring to Fig 4.6, detecting and measuring the effects of IDMI on vortex cores using MFM is likely to be possible, though challenging. As with the vortex expulsion field experiment used here, a direct comparison between samples with and without IDMI would be helpful. On the other hand, measurement of the vortex core width using DPC imaging as a method to detect/measure  $D$  would be virtually impossible, according to Fig 4.5c). While simulations show that the IDMI causes the magnetisation around vortex core to become divergent, it is integrated induction, not magnetisation that is mapped by DPC; the FWHM that is measured from the calculated images does not change until  $D > 1 \text{ mJm}^{-2}$ . Although, perhaps the pixel size of the simulations masks some variation in the vortex width.

From a technological perspective, the ability to influence the magnetisation processes of thin films and nanostructures is extremely attractive. The Walker field in perpendicularly magnetised thin films is predicted to increase strongly with  $D$  [22] (by a factor of five for  $0.5 \text{ mJm}^{-2}$ ); while the dependence may be different for in-plane materials, suppression of Walker breakdown is an attractive prospect for memory devices such as racetrack memory [71]. In addition, in light of work suggesting that the strength of  $D$  can be tuned [24], this is attractive for memory devices based on magnetic vortices, as the expulsion field can be manipulated, as shown in Fig 4.8.

## 4.4 Conclusions

In conclusion, the interface-induced DMI has been detected in vortex states confined to discs in a soft magnetic material, Py. The IDMI is shown to cause the magnetisation around the core to be increasingly divergent with increasing  $D$  and the vortex expulsion field is predicted to be reduced with increasing  $D$ . Measurement of the vortex expulsion field, in this case by Lorentz TEM in-situ magnetising experiments, provides a method by which the IDMI can be detected and its strength,  $D$ , measured. A comparison of simulation and experimental results allows a value of  $D$  to be inferred. A value of  $D = 0.5 \text{ mJm}^{-2}$  is obtained, while this is thought to be the first measurement for soft magnetic materials, this value falls within the range of values measured for perpendicularly magnetised materials. The advantage of this method is that it is not limited to Lorentz TEM but any technique that allows the direct imaging of the vortex core, for example, MFM and, in addition, the fabrication methods used here are trivial.

The possibility of directly measuring the effects of the IDMI on the vortex core was assessed for MFM and the DPC mode of Lorentz microscopy. Simulations show that measuring the increasing width of the core using DPC would be impossible for the reported value of  $D = 0.5 \text{ mJm}^{-2}$ ; however, the possibility of measurement using MFM is possible. Due to the increased divergence at the core, the strength of the external field around the core is weaker or stronger, depending on the vortex chirality.

These observations can be expected to be applicable to other soft magnetic materials, with the observed effects scaling with the exchange length. The IDMI is expected to modify the structure of other spin textures in soft magnetic systems, in particular those with some out-of-plane component, such as cross-tie and vortex domain walls; as with the vortices studied here, the magnetisation processes of these systems will also be affected. This may be attractive for technological applications such as memory devices based on magnetic vortices.

# 5

## Tunable frustration in nanomagnet arrays

### 5.1 Introduction

Frustration, the failure of a system to satisfy competing interactions within a system, is a phenomenon present in many naturally occurring condensed matter systems. Originally, it was shown that geometrical frustration of the molecules in water ice leads to a large number of degenerate states, which results in non-zero entropy at zero temperature, in apparent violation of the third law of thermodynamics[128]. The origin of the geometrical frustration is the conflict of the bond lengths and the tetrahedral crystal structure, which leads to the “ice rule”, where the lowest energy state at a tetrahedron is with two protons close to the oxygen and two further away (two in-two out). An analogous case for a magnetic system is found in ferromagnetic rare earth pyrochlores, such as  $\text{Ho}_2\text{Ti}_2\text{O}_7$  [129], where the crystal structure dictates that magnetic moments on  $\text{Ho}^{3+}$  follow the two in-two out ice rule,

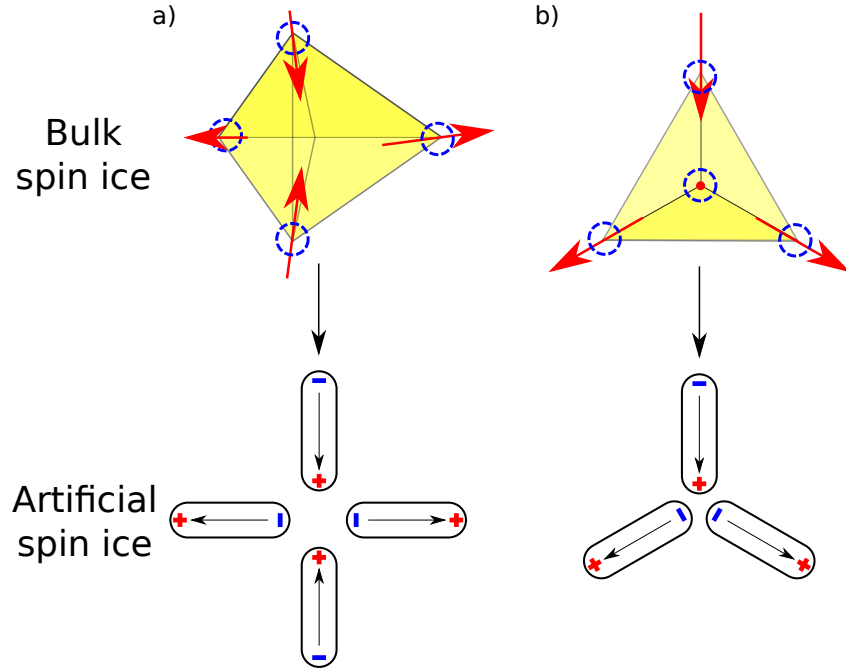


**Figure 5.1:** By projecting through different crystallographic orientations of the bulk spin ice crystal (top) the a) square and b) kagome vertices that comprise the most commonly studied artificial spin ice systems can be created (bottom). The spins on the crystal lattice (blue circles and red arrows) are replaced by single-domain elongated nanomagnets.

leading to the name spin ice. This is illustrated at the top of Fig 5.1 where spins are represented by red arrows on blue dashed  $\text{Ho}^{3+}$  ions. The ability to lithographically define arrays of single-domain nanomagnets with stable ferromagnetism at room temperature provides the possibility for engineering artificially frustrated systems. As illustrated in Fig 5.1, a frustrated arrangement of nanomagnets can be fabricated by projecting along different crystallographic axes of tetrahedral magnetic spin ice onto a two dimensional plane. Fig 5.1a) and b), respectively, show vertices that comprise square and kagome arrays; these artificial frustrated magnetic systems are artificial spin ice (ASI) arrays [130, 131]. The moments of the elongated single-domain elements in ASI arrays replace the atomic spins in bulk spin ice materials. While the lowest energy state can be defined, not all interactions at square and kagome vertices can be satisfied *i.e.* all of the nanomagnets cannot align head-to-tail.

ASI arrays therefore allow the creation of model frustrated systems that exhibit the same phenomena as bulk spin ice; the advantage being that artificial systems'

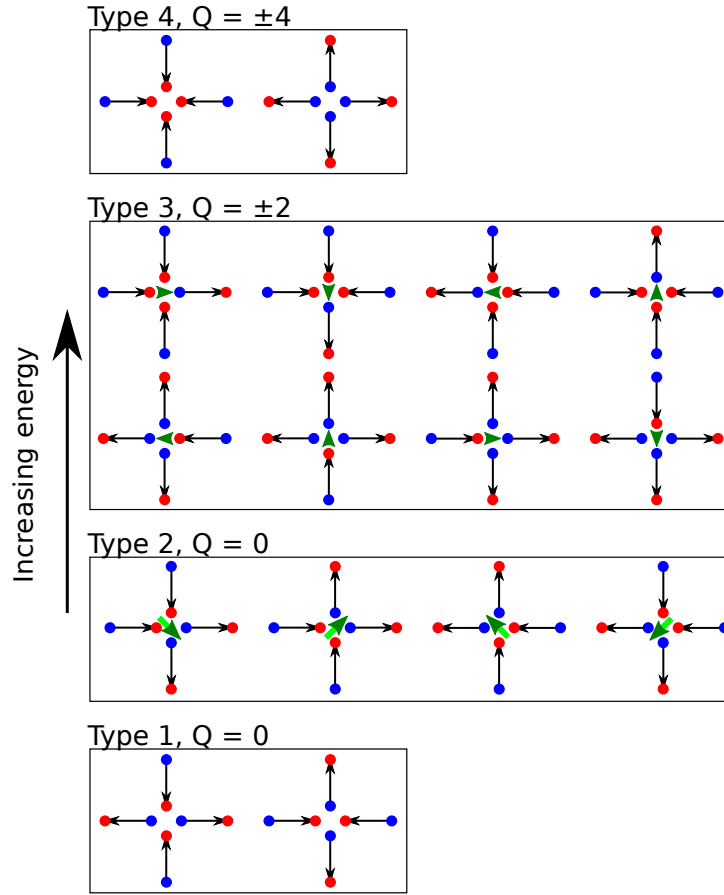


**Figure 5.2:** All possible vertex configurations for square ASI ranked in terms of energy. Green arrows, placed at the vertex centre, show size and direction of net moment, where applicable.

behaviour is tunable through the fabrication process, which facilitates the study of various processes present in frustrated and disordered systems [132, 133]. Furthermore, since each microstate of ASI may be imaged directly using modern magnetic microscopy at room temperature, these phenomena more easily observed than bulk spin ice. An example of this is emergent monopoles, connected by Dirac strings, that were observed in reciprocal space in bulk spin ice [134, 135] but could only be directly imaged [136] and characterised under applied field [137] in ASI. In addition, ASI arrays also have the potential for technological applications. Emergent monopoles raise the possibility of devices based on movement of magnetic, rather than electrical, charges, *i.e.* magnetricity. Although magnetricity has been demonstrated in bulk spin ice [138] at low temperature, ASI offers an alternative system for the generation of monopoles at room temperature. The creation and control of emergent monopoles is seen to depend on the topology of the array [139] and its



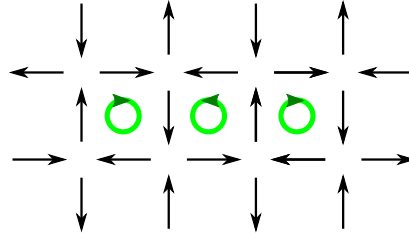


**Figure 5.3:** Anti-ferromagnetic ground state for square artificial spin ice, which is composed of degenerate Type 1 vertices. Green circles show the circulation of magnetic flux.

thermal properties [140]. Another example of a technological application of ASI is in magnonic crystals, used for microwave devices, which offer low power operation and scalability over electronic and photonic alternatives [141].

relies on the engineering of the element material and

In some respects ASI does not exactly reflect the behaviour of bulk spin ice. Square ASI is unlike bulk ASI because interactions between all elements are not equivalent, which leads to a breaking of degeneracy of the ground state (two in-two out) configuration. Fig 5.2 shows all  $16 (= 2^n)$  possible vertex configurations for square ASI, ranked by energy; the direction of magnetisation within each element is represented by a single arrow (spin) and associated surface charge by red and blue circles, showing positive and negative charge (or equivalently, north and south poles). The four different vertex types can be further classified in terms of net moment (illustrated using a green arrow at the vertex centre) and charge. The lowest energy states are zero moment Type 1 vertices whose splitting with Type 2 arises from the fact that adjacent elements are closer than opposite elements; it should be noted that the energy difference between Type 1 and 2 is low [142]. Type 3 and 4 are higher energy states due to their net charge. While the all interactions at each vertex cannot be satisfied, an overall ground state can be defined for a square ASI lattice. This ground state is shown in Fig 5.3, which shows an anti-ferromagnetic domain composed of alternating Type 1 vertices; however, finding this ground state is non-trivial. Approaches used to reach the ground state have focused on demagnetising [143] or, more successfully, thermalising the arrays. Thermalisation can occur by several methods: heating the ASI until the elements overcome the blocking temperature [142, 144], fabricating elements thin enough to encourage thermal

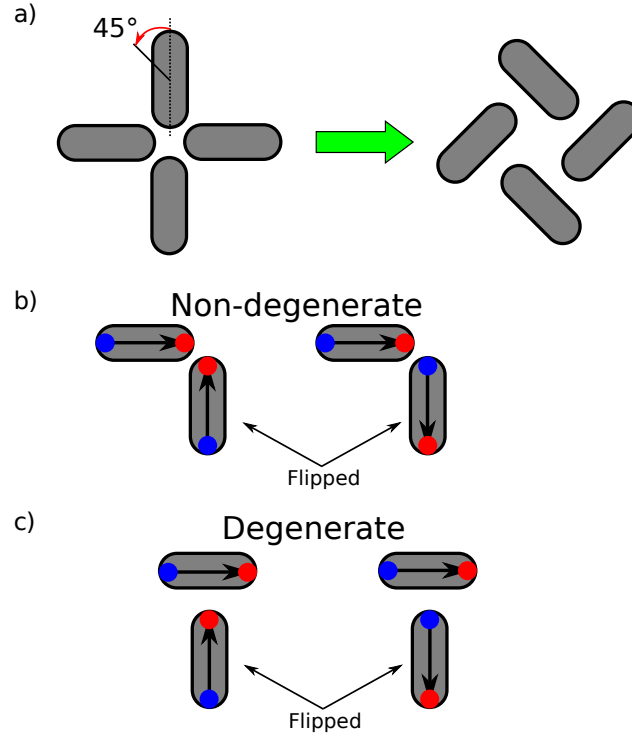


**Figure 5.4:** Diagram showing a) the transformation between square and rotated square ASI and b),c) the difference in number of degenerate states considering adjacent elements, only.

flipping [145] or during deposition of magnetic material in the fabrication process [146]. This allows large domains of Type 1 vertices to form; however, higher energy vertices still remain.

In contrast to the most commonly studied systems, in this chapter, a modified version of the square ASI lattice is studied. This geometry is generated by rotating all of the elements at the vertex in a square ASI about their centre point by  $45^\circ$ , as demonstrated in Fig 5.4, to form a new configuration, referred to as the rotated-square (RS) vertex. This differs from the square vertex in that the ends of the elements now point into the centre of adjacent neighbours, as shown in Fig 5.6b) and c), where only two adjacent elements in a vertex are considered. The consequence of this is seen by flipping the direction of the spin of the vertically aligned element. The energy is lowered for the square lattice in Fig 5.4b), as two positive charges meeting is replaced by a positive and negative; in contrast, the two states for the RS case are degenerate, energetically, it makes no difference whether the vertical arrow points up or down. Vertices for the square lattice can be constructed by adding

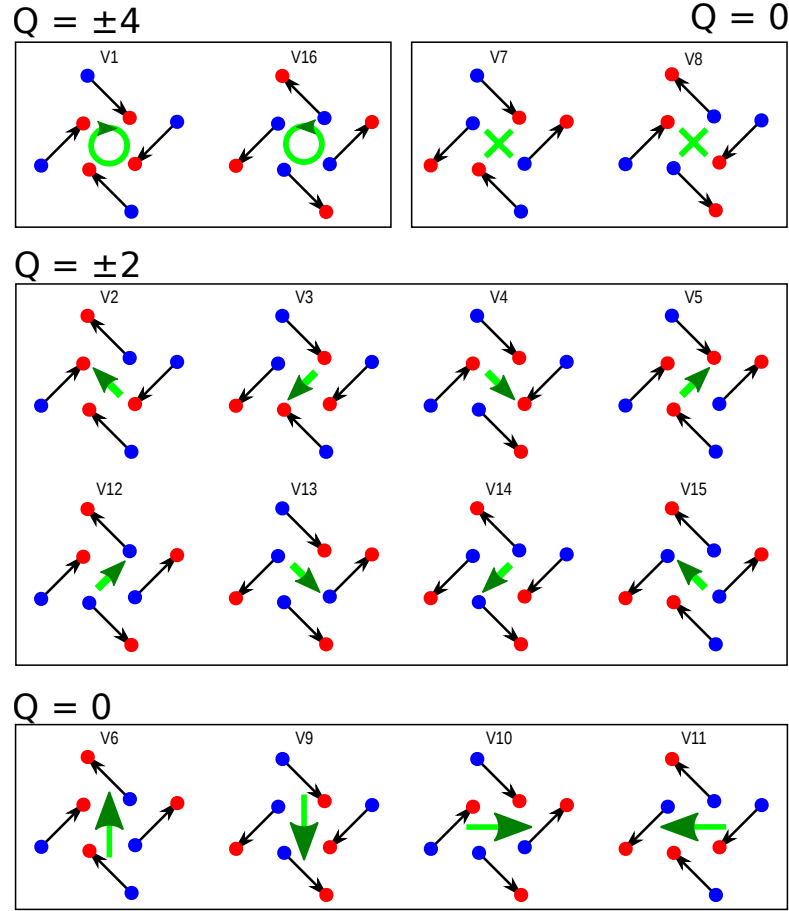


**Figure 5.5:** All possible configurations of magnetisation in single-domain RS elements. Vertices are categorised in terms of charge and net moment. Moment is represented by green arrows.

high energy (head-to-head) and low energy pairs (head-to-tail) together; no matter what the size of the elements and the lattice constant the ground state vertex is always known. In contrast, the lowest energy RS vertex is not immediately obvious, considering that all configurations of adjacent pairs of elements are degenerate.

Fig 5.5 shows all possible vertex configurations for the RS lattice, categorised in terms of their net moment and internal charge. Like the square ASI in Fig 5.2, there are four vertex types; two types that have zero moment and two types with net moment of different magnitude and direction. The configurations with zero moment, at the top of Fig 5.5, resemble vortex and anti-vortex spin states, as indicated by the  $\circ$  and  $\times$  annotations at their centre. The zero moment vertices in Fig 5.5 could be expected to be the ground states of the RS lattice, as they resemble the anti-ferromagnetic domains in square ASI; however, the four-fold degeneracy of adjacent

pairs means that the energies are likely to be energetically similar, if not degenerate. The modified energy landscape of the RS lattice therefore provides an interesting alternative to the square ASI. In addition, the observation of the reversal of this array type by the formation of flux-closure states with a preferred chirality depending on the applied field direction provides motivation for the investigation of the reversal behaviour of the RS lattice [147].

In this chapter, the reversal behaviour of the RS lattice under an external applied field is investigated experimentally. The ASI array is fabricated using electron beam lithography and the reversal of the elements is imaged directly using in-situ magnetising experiments with Lorentz transmission electron microscopy (LTEM). Using OOMMF simulations, the energies of all possible vertex configurations are calculated and used to aid the understanding of the reversal process. Consequently, it is predicted that the coupling of the elements in the array depends on the elements' spacing and that the behaviour of the array can be controlled by adjusting this parameter.

## 5.2 Methods

RS arrays were fabricated using the lift-off technique of EBL, as described in Chapter 2. The desired geometry is shown in Fig 5.6a), the elements in the figure are arranged so that their long axes point along horizontal and vertical directions with a spacing between elements' centres,  $a = 420$  nm. The elements are lozenge-shaped, with a width of 170 nm and length 470 nm; similar dimensions are used in other studies and provide thermally stable single-domain elements [137]. The radius of curvature of the element ends was set to be half of the width, 85 nm. As described in Chapter 2, the desired geometry was achieved by designing the elements to be smaller than the target dimensions. The array was constructed by repeating the structure in Fig 5.6a) in the positive  $x$  and  $y$  directions, as indicated in Fig 5.6b). A permalloy thin film of thickness 10 nm was deposited using thermal evaporation and subsequently capped with Al to avoid oxidation, which has been shown to be responsible for exchange bias that influences the switching behaviour of elements in ASI arrays [148].

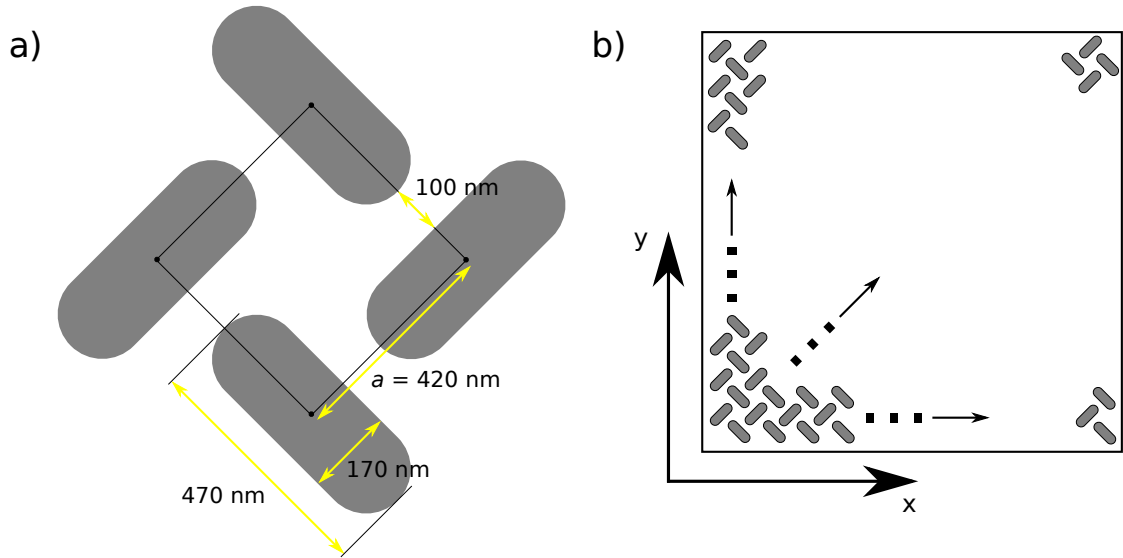


**Figure 5.6:** Geometry of the RS array and b) the direction in which it is repeated.

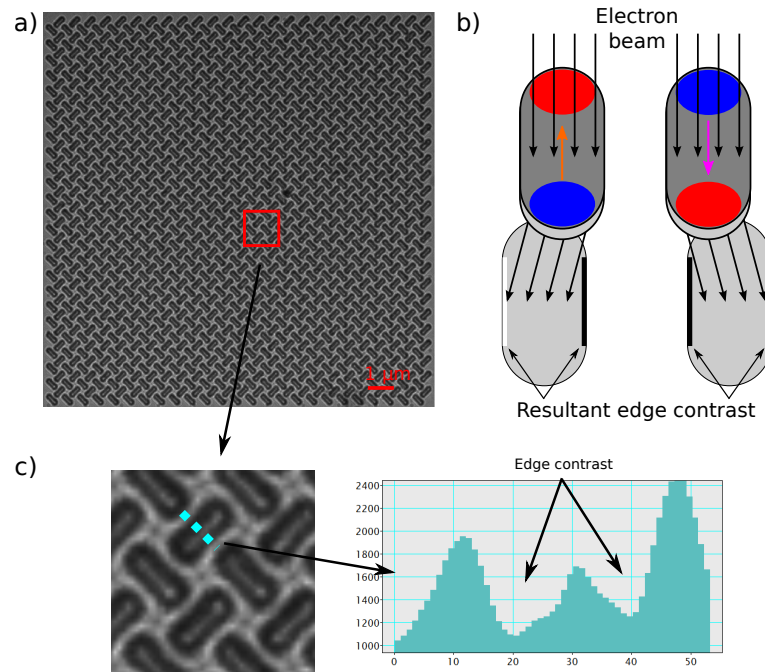


**Figure 5.7:** Fresnel imaging of an ASI array. a) shows a typical Fresnel image of the array and b) shows a simple schematic representation of the contrast expected from Fresnel imaging; depending on the orientation of magnetisation along the axis of an element, the order of bright/dark contrast changes. c) shows an enlarged image of the area bounded by the red box on the image in a); the line profile across the element shows that one side is “brighter” than the other allowing the direction of magnetisation to be determined. Scale in the line profile is  $\sim 5$  nm per pixel.

Magnetic characterisation of the arrays was performed using the Fresnel mode of LTEM, with images acquired on the JEOL ARM 200-CF, as described in Chapter 2.

The objective lens was excited so that the vertical field strength was  $\sim 1200$  Oe. It is not expected that this vertical field will significantly change the magnetic state of the elements given their strong shape anisotropy. Fig 5.7a) shows a typical Fresnel image of the entire  $24 \times 24$  vertex array and b) shows a schematic explaining the expected magnetic contrast. Depending on the direction of magnetisation in parallel elements, it is expected, that one side of the elements' long axis is darker/brighter than the other due to the Lorentz deflection. Fig 5.7c) shows an enlarged image of the area bounded by the red box in a) and displays a line profile across the short axis of an element, which indicates that one side of the element is "darker" than the other, corresponding to one particular orientation of magnetisation. The magnetic edge contrast is therefore detectable, regardless of the presence of strong electrostatic phase contrast, which is uniform around the element edges.

The Fresnel image in Fig 5.7b) does not provide an as easily interpretable map of magnetisation as a differential phase contrast (DPC) image would do. Thus, the image must be processed to provide an image that shows magnetisation direction; the justification for using Fresnel, rather than DPC, imaging will be given later. A MATLAB script, presented in Appendix B, was written to convert Fresnel images into magnetisation maps. The script works in two stages: first, a lattice of points is found for elements of a given direction of magnetisation using cross-correlation; the lattice is convolved with a motif, which is set to be the image of an arrow.

To find the lattice of points for elements corresponding to one orientation of magnetisation, a Fresnel image is thresholded and cross-correlated with a thresholded image of an individual element, the "kernel", as shown in Fig 5.8a). The cross-correlation b) is subsequently thresholded to give the binary image in c), this gives the positions of all the horizontal elements with the same magnetisation as the kernel in Fig 5.8a). Fig 5.9 summarises the second stage, in which arrows are placed at every point of the lattice. Fig 5.9a) shows the convolution of the lattice with the motif; the convolution is thresholded so that a binary image of arrows is obtained, as in Fig 5.9b). By repeating the process from Fig 5.8a) to Fig 5.8b) for  $90^\circ$ ,  $180^\circ$  and  $270^\circ$  rotations of the kernel, all orientations of magnetisation are mapped. All four orientations of magnetisation are mapped in binary images that are then added

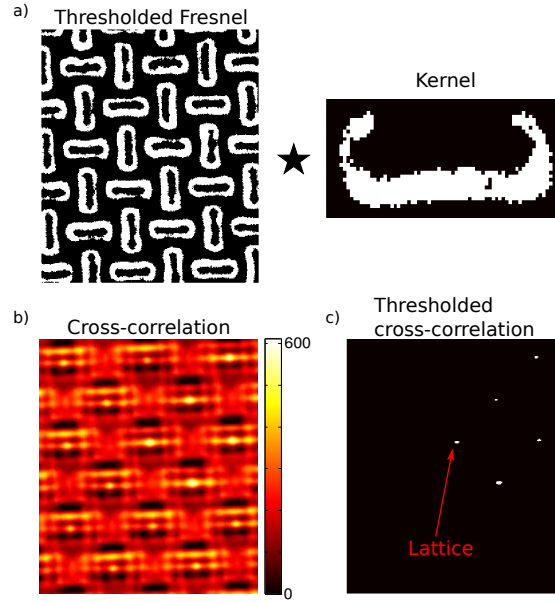


**Figure 5.8:** First step in processing of Fresnel images - finding a lattice for each magnetisation orientation. a) Thresholded Fresnel image and individual thresholded element are cross-correlated. By thresholding the b) cross-correlation gives the c) lattice of points.

together. By multiplying each binary image multiplied by different factors, the final image produced shows different magnetisation directions with different coloured arrows, as in Fig 5.9c).

The advantage of using Fresnel imaging, alongside the image processing routine, over DPC is in the speed of image acquisition. An example of a colour image obtained from DPC is shown in Fig 5.10 beside the bright field “sum” image. The colour image shows different orientations of magnetisation, defined by the inset colourwheel, corresponding to the elements in the sum image. While this is easily interpretable, it is unsuitable for collecting a series of images necessary for mapping the reversal of an entire array. Since DPC is a scanning technique, images are recorded serially, pixel-by-pixel, which means that images with sufficient resolution and signal-to-noise ratio can take a significant amount of time compared to Fresnel imaging, which records images in parallel. For example, a DPC images that measures  $1024 \times 1024$  pixels with a pixel dwell time of  $100 \mu\text{s}$  takes around 105 s to record, compared to just 2-3 s camera acquisition time for a Fresnel image and 10-15 s for the MATLAB script runtime (image size =  $4008 \times 2672$  pixels). In addition to this, as described in Chapter 2, JEM Toolbox can be used to control the stage tilt angle

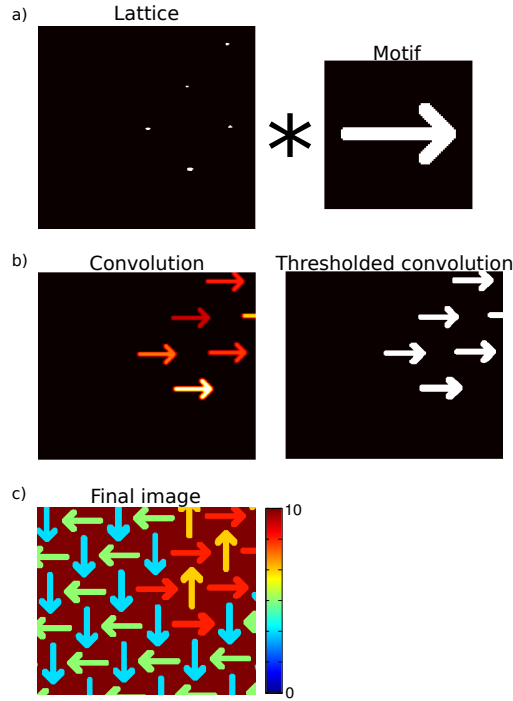


**Figure 5.9:** Convolution of an arrow with the lattice defined in Fig 5.8b). The binary images are shown in a) and the result of the convolution and the binary version are displayed in b). The final image is in c).

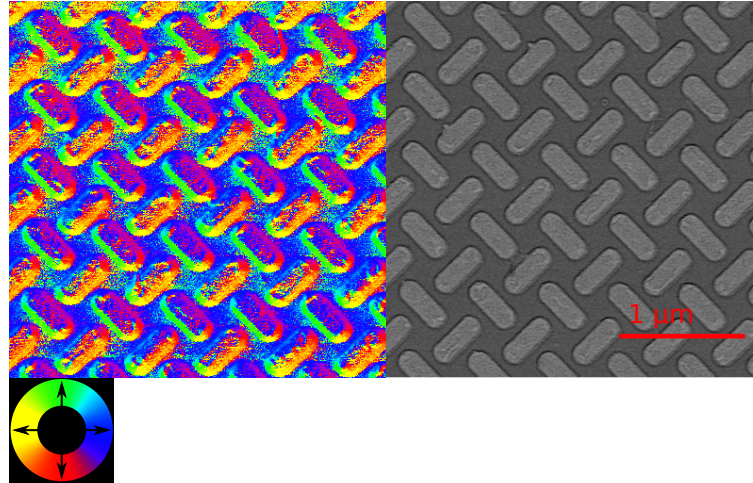


**Figure 5.10:** DPC colour image of an ASI array (left) alongside a bright field "sum" images. Different orientations of magnetisation within elements are directly mapped.

and camera of the JEOL ARM 200-CF microscope allowing quick acquisition of a series of images and thus the automation of in-situ magnetising experiments.

OOMMF simulations were used to calculate the energies of all vertex configurations, allowing a simple model of the array reversal to be proposed. To speed

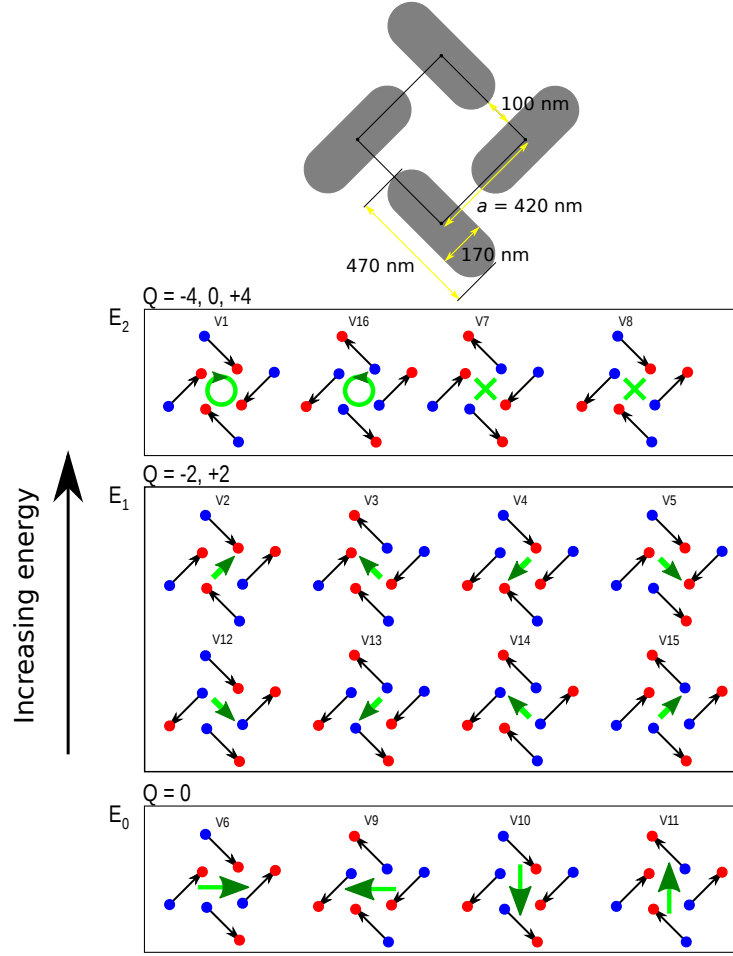


up simulations, the magnetisation in each element was fixed, resulting in uniform magnetisation for all elements, meaning that each one is like a single spin, with *zero* exchange energy. Given that all elements in a vertex are expected to form degenerate C (or S) states or flower states, the exclusion of this term is not expected to change the energy levels of each configuration.

### 5.3 Results

OOMMF simulations were used to calculate the energies of all the RS vertex configurations that are displayed in Fig 5.5. The vertices are displayed again in Fig 5.11, now arranged with increasing energy. There are three energy levels:  $E_0$  and  $E_3$  each have four degenerate states and  $E_2$  has eight degenerate states. Vertex net moment, represented by green arrows at the centre of vertices in Fig 5.11, decreases with increasing energy; the highest moment vertices represent the ground state and the vertices with zero moment are the highest energy states. The four degenerate states associated with the highest energy states are from two different classifications, both of which have zero moment; the vortex configuration, for which  $Q \pm 4$ , and the anti-vortex, which has  $Q = 0$ . This is perhaps surprising, the rotational character of the  $V_1$  and  $V_{16}$  resembles that of a vortex flux-closure state that forms in micron-sized magnetic discs (as studied in Chapter 4) to lower the magnetostatic energy. Given that there is no cost in exchange energy here, as with vortices in discs, this state could reasonably be expected to be the ground state.

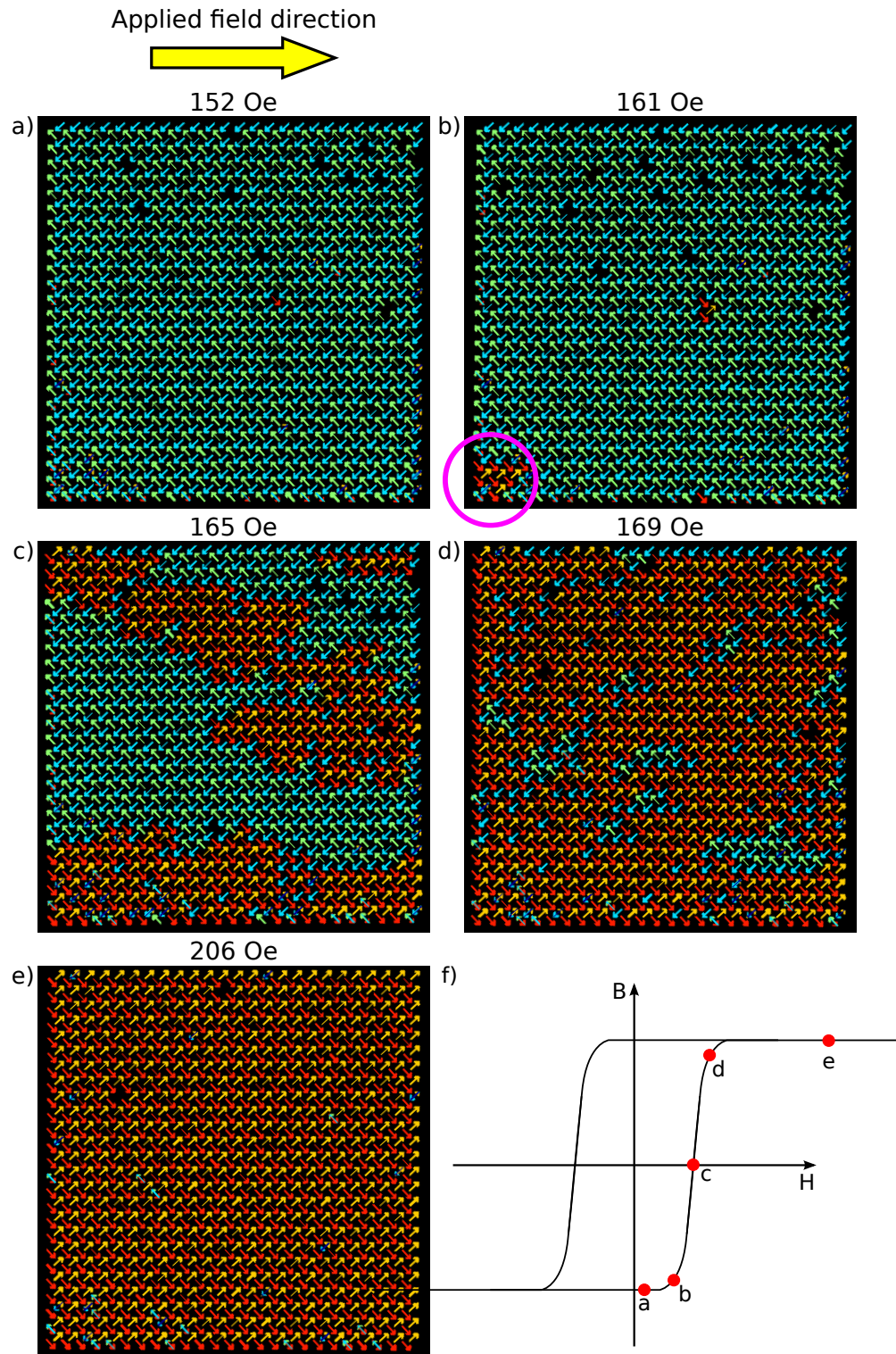
As  $E_3$  in Fig 5.11 shows, in contrast to the square ASI, different vertex types in the RS lattice can be degenerate. Table 5.1 lists the energies of the vertices displayed in Fig 5.11, normalised to the lowest energy,  $E_0$ ; for comparison, the energies of each vertex type in a square ASI of the same dimensions are shown in Table 5.2, again normalised to the energy of the lowest energy vertex. Table 5.1 shows that the energy differences between states of the RS lattice are very small, compared to those of the square ASI; this is unsurprising considering Fig 5.4b) and c), the square ASI has high and low energy states for adjacent elements corresponding to the elements pointing head-to-head or head-to-tail whereas states for RS adjacent



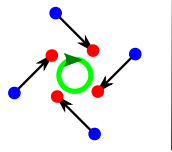
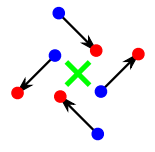
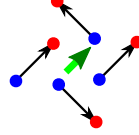
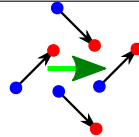
**Figure 5.11:** All vertex configurations ranked by energy. As energy increases, net moment associated with vertex configurations decreases.  $Q$  denotes the net charge at the centre of the vertex.

elements are degenerate. The simple  $45^\circ$  rotation that transforms the square ASI to the RS lattice significantly modifies the energies of the vertices and, thus, the energy landscape of the array.

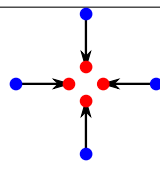
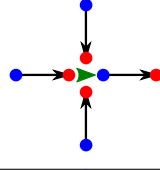
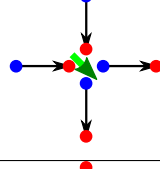
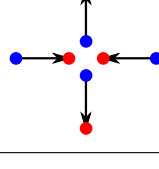
The procedure for the in-situ magnetising experiments was as follows: a large field (420 Oe) was applied at  $45^\circ$  to the axis of the elements *i.e.* along the  $x$  or  $y$  directions in Fig 5.6, so that the array was “saturated” along that direction. The field was incrementally reduced to zero, then applied in the opposite direction and increased until the array was saturated again. A typical sequence of images is shown in Fig 5.12; when the field is reduced to zero, the array is still uniformly magnetised, and only starts to reverse when a field is applied in the opposite direction. The reversal process occurs in several stages, illustrated schematically in Fig 5.13 where



**Figure 5.12:** Characteristic example of reversal of the array. Each stage is shown: a) uniform magnetisation; b) nucleation (circled) of a domain of opposite magnetisation; c) growth of domains aligned with the field; d) islands opposed to the field; and e) uniform magnetisation in the field direction. f) shows a sketched hysteresis loop with each image placed at an estimated position.

Vertex type	Vertices	Energy level	$E_n/E_0$
	$V_{1,7,8,16}$	$E_2$	1.0030
			
	$V_{2-5,12-15}$	$E_1$	1.0015
	$V_{6,9-11}$	$E_0$	1

**Table 5.1:** Table listing the calculated energies for RS vertices of the same dimensions as the fabricated array. Energies are normalised to the lowest energy,  $E_0$ .

Vertex type	Type	$E_n/E_0$
	4	1.2408
	3	1.0897
	2	1.0578
	1	1

**Table 5.2:** Table listing the calculated energies for square ASI vertices where the element dimensions are the same as the fabricated array with a minimum spacing of opposite elements of 180 nm. Energies are normalised to the lowest energy, which is the Type 1 vertex.

the outline of Fig 5.12 is shown with arrows to represent the direction of “uniform” magnetisation. There are several stages in the reversal process, shown in Fig 5.12

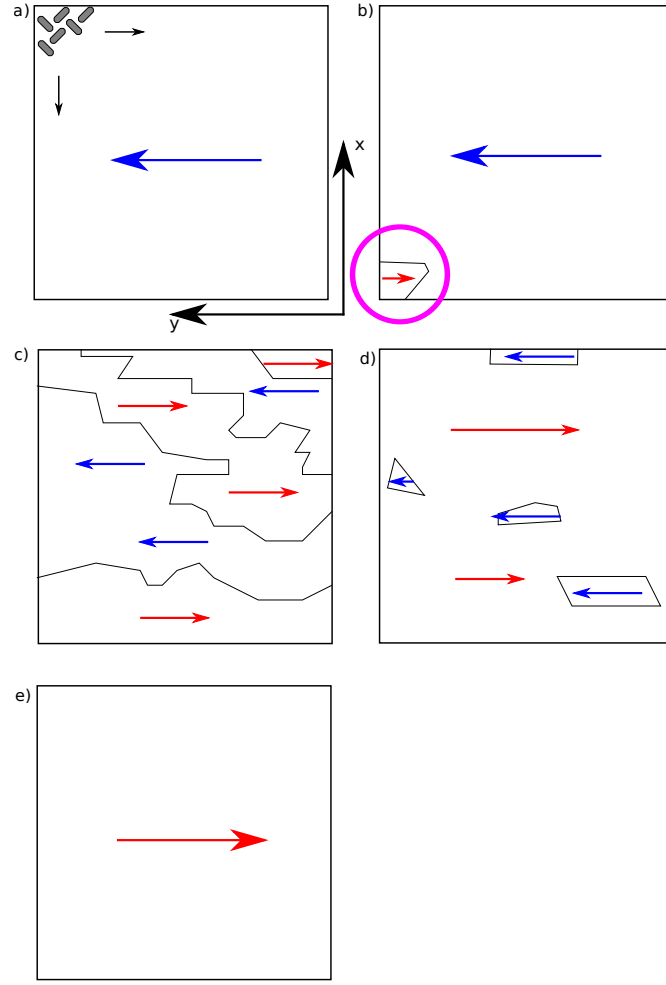


**Figure 5.13:** Outline of reversal sequence shown in Fig 5.12 highlighting each stage: a) uniform magnetisation; b) nucleation of a domain of opposite magnetisation; c) growth of domains aligned with the field; d) islands opposed to the field; and e) uniform magnetisation in the field direction.

and 5.13: a) the reversal starts after remanence, which is uniform magnetisation; b) domain(s) of opposite orientation are nucleated; c) the domains aligned with the field begin to grow; d) only small islands remain opposed to the field; and e) the array is uniformly magnetised in the direction of the field. The same reversal is observed for the situation when the field is applied in the opposite direction, suggesting that the hysteresis loop for this system is quite square, as sketched in Fig 5.12f). The estimated position of all stages of the array reversal in Fig 5.12a)-e) are marked on this hysteresis loop sketch. It should be noted that the same behaviour is observed when the field is applied  $90^\circ$  to the axis in Fig 5.12. From the observations in Fig 5.12, it appears that the array behaves like a ferromagnetic thin

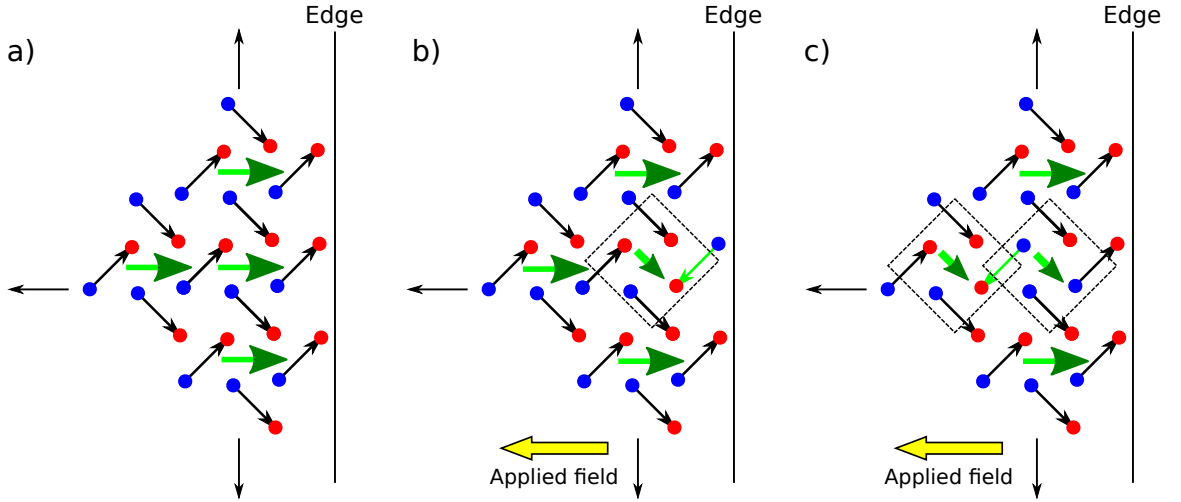


**Figure 5.14:** Images showing the nucleation process. a) shows a uniformly magnetised domain, which terminates at the vertical line, at zero field. b) and c) contrast the situations for a single spin flip, when a field is applied, at the edge and in the bulk. Outlines of boxes show higher energy vertices present after the spin flip.

film with in-plane magnetisation and strong in-plane biaxial anisotropy so that the magnetisation remains uniformly magnetised along the  $x - y$  directions. The “film” only begins to reverse when a field is applied in the opposite direction, nucleating a domain of opposite magnetisation. This is in contrast with a magnetic thin film of the same size ( $\sim 15 \times 15 \mu\text{m}^2$ ), which would form domain walls to minimise the magnetostatic energy.

The behaviour of the array at all stages in Fig 5.12 can be understood by considering the energies of the vertices, in Table 5.1 and Fig 5.11. The ground state vertices are those with a large moment that points in a horizontal or vertical direction. This explains why the array requires a field applied opposite to the moment direction to switch any of the vertices, the ground state of the entire array is to be uniformly magnetised along one of the axes. The fact that a ground state can easily be defined and experimentally found means that the RS array is not a frustrated system and, therefore, is not a true ASI array. In “real” square ASI systems, a ground state can be defined but is difficult to reach. Long range ground state order may be achieved through thermalisation [142, 145, 146], disrupting the ground state ordering are “excitations” [146] composed of higher energy Type 2 and 3 vertices. In fact, it is surprising that there are no equivalent excitations in the RS lattice consid-

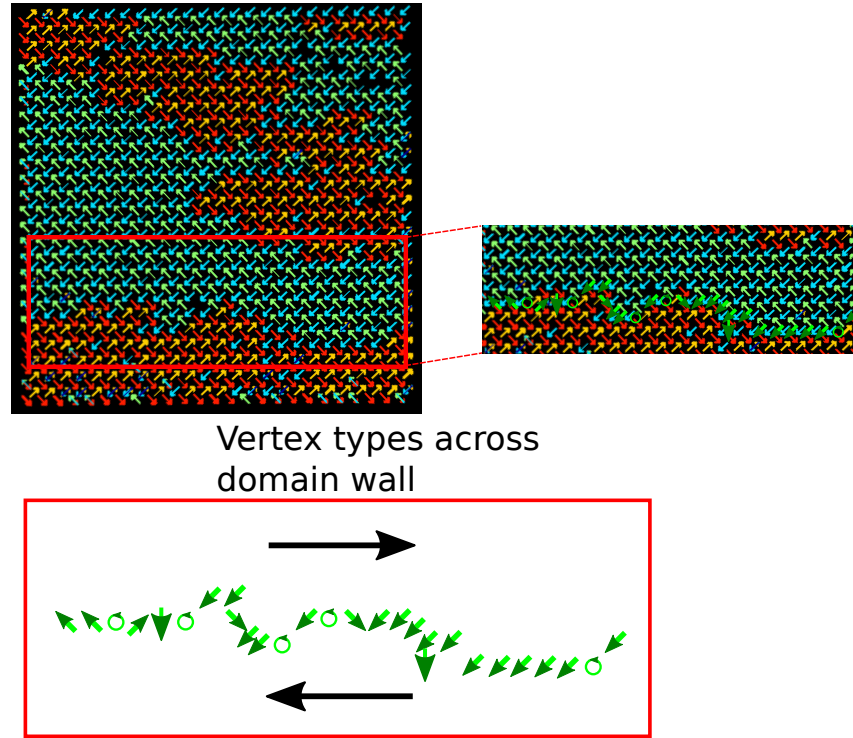


**Figure 5.15:** Identification of vertices at a DW from Fig 5.12c).

ering that the energies between vertices are relatively much closer than the square ASI, as in Tables 5.1 and 5.2. The ground state in the RS lattice is achieved simply by applying a simple dc field parallel to the array axis, which would ordinarily cause square ASI array to become “polarised” [149].

When an applied field is sufficiently strong, a domain of opposite magnetisation is nucleated. From experimental observations, this always occurs at the edge or corner of the array, as circled in Fig 5.12b) and Fig 5.13b). This feature of the nucleation process can be explained by Fig 5.14, which shows a section of the edge of a uniformly magnetised array. By applying a field as in b) and c), a single spin, coloured green, flips. In b) the spin flips at the edge, whereas the flip occurs in the bulk in c). The process in Fig 5.14b) is in lower energy than Fig 5.14c) because it produces fewer high energy vertices ( $E_{vert} > E_0$ ), outlined by boxes, which is simply down to the fact that the edge spin has fewer neighbours than the bulk spin. While this proposal explains the initial spin flip that starts the nucleation, smaller field steps in the experiment need to be used to image this behaviour.

The second stage of reversal, the growth of domains with opposite orientation,

follows nucleation. By definition, the sample now contains one or more domain walls (DWs). Given that the ground state of the array is uniform magnetisation, DWs must consist of high energy states. The configuration of one DW in Fig 5.12c) is shown in Fig 5.15, a section of the array is selected and the vertices along the DW are marked with the symbols that define the configuration of their moment. The DW is unlike that found in an ordinary magnetic thin film where DWs will have the same spin structure across their length, in the RS lattice the “wall” structure changes as it consists of different vertex types. While not numerous, high energy  $E_2$  vortex states form, it should be noted that there is no noticeable preferred chirality across all of the reversal experiments. The most numerous vertices in the DW are those of energy  $E_1$ , which can be understood by considering Fig 5.16. This shows two domains of opposite orientation, similar to the configuration in Fig 5.15, consisting of lowest energy ( $E_0$ ) vertices  $V_6$  and  $V_9$ ; rotation from one direction of magnetisation to another occurs by  $E_1$  vertices. By placing magenta arrows at the positions between vertices to show continuous magnetic moment, it can be seen that the magnetisation rotates in a manner similar to a Néel wall in thin films. By rotating in this way, the highest energy vertices are avoided. Random spin flips and the non-uniform DW structure may be responsible for the appearance of higher energy vertices, as found experimentally in Fig 5.15. Interestingly, head-to-head configurations of magnetisation are avoided, which supports the analogy of the array behaving like a thin film. The reason that head-to-head DWs are not as common as the Néel-like wall, shown in Figs 5.15 and 5.16, is illustrated by Fig 5.17, where two domains of opposite magnetisation have been set up to meet head-to-head. In this case, the spaces in between vertices at the DW position, shown by the magenta markers, are equivalent to the highest energy, zero moment configurations. Therefore, a head-to-head DW is less likely than the Néel-like wall.

The categorisation of vertices on the basis of net moment, as in Fig 5.5, allows the entire array to be classed as having “ferromagnetic” behaviour because the ground state vertices are configurations with net moment. The basis for which ferromagnetic alignment is the lowest energy state is dependent on the spacing of the elements,  $a$ , depicted in Fig 5.6a). Fig 5.18 considers the relative alignment of two parallel



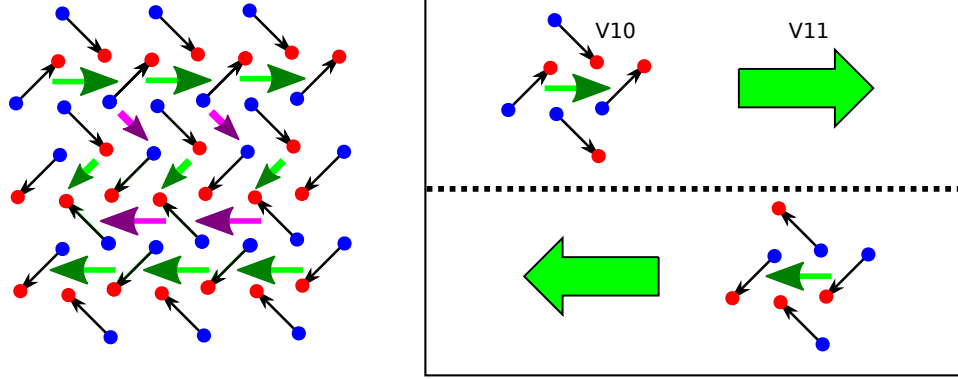


**Figure 5.16:** Illustration of most common DW configuration that occurs during the reversal of the array. The vertices at the DW position are from the  $E_1$  level. By drawing the moment in between vertices (magenta arrows), the DW can be seen to resemble a Néel wall in thin films.

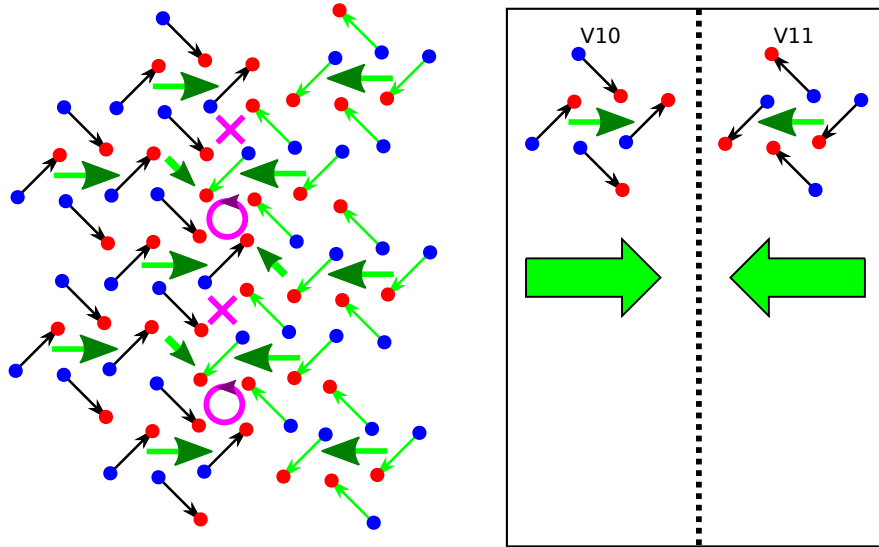


**Figure 5.17:** Representation of a head-to-head domain wall in which two domains with oppositely oriented magnetisation meet. In between the vertices (magenta annotations), configurations associated with  $E_2$  vertices are found *i.e.* high energy configurations.

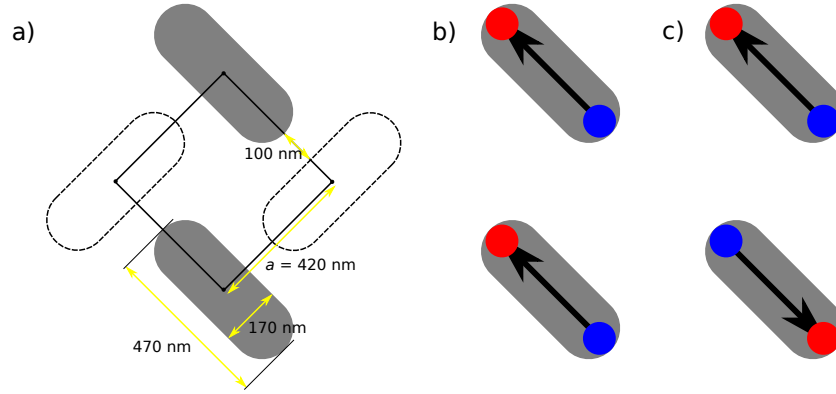


**Figure 5.18:** Geometry for which only two elements are simulated. Two different energy levels will be present, for parallel and anti-parallel alignment of spins.

elements from the RS vertex; a) shows this new geometry with a dashed line showing the outline of the two elements that have been removed. Fig 5.18b) and c) show two possible states, parallel and anti-parallel alignment of spins, respectively. The only interaction that is considered is the interaction between the magnetostatic energy arising from the poles at the elements' ends. For the value of  $a$  that corresponds to the fabricated array,  $a = 420$  nm, the parallel state in Fig 5.18b) is lower energy than anti-parallel alignment in c). This correlates with the experimentally observed ferromagnetic behaviour of the array. It would be expected that, for decreasing  $a$ , the favoured alignment of the two elements in Fig 5.18a) would switch from parallel to anti-parallel alignment *i.e.* ferromagnetic to anti-ferromagnetic ordering. The process of reducing  $a$  in Fig 5.18 is similar to moving two bar magnets closer together and observing that at a certain point they prefer to point anti-parallel to each other. OOMMF simulations were used to calculate the energies of both states with decreasing  $a$ , keeping the elements' dimensions the same as previous models and experiment. The difference in energy of the two states is plotted in Fig 5.19 for  $a = 330$ -420 nm, which corresponds to a minimum separation between elements of 10-100 nm. Negative regions of the graph correspond to the situation where parallel, ferromagnetic alignment is favoured; positive regions have a spacing where anti-ferromagnetic ordering is lower energy.

The vertex energies were calculated for a spacing of 20 nm, corresponding to a value of  $a = 340$  nm *i.e.* where anti-parallel alignment is favoured. The results

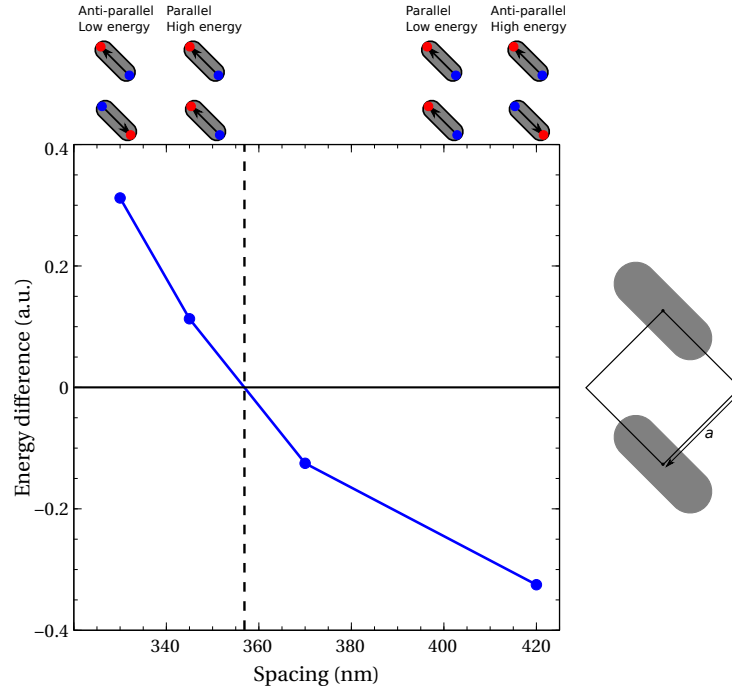


**Figure 5.19:** Energy difference of parallel alignment and anti-parallel alignment of vertical elements only in an RS array plotted as a function of corresponding element separation in a full vertex.

are shown in Fig 5.20, which shows that, compared to Fig 5.11, the lowest and highest energy levels have swapped positions - the ground state is now a configuration that prefers zero net moment. Therefore, by changing the spacing of the elements, the ground state of the array may be changed between ferromagnetic and anti-ferromagnetic. In addition, since the lowest energy state for anti-ferromagnetic ordering has two degenerate but non-equivalent vertex types, the possibility now exists for a system that exhibits frustration and is true ASI. Simply by fabricating elements that are closer together, the reversal properties of the array may be tuned as well as possible frustration, as the vertex energy is dependent on the spacing of the elements as demonstrated for a system consisting of parallel elements only [150]. An interesting situation arises at the point where the plot in Fig 5.19 crosses the x-axis, at this point ferromagnetic and anti-ferromagnetic alignment is just as likely. If an array of elements were fabricated so that  $a \sim 355$  nm, the prospect arises of an array that displays “superparamagnetic” behaviour, such an array would also display frustration and, thus, be a true ASI array.

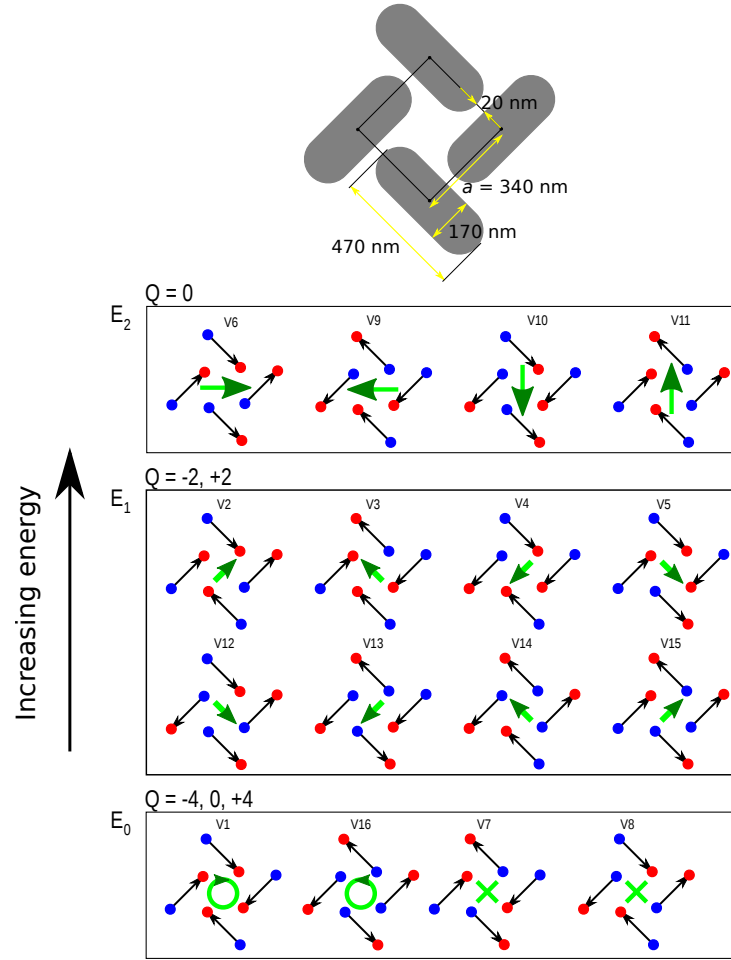


**Figure 5.20:** Calculated energy levels for vertices where the minimum spacing between elements is 20 nm, corresponding to  $a = 340$  nm.

## 5.4 Conclusions

In conclusion, by rotating the elements at a vertex of the square lattice artificial spin ice, a new arrangement of interacting nanomagnets can be created using electron beam lithography, called a rotated-square lattice. Using Lorentz microscopy, the reversal behaviour of the array can be characterised. It is found that the fabricated array behaves like a thin film with in-plane magnetisation with strong biaxial anisotropy so that vertices with net moment align along the axis of the array. This is explained by calculating the energy of all possible vertices, which shows that the lowest energy state is one with a net moment, therefore explaining the preferred uniform magnetisation. The ability to easily find a ground state means that the array cannot be described as artificial spin ice. Reversal occurs when a field of ap-

proximately 160 Oe is applied anti-parallel to the direction of net moment so that a “domain” of opposite moment is nucleated which then expands, forming domain walls similar to that in soft magnetic thin films and avoiding head-to-head moment, which involves the formation of high energy vertices.

The ferromagnetic ordering, due to the ground state vertices with net moment, is dependent on the elements’ spacing. By reducing the distance between two vertical elements, it was shown using OOMMF simulations that the lowest energy configuration became anti-parallel, rather than parallel, alignment of spins. This coincides with a change in the ground state vertices of the rotated-square lattice to configurations with no net moment. Therefore, by changing the spacing of the elements, their ordering can fundamentally change from ferromagnetic to anti-ferromagnetic. In addition, the zero net moment ground state contains degenerate but non-equivalent states, leading to the prediction that frustration may be present in this system, and thus the idea that frustration may be tuned.

# 6

## Conclusions and future work

Modification of the intrinsic and extrinsic properties of magnetic nanostructures leads to novel magnetic behaviour, exemplified by exotic spin textures. The ability to directly image the magnetisation configuration of these nanostructures provides an enormously powerful tool for understanding their behaviour when correlated with the results of micromagnetic simulations. Each of the studies presented in this thesis benefits from the use of Lorentz transmission electron microscopy (LTEM), a collection of techniques that generally provides high resolution magnetic imaging. The specialised JEOL ARM 200-F instrument within the Materials and Condensed Matter Physics group, with the scripting functionality provided by JEM Toolbox, allowed optimised and automated acquisition of LTEM images, as outlined in Chapter 2.

Three dimensional (3-D) head-to-head magnetic domain walls (DWs) were investigated in **Chapter 3**. Simulations of cylindrical nanowires and nanotubes were

used to characterise their complex spin structure and determine their stability across a range of radii. The key result from these simulations was the calculation of a phase diagram from which the stability/metastability of three different DW types were determined as a function of radius. In agreement with the literature, the transverse domain wall (TDW) was found to be stable for smaller radii and, above a critical radius of 20 nm, the Bloch point wall (BPW) was stable for wider wires. The less well-known asymmetric transverse domain wall (ATDW) was found to be a metastable state that stabilised above the critical radius. By analysing the surface spin states of the TDW and ATDW and calculating the surface charge of each, it was found that the ATDW is a chiral, less symmetric version of the TDW. In order to characterise 3-D DWs experimentally, square cross-section nanowires were fabricated using electron beam lithography. A combination of Fresnel and DPC imaging was used to identify three different DWs, two of which have not previously been identified: chain-link DW, a displaced vortex DW (DVDW) and a DW identified as a TDW or BPW. The stability of different DWs at the same dimensions leads to the conclusion that the DWs are metastable. The DVDW was imaged as an external applied field was applied and found to be strongly pinned at it propagated along the wire.

Several outstanding questions remain over results presented in Chapter 3 as well as opportunity for further work. The uncertainty over the identification of the last DW leads to one reason for the need for further experiments. By acquiring images at large positive and negative ( $\pm 30^\circ$ ) tilt angles and comparing with simulated images, this can be identified as a BPW or TDW. In addition, the chain-link DW was identified using Fresnel but not DPC imaging; it is likely that it has a 3-D structure but DPC imaging, as well as images taken at large positive and negative tilt angles, could be used to confirm this and aid in a full characterisation of its structure. Further experiments are required to fully characterise the pinning behaviour of the DVDW, in particular whether the pinning behaviour changes with reduced edge roughness and the pinning/depinning behaviour at a deliberately patterned pinning site such as a notch or anti-notch. Similarly, the behaviour of the chain-link and BPW/TDW under an applied field could be characterised; given that their structure

is less extended than the DVDW, they may be less susceptible to pinning. An understanding of the dynamic behaviour of 3-D DWs is essential if they are to be used in devices such as racetrack memory, in particular their motion under spin-polarised current. This is expected to be important given the potential for 3-D device architectures made possible through novel fabrication techniques [85, 151].

**Chapter 4** investigated interface-induced Dzyaloshinskii-Moriya interaction (IDMI) in soft magnetic thin films, with particular focus on experimental detection and determination of the magnitude of the effective strength,  $D$ . Micromagnetic simulations were used to model the IDMI in micron-sized discs that support vortex spin states, since the IDMI is expected to be most evident when the magnetisation points out-of-plane. Simulations found that increasing IDMI caused the magnetisation around the vortex core to become more divergent and caused the core to be more easily expelled from the disc. Automated in-situ magnetising experiments in Fresnel mode were used to image the vortex core and thus determine the vortex expulsion fields of Py/Pt and a control Py/Cu discs, which allowed a value of  $D = 0.5 \text{ mJm}^{-2}$  to be proposed by comparing with simulation results, assuming that other effects are absent or negligible.

While measuring the vortex expulsion field provided a measure of  $D$ , the viability of other experimental techniques were assessed that may provide alternative methods. The increased charge around the core caused by IDMI was shown to change the H-field distribution above the core, which is likely to be detectable by magnetic force microscopy (MFM); due to time constraints, this experiment was not attempted. In addition, the DPC mode of LTEM could be used to measure the width of the core, which becomes wider with increasing  $D$ . This may be challenging due to difficulties that arise from noise from diffraction contrast; however, the development pixelated detector systems in magnetic imaging in TEM can remove this problem, having been shown to remove diffraction contrast to a greater degree than modified DPC [152].

Recently, it was shown that the IDMI was detectable in Py/Pt bilayers using Brillouin light scattering to measure non-reciprocal spin wave dispersion [153]. It was later demonstrated using the same method that the value of  $D$  varied with the thickness of the Py film, with increasing  $D$  observed for thinner films [154]. The



value measured in this work is around an order of magnitude less than measured in Chapter 4 using the vortex expulsion field. In light of this outcome, the results in Chapter 4 should therefore be tested by varying the thickness of the Py layer and thus confirm whether the effect on the vortex expulsion field is solely (or mainly) due to IDMI.

The presence of the IDMI may also have consequences for memory devices based on vortices [155] as the expulsion field is reduced. While the strength of  $D$  reported here results in a small reduction, IDMI can be tuned by changing the material used in the non-magnetic layer and varying the thickness [23, 24]. In terms of other technological applications, the fact that Walker breakdown is predicted to be suppressed for DWs in perpendicularly magnetised films is advantageous for devices based on DW motion such as racetrack memory [71]. This dynamic behaviour has not been modelled for soft magnetic materials, though presents an interesting problem given the effect IDMI has on vortex spin states, since Walker breakdown occurs in planar nanowires through the nucleation of an anti-vortex structure. The IDMI could suppress the anti-vortex nucleation or modify its structure and, thus, its dynamic behaviour.

The work in **Chapter 5** was the characterisation of an array of single domain nanomagnets based on square lattice artificial spin ice (ASI). By rotating the elements of the square ASI about their centre, a rotated square (RS) lattice was designed whose vertex arrangements were expected to have a more extensive degeneracy compared to the square ASI. An RS lattice array was fabricated using electron beam lithography and its switching behaviour under an applied field was determined by automated in-situ LTEM magnetising experiments. From this experiment, it was determined that the array behaved as a ferromagnetic thin film with strong cubic anisotropy, directed parallel to the array edges. The switching behaviour of the array is characterised by the nucleation of a “domain” of opposite magnetisation that grows with increasing field until the array is uniformly magnetised in the opposite direction. This behaviour of the RS lattice is in complete contrast to the anti-ferromagnetic ground state of square ASI. Its character was also contrary to expectations, which held that a vertex configuration resembling a

flux-closure vortex state was a likely ground state vertex. While this “vortex” state was imaged it was not a common vertex type. OOMMF simulations of all vertex configurations and showed that the energy of the vertices increased with decreasing net moment, therefore favouring the vertices with large net moment and causing anti-ferromagnetic vertices to be high energy configurations. The fact that a ground state could easily be defined and found means that the array was not a frustrated system and, therefore, not a true ASI array.

Further OOMMF simulations showed that the energy of the vertices depended on the lattice constant,  $a$ , suggesting a direction for future experiments. Below a critical separation, anti-parallel alignment of elements is energetically favourable over parallel alignment. The vertex energies were calculated below this critical value, which showed that the lowest energy vertices were anti-ferromagnetic, zero moment arrangements. In addition, because the ground state consists of two degenerate vertex types, the array could also display frustration. Designing the array such that  $a$  is at the critical value opens the possibility of degenerate ferromagnetic and anti-ferromagnetic vertices, which could potentially lead to an effectively superparamagnetic state.

In the future, research will focus on magnetic material systems with potential technological applications. With this in mind, the results in this thesis provide a base for future work. Evidence of this can be seen in the most recent version of racetrack memory [156], a device which incorporates the two themes from Chapter 3 and 4 *i.e.* DWs in magnetic nanowires and IDMI. Now the DWs in perpendicularly magnetised nanostrips provide a means for storing information; however, this is only possible with Néel DWs stabilised through the DMI, which demonstrates the potential for it to control magnetic spin structure. In the future, data storage devices based on a racetrack memory system architecture could potentially be DMI stabilised spin textures in thin films such as skyrmions [157, 158]. This has the potential for increased reliability [159], superior storage density and reduced power consumption [160], in addition to a 3-D architecture.

The nanomagnet array in Chapter 5 shows another geometry from which it may be possible to create a microwave device known as a magnonic crystal [141, 161],

the magnetic analogue of a photonic crystal. The magnonic crystal potentially has the advantage of a reprogrammable band structure since it relies on the dispersion of spin waves dynamics that depend, for example, on the magnetic state. The geometry in Chapter 5 is interesting in this respect as its ground states may be altered, depending on the spacing of the elements.

# Bibliography

- [1] A. Fert, V. Cros, and J Sampaio. Skyrmions on the track. *Nature nanotechnology*, 8:152, 2013.
- [2] P. Weiss. L'hypothèse du champ moléculaire et la propriété ferromagnétique. *J. de Phys.*, 6:661, 1907.
- [3] W. Heisenberg. Zur quantenmechanik ii. *Z. Phys.*, 38:411, 1926.
- [4] W. Heisenberg. Zur theorie des ferromagnetismus. *Z. Phys.*, 49:619, 1928.
- [5] W. Pauli. Über den zusammenhang des abschlusses der elektronengruppen im atom mit der komplexstruktur der spektren. *Z. Physik*, 31:765, 1925.
- [6] S. Blundell. *Magnetism in Condensed Matter*. Oxford University Press, 2001.
- [7] E.C. Stoner. Collective electron ferromagnetism. *Proc. Roy. Soc.*, A165:372, 1938.
- [8] E.C. Stoner. Collective electron ferromagnetism. II. energy and specific heat. *Proc. Roy. Soc.*, A169:339, 1939.
- [9] A.H. Morrish. *The Physical Principles of Magnetism*. J. Wiley and Sons, Inc., 1 edition, 1965.
- [10] J. Coey. *Magnetism and Magnetic Materials*. Cambridge University Press, 1 edition, 2009.

- [11] A. Aharoni. *Introduction to the theory of ferrromagnetism*. Oxford University Press, 1996.
- [12] A Hubert and R. Schäfer. *Magnetic domains*. Springer, 1998.
- [13] C. H. Marrows. Spin-polarised currents and magnetic domain walls. *Advances in Physics*, 54(8):585–713, December 2005.
- [14] I. Dzyaloshinskii. A thermodynamic theory of “weak” ferromagnetism of antiferromagnetics. *J. Phys. Chem. Solids*, 4:241–255, 1958.
- [15] T. Moriya. Anisotropic superexchange interaction and weak ferromagnetism. *Phys. Rev.*, 120:91–98, 1960.
- [16] P.W. Anderson. New approach to the theory of superexchange interactions. *Phys. Rev.*, 115:2–13, 1958.
- [17] A. Fert and Peter M. Levy. Role of anisotropic exchange interactions in determining the properties of spin-glasses. *Phys. Rev. Lett.*, 1980.
- [18] Y. Togawa, Y. Kousaka, S. Nishihara, K. Inoue, J. Akimitsu, A. S. Ovchinnikov, and J. Kishine. Interlayer magnetoresistance due to chiral soliton lattice formation in hexagonal chiral magnet  $\text{CrNb}_3\text{S}_6$ . *Phys. Rev. Lett.*, 111:197204, 2013.
- [19] A Crépieux and C Lacroix. DzyaloshinskyMoriya interactions induced by symmetry breaking at a surface. *J. Magn. Magn. Mater.*, 182:341–349, 1998.
- [20] A. Fert. Magnetic and transport properties of metallic multilayers. *Mater. Sci. Forum*, 59-60:439–480, 1990.
- [21] M. Bode, M. Heide, K. von Bergmann, P. Ferriani, S. Heinze, G. Bihlmayer, A. Kubetzka, O. Pietzsch, S. Blugel, and R. Wiesendanger. Chiral magnetic order at surfaces driven by inversion asymmetry. *Nature*, 447:190–193, 2007.
- [22] André Thiaville, Stanislas Rohart, Émilie Jué, Vincent Cros, and Albert Fert. Dynamics of Dzyaloshinskii domain walls in ultrathin magnetic films. *Europhys. Lett.*, 100(5):57002, 2012.

- [23] Soong-Geun Je, Duck-Ho Kim, Sang-Cheol Yoo, Byoung-Chul Min, Kyung-Jin Lee, and Sug-Bong Choe. Asymmetric magnetic domain-wall motion by the Dzyaloshinskii-Moriya interaction. *Phys. Rev. B*, 88:214401, 2013.
- [24] A. Hrabec, N. A. Porter, A. Wells, M. J. Benitez, G. Burnell, S. McVitie, D. McGrouther, T. A. Moore, and C. H. Marrows. Measuring and tailoring the Dzyaloshinskii-Moriya interaction in perpendicularly magnetized thin films. *Phys. Rev. B*, 90:020402, 2014.
- [25] M.A. Ruderman and C. Kittel. Indirect exchange coupling of nuclear magnetic moments by conduction electrons. *Phys. Rev.*, 96:99, 1954.
- [26] T. Kasuya. A theory of metallic ferro- and antiferromagnetism on zener’s model. *Prog. Theor. Phys.*, 16:4558, 1956.
- [27] K. Yosida. Magnetic properties of CuMn alloys. *Phys. Rev.*, 106:893, 1957.
- [28] M.D. Stiles. Interlayer exchange coupling. *J. Magn. Magn. Mater.*, 200(13):322 – 337, 1999.
- [29] W.H. Meiklejohn and C.P. Bean. New magnetic anisotropy. *Phys. Rev.*, 102:1413, 1956.
- [30] R. Skomski. Nanomagnetism. *J. Phys. Condens. Matter.*, 15:841–896, 2003.
- [31] Harrison W. Fuller and Murray E. Hale. Determination of magnetization distribution in thin films using electron microscopy. *J. Appl. Phys.*, 31(2):238–248, 1960.
- [32] M.J. Donahue and R.D. McMichael. Exchange energy representations in computational micromagnetics. *Phys. B: Cond. Matter*, 233(4):272–278, 1997.
- [33] Thomas Fischbacher, Matteo Franchin, Giuliano Bordignon, and Hans Fangohr. A Systematic Approach to Multiphysics Extensions of Finite-Element-Based Micromagnetic Simulations: Nmag. *IEEE. Trans. Magn.*, 43:2896–2898, 2007.

- [34] Arne Vansteenkiste, Jonathan Leliaert, Mykola Dvornik, Mathias Helsen, Felipe Garcia-Sanchez, and Bartel Van Waeyenberge. The design and verification of mumax3. *AIP Advances*, 4(10):–, 2014.
- [35] L.D. Landau and E. Lifshitz. On the theory of the dispersion of magnetic permeability in ferromagnetic bodies. *Phys. Z. Sowjetunion*, 8:153, 1935.
- [36] N.D. Mermin. The topological theory of defects in ordered media. *Rev. Mod. Phys.*, 51(3):591, 1979.
- [37] E. E. Huber, D. O. Smith, and J. B. Goodenough. Domain wall structure in permalloy films. *J. Appl. Phys.*, 29(3):294–295, 1958.
- [38] T. Shinjo. Magnetic vortex core observation in circular dots of permalloy. *Science*, 289:930–932, 2000.
- [39] Yoshinobu Nakatani, André Thiaville, and Jacques Miltat. Head-to-head domain walls in soft nano-strips: a refined phase diagram. *J. Magn. Magn. Mater.*, 290-291:750–753, April 2005.
- [40] L.J. Heyderman and R.L. Stamps. Artificial ferroic systems: novel functionality from structure, interactions and dynamics. *J. Phys. Condens. Matter*, 25(36):363201, 2013.
- [41] E Ruska. Nobel lecture. The development of the electron microscope and of electron microscopy. *Biosci. Rep.*, 7:607–629, 1987.
- [42] L. de Broglie. La nouvelle dynamique des quanta. *Annalen der Physik*, 3.3(22), 1925.
- [43] Rolf Erni, Marta D. Rossell, Christian Kisielowski, and Ulrich Dahmen. Atomic-resolution imaging with a sub-50-pm electron probe. *Phys. Rev. Lett.*, 102:096101, 2009.
- [44] David B Williams and Barry C Carter. *Transmission Electron Microscopy: A Textbook for Materials Science*, volume V1-V4. 2009.

- [45] L. Reimer. *Transmission Electron Microscopy*. Springer, 5 edition, 2008.
- [46] Knut Urban, Bernd Kabius, Max Haider, and Harald Rose. A way to higher resolution: spherical-aberration correction in a 200 kV transmission electron microscope. *Journal of Electron Microscopy*, 48(6):821–826, 1999.
- [47] M. Ali Omar. *Elementary Solid State Physics*. Pearson Education, 5th edition edition, 2005.
- [48] JN Chapman, A.B. Johnston, L.J. Heyderman, S. McVitie, W.A.P. Nicholson, and B. Bormans. Coherent magnetic imaging by TEM. *IEEE. Trans. Magn.*, 30:4479–4484, 1994.
- [49] J.N Chapman and M.R Scheinfein. Transmission electron microscopies of magnetic microstructures. *J. Magn. Magn. Mater.*, 200(1-3):729–740, October 1999.
- [50] Y Aharonov and D Bohm. Significance of electromagnetic potentials in the quantum theory. *Phys. Rev.*, 1(3), 1959.
- [51] S McVitie and G S White. Imaging Amperian currents by Lorentz microscopy. *Journal of Physics D: Applied Physics*, 37(2):280–288, January 2004.
- [52] S McVitie and M Cushley. Quantitative Fresnel Lorentz microscopy and the transport of intensity equation. *Ultramicroscopy*, 106(4-5):423–31, March 2006.
- [53] D. McGrouther, S. McVitie, J. N. Chapman, and a. Gentils. Controlled domain wall injection into ferromagnetic nanowires from an optimized pad geometry. *appl. phys. lett.*, 91(2):022506, 2007.
- [54] Duc-The Ngo and Stephen McVitie. Visualization of vortex core polarity in NiFe nanodots by tilted Fresnel images. *Ultramicroscopy*, 111(8):1276–85, July 2011.
- [55] L. Bogart, D. Atkinson, K. OShea, D. McGrouther, and S. McVitie. Dependence of domain wall pinning potential landscapes on domain wall chirality



- and pinning site geometry in planar nanowires. *Phys. Rev. B*, 79(5):054414, February 2009.
- [56] Stephen McVitie, Gordon S. White, Jamie Scott, Patrick Warin, and John N. Chapman. Quantitative imaging of magnetic domain walls in thin films using lorentz and magnetic force microscopies. *J. Appl. Phys.*, 90(10):5220–5227, 2001.
- [57] J.N. Chapman, I.R. McFadyen, and S. McVitie. Modified differential phase contrast Lorentz microscopy for improved imaging of magnetic structures. *IEEE Trans. Magn.*, 26(5), 1990.
- [58] K.J. O’Shea. *Putting a leash on the domain wall: A TEM investigation into the controlled behaviour of domain walls in ferromagnetic nanostructures*. PhD thesis, University of Glasgow, 2010.
- [59] D.F. Kyser. Spatial resolution limits in electron beam nanolithography. *J. Vac. Sci. Technol. B.*, 1:1391, 1983.
- [60] C. Brownlie. *A TEM Investigation of Controlled Magnetic Behaviour in Thin Ferromagnetic Films*. PhD thesis, University of Glasgow, 2007.
- [61] L. D. Jackel, R. E. Howard, P. M. Mankiewich, H. G. Craighead, and R. W. Epworth. Beam energy effects in electron beam lithography: The range and intensity of backscattered exposure. *appl. phys. lett.*, 45(6):698–700, 1984.
- [62] M.A. Basith. *A TEM investigation of patterned ferromagnetic nanostructures by lithographic techniques*. PhD thesis, University of Glasgow, 2011.
- [63] Steve Reyntjens and Robert Puers. A review of focused ion beam applications in microsystem technology. *J. Micromech. Microeng.*, 11(4):287, 2001.
- [64] G. Binnig, C. F. Quate, and Ch. Gerber. Atomic force microscope. *Phys. Rev. Lett.*, 56:930–933, Mar 1986.

- [65] U. Hartmann, T. Göddenhenrich, and C. Heiden. Magnetic force microscopy: Current status and future trends. *J. Magn. Magn. Mater.*, 101:263 – 270, 1991.
- [66] P.R. Wilmott and J.R. Huber. Pulsed laser vaporization and deposition. *Rev. Mod. Phys.*, 72.1:315, 2000.
- [67] David P. Norton. Synthesis and properties of epitaxial electronic oxide thin-film materials. *Materials Science and Engineering: R: Reports*, 43(5-6):139–247, March 2004.
- [68] Hans-Ulrich Krebs and Olaf Bremert. Pulsed laser deposition of thin metallic alloys. *appl. phys. lett.*, 62:2341, 1993.
- [69] J. Shen, Zheng Gai, and J. Kirschner. *Growth and magnetism of metallic thin films and multilayers by pulsed-laser deposition*, volume 52. 2004.
- [70] Stuart S P Parkin, Masamitsu Hayashi, and Luc Thomas. Magnetic domain-wall racetrack memory. *Science*, 320(5873):190–4, April 2008.
- [71] Masamitsu Hayashi, Luc Thomas, Rai Moriya, Charles Rettner, and Stuart S P Parkin. Current-controlled magnetic domain-wall nanowire shift register. *Science*, 320(5873):209–11, April 2008.
- [72] D.A. Allwood, G. Xiong, C.C. Faulkner, D. Atkinson, D. Petit, and R.P. Cowburn. Magnetic domain-wall logic. *Science*, 309:1688–92, 2005.
- [73] N. L. Schryer and L. R. Walker. The motion of  $180^\circ$  domain walls in uniform DC magnetic fields. *J. Appl. Phys.*, 45:5406, 1974.
- [74] Y. Nakatani, A. Thiaville, and J. Miltat. Faster magnetic walls in rough wires. *Nat. Mater.*, 2:521, 2003.
- [75] M. Yan, A. Kákay, S. Gliga, and R. Hertel. Beating the Walker Limit with Massless Domain Walls in Cylindrical Nanowires. *Phys. Rev. Lett.*, 104:057201, 2010.

- [76] M. Yan and C. Andreas. Fast domain wall dynamics in magnetic nanotubes: Suppression of Walker breakdown and Cherenkov-like spin wave emission. *Appl. Phys. Lett.*, 99:122505, 2011.
- [77] Ming Yan, Christian Andreas, Attila Kákay, A.kay, Felipe García-Sánchez, and Riccardo Hertel. Chiral symmetry breaking and pair-creation mediated Walker breakdown in magnetic nanotubes. *Appl. Phys. Lett.*, 100:252401, 2012.
- [78] X. Liu, J. N. Chapman, S. McVitie, and C. D. W. Wilkinson. Reversal mechanisms and metastable states in magnetic nanoelements. *J. Appl. Phys.*, 96(9):5173, 2004.
- [79] P. Landeros, O. Suarez, A. Cuchillo, and P. Vargas. Equilibrium states and vortex domain wall nucleation in ferromagnetic nanotubes. *Phys. Rev. B*, 79:024404, 2009.
- [80] R. Hertel. Computational micromagnetism of magnetization processes in nickel nanowires. *J. Magn. Magn. Mater.*, 249:251–256, 2002.
- [81] P. Landeros, S. Allende, J. Escrig, E. Salcedo, D. Altbir, and E. E. Vogel. Reversal modes in magnetic nanotubes. *Appl. Phys. Lett.*, 90:102501, 2007.
- [82] J.A. Otálora, J.A.. López-López, P. Landeros, P. Vargas, and A.S. Núñez. Breaking of chiral symmetry in vortex domain wall propagation in ferromagnetic nanotubes. *J. Magn. Magn. Mater.*, 341:86–92, 2013.
- [83] Daihua Zhang, Zuqin Liu, Song Han, Chao Li, and Bo Lei. Magnetite (Fe<sub>3</sub>O<sub>4</sub>) core-shell nanowires: Synthesis and magnetoresistance. *Nano Lett.*, pages 1–5, 2004.
- [84] Y.-L. Chueh, M.-W. Lai, J.-Q. Liang, L.-J. Chou, and Z. L. Wang. Systematic Study of the Growth of Aligned Arrays of  $\alpha$ -Fe<sub>2</sub>O<sub>3</sub> and Fe<sub>3</sub>O<sub>4</sub> Nanowires by a VaporSolid Process. *Adv. Func. Mater.*, 16:2243–2251, 2006.
- [85] Amalio Fernández-Pacheco, Luis Serrano-Ramón, Jan M. Michalik, M. Riccardo Ibarra, José M. De Teresa, Liam O’Brien, Dorothée Petit, Jihyun Lee,

- and Russell P. Cowburn. Three dimensional magnetic nanowires grown by focused electron-beam induced deposition. *Sci. Rep.*, 3:1492, 2013.
- [86] M Zheng, R Skomski, Y Liu, and D J Sellmyer. Magnetic hysteresis of Ni nanowires. *J. Phys. Condens. Matter*, 12(30):L497, 2000.
- [87] J. Bao, C. Tie, Z. Xu, Q. Zhou, D. Shen, and Q. Ma. Template synthesis of an array of nickel nanotubules and its magnetic behavior. *Adv. Mater.*, 13:1631–1633, 2001.
- [88] C. A. Ross, M. Hwang, M. Shima, J. Y. Cheng, M. Farhoud, T. A. Savas, Henry I. Smith, W. Schwarzacher, F. M. Ross, M. Redjdal, and F. B. Humphrey. Micromagnetic behavior of electrodeposited cylinder arrays. *Phys. Rev. B*, 65:144417, 2002.
- [89] Y. C. Sui, R. Skomski, K. D. Sorge, and D. J. Sellmyer. Nanotube magnetism. *Appl. Phys. Lett.*, 84:1525–1527, 2004.
- [90] M P Proenca, K J Merazzo, L G Vivas, D C Leitao, C T Sousa, J Ventura, J P Araujo, and M Vazquez. Co nanostructures in ordered templates: comparative forc analysis. *Nanotechnology*, 24:475703, 2013.
- [91] M P Proenca, K J Merazzo, L G Vivas, D C Leitao, C T Sousa, J Ventura, J P Araujo, and M Vazquez. Co nanostructures in ordered templates: comparative FORC analysis. *Nanotechnology*, 24:475703, 2013.
- [92] L G Vivas, Yu P Ivanov, D G Trabada, M P Proenca, O Chubykalo-Fesenko, and M Vzquez. Magnetic properties of co nanopillar arrays prepared from alumina templates. *Nanotechnology*, 24(10):105703, 2013.
- [93] M.-T. Chang, L.-J. Chou, C.-H. Hsieh, Y.-L. Chueh, Z. L. Wang, Y. Murakami, and D. Shindo. Magnetic and Electrical Characterizations of Half-Metallic Fe<sub>3</sub>O<sub>4</sub> Nanowires. *Adv. Mater.*, 19(17):2290–2294, September 2007.
- [94] Azadeh Akhtari-Zavareh, L. P. Carignan, A. Yelon, D. Mnard, T. Kasama, R. Herring, R. E. Dunin-Borkowski, M. R. McCartney, and K. L. Kavanagh.

- Off-axis electron holography of ferromagnetic multilayer nanowires. *J. Appl. Phys.*, 116(023902), 2014.
- [95] Y. Henry, K. Ounadjela, L. Piraux, S. Dubois, J.-M. George, and J.-L. Duval. Magnetic anisotropy and domain patterns in electrodeposited cobalt nanowires. *Eur. Phys. J. B.*, 20:35–54, 2001.
- [96] Yu. P. Ivanov, L. G. Vivas, A. Asenjo, A. Chuvilin, O. Chubykalo-fesenko, and M. Vázquez. Magnetic structure of a single-crystal hcp electrodeposited cobalt nanowire. *Europhys. Lett.*, 102:17009, 2013.
- [97] A. Buchter, J. Nagel, D. Ruffer, F. Xue, D. P. Weber, O. F. Kieler, T. Weimann, J. Kohlmann, a. B. Zorin, E. Russo-Averchi, R. Huber, P. Berberich, a. Fontcuberta I Morral, M. Kemmler, R. Kleiner, D. Koelle, D. Grundler, and M. Poggio. Reversal mechanism of an individual Ni nanotube simultaneously studied by torque and SQUID magnetometry. *Phys. Rev. Lett.*, 111:1–5, 2013.
- [98] T Wang, Y Wang, Y Fu, T Hasegawa, F S Li, H Saito, and S Ishio. A magnetic force microscopy study of the magnetic reversal of a single Fe nanowire. *Nanotechnology*, 20:105707, 2009.
- [99] Nicolas Biziere, Christophe Gatel, Rémy Lassalle-Balier, Marie Claude Clochard, Jean Eric Wegrowe, and Etienne Snoeck. Imaging the fine structure of a magnetic domain wall in a Ni nanocylinder. *Nano Lett.*, 13:2053–7, 2013.
- [100] Yoshinobu Nakatani and André Thiaville. Domain-Wall Dynamics in Nanowires and Nanostrips. In *Spin Dynamics in Confined Magnetic Structures III Topics in Applied Physics Volume 101*. 2006.
- [101] C. Brownlie, S. McVitie, J. N. Chapman, and C. D. W. Wilkinson. Lorentz microscopy studies of domain wall trap structures. *J. Appl. Phys.*, 100:033902, 2006.
- [102] J. d’Albuquerque e Castro, D. Altbir, J. Retamal, and P. Vargas. Scaling

- Approach to the Magnetic Phase Diagram of Nanosized Systems. *Phys. Rev. Lett.*, 88:237202, 2002.
- [103] P. Landeros, J. Escrig, D. Altbir, D. Laroze, J. dAlbuquerque e Castro, and P. Vargas. Scaling relations for magnetic nanoparticles. *Phys. Rev. B*, 71:094435, 2005.
- [104] J. Escrig, P. Landeros, D. Altbir, and E.E. Vogel. Effect of anisotropy in magnetic nanotubes. *J. Magn. Magn. Mater.*, 310:2448–2450, 2007.
- [105] N. Wiese, S. McVitie, J. N. Chapman, A. Capella-Kort, and F. Otto. On the scaling behaviour of cross-tie domain wall structures in patterned NiFe elements. *Europhys. Lett.*, 80:57003, 2007.
- [106] A. Halder and K. S. Buchanan. Magnetic antivortex formation in pound-key-like nanostructures. *Appl. Phys. Lett.*, 102:112401, 2013.
- [107] C. Phatak, A. K. Petford-Long, and O. Heinonen. Direct observation of unconventional topological spin structure in coupled magnetic discs. *Phys. Rev. Lett.*, 108:067205, 2012.
- [108] S. Wintz, C. Bunce, A. Neudert, M. Körner, T. Strache, M. Buhl, A. Erbe, S. Gemming, J. Raabe, C. Quitmann, and J. Fassbender. Topology and Origin of Effective Spin Meron Pairs in Ferromagnetic Multilayer Elements. *Phys. Rev. Lett.*, 110:177201, 2013.
- [109] J. Rothman, M. Kläui, L. Lopez-Diaz, C. A. F. Vaz, A. Bleloch, J. A. C. Bland, Z. Cui, and R. Speaks. Observation of a bi-domain state and nucleation free switching in mesoscopic ring magnets. *Phys. Rev. Lett.*, 86:1098–1101, 2001.
- [110] S. Mühlbauer, B. Binz, F. Jonietz, C. Pfleiderer, A. Rosch, A. Neubauer, R. Georgii, and P. Böni. Skyrmion lattice in a chiral magnet. *Science*, 323:915–919, 2009.
- [111] P. Ferriani, K. von Bergmann, E. Y. Vedmedenko, S. Heinze, M. Bode, M. Heide, G. Bihlmayer, S. Blügel, and R. Wiesendanger. Atomic-scale spin

- spiral with a unique rotational sense: Mn monolayer on W(001). *Phys. Rev. Lett.*, 101:027201, 2008.
- [112] S. V. Grigoriev, Yu. O. Chetverikov, D. Lott, and A. Schreyer. Field induced chirality in the helix structure of Dy/Y multilayer films and experimental evidence for Dzyaloshinskii-Moriya interaction on the interfaces. *Phys. Rev. Lett.*, 100:197203, May 2008.
- [113] M. Heide, G. Bihlmayer, and S. Blügel. Dzyaloshinskii-Moriya interaction accounting for the orientation of magnetic domains in ultrathin films: Fe/W(110). *Phys. Rev. B*, 78:140403, 2008.
- [114] Ryo Hiramatsu, Kab-Jin Kim, Yoshinobu Nakatani, Takahiro Moriyama, and Teruo Ono. Proposal for quantifying the Dzyaloshinskii-Moriya interaction by domain walls annihilation measurement. *Jpn. J. Appl. Phys.*, 53:108001, 2014.
- [115] M. J. Benitez, A. Hrabec, a. P. Mihai, T. A. Moore, G. Burnell, D McGrouther, C H Marrows, and S McVitie. Magnetic microscopy of topologically protected homochiral domain walls in an ultrathin perpendicularly magnetized co film. *arXiv*, 1503:07668, 2015.
- [116] A. Butenko, A. Leonov, A. Bogdanov, and U. Rößler. Theory of vortex states in magnetic nanodisks with induced Dzyaloshinskii-Moriya interactions. *Phys. Rev. B*, 80:134410, 2009.
- [117] Weiwei Wang, Maximilian Albert, Marijan Beg, Marc-Antonio Bisotti, Dmitri Chernyshenko, David Cortés-Ortuño, Ian Hawke, and Hans Fangohr. Magnon-driven domain-wall motion with the Dzyaloshinskii-Moriya interaction. *Phys. Rev. Lett.*, 114:087203, 2015.
- [118] Riccardo Hertel and Claus Schneider. Exchange Explosions: Magnetization Dynamics during Vortex-Antivortex Annihilation. *Phys. Rev. Lett.*, 97(17):177202, October 2006.
- [119] R. Hertel, S. Gliga, M. Fähnle, and C. M. Schneider. Ultrafast nanomagnetic toggle switching of vortex cores. *Phys. Rev. Lett.*, 98(March):1–4, 2007.

- [120] W. Dring. Point singularities in micromagnetism. *J. Appl. Phys.*, 39(2):1006–1007, 1968.
- [121] Christian Andreas, Sebastian Gliga, and Riccardo Hertel. Numerical micromagnetism of strong inhomogeneities. *J. Magn. Magn. Mater.*, 362:7 – 13, 2014.
- [122] Christian Andreas, Sebastian Gliga, and Riccardo Hertel. Numerical micromagnetism of strong inhomogeneities. *J. Magn. Magn. Mater.*, 362:7 – 13, 2014.
- [123] R. P. Cowburn, D. K. Koltsov, A. O. Adeyeye, M. E. Welland, and D. M. Tricker. Single-domain circular nanomagnets. *Phys. Rev. Lett.*, 83:1042–1045, Aug 1999.
- [124] S. Pizzini, J. Vogel, S. Rohart, L. D. Buda-Prejbeanu, E. Jué, O. Boulle, I. M. Miron, C. K. Safeer, S. Auffret, G. Gaudin, and A. Thiaville. Chirality-induced asymmetric magnetic nucleation in Pt/Co/AlO<sub>x</sub> ultrathin microstructures. *Phys. Rev. Lett.*, 113:047203, 2014.
- [125] Felipe Garcia-Sanchez, Pablo Borys, Arne Vansteenkiste, Joo-Von Kim, and Robert L. Stamps. Nonreciprocal spin-wave channeling along textures driven by the Dzyaloshinskii-Moriya interaction. *Phys. Rev. B*, 89:224408, 2014.
- [126] S. McVitie, D. McGrouther, S. McFadzean, D.A. MacLaren, K.J. OShea, and M.J. Benitez. Aberration corrected Lorentz scanning transmission electron microscopy. *Ultramicroscopy*, 152:57 – 62, 2015.
- [127] M. A. Basith, S. McVitie, D. McGrouther, J. N. Chapman, and J. M. R. Weaver. Direct comparison of domain wall behavior in permalloy nanowires patterned by electron beam lithography and focused ion beam milling. *J. Appl. Phys.*, 110(8):–, 2011.
- [128] Linus Pauling. The structure and entropy of ice and of other crystals with some randomness of atomic arrangement. *J. Am. Chem. Soc.*, 57(12):2680–2684, 1935.



- [129] M. J. Harris, S. T. Bramwell, D. F. McMorrow, T. Zeiske, and K. W. Godfrey. Geometrical frustration in the ferromagnetic pyrochlore  $\text{Ho}_2\text{Ti}_2\text{O}_7$ . *Phys. Rev. Lett.*, 79:2554–2557, 1997.
- [130] R. F. Wang, C. Nisoli, R. S. Freitas, J. Li, W. McConville, B. J. Cooley, M. S. Lund, N. Samarth, C. Leighton, V. H. Crespi, and P. Schiffer. Artificial spin ice in a geometrically frustrated lattice of nanoscale ferromagnetic islands. *Nature*, 439:303–306, 2006.
- [131] M. Tanaka, E. Saitoh, H. Miyajima, T. Yamaoka, and Y. Iye. Magnetic interactions in a ferromagnetic honeycomb nanoscale network. *Phys. Rev. B*, 73:052411, 2006.
- [132] Cristiano Nisoli, Roderich Moessner, and Peter Schiffer. *Colloquium: Artificial spin ice: Designing and imaging magnetic frustration.* *Rev. Mod. Phys.*, 85:1473–1490, 2013.
- [133] J Cumings, L J Heyderman, C H Marrows, and R L Stamps. Focus on artificial frustrated systems. *New. J. Phys.*, 16(7):075016, 2014.
- [134] T. Fennell, P. P. Deen, A. R. Wildes, K. Schmalzl, D. Prabhakaran, A. T. Boothroyd, R. J. Aldus, D. F. McMorrow, and S. T. Bramwell. Magnetic coulomb phase in the spin ice  $\text{Ho}_2\text{Ti}_2\text{O}_7$ . *Science*, 326:415–417, 2009.
- [135] D. J. P. Morris, D. A. Tennant, S. A. Grigera, B. Klemke, C. Castelnovo, R. Moessner, C. Czternasty, M. Meissner, K. C. Rule, J.-U. Hoffmann, K. Kiefer, S. Gerischer, D. Slobinsky, and R. S. Perry. Dirac strings and magnetic monopoles in the spin ice  $\text{Dy}_2\text{Ti}_2\text{O}_7$ . *Science*, 326:411–414, 2009.
- [136] S. Ladak, D. E. Read, G. K. Perkins, L. F. Cohen, and W. R. Branford. Direct observation of magnetic monopole defects in an artificial spin-ice system. *Nat Phys*, 6:359–363, 2010.
- [137] E. Mengotti, L. J. Heyderman, A.F. Rodriguez, F. Nolting, R.V. Hugli, and H. Braun. Real-space observation of emergent magnetic monopoles and associated dirac strings in artificial kagome spin ice. *Nat Phys*, 7:68–74, 2011.

- [138] S. T. Bramwell, S. R. Giblin, S. Calder, R. Aldus, D. Prabhakaran, and T. Fennell. Measurement of the charge and current of magnetic monopoles in spin ice. *Nature*, 461:956–959, 2009.
- [139] R. P. Loreto, L. A. Morais, C. I. L. de Araujo, W. A. Moura-Melo, A. R. Pereira, R. C. Silva, F. S. Nascimento, and L. A. S. Møl. Emergence and mobility of monopoles in a unidirectional arrangement of magnetic nanoislands. *Nanotechnology*, 26:295303, 2015.
- [140] V. Kapaklis, U. B. Arnalds, A. Farhan, R. V. Chopdekar, Balan A., A. Scholl, L. J. Heyderman, and B. Hjorvarsson. Thermal fluctuations in artificial spin ice. *Nature Nanotechnology*, 9:514–519, 2014.
- [141] M Krawczyk and D Grundler. Review and prospects of magnonic crystal-sand devices with reprogrammable band structure. *J. Phys. Condens. Matter*, 26(12):123202, 2014.
- [142] J M Porro, A Bedoya-Pinto, A Berger, and P Vavassori. Exploring thermally induced states in square artificial spin-ice arrays. *New. J. Phys.*, 15(5):055012, 2013.
- [143] R. F. Wang, J. Li, W. McConville, C. Nisoli, X. Ke, J. W. Freeland, V. Rose, M. Grimsditch, P. Lammert, V. H. Crespi, and P. Schiffer. Demagnetization protocols for frustrated interacting nanomagnet arrays. *J. Appl. Phys.*, 101(9):–, 2007.
- [144] Sheng Zhang, Ian Gilbert, Cristiano Nisoli, Gia-Wei Chern, Michael J Erickson, Liam O’Brien, Chris Leighton, Paul E Lammert, Vincent H Crespi, and Peter Schiffer. Crystallites of magnetic charges in artificial spin ice. *Nature*, 500(7464):553–7, August 2013.
- [145] A. Farhan, P. M. Derlet, A. Kleibert, A. Balan, R. V. Chopdekar, M. Wyss, J. Perron, A. Scholl, F. Nolting, and L. J. Heyderman. Direct observation of thermal relaxation in artificial spin ice. *Phys. Rev. Lett.*, 111:057204, 2013.

- [146] J. P. Morgan, A. Stein, S. Langridge, and C. H. Marrows. Thermal ground-state ordering and elementary excitations in artificial magnetic square ice. *Nat Phys*, 7:75–79, 2011.
- [147] R.L. Stamps. Private communication. 2014.
- [148] B. L. Le, D. W. Rench, R. Misra, L. O'Brien, C. Leighton, N. Samarth, and P. Schiffer. Effects of exchange bias on magnetotransport in permalloy kagome artificial spin ice. *New. J. Phys.*, 17:023047, 2015.
- [149] V. Kapaklis, U. B. Arnalds, A. Harman-Clarke, E. T. Papaioannou, M. Karimipour, P. Korelis, A. Taroni, P. C. W. Holdsworth, S. T. Bramwell, and B. Hjörvarsson. Melting artificial spin ice. *New. J. Phys.*, 14:035009, 2012.
- [150] X. Ke, J. Li, S. Zhang, C. Nisoli, V. H. Crespi, and P. Schiffer. Tuning magnetic frustration of nanomagnets in triangular-lattice geometry. *Appl. Phys. Lett.*, 93:252504, 2008.
- [151] C. Phatak, Y. Liu, E. B. Gulsoy, D. Schmidt, E. Franke-Schubert, and A. Petford-Long. Visualization of the magnetic structure of sculpted three-dimensional cobalt nanospirals. *Nano Lett.*, 14:759–764, 2014.
- [152] S McVitie and M. Krajenak. Private communication. 2015.
- [153] A. A. Stashkevich, M. Belmeguenai, Y. Roussigné, S. M. Cherif, M. Kostylev, M. Gabor, D. Lacour, C. Tiusan, and M. Hehn. Experimental study of spin-wave dispersion in Py/Pt film structures in the presence of an interface Dzyaloshinskii-Moriya interaction. *Phys. Rev. B*, 91:214409, 2015.
- [154] Hans T. Nembach, Justin M. Shaw, Mathias Weiler, Emilie Jue, and Thomas J. Silva. Linear relation between heisenberg exchange and interfacial dzyaloshinskiimoriya interaction in metal films. *Nat Phys*, advance online publication:1745–2481, 2015.
- [155] Riccardo Hertel. Magnetic nanostructures: Vortex states à la carte. *Nature nanotechnology*, 8(5):318–20, May 2013.

- 
- [156] S. S. P. Parkin and S. Yang. Memory on the racetrack. *Nat. Nanotechnol.*, 10:195, 2015.
- [157] X. Z. Yu, N. Kanazawa, Y. Onose, K. Kimoto, W. Z. Zhang, S. Ishiwata, Y. Matsui, and Y. Tokura. Near room-temperature formation of a skyrmion crystal in thin-films of the helimagnet fege. *Nat. Mater.*, 10:106–109, 2011.
- [158] Wanjun Jiang, Pramey Upadhyaya, Wei Zhang, Guoqiang Yu, M. Benjamin Jungfleisch, Frank Y. Fradin, John E. Pearson, Yaroslav Tserkovnyak, Kang L. Wang, Olle Heinonen, Suzanne G. E. te Velthuis, and Axel Hoffmann. Blowing magnetic skyrmion bubbles. *Science*, 349:283–286, 2015.
- [159] Xichao Zhang, G. P. Zhao, Hans Fangohr, J. Ping Liu, W. X. Xia, J. Xia, and F. J. Morvan. Skyrmion-skyrmion and skyrmion-edge repulsions in skyrmion-based racetrack memory. *Sci. Rep.*, 5:7643, 2015.
- [160] C. Pfleiderer A. Neubauer W. Münzer1 A. Bauer T. Adams R. Georgii P. Böni R. A. Duine K. Everschor M. Garst A. Rosch F. Jonietz, S. Mühlbauer. Spin transfer torques in MnSi at ultralow current densities. *Science*, 330:1648, 2010.
- [161] D. Grundler. Reconfigurable magnonics heats up. *Nat Phys*, 11:438–441, 2015.



## Nmag interpolation

```
function []=InterpNmag(file,newmesh,DW)
% function []=InterpNmag(file,newmesh,DW)
% CA Ferguson Jan 2013
% Takes an Nmag result of relaxed magnetisation in a cylindrical nanowire
% or nanotube, from the .h5 output file given by the variable "file", and
% interpolates the result onto a new mesh geometry, "newmesh", generated by
% Netgen. Results can be interpolated from and to hollow and solid
% cylinders.

% Read 3xN matrix that gives x, y, z coordinates, separate into
% vectors of x, y, z
points=h5read(file,'/mesh/points');
```

```
x=double(points(1,:));
y=double(points(2,:));
z=double(points(3,:));

% Read magnetisation data from file, separate in to Mx, My, Mz components
% for initial and final states
M=h5read(file,'/data/fields/M');
Mag=M.M_Py;
M_final=Mag(:,:,2);

Mx=double(M_final(1,:));
My=double(M_final(2,:));
Mz=double(M_final(3,:));

% Read points for new mesh
newpoints=h5read(newmesh,'/mesh/points');
xn=double(newpoints(1,:));
yn=double(newpoints(2,:));
zn=double(newpoints(3,:));
newpoints=double(newpoints);

% Scaling of the x-axis values, the long axis of the wire
if max(x(:))==max(xn(:))
    stx=x;
else
    stx=x*(max(xn)/max(x));
end

% Basically stretching or shrinking the original points
```

```
[~,newr]=cart2pol(yn,zn); % Theta and r values from new points
[th,r]=cart2pol(y,z);
```

```
if min(r)<min(newr)
    r=r*((max(yn)-(min(newr)-min(r)))/max(y));
    r=r+(min(newr)-min(r));
    [sty,stz]=pol2cart(th,r);
elseif min(r)>min(newr)
    r=r*((max(yn)-(min(newr)+min(r)))/max(y));
    r=r+(min(newr)+min(r));
    [sty,stz]=pol2cart(th,r);
end
```

```
% Interpolation of old magnetisation components onto new mesh. Method
% nearest needs to be used here.
```

```
NewMx=griddata(stx,sty,stz,Mx,xn,yn,zn,'nearest');
NewMy=griddata(stx,sty,stz,My,xn,yn,zn,'nearest');
NewMz=griddata(stx,sty,stz,Mz,xn,yn,zn,'nearest');
```

```
NewM=[NewMx;NewMy;NewMz];
```

```
% Create wee filenames for the output files
```

```
if min(newr)<1
    filename=[DW 'on' num2str(max(stx(:))*2) '_r' num2str(max(yn))];
else
    filename=[DW 'on' num2str(max(stx(:))*2) '_r' num2str(max(yn)) 'i' num2str(
end
```

```
% Nmag uses python, easy to read csv files.
```

```
dlmwrite([filename '.csv'],NewM');
```

# B

## Artificial spin ice processing from Fresnel image

```
function [R]=SpinIce(file,K,thresh,M,Tcorr,Q)

% Import dm3 file and remove image ramp found in images from 3/6/15 ARM
% session
D=DM3Import(file);
I=D.image_data;
xlin=linspace(1,470,4008);

% Manually checked image ramp, this seems to flatten OK
[X,~]=meshgrid(xlin,1:size(I,2));
Iflat=I-X';
```



```

% Threshold Fresnel image, need to find optimal value manually. Easier to
% use rotated array.
Ibin=I<thresh;
Irot=imrotate(Ibin,53);
% Xcorr requires double, rather than logical array
Ithresh=Irot.*ones(size(Irot,1),size(Irot,2));

% Cross-correlation of thresholded Fresnel image with kernel. Rotate
% kernel by 90, 180 & 270 degrees to get all four orientations of
% magnetisation in separate arrays.
R=xcorr2(Ithresh,K);R2=xcorr2(Ithresh,rot90(K));
R3=xcorr2(Ithresh,rot90(K,2));R4=xcorr2(Ithresh,rot90(K,3));

% Thresholding the Xcorr arrays. Optimisation is done manually. This gives
% lattice of points corresponding to different directions of magnetisation.
Rthresh=R>Tcorr;
Rthresh2=R2>Tcorr;Rthresh3=R3>Tcorr;Rthresh4=R4>Tcorr;
Rthreshd=Rthresh.*ones(size(R,1),size(R,2));
Rthreshd2=Rthresh2.*ones(size(R2,1),size(R2,2));
Rthreshd3=Rthresh3.*ones(size(R3,1),size(R3,2));
Rthreshd4=Rthresh4.*ones(size(R4,1),size(R4,2));

% Convolve lattice for each direction of magnetisation with a suitable
% motif - an arrow or plus/minus symbol.
C=conv2(Rthreshd,M);
C2=conv2(Rthreshd2,rot90(M));
C3=conv2(Rthreshd3,rot90(M,2));
C4=conv2(Rthreshd4,rot90(M,3));

% Thresholding of convolution.

```

```

% Process for adding four directions together is slightly different when
% using arrows compared to plus/minus. For arrows (first condition) four different
% colours are required, therefore multiply arrays by different factors.
if strcmp(Q,'Q')==0
    Cthresh=(C==0);
    Cthresh2=(C2==0);
    Cthresh3=(C3==0);
    Cthresh4=(C4==0);
    Ct=Cthresh.*ones(size(C,1),size(C,2));
    Ct2=Cthresh2.*ones(size(C2,1),size(C2,2))*2;
    Ct3=Cthresh3.*ones(size(C3,1),size(C3,2))*3;
    Ct4=Cthresh4.*ones(size(C4,1),size(C4,2))*4;
else
    Cm=C<0.*ones(size(C,1),size(C,2));Cp=C>0.*ones(size(C,1),size(C,2));
    Cm2=C2<0.*ones(size(C,1),size(C,2));Cp2=C2>0.*ones(size(C,1),size(C,2));
    Cm3=C3<0.*ones(size(C,1),size(C,2));Cp3=C3>0.*ones(size(C,1),size(C,2));
    Cm4=C4<0.*ones(size(C,1),size(C,2));Cp4=C4>0.*ones(size(C,1),size(C,2));
    Ct=(Cm*-1+Cp);Ct2=(Cm2*-1+Cp2);Ct3=(Cm3*-1+Cp3);Ct4=(Cm4*-1+Cp4);
end

% Final array
A=Ct+Ct2+Ct3+Ct4;

figure('name',[num2str(thresh) ' / ' num2str(Tcorr)]);
imagesc(A);axis equal tight;
colormap jet;fig=gcf;%caxis([-2 1.5]);
set (fig, 'Units', 'normalized', 'Position', [0,0,1,1]);

```